Numerical modelling of electrical stimulation for cartilage tissue engineering

Dissertation
zur
Erlangung des akademischen Grades
Doktor-Ingenieur (Dr.-Ing.)
der Fakultät für Informatik und Elektrotechnik
der Universität Rostock

vorgelegt von

Julius Zimmermann, geboren am 10.02.1994 in Winsen/Luhe
aus Rostock

Rostock, 29.08.2022

Tag der Verteidigung: 09.12.2022

Gutachter:
Prof. Dr. Ursula van Rienen, Universität Rostock
Prof. Dr. Ludger Klinkenbusch, Christian-Albrechts-Universität Kiel
Prof. Dr. Rüdigker Köhling, Universitätsmedizin Rostock

https://doi.org/10.18453/rosdok_id00004117

Acknowledgement

Without the support of many people, I could not have finished this thesis. I would like to thank:

- Ursula van Rienen for acquiring the funding for my PhD project and supervising my work. In particular, I would like to thank you for giving me a lot of freedom, supporting my ideas and sharing your experience with me.
- Professor Klinkenbusch and Professor Köhling for agreeing to review the thesis.
- Kai Budde for many fruitful discussions, critical proofreading and the good collaboration.
- Nils Arbeiter and Henning Bathel for supporting the realisation of many experiments and for tolerating me as an office mate.
- Simon Adrian, Pawel Naliwajko and the rest of the Mensa team.
- the BioEM team (in particular Andrea Andree, Konstantin Butenko, Hendrikje Raben, Lam Vien Che and Abdul Farooqi) for fruitful discussions, sharing code and ideas, coffee breaks and conference visits.
- Kathrin Krebs, Jörg Romahn, Dirk Hecht and Bernhard Himmel for their support to cope with bureaucracy and technical issues.
- the ELAINE consortium (in particular Francia Molina, Alexander Storch, Franziska Sahm, Ingo Speller, Regina Lange, Sylvia Speller, Adelinde Uhrmacher, Michael Dau, Anika Jonitz-Heincke, Rainer Bader, Frank Krüger and Max Schröder) for fruitful collaboration, providing devices and IT infrastructure, giving access to their labs, sharing ideas, critical assessment of my ideas and critical reading of manuscripts.
- the German Research Foundation (DFG) for generous funding.
- my friends and family for moral support and great shared experiences that make my PhD time unforgettable. And lastly also for calling me out to finally finish this work.

Abstract

Cartilage regeneration is an open clinical challenge. In particular, novel treatment approaches for articular cartilage lesions in, for example, the knee joint are urgently required in an ageing society. Due to the low intrinsic healing capacity of cartilage, external stimuli are assessed with the aim to foster chondrogenesis. The final goal is to engineer functional cartilage tissue to treat the lesion. Among the external stimuli, electrical stimulation is a versatile biophysical approach that can be applied in vitro to a cell culture or a cartilage-like scaffold but also in vivo directly to the lesioned tissue. As a physical intervention, it can be tuned in multiple ways by choosing, among others, different electrode configurations and stimulation signals. The main challenge lies in the accurate understanding and control of the applied stimulation. The local electric fields and current densities have to be known to quantify the interaction with the stimulated cartilage cells. To achieve this goal, numerical models of the electrical stimulation are usually considered.

In this thesis, the design and validity of the numerical models are critically assessed at different scales. In the first part, in vitro stimulation devices are studied at the macroscopic scale. Experimental concepts to validate the numerical models are introduced. Eventually, a so-called digital twin is realised. The digital twin permits to predict relevant stimulation properties on both the global and local level after initial experimental calibration. Thus, it can be used to control the applied stimulus and monitor the state of the stimulation device. Electrochemistry, particularly at the electrode-sample interface, plays a pivotal role in the understanding of an electrical stimulation device. Hence, special attention is paid to different methods that integrate electrochemistry into the numerical models. Finally, clear guidelines to develop reliable numerical models are formulated. In the second part, numerical models of single cells in capacitively coupled stimulation devices are investigated. Uncertainty quantification techniques are used to study the influence of model parameters on the induced transmembrane potential, which serves as a marker to quantify the stimulation effect. The results contribute to the planning of future experiments that are required to test hypotheses based on the numerical results. In the third part, cell geometries and distributions as they occur in small to medium-sized cartilage samples are investigated. A main focus is laid on the tissue dielectric properties because it is shown that literature resources do not provide unambiguous reference values. Numerical simulations are explored to gain a better understanding of the dielectric properties and to resolve the ambiguity. To cope with the complexity of the numerical models, high-performance computing solutions are introduced. In sum, the results of this thesis pave the way for experimentally validated numerical models of electrical stimulation devices for cartilage tissue engineering. Furthermore, models of tissue samples can be developed down to the cellular scale and will contribute to the development of patient-specific stimulation approaches.

Zusammenfassung

Therapeutische Ansätze zur Knorpelregeneration werden dringend benötigt. Besonders die Behandlung von Gelenkknorpelerkrankungen, zum Beispiel im Knie, ist in einer alternden Gesellschaft von großer Bedeutung. Da Knorpel kaum selbstständig heilt, soll das Gewebe durch externe Stimuli zur Heilung angeregt werden. Das Ziel ist, gesundes und funktionales Gewebe zu züchten. Elektrostimulation ist ein Ansatz, der vielseitig eingesetzt werden kann: in der Zellkultur aber auch direkt im Körper. Da es sich um eine physikalische Methode handelt, können verschiedene Parameter, zum Beispiel die Elektroden oder der Stimulationspuls, eingestellt werden. Die Herausforderung liegt im genauen Verständnis und einhergehend damit der Kontrolle des applizierten Stimulus. Die lokalen elektrischen Felder und Stromdichten müssen bekannt sein, um die Interaktion des Stimulus mit den Knorpelzellen zu quantifizieren. Um dieses Ziel zu erreichen werden üblicherweise numerische Modelle herangezogen.

In dieser Arbeit werden das Design und die Validität von numerischen Modellen auf verschiedenen Skalen evaluiert. Im ersten Teil werden Stimulationsgeräte betrachtet. Experimentelle Konzepte zur Validierung werden vorgestellt. Schlussendlich wird ein sogenannter digitaler Zwilling realisiert. Damit können relevante globale und lokale Stimulationsparameter nach initialer Kalibrierung vorhergesagt werden. Dadurch wird es möglich, die elektrische Stimulation zu kontrollieren und den Zustand des Stimulationsgeräts zu überwachen. Elektrochemische Prozesse, vor allem an der Elektrodenoberfläche, sind von besonderer Bedeutung für die Analyse von Stimulationsgeräten. Daher werden verschiedene Methoden zur Berücksichtigung elektrochemischer Effekte in numerischen Modellen evaluiert. Abschließend wird ein Leitfaden zur Entwicklung zuverlässiger numerischer Modelle formuliert. Im zweiten Teil werden numerische Modelle von einzelnen Zellen in kapazitiv gekoppelten Stimulationsgeräten betrachtet. Numerische Quantifizierung von Unsicherheiten (*uncertainty quantification*) wird genutzt, um den Einfluss einzelner Modellparameter auf das induzierte Transmembranpotential, welches eine Kennzahl für die Elektrostimulation ist, zu bestimmen. Die Ergebnisse tragen zu der Planung zukünftiger Experimente bei durch Hypothesen, die aus den numerischen Ergebnissen abgeleitet werden. Im dritten Teil werden Zellverbünde untersucht, wie sie in kleinen bis mittelgroßen Knorpelproben erwartet werden. Der Hauptfokus liegt auf den dielektrischen Gewebeeigenschaften, weil gezeigt wird, dass die vorhandenen Literaturdaten keine eindeutigen Referenzwerte liefern. Numerische Simulationen liefern einen Beitrag zum besseren Verständnis der dielektrischen Eigenschaften und tragen zur Aufklärung der uneindeutigen Referenzdaten bei. Aufgrund der Komplexität der Modelle werden Lösungen zum Einsatz auf Hochleistungsrechnern vorgestellt. Zusammenfassend legen die Ergebnisse dieser Arbeit den Grundstein für validierte numerische Modelle von Elektrostimulationsgeräten für die Knorpelgewebekonstruktion. Weiterhin trägt diese Arbeit zur Entwicklung von patientenspezifischen Stimulationsansätzen mit Gewebemodellen, die bis auf die zelluläre Skala reichen, bei.

Preface

The research that is presented in this thesis was conducted within the collaborative research centre SFB 1270 'Electrically Active Implants' - ELAINE, funded by the Deutsche Forschungsgemeinschaft (DFG, German Research Foundation) - 299150580.
Owing to the interdisciplinary setting of this project, I will try to make the methods and conclusions in this thesis as accessible as possible for a broad readership. However, not every aspect can be covered in great detail. Thus, I will refer the reader as often as possible to textbooks that can give a more detailed introduction and overview of the covered topics.

Generally, I will use the following notation:

- j is the imaginary unit (i.e., $\mathsf{j}^2 = -1$ by definition).
- Complex numbers are usually given in the complex plane, for example $z = a + \mathsf{j}b$. The real part of z is $\mathrm{Re}\ z = a$ and the imaginary part is $\mathrm{Im}\ z = b$. The absolute value of z is $|z| = \sqrt{a^2 + b^2}$. The phase or argument of z is $\phi = \arg z = \arctan(\mathrm{Im}\ z, \mathrm{Re}\ z)$. The complex conjugate is $z^* = a - \mathsf{j}b$. Please note that it is usual in some communities to define, for example, the complex permittivity as ε^* [1]. To avoid confusion with regard to the complex conjugate, I follow the notation of Harrington [2] and define the complex permittivity as $\hat{\varepsilon}$.
- Scalars are denoted by regular math symbols. For example, the electric current is written as I.
- Vectors are denoted by bold symbols. For example, the electric field is written as $\mathbf{E}$.
- Cartesian coordinates are used unless otherwise stated. Vector operations are defined following the classical textbook of Jackson [3].
- When alternating current (AC) signals are covered, they are reported in phasor notation using the amplitude and – if applicable – their phase.
- SI units are used throughout the entire thesis.

Contents

Acronyms

AC	alternating current
ACI	autologous chondrocyte implantation
AMG	algebraic multigrid
BEM	boundary element method
BC	boundary condition
BiCGSTAB	biconjugate gradient stabilized method
CAD	computer-aided design
CG	conjugate gradient
CPE	constant-phase element
DBS	deep brain stimulation
DC	direct current
DMEM	Dulbecco's Modified Eagle's Medium
DOF	degree of freedom
ECM	extracellular matrix
EDL	electrochemical double layer
EDX	energy dispersive x-ray analysis
EEI	electrode-electrolyte interface
EIS	electrochemical impedance spectroscopy
EIT	electrical impedance tomography
ELN	electronic lab notebook
EQS	electroquasistatic
ESI	electrode-sample interface
ETI	electrode-tissue interface
FEM	finite element method
FFT	fast Fourier transform
GMG	geometric multigrid
GMRES	generalized minimal residual method
HPC	high-performance computing
ILU	incomplete LU factorization
MACI	matrix-assisted autologous chondrocyte implantation
MPI	message passing interface
MST	Maxwell stress tensor
MQS	magnetoquasistatic
OCCT	Open CASCADE Technology
PEEK	polyether ether ketone

PEMF	pulsed electromagnetic field stimulation
PDE	partial differential equation
RMS	root-mean-square
UQ	uncertainty quantification
TFQMR	transpose-free quasi-minimal residual method
VVUQ	validation, verification, uncertainty quantification

1 Introduction

Cartilage is a versatile tissue that appears in different types and functions in the human body. Three cartilaginous tissues can be distinguished: elastic cartilage, fibrocartilage and hyaline cartilage [4]. Elastic cartilage can be found in the outer ear while intervertebral discs or the knee meniscus consist of fibrocartilage. Examples for the most common type, hyaline cartilage, are the nasal septum, costal cartilage connecting the ribs and the sternum and articular cartilage, which is, for example, present in the knee joint (Fig. 1.1) [5, 6]. There, hyaline articular cartilage acts as a lubricant and shock absorber [4, 6]. Thus, it has high relevance for pain-free articulation and protection of the joint. Due to its clinical relevance, the focus in this work will be on articular cartilage.

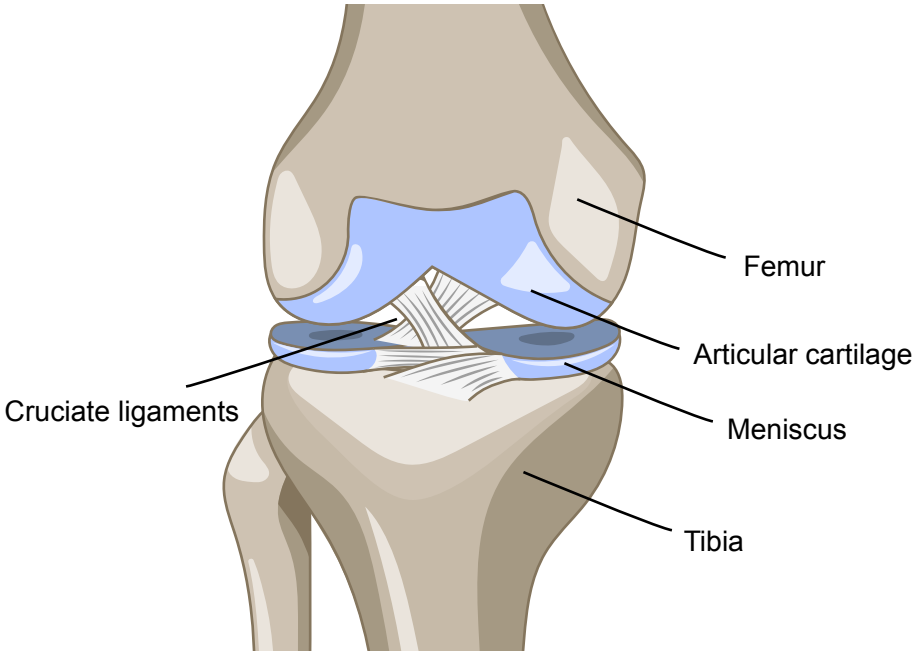

Figure 1.1: Front view of the knee joint. There is also articular cartilage below the meniscus, which is here not explicitly shown. This figure is a derivative of an image by the Database Center for Life Science (DBCLS), used under Creative Commons Attribution 4.0 International. It is licensed under the same license by me.

Cartilage is avascular (i.e., devoid of blood vessels) and has no lymphatics or nerves [6]. Hence, there is no direct supply of nutrients. Cartilage consists of the extracellular matrix, the pericellular matrix and the chondrocytes, which are the characteristic and predominant cells. The extracellular matrix of articular cartilage is composed of interstitial fluid (water, 60 to 80% of wet weight), fibrous proteins (mostly collagen fibres, about 10 to 30%) and polysaccharides (mostly negatively charged glycosaminoglycans) [4, 5, 7]. The volume fraction of the chondrocytes is

reported to be about 5% to 10% [7, 8], but there are also reports estimating it to be rather 1% to 2% [9]. Importantly, Hunziker *et al.* have pointed out differences between human and animal cartilage regarding the cell density [9].

The composition of the extracellular matrix marks the difference between the cartilage types: fibrocartilage contains more collagen fibres, which are densely braided and align the chondrocytes, while elastic cartilage has more fibres branched in different directions [4]. Moreover, the type of the collagen fibres vary. Type I collagen can be found in fibrocartilage in addition to type II collagen, which is the major component of hyaline cartilage. The chondrocytes maintain the extracellular matrix by protein synthesis. There exist different zones of the extracellular matrix (Fig. 1.2) [9]. The calcified zone connects the cartilage to the bone. The superficial zone contains flat and elliptic cells (oriented parallel to the cartilage surface), while the cells in the transitional zone (sometimes called middle zone [10]) are rounder, almost spherical. In the radial or deep zone, a few chondrocytes are organised in chondrons. The chondron comprises the chondrocyte and its pericellular matrix [11]. In the superficial and transitional zones, there is usually only one cell per chondron [9]. The pericellular matrix contains type VI collagen [11], which distinguishes it from the remaining extracellular matrix. In the deep zone adjacent to the subchondral bone, type X collagen is synthesised and leads to calcification.

The orientation of the collagen fibres varies in the zones [12] (Fig. 1.2B) resulting from maturation, which starts from an unordered fiber network [13]. In the beginning of the maturation process, mesenchymal stem cells differentiate into so-called chondroblasts, which are the precursor cells of chondrocytes [4]. Chondroblasts produce the initial extracellular matrix and divide to form chondrocytes. These chondrocytes spread over the tissue to form mature, healthy cartilage.

Unfortunately, cartilage has a very low intrinsic healing capacity. The main reasons for this limitation are the avascularity and limited replication potential of chondrocytes. Hence, cartilage lesions pose a clinical challenge. Particularly, for ageing societies it can be expected that the majority of the population will be affected by osteoarthritis [14]. Osteoarthritis is the disease that results from cartilage breakdown and leads to constant pain and wear-off of the subchondral bone. For Germany, it has recently been estimated that about 20% of the population had suffered of general osteoarthritis and 10% had suffered of knee osteoarthritis [15]. The probability to be diagnosed with osteoarthritis increases with age. However, also young people might be affected due to sports-related injuries. Furthermore, meniscus tear is related to the deterioration of articular cartilage [16].

Currently, surgical cartilage repair techniques are insufficient and are mostly considered for defects of less than $4\,\mathrm{cm}^2$ [14]. Eventually, a total joint replacement is inevitable for severe cases of osteoarthritis, which manifests itself in an increasing number of joint replacements [17]. To overcome this problem and develop successful interventions at an early stage of the disease, tissue engineering approaches are investigated. Such approaches will be introduced in the next section.

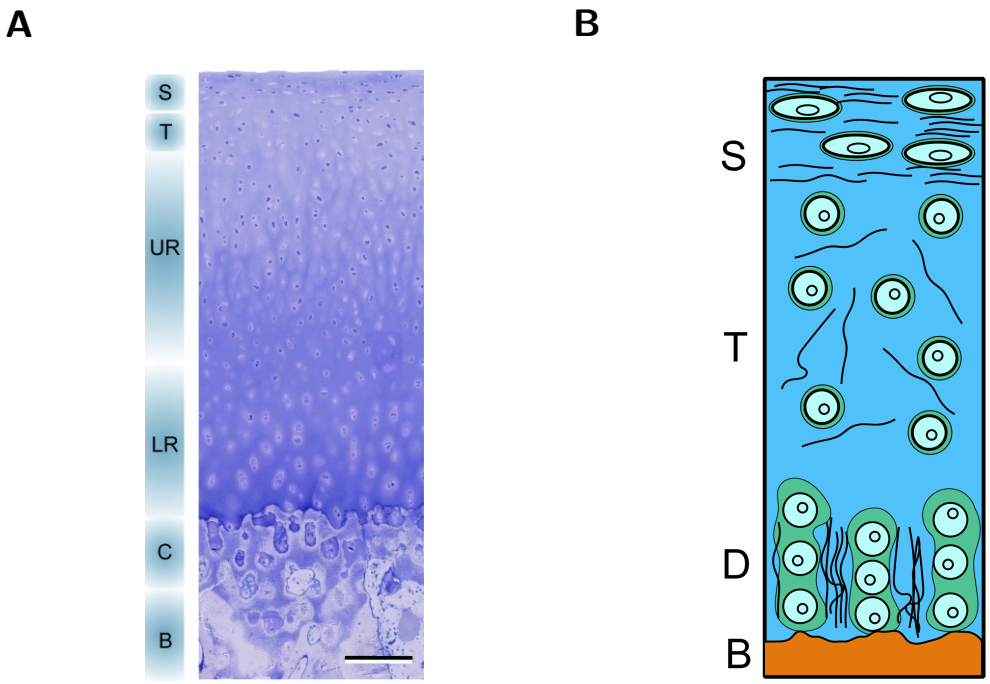

Figure 1.2: Overview of the different cartilage zones. **A**: Light micrograph of bovine articular cartilage (scale bar: 200 µm), re-printed from [18] with permission from Elsevier. The different cartilage zones are marked (S – superficial, T – transitional, UR – upper-radial, LR – lower-radial, C – calcified-cartilage) as well as the subchondral-bone (B). A statistical analysis quantifying the cell distributions in normal adult human articular cartilage has been reported in [9]. **B**: A simplified scheme of the cartilage zones with their characteristic cell shape and organisation is shown. Rounder cells are found in the transitional zone (T), while in the deep zone (D) a few cells are organised in a so-called chondron where the cells are aligned in columns. In contrast, cells in the superficial zone are elongated.

1.1 Repair and engineering of articular hyaline cartilage — open challenges

At first glance, engineering of cartilage appears relatively straightforward: only one cell type is required, vascular networks do not have to be built and simplistic shapes such as disks would suffice to treat certain lesions. Moreover, larger defect areas than in current surgical approaches could be treated [14]. However, unexpected challenges in cartilage tissue engineering have surfaced [5].

Approaches to engineer cartilage combine different scaffold materials, cells and biological or biophysical signals (Fig. 1.3). The tissue engineering cycle (Fig. 1.4) starts with cells. They can come from different sources and can be already differentiated chondrocytes or undifferentiated stem cells (mesenchymal stem cells) [19, 20].

These cells are expanded (i.e., cultured in, for example, a flask until a certain degree of confluency or number of cells is reached). Then, the cells are used for repair (in scaffold-free approaches) or seeded on a scaffold (a so-called 3D culture). Scaffold-free approaches are, for example, autologous chondrocyte implantation (ACI) or microfracturing, while matrix-assisted autologous chondrocyte implantation (MACI) is an example of 3D culture. The disadvantage of 2D culture (i.e., cells grown in a monolayer) is the dedifferentiation of chondrocytes [21–23]. The dedifferentiation manifests itself, for example, by the production of an undesired type of collagen while the chondrocytes lose their chondrogenic phenotype. There exist also cell-free scaffold approaches, which solely rely on scaffolds doped with growth factors [18].

The scaffolds considered for 3D culture are usually hydrogels [24–27]. Hydrogels have the potential to resemble the native extracellular matrix of tissues [28]. From an bioengineering point of view, they are attractive as they can be 3D-printed [29, 30]. Hence, they might pave the way towards patient-specific cartilage repair implants.

In addition to general biocompatibility, engineered constructs have to meet mechanical requirements [31]. Besides this challenge, the produced tissue is often more similar to mechanically inferior fibrocartilage than to hyaline cartilage [5, 22, 26]. The engineered tissue can then not act as, for example, a joint lubricant and cannot replace the native articular cartilage. It remains an open challenge to identify an approach that produces hyaline cartilage with mechanical properties close to the native tissue. One research direction is dedicated to stimuli that can be applied to cells before implantation to improve proliferation or differentiation, cell-seeded scaffolds to mature or the implantation site to improve tissue integration. Mechanical and electromagnetic stimulation are considered for application in cartilage repair and engineering [32]. The reasoning for mechanical stimulation is straightforward: it mimics the cyclic loading that appears during walking. The transduction of the mechanical signals has been investigated and a preliminary understanding of the involved cellular and molecular processes exists [32, 33]. Because it has been found that mechanical signals affect local electrical potentials and currents in the vicinity

of chondrocytes [34, 35], it appears natural to investigate the stimulation with electromagnetic signals for cartilage repair and engineering. In the next section, existing concepts for electromagnetic stimulation of cartilage will be introduced.

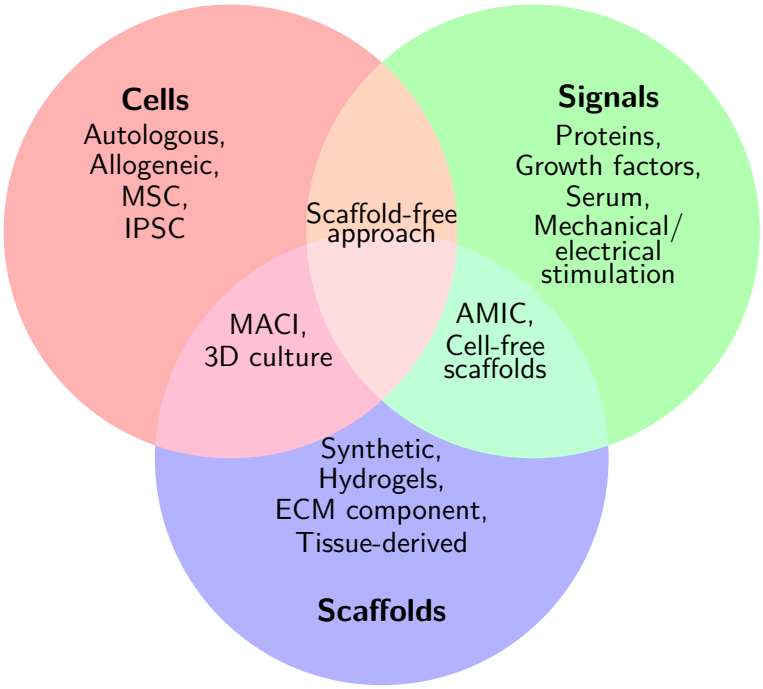

Figure 1.3: Overview of different approaches for cartilage tissue engineering with different ingredients. For example, hydrogels as a scaffold material can be seeded with cells (e.g., mesenchymal stem cells – MSC or induced pluripotent stem cells – IPSC) and implanted (matrix-assisted autologous chondrocyte implantation – MACI). On the other hand, cell-free scaffolds can be implanted and brought in contact with endogenous cells released by microfracturing (autologous matrix-induced chondrogenesis – AMIC). In addition, the scaffolds can be supplemented by, for example, growth factors or preconditioned by mechanical or electrical stimulation. Typically, the scaffolds should resemble the extracellular matrix (ECM). This figure has been inspired by the overview in [22].

1.1.1 The use of electromagnetic fields in cartilage engineering and repair

Electromagnetic stimulation of cartilage can be divided into two competing approaches: pulsed electromagnetic field stimulation (PEMF) and electrical stimulation. PEMF describes the external application of a magnetic field that induces an electric current in the sample to be stimulated [36]. Electrical stimulation comprises all approaches that only use electrical signals (voltage, current) to expose the sample to an electric field.

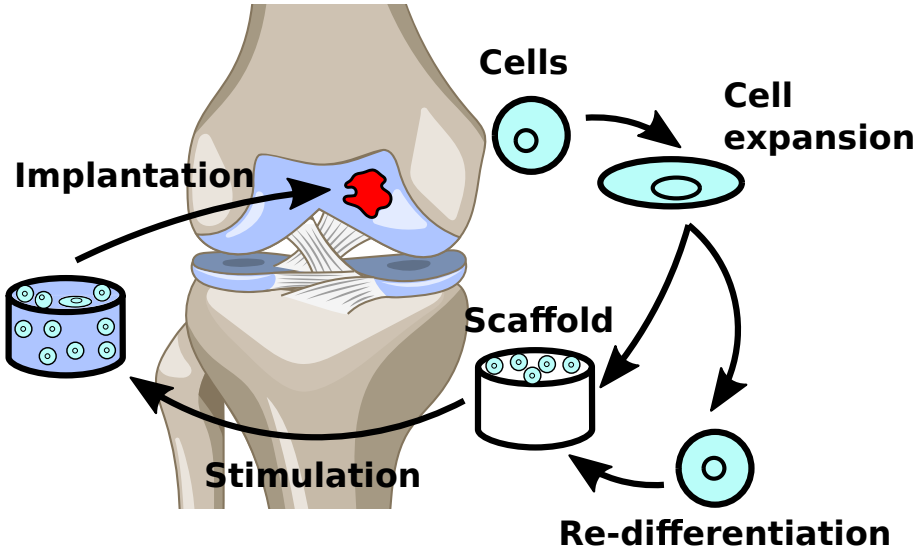

Figure 1.4: Summary of the tissue engineering cycle for cartilage regeneration. Cells are expanded and seeded on a scaffold, which is implanted at the defect site. The chondrogenic phenotype of the cells should be preserved to ensure that articular cartilage forms. This figure is a derivative of an image by the Database Center for Life Science (DBCLS), used under Creative Commons Attribution 4.0 International. It is licensed under the same license by me.

PEMF has been found to suppress an inflammatory response [32, 37]. This effect has also been found in vivo in a canine model when implanting an agarose hydrogel transplant [38]. In addition, improved histological scores have been reported. In the same study, microfracturing was investigated as a clinical control. PEMF in conjunction with microfracturing had no measurable beneficial effect and instead lead to bone thickening (i.e., appears to have stimulated bone growth). This demonstrates a fundamental drawback of PEMF systems: because the coils that produce a stimulating magnetic field are placed outside the body, localised stimulation is a challenge.

In contrast, electrical stimulation can be applied locally. Thus it is the method of choice for electrically active implants for cartilage regeneration. Such implants are the research goal of the collaborative research centre SFB 1270 ELAINE in which this work has been conducted. Naturally, this work is exclusively concerned with electrical stimulation.

Electrical stimulation can be delivered through direct contact of the electrodes with the sample to be stimulated. Alternatively, the electrodes can be insulated and the stimulation is delivered through capacitive coupling (i.e., displacement currents in the usually conductive sample).

In the context of cartilage repair and engineering, capacitive coupling has received much attention. Brighton's group has pioneered this field and established a stim-

ulation protocol [39, 40]. This electrical stimulation protocol has been shown to increase extracellular matrix synthesis [41, 42]. Later, it has been adapted by other researchers who found that similar approaches could support redifferentiation [23] or enhance chondrogenic differentiation of stem cells [43]. Redifferentiation is an important aspect because cultured cartilage cells grown in a monolayer tend to dedifferentiate (i.e., tend to a more fibroblastic phenotype) [21, 23]. Because it has been found that 3D culture (i.e., growing chondrocytes on scaffolds) also supports redifferentiation [21], combining cell-seeded scaffolds and electrical stimulation is currently subject of ongoing research [44]. The need for further research has also been identified by the authors of a recent review on the use of electrical stimulation for osteochondral regeneration of stem cells [45]. They remarked that it "seems that the results in the literature are imperfect with conflicting results" [45].

Under in vitro conditions, direct contact electrical stimulation has been applied to study the alignment and migration of chondrocytes in an external field [46]. Mesenchymal stem cells in culture have differentiated into hyaline chondrogenic cells upon electrical stimulation without the application of external growth factors [47]. Direct contact electrical stimulation has been considered for cartilage repair in rats [48] and rabbits [49]. Furthermore, electrical stimulation for treatment of knee osteoarthritis has been applied using electrodes placed on the skin and covered with conducting gel to ensure direct contact with the body [50–52]. In these studies, it has been reported that the electrical stimulation treatment improved symptoms and knee function. On the other hand, no significant effect has been reported by another group using a similar device [53].

Clinical results are usually compared in so-called systematic reviews, which select existing clinical studies based on certain criteria and give scores to the different studies. Regarding the application of electrical stimulation to cure osteoarthritis, it has been stressed that the results suggest a positive effect regarding improved function, but that more research is needed [54, 55]. Other authors have come to the conclusion that the existing clinical studies on treatment of osteoarthritis by means of electromagnetic fields provide evidence for pain relief but not for physical improvement without further studies [56]. Similarly, there is no solid evidence for the effectiveness of transcutaneous electrical stimulation for knee osteoarthritis [57]. The unclear situation holds also true for other electrical stimulation applications. The application of electrical stimulation for treatment of bone fractures or non-unions may be a benefit [58] but there is not enough evidence to provide clear recommendations [59]. As a prominent counterexample, deep brain stimulation (DBS) has been established as a clinical therapy [60] with already more than 160,000 patients treated [61].

In recent years, electrical stimulation has also been (re-)discovered in other fields of regenerative medicine [62, 63]. Examples are wound healing [64–66], cardiac tissue engineering [67], neural stimulation [68] and bone regeneration [69]. The different approaches of in vitro electrical stimulation are summarised in a considerable amount

of literature reviews [32, 62, 63, 70–73]. Still, most of the electrical stimulation approaches have in common that reasons for the therapeutical effect are (yet) elusive. In all these fields, well-controlled in vitro experiments are required to elucidate the interaction between cells and applied stimuli [74]. Hence, I will not limit the discussion in this work to cartilage but try to learn from other (more advanced) fields, point out similarities and possible applications in other fields.

A reader with a background in a technical field might have noticed that I avoided to give any technical details of the electrical stimulation. This purposely reflected the status in the literature, which mostly focusses on the biological effects but avoids a discussion of the technical parameters. The abundance of stimulation parameters and external influences on the stimulation makes it necessary to develop standardised, replicable electrical stimulation approaches. With this thesis, I would like to contribute to this effort. I aim at studying realistic in vitro models with the goal of translation into in vivo applications. This research is embedded into the wider context of the replicability crisis that we, in the view of some researchers, face. I will introduce this topic in the next section.

1.2 The replicability crisis and ways out

In 2014, a series in Lancet appeared that was dedicated to reducing "waste" [sic] [75] and increase value in biomedical research. An important aspect is replicability, which is hampered by incomplete or unusable reporting [76]. Briefly, replicability means that an experiment is documented such that it can be repeated by another scientist using a different experimental setup or simulation code to achieve the same result. Reproducibility is often used synonymously but usually implies that the same experimental setup or simulation code is used [77] and is thus less general. In this work, I aim at replicable science by explaining the underlying experimental and numerical methods in detail and trying to realise as much as possible using open software and open data.

Research on electrical stimulation takes place in an interdisciplinary setting involving, among others, biology, medicine, physics, chemistry, electrical engineering. Obviously, replicability of in vitro research needs to be ensured to enable translation into clinical application. In this respect, the development of public protocols and standards is crucial [78]. In the context of electrical stimulation, problems in the documentation and replicability of experimental studies have been identified in recent research [79–81]. Exemplarily, reported electric field strengths[1] appear to be highly uncertain. Nevertheless, the electric field strength is often used to characterise and compare electrical stimulation experiments [71, 73]. Simko *et al.* have investigated

[1]To a reader who could not find the term "electric field strength" in classical electrodynamics textbooks: I use this rather colloquial term because it dominates the biomedical literature. Unless otherwise stated, it refers to the magnitude of the electric field vector.

how the quality of studies investigating the effect of radiofrequency electromagnetic field exposure on cells in vitro correlated to the conclusions [82]. They have found that high quality studies were more likely to not find an effect. Consequently, they suggested to develop a standard operating procedure for research on the effect of electromagnetic field exposure. Likewise, Nicksic *et al.* have identified insufficient documentation and device specification as major reasons why electrical stimulation to foster bone growth has not yet made it into the common clinical practice despite about 60 years of research effort [83]. To reach the research goal for cartilage regeneration faster, we should find solutions to overcome the shortcomings of translational research. From a physicist's perspective, it is astonishing to see that papers suggesting experimental techniques to estimate the applied electric fields even down to the cellular scale [36, 84, 85] have had relatively little impact on the current state of the art of electrical stimulation experiments. Some of these papers date back to the early 1990's, which shows that I will not introduce new experimental concepts but rather combine existing knowledge with advanced numerical concepts.

I aim at exploring numerical models of electrical stimulation to contribute to standardisation and replicability of experiments. Building a validated numerical model requires detailed information about the experiment and can hence contribute to improved documentation and replicability. Additionally, validation, verification, uncertainty quantification (VVUQ) have to be performed to ensure correctness and specificity of the model [86]. Verification means to assess the accuracy and mathematical correctness of the numerical solution, while validation means to check if the model is complete and covers the relevant physical processes. Uncertainty quantification (UQ) is an additional step to assess the accuracy, reliability and the robustness of the model and to explain possible deviations from experimental data. Hence, UQ also contributes to the validation but validation is in principle possible without UQ. Thus, there are three individual steps in building a reliable in silico model. Ideally, a digital twin (i.e., a digital representation) of the electrical stimulation experiment can be established. Following Wright *et al.*, a digital twin consists of: "a model of the object, an evolving set of data relating to the object, and a means of dynamically updating or adjusting the model in accordance with the data" [87]. Having a reliable digital twin at hand helps to make optimal experiment choices and save time and resources on the way to an improved in vitro outcome [88]. Even quantities that are difficult to measure or cannot even be measured are then accessible. In the context of electrical stimulation, a digital twin should facilitate the choice of the stimulation parameters and eventually contribute to the explanation of the observed biological response.

1.3 Outline

This thesis is structured in three parts. In the first part, the numerical modelling of electrical stimulation devices is introduced. Concepts for the experimental validation of the numerical models are introduced and discussed. This part paves the way for formulating requirements for digital twins of electrical stimulation devices. The second part focuses on the integration of single cells into the numerical models and the estimation of the transmembrane potential as a marker for the biological effect of the electrical stimulation. In the third part, the transition to the tissue scale is presented. The focus is laid on the dielectric properties of tissue and the realistic modelling of cartilage tissue pieces under electrical stimulation.

Parts of this thesis have already been published in peer-reviewed conference proceedings and international journals. These publications together with additional information material have been reformulated and included in the text of the thesis. The parts, which are based on publications, will be indicated at the beginning of the respective chapter or section. The publications (and thus included figures) are under the Creative Commons Attribution 4.0 International (CC BY 4.0) license. Unless otherwise stated, I am the author of the figures taken from own publications in this thesis. I will indicate the source of reprinted figures if applicable and also if the figures have been adapted.

2 Theory

In this chapter, I will introduce the basic theoretical concepts for the description of the electrical stimulation of cartilage. As mentioned before, devices that use magnetic fields to induce electric fields (PEMF stimulation) will not be covered.

Following a top-down approach, the description of the stimulation devices starts at the macroscale. At this scale, global properties (voltage, current, impedance) are described. At smaller scales (tissue and cell scale), microscopic aspects become relevant (dielectric properties, electric field). Throughout this work, different aspects will be related to an equivalent circuit (Fig. 2.1). This circuit comprises all elements that are important to understand the response of the system to an applied electrical stimulus. While the impedance of the wiring and the stray capacitance are of importance for experimental validation and sensor applications [89], the electrode-sample interface (ESI) impedance[1] and the sample impedance are key parameters of the numerical models.

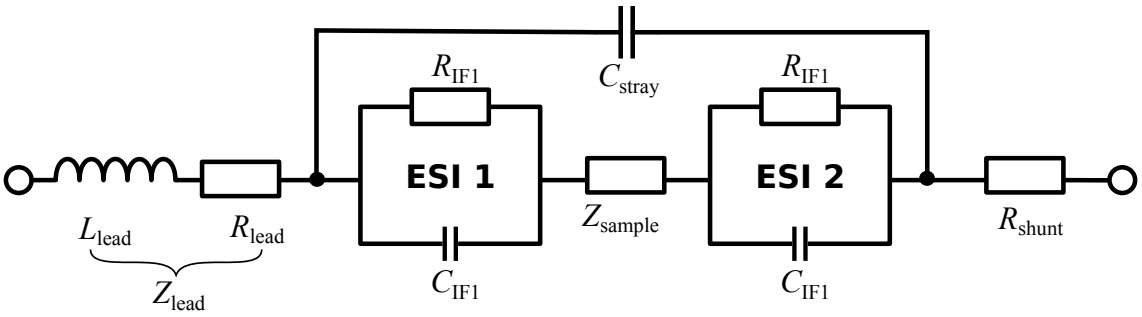

Figure 2.1: General, simplified equivalent circuit of a two-electrode device for electrical stimulation. The impedance of the wiring (cables, clips, etc.) Z_{lead} often contains a lead inductance L_{lead} and a lead resistance R_{lead}. The effect of this impedance can be expected to be relevant at relatively high frequencies (MHz range) [89]. At the electrode surfaces, interface impedances arise (Z_{ESI1}, Z_{ESI2}). When the electrodes are brought in direct contact, the interface impedances have both capacitive (expressed by C_{IF}) and resistive character (expressed by R_{IF}) and can even become non-linear [90]. Without an additional reference electrode placed in the sample, it is impossible to distinguish the interface impedances of the two electrodes. Between the interfaces, there is the impedance of the sample Z_{sample}, whose characteristics will be discussed extensively in this work. There might occur a stray capacitance parallel to the sample C_{stray}, which usually only has an effect at frequencies in the MHz range [89]. A shunt resistor R_{shunt} can be integrated to estimate the current through the circuit by measuring the voltage drop across the shunt resistor.

[1] Note that it is often common to speak of either electrode-electrolyte interface (EEI) or electrode-tissue interface (ETI). The term ESI is meant as a overarching term to refer to these impedances.

2.1 Comparison and description of stimulation devices

Three different experimental electrical stimulation approaches are usually considered for in vitro electrical stimulation (Fig. 2.2) [71, 72]:

1. Direct contact stimulation, where both electrodes are in immediate contact with the cell culture medium.

2. Capacitive coupling stimulation is performed with two insulated electrodes.

3. Semi-capacitive coupling is an intermediate type, where one electrode is in direct contact and one electrode is insulated.

In the following, semi-capacitive coupling will not be discussed in greater detail because it is rarely used for the electrical stimulation of cartilage. The focus in this section lies on the electrical aspects and characteristics of the chosen stimulation approaches. Consequently, for each type of stimulation a related measurement concept to characterise the sample will be presented.

In general, it is common to find incorrect units in the literature (e.g., $\mathrm{V\,m^{-1}}$ for the applied voltage) and incomplete information (e.g., no specification if the amplitude, peak-to-peak or root-mean-square (RMS) value is meant) or incorrect attributions (e.g., capacitive coupling albeit the electrodes have been in direct contact with the sample). I will report only SI units and will try to report the voltage or current amplitude to be consistent with the numerical approach.

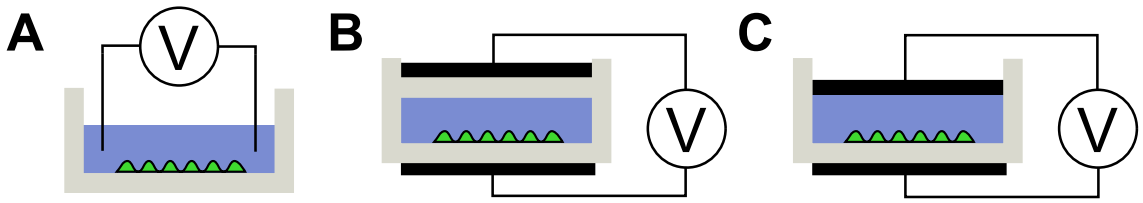

Figure 2.2: Overview of electrical stimulation approaches for in vitro cell culture experiments [71]: (**a**) direct contact stimulation, (**b**) capacitive coupling and (**c**) semi-capacitive coupling. The insulating Petri dish (grey) is shown together with the cell culture medium (blue), the cells (green) and the electrodes (black). Figure taken from [91] and adapted.

2.1.1 Direct contact stimulation

Direct contact stimulation is the most natural approach to electrical stimulation. The majority of existing electrical stimulation techniques such as DBS, pacemakers or defibrillators rely on this type of stimulation. Electrochemical processes are

closely related to this stimulation approach [90]. Particularly at low frequencies in the sub-kHz range, harmful byproducts of electrochemical reactions might be produced upon electrical stimulation [92, 93]. Hence, suitable electrode materials and safe stimulation parameters need to be chosen. Popular electrode materials are, for example, platinum, gold, iridium and corresponding oxides and alloys due to their corrosion resistance. Usually, there is no prior knowledge of the ESI available because it heavily depends on the electrode surface and geometry [93].

In the context of neural stimulation, safe waveforms have been identified [92]. In DBS, for example, charge-balanced current-controlled rectangular pulses are frequently used [60]. Likewise, rectangular pulses have been considered for cartilage tissue engineering. For example, a current-controlled 20 µA biphasic rectangular pulse, which by design is charge-balanced, with a frequency of 0.3 Hz and a pulse width of 10 ms has been used [48] to study cartilage repair in adult rats. Kwon *et al.* have used biphasic pulses with a frequency of 5 Hz and a pulse width of 8 ms but unknown voltage amplitude or current to promote chondrogenesis of mesenchymal stem cells [47]. The authors claim that the evoked electric fields had magnitudes between $100\,\mathrm{V\,m^{-1}}$ and $2500\,\mathrm{V\,m^{-1}}$. Rectangular pulses will be treated in greater detail in Sec. 5.1.

A device that has been used to assess clinical effectiveness for the treatment of electrical stimulation used a "pulsed, asymmetrically biphasic, exponentially decreasing waveform with a frequency of 100 Hz and pulse width of 4 ms" [53]. Other details (applied voltage or current) have been set by the participants of the clinical study and have not been monitored. A similar device featuring a similar waveform has been operated with a spike voltage (the voltage at the onset of the pulse) of −6.062 V [sic!] but no current has been reported [50]. Please note that such devices have been placed in direct contact with the skin but not with cartilage tissue. In the initial report of an application of the 100 Hz exponentially decreasing signal, a spike voltage of 1.59 V has led to a maximum current of 2 µA through a rabbit's knee [49]. Interestingly, this study is one of the rare examples, where the electric field in the tissue has been estimated by placing measurement electrodes inside the stimulated tissue. A peak value of $4\,\mathrm{V\,m^{-1}}$ and an average value of $0.2\,\mathrm{V\,m^{-1}}$ have been recorded [49]. Sometimes, the application of signals by electrodes attached to the skin is referred to as capacitive coupling stimulation [94]. This is explained by the rather capacitive properties of skin. Nevertheless, I consider the application of electrical stimuli through the skin as direct contact stimulation as there might occur electrochemical reactions at the electrode-skin interface depending on the skin wetting.

Collaborators in the SFB 1270 ELAINE have also considered low-frequency sine waves of, for example, 1 kHz for the in vitro stimulation of chondrocytes [95]. In the related field of bone regeneration, 20 Hz are common [96, 97]. The voltage amplitude in these experiments has usually been chosen in the range of a few hundred mV and 2 V. Again, the effective currents have not been reported. However, the prevailing

electric field in the cell culture medium has been estimated using local voltage measurements [97]. An improvement of this approach will be presented in Sec. 5.2.4.

There exist also experimental approaches that use direct current (DC) signals [71]. DC signals are mainly used to study an effect called galvanotaxis or electrotaxis. For example, currents of up to 5 mA have been shown to trigger cathodal migration of chondrocytes [46]. The authors have compared the expected resistance of the chamber to the measured value and also measured the voltage difference between two electrodes to estimate the electric field magnitude (which has been up to $60\,\mathrm{V\,m^{-1}}$). Because the DC current is mainly due to faradaic electrochemical reactions [98], electrically conductive agar-salt bridges are used in DC experiments to prevent contamination of the cell culture medium with chemical products of the electrochemical reactions at the metal electrodes [71].

Electrochemical effects at the electrode interface

To develop sound numerical models of electrical stimulation, a thorough understanding of the electrochemical effects at the electrode interface has to be developed.

A faradaic reaction is an electrochemical reaction, where electrons are transferred between the electrode and the electrolyte [92]. An example for such a reaction is the hydrogen atom plating, where a platinum atom, a proton and an electron react to form a platinum-hydrogen bond. This reaction is reversible, which means that changing polarity of the applied voltage can undo the reaction. The plating of platinum electrically leads to the so-called pseudocapacitance [92], which can be integrated into an equivalent circuit model [99].

If the applied voltage becomes too large, irreversible faradaic reactions take place. This could be, for example, water electrolysis (production of oxygen and hydrogen) or, chloride oxidation if chloride ions are present in the electrolyte (e.g. in aqueous NaCl solutions). To put it less scientifically: these reactions produce gas, bubbles at the electrodes can be seen and - in the case of the latter reaction - after some time the smell of chlorine gas appears. Irreversible reactions should be avoided because they change, for example, the pH value of the cell culture medium or might harm the cells due to released metal ions.

When the current starts to grow noticeably from a certain applied voltage, this is an indicator for the limits of the so-called water window. It indicates the voltage range in which no water electrolysis occurs. Electrodes should not be driven outside the water window [93]. Inside the water window, the reactions are mostly diffusion-limited. This means that once the reaction starts, reactants in the vicinity of the electrode are consumed and have to be supplied. The supply is mediated by diffusion, which imposes a limit on the reaction. A diffusion layer in the range of up to a few µm is formed at the electrode surface over time. In this layer, the concentrations of the charged ionic species differ from their value in the bulk volume and locally there is a different pH value than in the bulk volume [100].

Nonfaradaic processes are mostly related to the formation of an electrochemical double layer (EDL) [90, 98]. The EDL arises because ions of certain charge are dragged towards the electrode with opposite charge. The ions form a very thin layer (in the range of a few nm) that reveals capacitive behaviour [101].

Mathematically, the transient current resulting when a fixed DC voltage is applied can be approximately described by, for example, a function inversely proportional to $\sqrt{t}$, where t is the time after onset of the voltage. Such a current is typical for faradaic, diffusion-limited reactions. Likewise, a function decaying with $\exp(-t)$ can describe the current, which then is characteristic of nonfaradaic reactions due to charging of the EDL capacitance [98]. As multiple reactions can occur at the same time, the measured current may be a combination of the functions. Corresponding relations can be found for the voltage given a fixed DC current. In general, the solution of nonlinear partial differential equations (PDEs) is required to describe the interaction of ionic species with an external electric field [102, 103].

When time-harmonic signals are applied (e.g., sine waves), the analysis of the system response is usually carried out in frequency domain [102]. The response of the system is expressed by the impedance. In general, the application of a time-harmonic voltage signal as a perturbation to the system causes a nonlinear response [99]. However, if the voltage is small enough, the impedance can be linearised.

Thorough experimental and theoretical analyses of the linear and nonlinear properties of platinum electrodes for electrical stimulation can be found in the works of Schwan [104] and Richardot and McAdams [90]. Nonlinear effects have mostly been observed at frequencies below 1 kHz. They are evidenced by higher harmonics in the current signal. Nonlinear effects have occured, for example, when platinum electrodes have been used in physiological saline at voltages greater than 100 mV at 2 Hz [105]. Gold electrodes have evoked a nonlinear response of yeast cell suspension with a voltage of 2 V at 1 kHz [106] (i.e., with parameters used for cartilage stimulation).

At this point it is important to mention that equivalent circuit models (such as shown in Fig. 2.2) usually comprise only linear elements. Nonlinear effects could enter such models by using a Taylor series expansion of the current response [90, 102]. In this picture, the linear element is the first-order term of the Taylor series[2] (i.e., the term at the frequency of the applied voltage signal). This approach requires knowledge of the characteristic equation for the current response. For example, Richardot and McAdams [90] used the Butler-Volmer equation, which is commonly used to describe a single reversible electrochemical reaction [102], for their nonlinear model.

In this work, I will not attempt to develop such a nonlinear model for two reasons:

[2]Please note that the current response is often modelled using exponential functions. Taylor series of exponential functions contain a zeroth-order term (i.e., a DC term), which describes the effect of faradaic rectification

- Developing a detailed model for each biological sample appeared infeasible. Cell culture media and biological tissue contain many possible reactants (ions, charged proteins, etc.) such that a priori knowledge of the electrochemical reactions is not available. During the work on this thesis, I had no access to the experimental means to perform the required electrochemical analysis.

- Nonlinear behaviour indicates electrochemical reactions. As mentioned above, they might be harmful and would need to be studied extensively to judge if a possible biological effect of electrical stimulation is related to the electrical signal or the chemical stimulation due to the products of the electrochemical reactions.

Instead, I will resort to established linear models and use the knowledge presented in this section only to judge and optimise stimulation protocols. In linear models, faradaic reactions are described by a charge-transfer resistance and the EDL by a constant-phase element (CPE). These two elements are usually arranged in parallel (see also Fig. 2.2) [90].

The impedance of the CPE reads

$$Z_{\mathrm{CPE}} = \frac{\kappa}{(j\omega)^{\alpha}} \ , \tag{2.1}$$

where κ is the CPE amplitude and $\alpha \in [0, 1]$ [101]. The parameter α is decisive for the character of the CPE:

- $\alpha = 0$: The CPE becomes a real-valued, frequency-independent resistance, which is given by the CPE amplitude κ.

- $\alpha = 0.5$: The CPE describes an impedance with a phase of $-45°$. Such an impedance is characteristic of diffusion process and is also known as Warburg impedance [102].

- $\alpha = 1$: The CPE becomes the impedance of a pure capacitance. In this case, the CPE amplitude κ is the inverse of the capacitance.

A CPE exponent α between 0.7 and 0.9 is common for platinum electrodes in contact with electrolyte solutions if the applied voltage is chosen such that the electrode is in the linear regime [107, 108]. Nonlinear changes of the impedance manifest itself, among others, in changes of the impedance phase. For example, Moussavi *et al.* have observed a transition for a platinum electrode in saline from $-80°$ (rather capacitive characteristic) to $-45°$ (characteristic of diffusion) when the voltage amplitude at 2 Hz was increased from 30 mV to 1 V [105].

Evidently, the processes at the ESI have to be considered in a numerical model of electrical stimulation. Commonly, the ESI has been modelled by empirical relations such as Eq. (2.1) or models based on previous measurements [96, 109, 110]. As

mentioned above, the applied voltage, electrode material and electrochemical characteristics of the sample all contribute to the ESI in complex ways. The interface layer is very thin and usually does not extend further than a few nm. Thus, building a spatially resolved numerical model is not feasible for realistic stimulation systems with a characteristic size in the range of mm to cm. Hence, experimental measurements to determine the electrochemical characteristics of each stimulation electrode and to calibrate the aforementioned empirical relations are inevitable. The calibrated empirical relations enter the numerical model through boundary conditions, which circumvent the need to discretize the ESI. Such approaches will be discussed in greater detail in Chapter 5.

Electrochemical measurement approaches

For each stimulation protocol, an equivalent electrochemical characterisation method can be found. An introduction to and an overview of experimental techniques in electrochemistry can be found in [98].

DC stimulation with a fixed voltage leads to a time-dependent current. In electrochemistry, the monitoring of this current is known as chronoamperometry. Likewise, the measurement of the time-dependent voltage for a fixed current is known as chronopotentiometry. A related characterisation technique is cyclic voltammetry, where the voltage is swept between negative and positive values with regard to a reference electrode. From the resulting voltage-current curves, it can be determined at which voltages which reactions occur [93].

Electrochemical impedance spectroscopy (EIS) corresponds to AC stimulation with sine waves or periodic waveforms. In EIS, the impedance is measured over a broad frequency range. A good overview of EIS applications can be gained from the textbooks by Orazem and Tribollet [102] (general overview) or Grimnes and Martinsen [111] (focus on bioimpedance applications). Recently, an excellent primer has been written by Wang *et al.* [112].

It is important to mention, that EIS is concerned with the measurement of the linear system response. Thus, the applied voltage amplitude is chosen small (i.e., in the mV range) to avoid nonlinear electrochemical reactions. Then, the measured impedance is supposed to be the response of a linear, time-invariant, stable and causal system (comprehensive definitions of these terms can be found in the EIS textbooks and in [113]). A practical consequence of the EIS properties is that the impedance can be described by an equivalent circuit comprising linear elements (e.g., resistances, capacitances, inductances, CPEs, etc.). There exist validity tests to ensure that such an equivalent circuit can be found. They will be described in Sec. 4.2.2.

2.1.2 Capacitive coupling stimulation

At first glance, capacitive coupling appears to be contradictory: there is no direct current flow from the stimulation electrodes to the sample. An insulating layer blocks this current. Still, it has been used for the electrical stimulation of cartilage [114], chondrocytes [23, 115, 116], bone [117] and osteoblasts [118]. Higher frequencies (e.g., 60 kHz) are required to induce significant electric fields in the sample [119–121].

Evidently, the biocompatibility of this approach is increased in comparison to direct contact stimulation because no electrochemical reactions can take place at the electrode surface. However, there still might be an EDL at the insulator-electrolyte interface [1, 109].

In the field of cartilage tissue engineering and cartilage regeneration, most of the studies using capacitive coupling have been conducted by Brighton's group since the 1980's [39, 41, 42, 116, 122–124] or have been influenced by their work [23, 43, 125]. Chondrocytes under cell culture conditions [23, 39, 41, 116, 122, 125] as well as cartilage explants [42, 123, 124] have been stimulated using capacitive coupling. The frequency of 60 kHz has been established as the most popular choice. To the best of my knowledge, there is no explanation for this frequency value based on hypotheses about a physical interaction[3]. About 20 years ago, Brighton's group conducted a study, where also 30 kHz and 120 kHz were considered [41]. The result of the stimulation of bovine articular cartilage chondrocytes has been compared with respect to an up-regulation of the expression of aggrecan and type II collagen mRNA (i.e., checking if the production of extracellular matrix is fostered). An optimal outcome has been found for 60 kHz; thus confirming the previously chosen frequency. The stimulating electric field has been reported to have had a field strength of $2\,\mathrm{V\,m^{-1}}$ [39, 41, 42, 116, 123, 124]. Unfortunately, the experimental and theoretical coverage of the existing stimulation approaches is scarce. To my knowledge, there exists no experimental evidence for the reported electric field strength. An equation to compute the reported values has been reported in [119] and numerical models of the chamber will be discussed in Sec. 6.3.1. It is only known that a voltage of 44.81 V has been applied (but it remains unclear if the reported value has been peak-to-peak, amplitude or RMS voltage) [40]. In an earlier version of this stimulation chamber, a thicker insulation layer has been used, which necessitated a peak-to-peak voltage of up to 1 kV [122].

Recently, other researchers have considered smaller field strengths of $1\,\mathrm{V\,m^{-1}}$ [43] or about $5\,\mu\mathrm{V\,m^{-1}}$ [23]. The required voltages ranged between 140 mV [23] and 100 V [43]. Again, these values have been determined numerically but not experimentally.

I have only found one work on capacitive coupling of human cell lines in which

[3] However, 60 kHz is used as a carrier frequency to synchronise radio controlled clocks [126]. Thus, one could speculate that this frequency was chosen because it had been known to electrical engineers.

an experimental characterisation approach has been described [127]. The authors have suggested an equivalent circuit as in Fig. 2.2, where the electrode-electrolyte interface has been substituted by pure capacitors describing the insulating layer on the electrodes. They have measured the impedance of the stimulation device (electrodes glued on a plastic flask filled with medium) and also the voltage drop across a shunt resistor to obtain the current. The measured current density has been found to be in agreement with the current density predicted by numerical simulations.

Related measurement approaches

The use of electrodes covered with an insulating layer for EIS has been suggested. Electrodes prepared in this way are referred to as blocking electrodes [1].

They have been used, for example, for the capacitive sensing of bacteria [128]. Theoretical considerations show that the impedance of the EDL in this setting is negligible as the capacitance of the insulation layer dominates [128]. Likewise, capacitive coupling has been considered in electrical impedance tomography (EIT) to avoid the influence of ESI impedance [129].

Single frequency measurements in the kHz range (i.e., in the range relevant for cartilage stimulation) have been used to determine the conductivity of, for example, electrolytes [130]. For such applications, the electrolyte is guided through a thin capillary, which acts as the insulator. In contrast to direct contact EIS, the applied voltages are in the range of a few volts to a few hundred volts [130].

2.2 Biophysical theories of the interaction of electric fields and cells

While multiple studies have led to the hypothesis that electric fields can stimulate non-excitable cells such as chondrocytes to proliferate, differentiate or produce more proteins, it remains unclear which physical processes are causal. Most of the studies have focussed on finding correlations between physical properties characterising the applied stimulation (voltage, current, electric field). Nevertheless, biophysicists have developed theoretical approaches to describe the underlying mechanisms of interaction between electric fields and cells. A broad overview on the underlying physical theories can be found, for example, in [131]. In the following, selected aspects will be highlighted and linked to cartilage stimulation.

2.2.1 Induced transmembrane potential

The cell membrane is a lipid bilayer, which is about 7 nm thick [111]. It separates the cell interior (the cytoplasm) from the extracellular medium. In equilibrium, there

is a resting transmembrane potential, which is characteristic of each cell type. The transmembrane potential is defined as the difference between the potential on the inner side of the membrane Φ_i and the potential of the outer side Φ_o

$$\mathrm{TMP} = \Phi_\mathrm{i} - \Phi_\mathrm{o} \ . \tag{2.2}$$

The resting transmembrane potential can be determined by the Goldman equation, which requires information about the intra- and extracellular ion concentrations and the permeability of the membrane for the present ions.

Eukaryotic cells usually have a resting transmembrane potential of about -40 mV to −70 mV [132]. However, the resting transmembrane potential of chondrocytes is subject to discussion: it has been reported to lie between −46 mV and −11 mV [133]. If the transmembrane potential increases, one speaks of depolarisation while a decrease of the transmembrane potential is referred to as hyperpolarisation. For chondrocytes, an inhibition of anion channels by niflumic acid has caused hyperpolarisation of the membrane [134]. The hyperpolarisation has led to an increased Ca^{2+} influx through a non-voltage gated entry pathway. Chondrocytes hyperpolarised by voltage clamp have been shown to not be able to limit their volume upon a change of extracellular osmolarity [135]. A depolarisation has caused a reversible change in volume (i.e., chondrocytes have not lost their volume control). This finding has motivated the hypothesis that chondrocytes maintain a relatively 'positive' transmembrane potential with respect to other cells to withstand changes in the osmotic pressure. As mechanical load (e.g., during walking) induces a change in osmotic pressure [34], this hypothesis appears to be sensible. Evidently, the transmembrane potential of chondrocytes plays a role for the health of cartilage.

Voltage-dependent calcium channels have been identified as an important pathway in cartilage formation and for maintaining healthy cartilage [136]. They open upon membrane depolarisation. There exist different types of voltage-dependent calcium channels, which are grouped into high-voltage- and low-voltage-activated channels. Nevertheless, it is not exactly clear how they react to external electrical stimuli [32]. In general, electrical stimulation can induce a transmembrane potential that polarises the membrane. Xu *et al.* have found that blockers of, among others, voltage-dependent calcium channels completely inhibit the effects of electrical stimulation [116]. They have used the aforementioned capacitive coupling stimulation system (60 kHz, $2\,\mathrm{V\,m^{-1}}$) on adult bovine chondrocytes. The activation of voltage-gated calcium channels by electrical stimulation has also been reported for other cell types and stimulation approaches [137, 138]. This suggests that a sufficiently large induced transmembrane potential triggers a biological response through the activation of these channels. In the case of excitable cells, low-voltage-activated channels open in the range of −70 mV to −50 mV [139] (i.e., at transmembrane potentials increased by up to 20 mV). High-voltage-activated channels require larger changes of the transmembrane potential. To the best of my knowledge, there exist no estimates for the activation thresholds in chondrocytes.

If the induced transmembrane potential is in the range of hundreds of mV [132], electropermeabilisation occurs [132]. Electropermeabilisation refers to both the formation of aqueous pores in the membrane (electroporation) and chemical changes to the membrane constituents, which make the membrane more permeable. Due to the transmembrane potential, there is an electric field in the membrane that can be estimated by dividing the transmembrane potential by the membrane thickness (using again the parallel-plate capacitor approximation). As the membrane is very thin, the induced electric field may easily become very large.

The lower limit for the induced transmembrane potential to have an effect can be estimated by comparing the random diffusion current to the drift current. The diffusion current stems from the random thermal motion of the charge carriers (e.g, ions) while the drift current is caused by the applied electric field. Starting from transmembrane potential values of about 2 mV the drift current at room temperature becomes significant [140]. Transmembrane potential values in this range do not open membrane channels but ions would be driven through the cell membrane [141]. For example, Ca^{2+} influx into bovine endothelial cells has been observed at transmembrane potentials in the range of 1.1 mV to 2.2 mV [142]. As the influx has happened also after addition of different Ca^{2+} channel blockers, the observation has been attributed to influx through non-specific membrane pores.

In summary, it can be concluded that:

- Very large induced transmembrane potentials greater than 100 mV are likely to destroy the membrane. They should be avoided in cartilage tissue engineering.
- Intermediate transmembrane potentials roughly between 10 mV and 100 mV may trigger membrane channels. This can lead to a favourable biological response of chondrocytes.
- Small transmembrane potentials in the range of a few mV might lead to ion migration through the membrane. This might also positively influence biological cells.
- Even smaller transmembrane potentials are on the scale of thermal fluctuations and might play a role only in rare cases [140].

Both analytical [143–145] and numerical techniques [146] exist to estimate the transmembrane potential. In the analytical case, Laplace's equation is solved with suitable boundary and interface conditions. The numerical solution approach will be presented in greater detail in Sec. 6.1. The estimated induced transmembrane potentials have been experimentally validated using potentiometric dies [146, 147]. In a first approximation for spherical cells with negligible membrane conductivity exposed to a homogeneous, static electric field of magnitude E, the induced transmembrane potential can be estimated using Schwan's equation

$$\mathrm{TMP} = 1.5ER\cos\theta \ , \tag{2.3}$$

where R is the cell radius and θ is the angle of the location on the cell membrane with respect to the field direction (i.e., $\theta = 0°$ where the field is perpendicular to the membrane). Thus, there exist 'hot spots' on the membrane where the transmembrane potential assumes its maximum value while there are also spots where it becomes zero. Note that for applied time-harmonic signals the transmembrane potential is also assumed to be time-harmonic. Thus, it hyper- and depolarises the membrane continuously.

2.2.2 Electromechanical interaction

Another aspect of electrical stimulation is electromechanical interaction. The interaction can happen at the cellular scale as well as at the membrane or even membrane protein scale.

Interaction with membrane constituents

The effect of oscillating fields has been linked to a phenomenon referred to as electroconformational coupling, which has been investigated since the late 1980's [148]. electroconformational coupling causes a non-linear response of yeast cells to external fields of, for example, $200\,\mathrm{V\,m^{-1}}$ at 20 Hz [149] or $133\,\mathrm{V\,m^{-1}}$ at 10 Hz [150]. The electroconformational coupling effect in yeast cells has been confirmed by measuring the magnetic field generated by the time-dependent current [151, 152]. Biologically, electroconformational coupling has been shown to correspond to processes related to H^+-ATPase membrane pumps [150], which are also influenced by the membrane potential [153]. The electrical signals couple into the conformational transition of a molecule [154]. It has also been reported that the cell membrane can rectify an AC signal (i.e., that there is a voltage shift of the resting membrane potential [155]).

However, it must be mentioned that in 2009 the non-linear response could not be found using a tetrapolar measurement configuration [156]. A tetrapolar configuration (also called four-electrode configuration) permits to measure the response of the sample without significant influence of the ESI. The authors in [156] thus concluded that the previously reported non-linear response could solely be explained by the nonlinearities of the ESI. In contrast, another group has observed a non-linear response of yeast cells at 1 kHz using a tetrapolar configuration [157].

In chondrocytes, sodium potassium pumps (Na^+/K^+-ATPase) are expressed [158] and have gained attraction as a possible target for cartilage tissue engineering [159]. However, the coupling to external electric fields has not yet been explored.

Optical measurements have revealed that low-frequency electrical fields (up to 50 Hz) have induced clustering of lipid rafts at certain membrane areas in fibroblasts [160]. For extremely low-frequencies (< 10 Hz), it has been suggested that the rearrangement of receptors could lead to an increased induced transmembrane potential [161].

Chondrocytes possess a primary cilium, which is a membrane protrusion similar to a flagellum [162]. Its role in mechanotransduction is a matter of current research. It could also be possible that it interacts with external electric fields.

Furthermore, chondrocytes express mechanosensitive membrane channels such as TRPV4 [163] or Piezo channels [164, 165]. It has been proposed that stretch-activated calcium channels could be triggered by electrical stimulation [71]. The activation would lead to an increased Ca^{2+} influx.

In summary, the interaction of electric fields with the membrane and its constituents is not well understood. There exists no clear understanding of the membrane processes due to electrical stimulation, which could be exploited for cartilage tissue engineering.

While the processes at the membrane scale are elusive, the electromechanical interaction at the cellular scale is better understood. Particularly the availability of optical methods has enabled the observation of cell migration and deformation. They will be introduced in the following.

Cell migration: dielectrophoresis and galvanotaxis

It has been observed that cells migrate due to an externally applied electric field. The cell migration is referred to as galvanotaxis or electrotaxis (DC signals) and dielectrophoresis (AC signals) [131, 166, 167]. There exists also an effect called electrorotation (i.e., rotation of cells due to an external electric field). As it requires rotating electric fields, which are uncommon in cartilage tissue engineering, it is not considered here.

In galvanotaxis, the electric field acts as a compass for the cells [131]. Unlike electrophoresis, the cells are not steered by the electric field in a defined direction. Instead, galvanotaxis is rather a biological process. Cathodal and anodal migration can both be observed depending on the cell type but not on the field polarity. For example, chondrocytes reveal cathodal migration while electrophoresis theory would have predicted anodal migration [46]. Thus, galvanotaxis cannot be understood in the context of classical electromechanical coupling but has an active biological component to be accounted for. As the typical stimulation signals in cartilage tissue engineering are AC signals, galvanotaxis will not be further discussed in this work.

Cells can also migrate upon AC electrical stimulation due to dielectrophoresis. In contrast to galvanotaxis, dielectrophoresis can be understood by classical electrodynamics [166].

The force acting on a spherical cell in an AC field reads [166]

$$\mathbf{F}_{\mathrm{DEP}} = 2\pi\varepsilon_1 R^3 \,\mathrm{Re}\;\mathrm{CM}\nabla E^2_{\mathrm{RMS}} \ , \tag{2.4}$$

where ε_1 is the permittivity of the extracellular medium, R the cell radius, and CM

is the so-called Clausius-Mossotti factor. The Clausius-Mossotti factor is given by

$$\mathrm{CM} = \frac{\hat{\varepsilon}_2 - \hat{\varepsilon}_1}{\hat{\varepsilon}_2 + 2\hat{\varepsilon}_1} \ , \tag{2.5}$$

where $\hat{\varepsilon}_1$ is the complex permittivity of the surrounding medium and $\hat{\varepsilon}_2$ is the complex permittivity of the cell. The force (Eq. (2.4)) can also be derived using the Maxwell stress tensor (MST) [166, 168]. This approach is more general as it is also suitable for non-spherical cells and can be employed to estimate the force on the membrane in numerical simulations [169].

The direction of the migration due to dielectrophoresis depends on the sign of the real part of the Clausius-Mossotti factor. If it is positive, cells experience a force in the direction of higher field strengths and one speaks of positive dielectrophoresis (pDEP or +DEP). Vice versa, a negative real part of the Clausius-Mossotti factor indicates that cells are attracted by lower field strengths and one speaks of negative dielectrophoresis (nDEP or -DEP). These relations become clearer when recalling that the force (Eq. (2.4)) depends on the gradient of the RMS electric field strength $\nabla E_{\mathrm{RMS}}^2$. Evidently, a homogenous electric field cannot induce cell migration as there is no net force acting on the cell. Thus, inhomogeneous electric fields are used in devices leveraging dielectrophoresis. For example, dielectrophoresis has been used to arrange cellular organisation of chondrocytes inside hydrogels [170][4]. As the Clausius-Mossotti factor depends on the cellular dielectric properties, dielectrophoresis has been used to infer these properties [131, 167]. The typical frequencies in dielectrophoresis applications range from a few kHz to MHz and the applied maximal electric field strengths are in the order of $\mathrm{kV\,m^{-1}}$ or even $\mathrm{MV\,m^{-1}}$ but are usually applied only for a short period of time (not more than a few minutes) [167].

Electrodeformation

Even though homogeneous fields cannot induce migration of spherical cells, they can deform the cells [171, 172]. In the context of electrical stimulation, it has been reported that mesenchymal stem cells immersed in hydrogels stimulated by capacitive coupling with $1\,\mathrm{V\,m^{-1}}$ at 60 kHz become 'rounder' (i.e., assume a more spherical shape compared to the control group) [43]. Similarly, direct contact stimulation with $2\,\mathrm{V\,m^{-1}}$ at 60 kHz has led to a rounder shape of human mesenchymal stem cells [173]. Interestingly, the capacitive coupling stimulation has improved chondrogenic differentiation [43] while direct contact stimulation has fostered osteogenic differentiation [173].

The forces guiding the deformation have been estimated in different ways. MacQueen *et al.* have used the dielectrophoresis force (Eq. (2.4)) and assumed that

[4] I recommend the interested reader to watch the videos published as supplementary information of [170] to get an impression of the cellular organisation.

it acts in different directions on each half-sphere of a spherical cell. Others have computed the force from the MST in numerical simulations [169].

To understand the mechanism behind electrodeformation, giant vesicles, which are cell-like constructs usually without a nucleus, have been studied [174]. It could have been shown that morphological changes in AC fields depend on the conductivity ratio (i.e., the ratio of the conductivity inside and outside the cell) [175]. Four shape transitions have been described: prolate-/oblate-to-spherical and prolate-to-oblate (and their counterparts). A spherical cell shape has been shown to improve chondrogenesis [176]. Theories relying only on the MST could only find three shape transitions [169]. If the models are augmented by electrohydrodynamics [177], all four transitions could be described. The same holds true for models based on energy considerations [178, 179].

2.2.3 Summary and plan for the numerical modelling approach

The comparison of the existing stimulation devices indicates that to date there is no clear picture how the electrical stimulation of cartilage should be designed. No clear goal function regarding the applied voltages, currents, electric fields, waveforms and/or frequencies can be derived from the state-of-the-art literature. The relevant parameters of the different stimulation types are summarised and connected to equivalent circuit models in Fig. 2.3. A corresponding measurement approach can be found for each stimulation type (Table 2.1). Thus, a primary goal of this thesis is to explore the relation between numerical models and experimental observations. The focus lies on the following properties:

- The system response as characterised by the impedance Z. For direct contact stimulation, numerical simulations can mainly contribute by predicting the impedance of the sample Z_{sample} while the impedance related to electrochemical processes at the electrode surface is described by empirical models. For capacitive coupling stimulation, the total impedance can be predicted by numerical simulations.

- The electric field $\mathbf{E}$ in the sample. It becomes accessible through numerical simulations and can be used to estimate, for example, the transmembrane potential. Furthermore, the current density is automatically known because it equals the electric field multiplied by the conductivity.

In the next section, the mathematical framework to achieve the posed goal will be introduced.

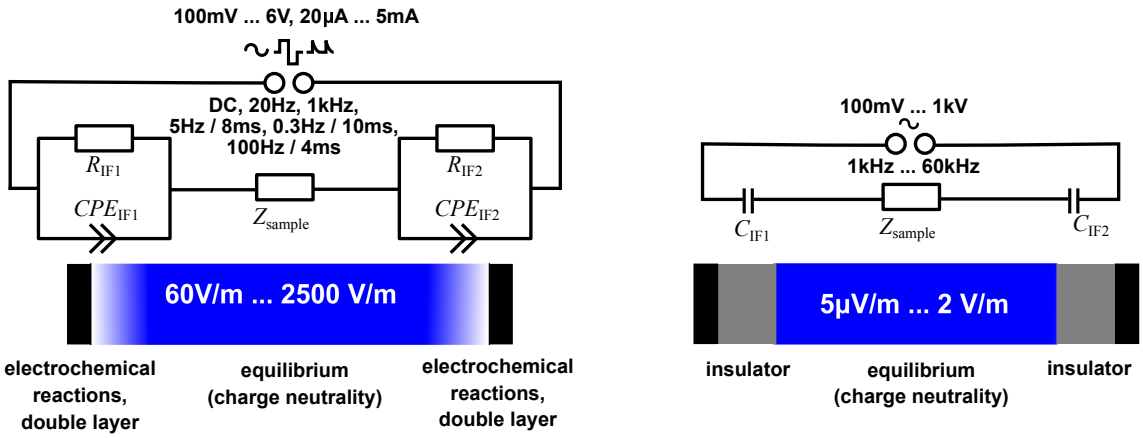

Figure 2.3: Overview of stimulation approaches for cartilage tissue engineering and their corresponding equivalent circuit model. Direct contact stimulation (left panel) has been used together with different waveforms. These waveforms were all periodic signals that are either time-harmonic (sine waves) or can be described by Fourier series (rectangular waves, decaying exponentials) [113]. Thus, they can be described in frequency domain. The same holds true for capacitive coupling stimulation (right panel). However, a model of direct contact stimulation needs to account for electrochemical processes at the electrode surface. For that, empirically determined equivalent circuit elements, which need to be calibrated for each electrode and sample, are used. In contrast, capacitive coupling stimulation can presumably be modelled without calibration using existing knowledge of the dielectric and geometric material properties.

Table 2.1: Relation between methods of electrical stimulation and electrochemical characterisation methods and their relevance for a numerical model.

Stimulation signal	Characterisation Method	Relevance
DC current / voltage	Chronopotentiometry/ Chronoamperometry	DC stimulation, monophasic rectangular waveforms contain DC component
Sine wave	Electrochemical impedance spectroscopy (EIS)	AC stimulation, frequency sweep permits to characterise entire system (Fig. 2.2), needed to calibrate and augment numerical model
Rectangular pulse	Broadband impedance spectroscopy	Like EIS, but simultaneous measurement at many frequencies, can be derived from frequency spectrum of rectangular stimulation waveforms

2.3 Electromagnetic field theory

While global properties (impedance, voltage, current) can be described by lumped-element models (i.e., equivalent circuits), the description of local properties (e.g., the electric field) relies on electromagnetic field theory.

The signals relevant for the electrical stimulation of cartilage can be represented by time-harmonic functions (or a linear superposition of time-harmonic functions, e.g. Fourier series). Furthermore, the frequency has been identified as a crucial parameter, which suggests to pose the mathematical problem in frequency domain. Time-harmonic electromagnetic fields are described by the Maxwell's equations [180]

$$\nabla \cdot \mathbf{D} = \varrho \tag{2.6}$$
$$\nabla \cdot \mathbf{B} = 0 \tag{2.7}$$
$$\nabla \times \mathbf{E} + \mathrm{j}\omega\mathbf{B} = 0 \tag{2.8}$$
$$\nabla \times \mathbf{H} - \mathrm{j}\omega\mathbf{D} = \mathbf{J} \tag{2.9}$$

with ω the angular frequency, $\mathbf{E}$ the electric field, $\mathbf{B}$ the magnetic induction, $\mathbf{H}$ the magnetic field, $\mathbf{D}$ the electric displacement, ϱ the charge density, and $\mathbf{J}$ the current density. All vector fields are complex-valued and their scalar components are described by a distinct magnitude A and phase ϕ as $A\mathrm{e}^{\mathrm{j}\phi}$. The time evolution of the physical fields is described by $A(t) = \mathrm{Re}\ A\mathrm{e}^{\mathrm{j}(\omega t+\phi)}$. Importantly, this means that a visualization of the field vector is only a snapshot (usually at the time $t = 0$).

For time-invariant, isotropic and linear material behaviour, the constitutive relations read

$$\mathbf{D} = \varepsilon_r\varepsilon_0\mathbf{E} \equiv \varepsilon\mathbf{E} \tag{2.10}$$
$$\mathbf{H} = \tfrac{1}{\mu_r\mu_0}\mathbf{B} \equiv \tfrac{1}{\mu}\mathbf{B} \tag{2.11}$$

with ε_r the relative permittivity, ε_0 the vacuum permittivity, ε the permittivity, μ_r the relative permeability, μ_0 the vacuum permeability and μ the permeability. The material properties express the response to an external field. For example, the permittivity is related to the polarisation response of a dielectric due to microscopic processes [1].

The full set of Maxwell's equations (Eqs. (2.6)–(2.9)) can be simplified in the so-called electroquasistatic (EQS) limit, which usually involves low frequencies and rather poor conductors [181]. The EQS representation can be used if the following conditions are fulfilled [180]:

- The frequency ω and characteristic size L are so small that the characteristic time $\tau = 1/\omega$ of the signal is much smaller than the time an electromagnetic wave takes to propagate. In other words: the wavelength has to be much larger than the characteristic size of the sample. Then, wave propagation effects can

be neglected. An upper frequency limit can be formulated by $\omega \ll \omega_\mathrm{q}$, where $\omega_\mathrm{q} = \left(L\sqrt{\varepsilon_\mathrm{max}\mu}\right)^{-1}$ with ε_max is the largest permittivity in the system. Please note that $\mu_r \approx 1$ and hence $\mu \approx \mu_0$ for most of the materials to be considered in electrical stimulation of biological tissue.

- There is no eddy current induced. An upper frequency limit for this case is given by

$$\omega \ll \omega_\mathrm{q}^2 \frac{\varepsilon_\mathrm{max}}{\sigma_\mathrm{max}} \ , \tag{2.12}$$

where σ_max is the largest conductivity in the system.

Both conditions can be combined in one criterion [182]

$$|kL| \ll 1 \quad \text{with} \quad k = \omega\sqrt{\mu\varepsilon\left(1 - \mathrm{j}\frac{\sigma}{\omega\varepsilon}\right)} \ . \tag{2.13}$$

An overview of typical frequencies and characteristic sizes is given in Fig. 2.4. It must be noted at this point that in a realistic experiment there might be different subsystems with different behaviour. For example, the skin effect, which might occur at higher frequencies in the cables connecting the stimulation electrodes to the power source, is a magnetoquasistatic (MQS) but not an EQS effect [181]. In this work, I will exclusively focus on the EQS subsystem (i.e., the biological sample in its environment comprising, for example, cell culture medium, culture dish, sample holder and air).

As a result of the EQS approximation, Maxwell's equations decouple and the electric and magnetic field can be treated separately. This means that Eq. (2.8) reduces to

$$\nabla \times \mathbf{E} = 0 \ , \tag{2.14}$$

that is the electric field becomes curl-free. Hence, it can be described by a scalar potential Φ by

$$\mathbf{E} = -\nabla\Phi \ . \tag{2.15}$$

The EQS field equation reads

$$\nabla \cdot (\hat{\sigma}\nabla\Phi) = 0 \ , \tag{2.16}$$

where $\hat{\sigma} = \sigma + j\omega\varepsilon$ is the complex conductivity. The current density is given by

$$\mathbf{J} = \hat{\sigma}\mathbf{E} \ , \tag{2.17}$$

which shows that essentially the EQS equation is a flux continuity condition for charge-neutral systems

$$\nabla \cdot \mathbf{J} = 0 \ . \tag{2.18}$$

This formulation assumes that there is no external current density, which would enter the right-hand side [182]. Instead, the connection to electrically active sources is mediated by boundary conditions, which will be introduced in the following.

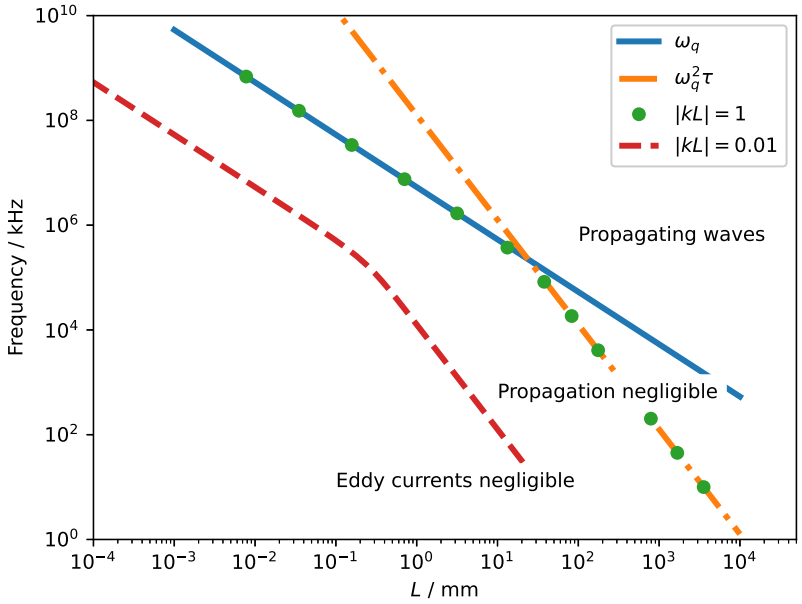

Figure 2.4: Limits of EQS regime for parameter values that are typical for cell culture media ($\varepsilon_r = 80$, $\sigma = 1\,\mathrm{S\,m^{-1}}$, see also Sec. 2.3.2). The limits depend on the characteristic size of the sample L and the frequency of the applied signal. The property ω_q poses a limit with regard to wave propagation, while $\omega_\mathrm{q}^2\tau = \omega_\mathrm{q}^2\varepsilon_\mathrm{max}/\sigma_\mathrm{max}$ poses a limit with regard to the induction of eddy currents [180]. The unified estimate $|kL|$ has been introduced in [182] and combines both effects. The frequency and/or characteristic size should be well below the estimated limits, which can, for example, be assumed for $|kL| = 0.01$ (or in general $|kL| \leq 1$). Then, a cell culture medium sample of characteristic size 1 mm can, for example, be expected to be EQS up to about 1 GHz. For larger frequencies, mainly wave propagation effects are expected to occur. For a larger sample of characteristic size 1 cm, induced eddy currents can be expected from about 100 kHz (before wave propagation occurs, which would start from about 10 MHz). Note that a more relaxed estimate of $|kL| = 0.1$ would lead to higher frequency limits. In general, it can be expected that most of the biological samples, which have characteristic size in the cm or mm range, are EQS for frequencies up to the MHz range.

2.3.1 Boundary conditions

To solve Eq. (2.16) for realistic scenarios, boundary conditions (BCs) have to be imposed. They can be classified into [183]

1. Dirichlet BC: a fixed value for the electric potential U is assigned to a boundary region. An example for such a BC is the voltage that is applied by the stimulation unit.

2. Neumann BC: a fixed value for the normal component of the current density J_n is assigned to a boundary region. This BC is, for example, used to model the boundary with insulators, where $J_\mathrm{n} = 0$.

3. Robin BC: the normal component of the current density J_n is related to a constant γ multiplied with the unknown electric potential and an additive constant q

$$J_\mathrm{n} = \gamma\Phi + q \ . \tag{2.19}$$

   A Robin BC can be used to model the surface impedance due to the ESI [109]. Then the local impedance z_s[5] is used together with Ohm's law to model the surface impedance

$$J_\mathrm{n} = \frac{1}{z_\mathrm{s}}(\Phi - q) \ . \tag{2.20}$$

   Here, $(\Phi - q)$ can be understood as the voltage drop across a very thin layer that has an equally distributed impedance along its surface.

A less common BC is related to the modelling of floating conductors (i.e., conductors that are not connected to a fixed potential). Examples are reference electrodes, which are used to measure the local voltage [184], as well as screws or other metal pieces that might be placed in the vicinity of an electrically active implant [96]. Almost perfect conductors such as metals can be assumed to be field-free. Then, the voltage of these conductors can only assume one value in the entire conductor (the so-called floating potential). However, it has been shown that experimental results are better matched by a modified Robin BC (see Eq. (2.20)) with also an unknown potential q [184].

Likewise, an interface condition similar to Eq. (2.20) can be formulated at the interface of two materials that are separated by a thin layer. The normal current density entering and leaving the thin layer is given by [166]

$$J_\mathrm{n,o} = \hat{\sigma}_o E_\mathrm{n,o} = \frac{1}{z_\mathrm{m}}\left(\Phi_\mathrm{o} - \Phi_\mathrm{i}\right) \quad \text{and} \quad J_\mathrm{n,i} = J_\mathrm{n,o} \ . \tag{2.21}$$

[5] Please be referred to [102] for a mathematical definition and to [109] for a practical application example.

Instead of the local impedance z_m, the complex conductivity and the thickness of the thin layer d_m can be considered, which is common to model cell membranes [146]. Then, the specific surface admittance in Eq. (2.21) reads

$$\frac{1}{z_\mathrm{m}} = \frac{\hat{\sigma}_\mathrm{m}}{d_\mathrm{m}} \ . \tag{2.22}$$

In this picture, Eq. (2.21) can be understood as parallel-plate capacitor approximation because

$$J_\mathrm{n,o} = \hat{\sigma}_\mathrm{m} \frac{\Phi_\mathrm{o} - \Phi_\mathrm{i}}{d_\mathrm{m}} = \hat{\sigma}_\mathrm{m} E_\mathrm{m} \ , \tag{2.23}$$

where E_m is the magnitude of the electric field in the parallel-plate capacitor (voltage drop over plate spacing). The interface condition Eq. (2.21) and its numerical implementation will be discussed in greater detail in Sec. 3.1.2.

As (modified) Robin BCs and the aforementioned interface condition describe very thin layers, they will be referred to as thin layer approximations in the following.

2.3.2 Dielectric properties of relevant materials

The dielectric properties are a key ingredient of the EQS equation (Eq. (2.16)). In cartilage tissue engineering, different materials are used and need to be modelled; for example, the culture dish or the cell culture medium. In the following, an overview of their dielectric properties is given.

Culture dishes

Cell culture dishes are usually made of polystyrene. Polystyrene has a relative permittivity of 2.6 [111]. The relative permittivity of polystyrene is characteristic for plastics (for example, polyethylene has almost the same relative permittivity [185]). Some culture dishes or cell containers are made of glass, which has a slightly increased permittivity [111]. The conductivity of the materials used for culture dishes is extremely small (e.g., $10^{-15}\,\mathrm{S\,m^{-1}}$ for polyethylene [102]). They can be assumed to be perfect insulators. The permittivity of these materials is almost frequency-independent in the frequency range relevant for cartilage tissue engineering [111, 185] and does not significantly depend on the temperature between 20 °C and 100 °C [185]. However, the permittivity can depend on the thickness of the plastic sample [185].

Cell culture media

Cell culture media are aqueous electrolyte solutions. Usually, a basal medium, which contains different salts, amino acids and vitamins, is used with supplements [186]. The supplements can be synthetic or natural (e.g., horse serum). Due to the variety of compositions, knowledge of the dielectric properties does not exist for every medium.

Sodium chloride (NaCl) is usually the component with the highest concentration in the medium. For example, Dulbecco's Modified Eagle's Medium (DMEM) contains 0.110 mol/L NaCl and Neurobasal A medium contains 0.068 mol/L NaCl (according to the manufacturer Thermo Fisher Scientific). Hence, physiological saline with a NaCl concentration of 0.153 mol/L or other aqueous NaCl solutions can be used for comparison.

While the literature on the dielectric properties of cell culture media is scarce, the dielectric properties of aqueous solutions of binary electrolytes such as NaCl or KCl have been described in great detail. Experimental investigations have led to empirical laws for the temperature-, frequency- and concentration-dependent dielectric properties of NaCl and KCl solution [187–191]. The frequency dependence of the dielectric properties is commonly modelled by empirical models. These models account for the underlying dielectric relaxation mechanisms. The Havriliak-Negami model is a general model that describes the complex permittivity $\hat{\varepsilon}_\mathrm{r}$ of asymmetric and broadened dispersions by

$$\hat{\varepsilon}_\mathrm{r} = \varepsilon_\infty + \frac{\Delta\varepsilon}{(1+(j\omega\tau)^a)^\beta} + \frac{\sigma_\mathrm{DC}}{j\omega\varepsilon_0} \ , \tag{2.24}$$

with σ_DC being the static (ionic) conductivity, ε_∞ the high-frequency limit of the relative permittivity, τ the mean relaxation time, $\Delta\varepsilon$ the magnitude of the dispersion and $a \in [0,1]$ and $\beta \in [0,1]$ describe the broadening and asymmetry. The complex permittivity $\hat{\varepsilon}$ is related to the conductivity σ and the permittivity ε_r through

$$\hat{\varepsilon}_\mathrm{r} = \varepsilon_r - \mathrm{j}\frac{\sigma}{\omega\varepsilon_0} \ . \tag{2.25}$$

Hence, it can be straightforwardly converted into the complex conductivity $\hat{\sigma}$ (see also [192]).

The Cole-Cole ($\beta = 1$) and Cole-Davidson ($a = 1$) models are special cases of the Havriliak-Negami model (Eq. (2.24)). The Debye model ($\beta = 1$ and $a = 1$), which describes only a single dispersion, is contained in the Havriliak-Negami model. In practice, a single dispersion can be identified by a transition of the permittivity from one level to a lower level with increasing frequency [111]. In contrast, the conductivity increases from one level to a higher level. The characteristic frequency f_c of the dispersion is related to the relaxation time by $f_\mathrm{c} = (2\pi\tau)^{-1}$. For NaCl solutions, the characteristic frequency is in the order of 10 GHz (see Fig. 2.5). More information on the visual identification of dispersions can be found in [111].

The static conductivity σ_DC of aqueous solutions of electrolytes can in principle be estimated from the ion concentrations and the ion mobilities [190]. For this reason, it is also sometimes referred to as ionic conductivity. At room temperature or culture conditions (37 °C), the static conductivities of saline and cell culture media are about $1\,\mathrm{S\,m^{-1}}$ to $2\,\mathrm{S\,m^{-1}}$ [193].

The dielectric properties have to satisfy the Kramers-Kronig relations [3, 194]

$$\mathrm{Re}\ \hat{\varepsilon}(\omega) = \varepsilon_\infty + \frac{2}{\pi}\int_0^\infty \frac{x\,\mathrm{Im}\ \hat{\varepsilon}(x)}{x^2-\omega^2}\mathrm{d}x \tag{2.26}$$

$$\mathrm{Im}\ \hat{\varepsilon}(\omega) = \frac{\sigma_{\mathrm{DC}}}{\omega\varepsilon_0} - \frac{2\omega}{\pi}\int_0^\infty \frac{\mathrm{Re}\ \hat{\varepsilon}(x)-\varepsilon_\infty}{x^2-\omega^2}\mathrm{d}x\ , \tag{2.27}$$

which relate the real and imaginary part of the complex permittivity. Please note that the permittivity asymptotically tends to 1 (i.e., $\varepsilon_\infty = 1$ [3]). Thus, the dielectric properties cannot be chosen arbitrarily but a model fulfilling the Kramers-Kronig relations such as the above-mentioned empirical models has to be used. However, a change in the static conductivity does not alter the relative permittivity as it does appear only in Eq. (2.26) but not in Eq. (2.27).

The dielectric properties of cells, hydrogels and tissues are much less understood and will be subject later in this work in Chapter 7. The stimulation electrodes can be assumed to be perfect electrical conductors (i.e., having an infinitely large conductivity) because they are much more conductive than all other parts of the system. Thus, the potential on the electrodes is assumed to have a fixed value (i.e., the electrodes are field-free). With the knowledge of the expected dielectric properties, it becomes possible to formulate simplifications of Eq. (2.16), which will be presented in the following section.

2.3.3 Simplifications of the electroquasistatic equation

For direct contact stimulation, the electrodes are often not only in contact with the relatively conductive medium but also with insulators (air, culture dish). Then, all insulators can be accounted for by an insulating boundary condition because no current will enter the insulators. The current flows exclusively through the medium. For capacitive coupling stimulation, the electrodes are entirely insulated and the aforementioned approximation is not applicable.

The electrodes can be described by Dirichlet boundary conditions because it is not to be expected that there will be a non-zero electric field induced inside the electrodes. The conductivity and permittivity of cell culture media can be assumed as frequency-independent up to very high frequencies far above 1 MHz (see Fig. 2.5). For the characteristic properties of aqueous electrolytes similar to cell culture media, one can show that $\sigma \gg \omega\varepsilon$ for frequencies up to a few MHz (i.e., they show resistive but not capacitive behaviour). Then, it suffices to solve Eq. (2.16) only using the conductivity. Hence, the material properties and the solution are real-valued (i.e., have a phase of zero).

If there is more than one domain to model (e.g., a hydrogel in medium), $\sigma \gg \omega\varepsilon$ must hold true for all domains in the considered frequency range. For capacitive coupling stimulation, the aforementioned condition does not hold true because the

insulating layers on the electrodes reveal capacitive behaviour. In this case, the real part can be neglected if $\omega\varepsilon \gg \sigma$ and only the permittivity needs to be considered. Then, the material properties and the solution are complex-valued (i.e., have a phase of $-90°$).

If there is only one domain (e.g., only the cell culture medium), Eq. (2.16) reduces to Laplace's equation

$$\nabla^2\Phi = 0 \ . \tag{2.28}$$

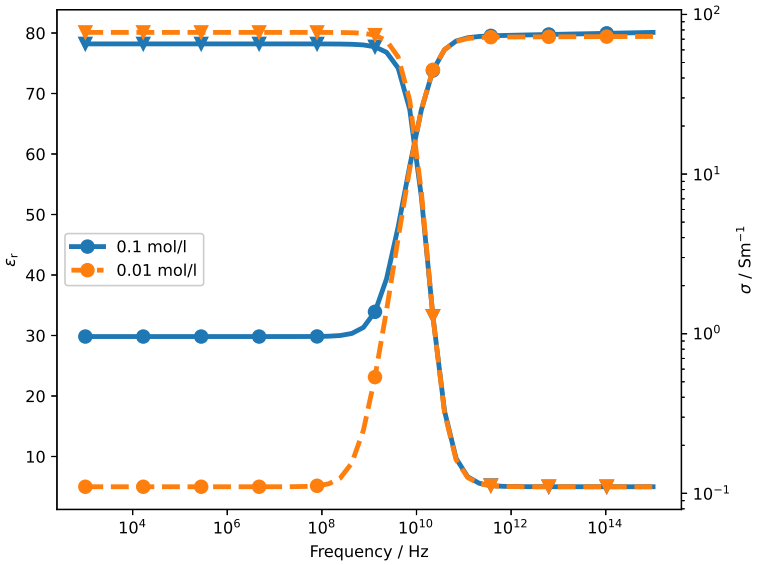

Figure 2.5: Permittivity (triangles) and conductivity (circles) of NaCl solution over a broad frequency range. The dielectric properties were modelled by a Cole-Cole model with values taken from [188]. Two concentrations are compared: the higher concentration is similar to physiological saline, which has a concentration of 0.15 mol/L. It becomes evident that the main difference lies in the static conductivity that is larger for higher concentrations. The relative permittivity and dispersion do not change significantly with changing concentration. The dispersion and its characteristic frequency (about 10^{10} Hz) are evident from the transition of the dielectric properties from one level to another level.

2.3.4 Observables

The solution of Eq. (2.16) can be post-processed to obtain observables, which are, for example, the total current and the sample resistance, capacitance or impedance.

The impedance of the stimulated sample can be computed from the solution of Eq. (2.16), which is the electric potential Φ, in two ways. On the one hand, the normal current density on a closed surface S can be integrated to obtain the current

through the sample

$$I = \int_S \mathbf{J} \cdot \mathbf{n} \, \mathrm{d}A \ , \tag{2.29}$$

where $\mathbf{n}$ is the normal vector on S. With the known applied potential U, the impedance becomes $Z = U/I$. On the other hand, the instantaneous power dissipation P in the sample is given by

$$P = \int_\Omega \mathbf{J}^* \cdot \mathbf{E} \, \mathrm{d}\Omega \ , \tag{2.30}$$

which is related to the admittance Y (defined as Z^{-1}) by [2]

$$P = U^2 Y^* \ . \tag{2.31}$$

Note that in the complex-valued case usually the time-averaged power dissipation is considered, which is equal to $P/2$ [2, 3]. However, the formulation here also includes the static case [183].

The electric field is not included in this context because it is not straightforward to measure. Instead, the voltage distribution, from which the electric field can be computed by Eq. (2.15), or the current through the sample are measured to infer the electric field [195]. These experimental approaches will be discussed in greater detail in Chapter 5.

3 Numerical methods

In the following chapter, numerical methods to solve the EQS field equation under consideration of the various BCs mentioned in Sec. 2.3.1 will be introduced. Moreover, methods to account for uncertainties in the input parameters will be presented.

3.1 Finite element method

The finite element method (FEM) has become a popular choice to solve boundary value problems for bioelectric phenomena on complex domains with possible anisotropy [196]. Other methods in computational electromagnetics are, for example, the finite integration technique [182], the finite difference method or the boundary element method [183]. They can either not deal well with complex geometries (finite difference method), lead to dense matrices (boundary element method) [183] or require additional efforts to implement full anisotropy (finite integration technique) [197]. Nevertheless, the aforementioned methods have advantages for time-domain simulations compared to FEM. As time-domain simulations are not performed in this work, I exclusively use the FEM to solve Eq. (2.16). In the following, the FEM approach will be introduced and practical aspects of its implementation will be discussed. In the last years, the software framework *FEniCS* [198] has revolutionised the field of FEM software and paved the way for automated modelling. Hence, the focus will be laid on formulations that can be used in software packages following the *FEniCS* approach such as *NGSolve* [199]. In this work, I will rather discuss the physical interpretation of the FEM. The mathematical background of the treatment of elliptic PDEs (as the EQS field equation) is described in mathematics textbooks (e.g., [200]).

3.1.1 General concept

In the first step of the FEM approach, the weak form of the EQS field equation (Eq. (2.16)) is derived. For that, the equation is multiplied by a suitable test function v and integrated over the solution domain Ω, yielding

$$\int_\Omega \nabla \cdot (\hat{\sigma} \nabla \Phi)\, v \, \mathrm{d}\Omega = \int_\Omega f v \, \mathrm{d}\Omega \ . \tag{3.1}$$

Here, a general right-hand side f has been considered, which in the EQS case is zero reflecting the absence of current sources. Equation (3.1) can be reformulated using integration by parts

$$\int_{\partial\Omega} (\hat{\sigma} \nabla \Phi \cdot \mathbf{n})\, v \, \mathrm{d}s - \int_\Omega \hat{\sigma} \nabla \Phi \nabla v \mathrm{d}\Omega = \int_\Omega f v \, \mathrm{d}\Omega \ . \tag{3.2}$$

The BCs mentioned in Sec. 2.3.1 can already enter the weak form. Consider a part of the boundary Γ_N, where a Neumann BC with the boundary flux $g = -\hat{\sigma}\nabla\Phi \cdot \mathbf{n}$ is applied, and a part Γ_R, where a Robin BC with known surface admittance $p = z_\mathrm{s}^{-1}$ (compare Eq. (2.20)) and known fixed potential q is applied. Please note that all values involved are in general complex numbers here. A Dirichlet BC is applied on Γ_D. Thus, the solution is known on this part of the boundary and the test function v vanishes. Eventually, Eq. (3.2) becomes

$$\int_\Omega \hat{\sigma}\nabla\Phi\nabla v \mathrm{d}\Omega + \int_{\Gamma_\mathrm{N}} g v \mathrm{d}s + \int_{\Gamma_\mathrm{R}} p(\Phi - q) v \mathrm{d}s = \int_\Omega f v \mathrm{d}\Omega \ . \tag{3.3}$$

From this intermediate result, the weak form of the variational problem is formulated as

$$a(\Phi, v) = f(v) \ , \tag{3.4}$$

where Φ is sought for a given v [200]. The left-hand side of Eq. (3.4) is referred to as bilinear form, while the right-hand side is referred to as linear form.

From the mathematical point of view, Φ and v belong to a suitable function space. It is known that the Sobolev space H^1 is a suitable space [200]. Functions belonging to H^1 are continuous but may have a discontinuous derivative (gradient). The electric potential is a scalar quantity and continuous but the electric field (the negative gradient of the electric potential) can be discontinuous (for example, at material interfaces) [3]. This explains the choice of the function space from a physics point of view.

There exist also discretisations of the Maxwell's equations and related equations employing vectorial quantities (electric field and/or magnetic field). Then, the H^1 space is not appropriate but a space with additional conditions should be used. Examples are divergence-free vector functions, which belong to the Sobolev space $H(\mathrm{div})$, or curl-conforming vector functions, which belong to the Sobolev space $H(\mathrm{curl})$. The $H(\mathrm{div})$ space is used in mixed finite element methods, where the flux (the current density) belongs to $H(\mathrm{div})$ [201]. Furthermore, $H(\mathrm{div})$ will be used for adaptive mesh refinement strategies (see Sec. 3.1.4). The $H(\mathrm{curl})$ space has no relevance for the applications considered in this work but is used to solve, for example, the curl-curl equation, which arises when considering electromagnetic waves in, for example, waveguides or cavities [183].

For the numerical discretisation, an H^1-conforming space is chosen. In this work, the same space is used for both the solution and the test function. This approach is called Ritz-Galerkin method or simply Galerkin method [183, 200]. It can be shown that the same finite element solution as by the Galerkin method can be obtained from variational principles [202]. The variational principle is a scalar quantity; a so-called functional. For electrostatic fields it could be, for example, the electrostatic field energy [183]. Similarly, in EQS it would be the power dissipation. The FEM solution is then the function that minimizes the functional. The variational approach

permits to introduce constraints via Lagrange multipliers, which will be important to implement certain BCs [202].

After having established the weak form and having chosen a suitable function space, the FEM problem is formulated with respect to a triangulation (discretization) of the domain. For that, the domain Ω is subdivided into small sub-domains (the finite elements). Common element shapes are tetrahedra or hexahedra (in 3D) and triangles or rectangles (in 2D). All elements together form the so-called mesh. In this work, only matching meshes are considered. This means that all elements share their vertices, edges and faces with their immediate neighbours. Hence, there must be, for example, no hanging nodes in the mesh. Knowing the mesh, an H^1-conforming finite element space is constructed. The FEM solution Φ_{FEM} is a linear superposition of weighted basis functions

$$\Phi_{\mathrm{FEM}}(\mathbf{r}) = \sum_{i}^{\mathrm{N}} \Phi_i \varphi_i(\mathbf{r}) \ , \tag{3.5}$$

where N is the number of degrees of freedom (DOFs). Contrasting the test function, the function Φ_{FEM} is usually referred to as trial function in FEM software packages such as *FEniCS* or *NGSolve*. The weights Φ_i are to be determined and are allocated to the DOFs. An H^1-conforming function space can, for example, be built of nodal basis functions. They are called nodal because one basis function is associated with one mesh node (see Fig. 3.1). Inside the triangle, the nodal basis functions are linear (see Fig. 3.2).

The error of the FEM solution w.r.t. the true solution Φ can be estimated *a priori*. In the H^1-norm, the error is

$$||\Phi_{\mathrm{FEM}} - \Phi||_{H^1} = \sqrt{\int_{\Omega} \left[\left(\Phi_{\mathrm{FEM}} - \Phi\right)^2 + \left(\nabla\Phi_{\mathrm{FEM}} - \nabla\Phi\right)^2 \right] \mathrm{d}\Omega} \propto h \ , \tag{3.6}$$

while it is in the L^2-norm

$$||\Phi_{\mathrm{FEM}} - \Phi||_{L^2} = \sqrt{\int_{\Omega} \left(\Phi_{\mathrm{FEM}} - \Phi\right)^2 \mathrm{d}\Omega} \propto h^2 \ . \tag{3.7}$$

These estimates only hold true for shape-regular meshes with characteristic mesh size h and a sufficiently smooth and regular solution Φ [200]. Thus, they are also referred to as the optimal order of convergence. The order of convergence can be increased from $\mathcal{O}(h)$ to $\mathcal{O}(h^k)$ (H^1-norm) and $\mathcal{O}(h^2)$ to $\mathcal{O}(h^{k+1})$ (L^2-norm) by using suitable polynomials of order k as basis functions. These higher-order elements are available in modern software packages like *FEniCS* and the polynomial order can be straightforwardly adjusted by the user. An example of second-order elements is shown in Fig. 3.1. In this case, the second-order basis functions are associated with the edges (2D) or faces (3D) of the elements but not with the nodes. More details can also be found in [203]. As a result of the convergence estimate, two strategies for reducing the numerical error of the solution can be devised:

1. h-refinement: The mesh cells are split to reduce the characteristic mesh size.

2. p-refinement: The polynomial order is increased while the mesh does not change.

There exists also a combined strategy called hp-refinement, which will not be further discussed in this work.

Furthermore, the accuracy of the solution can be improved by curving boundary elements. For round geometries, such as the quarter circle considered in Fig. 3.1, it makes sense to use polynomials of the same order as the basis functions to better approximate the geometry (so-called curved elements). If not stated otherwise, I used second-order H^1-conforming elements and a second-order geometry representation in all computations.

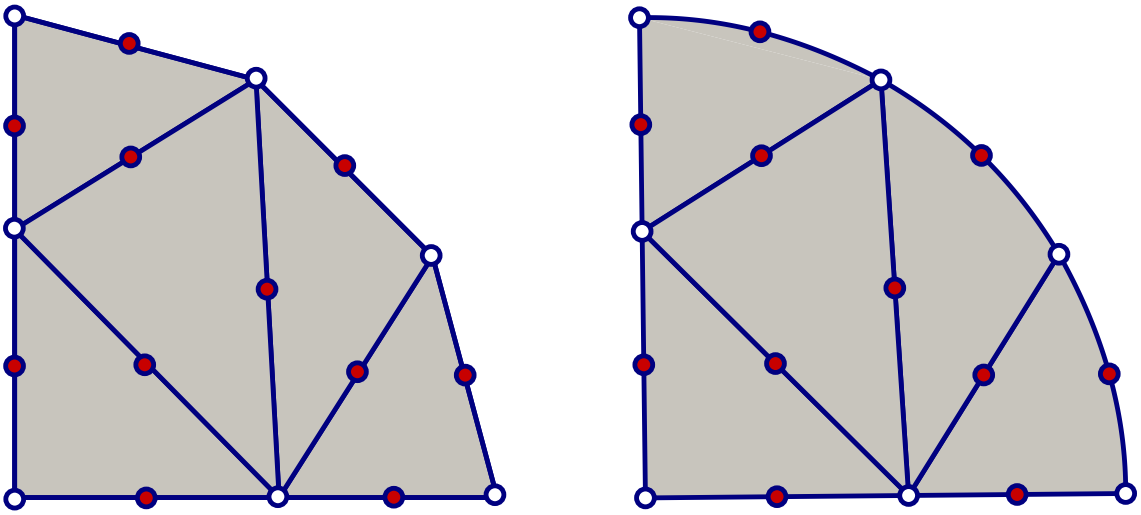

Figure 3.1: Simple mesh of a quarter circle. On the left, uncurved linear elements are shown while curved, second-order elements are shown on the right. The first-order degrees of freedom (linear nodal basis functions, empty circles) are associated with mesh nodes. The second-order degrees of freedom are associated with element edges (red circles). Evidently, the curved element (shown on the right) better approximates the circular geometry.

Eventually, the discretised potential Φ_{FEM} (Eq. (3.5)) and the test function v are inserted into the weak form (Eq. (3.3)). The bilinear form leads to a square matrix $\mathbf{A}$, while the linear form leads to a vector $\mathbf{b}$. The number of matrix rows and columns is given by the number of DOFs. The matrix entries are computed by evaluating the arising integrals in the weak form. In FEM software libraries, this step is called matrix assembly. Due to the properties of the chosen basis functions, many integrals evaluate to zero. Thus, the matrix is a sparse matrix. An instructive example of the exact procedure can, for example, be found in [183].

Finally, the solution is obtained by solving the linear system of equations

$$\mathbf{A}\mathbf{x} = \mathbf{b} \ , \tag{3.8}$$

where $\mathbf{x}$ contains the DOFs Φ_i (i.e., the approximation of the potential).

Thanks to the chosen Galerkin approach, certain properties of the matrix $\mathbf{A}$ are known [200]. If the full EQS equation is considered, the matrix is complex-symmetric. If only the real or imaginary part are considered (e.g., in the electrostatic case), the matrix is symmetric positive-definite. The properties of the matrix are important for the choice of an appropriate numerical solution strategy for Eq. (3.8), which will be discussed later in this section.

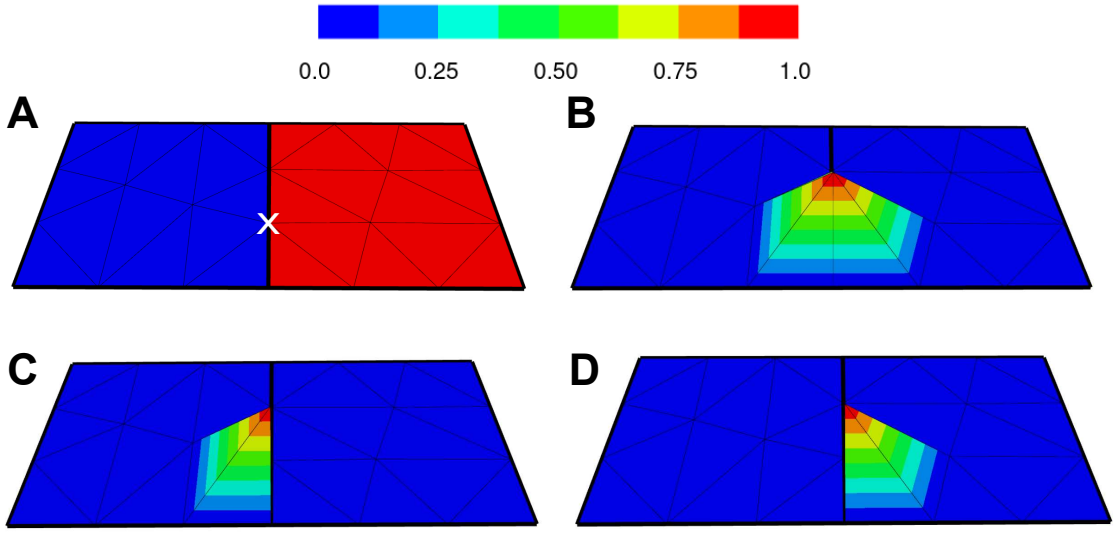

Figure 3.2: **A**: Exemplary mesh for two materials (displayed in blue and red) separated by an interface. The node, at which the shape functions are shown, is highlighted by a white cross. In **B**, the associated nodal shape functions of an H^1-conforming function space defined on the entire mesh are shown. In contrast, in **C** and **D**, the shape functions are shown for function spaces defined only on either side of the interface. The restriction of function spaces to sub-domains is required to implement thin layer approximations, which feature jumps in the potential.

3.1.2 Implementation of boundary conditions

The BCs specified in Sec. 2.3.1 have to be integrated into the FEM approach. While Neumann- and Robin-type BCs are already accounted for in the weak form (Eq. (3.3)), Dirichlet BCs, thin layer interface conditions (Eq. (2.21)) and floating potential conditions have to be treated separately.

Dirichlet boundary conditions

The solution is known for DOFs that are located on a boundary, where a Dirichlet BC is imposed. To integrate the Dirichlet BC in the linear system of equations (Eq. (3.8)), different approaches exist. An approach, which is for example used in *FEniCS*, relies on modifying the entries in the matrix $\mathbf{A}$ and right-hand side $\mathbf{b}$ such that the Dirichlet BC is fulfilled [198]. This approach does not preserve the (complex) symmetry, which has an influence if iterative solvers are used. Instead, the free DOFs and the Dirichlet DOFs can be separated. For each group of DOFs, sub-matrices are formed and used to solve the problem [183]. This approach preserves the matrix properties[1].

Thin layer approximation

The thin layer approximation is also known as contact resistance or contact impedance approach. It is also used to model heat transfer [204]. The underlying equation (Eq. (2.21)) comprises the jump of the potential across an interface. As functions in H^1 are continuous, the equation cannot be implemented straightforwardly with the standard FEM approach. Instead, the problem is formulated on M connected sub-domains. On each sub-domain, an H^1-conforming space is used. Consequently, there are two DOFs defined at the same point on an interface Γ_I between two subdomains (see Fig. 3.2C–D), which describe the jump of the solution. Then, the normal flux in Eq. (3.2) is substituted by Eq. (2.21). The new weak form reads (omitting Neumann and Robin BCs)

$$\sum_{m=1}^{M} \int_{\Omega_\mathrm{m}} \hat{\sigma}_\mathrm{m} \nabla \Phi_\mathrm{m} \nabla v_\mathrm{m} \mathrm{d}\Omega + \sum_{I=1}^{M-1} \int_{\Gamma_\mathrm{I}} \frac{1}{z_\mathrm{I}} [\Phi][v] \mathrm{d}s = -\sum_{m=1}^{M} \int_{\Omega_\mathrm{m}} f_\mathrm{m} v_\mathrm{m} \mathrm{d}\Omega \ . \tag{3.9}$$

Here, the quantities in the squared brackets $[\bullet]$ refer to the jump through the interface Γ_I (e.g., the potential difference across the thin layer). Evidently, the thin layer approximation is similar to Robin BCs, where the potential to one side of the interface is fixed and only the potential to the other side is unknown.

The errors of the FEM discretization are measured in the broken norms

$$||\Phi_\mathrm{FEM} - \Phi||_{H^1/L^2} = \sqrt{\sum_{m=1}^{M} ||\Phi_\mathrm{M} - \Phi||^2_{H^1/L^2}} \ . \tag{3.10}$$

The optimal orders of convergence in the respective norms are the same as for the standard FEM (see Eqs. (3.6) and (3.7)) [204, 205].

[1] A detailed comparison of the approaches can also be found in Lecture 21.6 at `https://www.math.colostate.edu/~bangerth/videos.html`.

Floating electrodes

A floating electrode is characterised by a fixed potential (the so-called floating potential) because it is assumed that the inside of the electrode is field-free as it is considered a perfect conductor. Thus, an additional unknown that is simply a complex number has to be introduced for each floating conductor.

Under the assumption of a perfectly conducting electrode without surface impedance, the integral of the normal component of the current density on the electrode surface is zero (i.e., the floating electrode does not draw any current). The constraint of the normal component of the current density can be introduced by Lagrange multipliers on the electrode surface (see [206] for the electrostatic case). The Lagrange multipliers are defined only on the respective boundary of the volume and belong to the Sobolev space $H^{-1/2}$. The left-hand side of the weak form (Eq. (3.3)) is augmented for each floating conductor (defined by its surface Γ_F) by the term

$$\int_{\Gamma_\mathrm{F}} (\lambda(v - v_\mathrm{F}) + (\Phi - \Phi_\mathrm{F})\mu)\,\mathrm{d}S \ , \tag{3.11}$$

where λ and μ are the solution and the test function of the Lagrange multipliers from a $H^{-1/2}$-conforming space. Φ_F is the floating potential and v_F the corresponding test function from the space of complex numbers.

The right-hand side of the weak form (Eq. (3.3)) is augmented by

$$\int_{\Gamma_\mathrm{F}} J_\mathrm{F} v_\mathrm{F} \mathrm{d}S \ , \tag{3.12}$$

where J_F is the current density on the floating conductor surface (i.e., the total current divided by the surface area). Note that this implies that a non-zero current can in principle be imposed through this condition. Nevertheless, the focus is here on passive electrodes, where J_F is zero.

The augmented formulation leads to a saddle point problem to be solved. The matrix arising from the saddle-point formulation has the block structure [207]

$$\begin{bmatrix} \mathbf{A} & \mathbf{C}^H \\ \mathbf{C} & 0 \end{bmatrix} \ , \tag{3.13}$$

where $\mathbf{C}$ is the additional sub-matrix due to the Lagrange multipliers and the fixed potential.

If a distributed impedance on the floating electrode is assumed, the constraint on the current density is not required. The distributed impedance is the surface impedance z_s of the electrode, which arises for example due to an EDL. In contrast to the Robin BC defined in Eq. (2.20), the potential to both sides of the ESI is

unknown. To implement this condition, the left-hand side of the weak form (Eq. (3.3)) is augmented only by the term [184]

$$\int_{\Gamma_\mathrm{F}} \frac{1}{z_\mathrm{s}} \left(\Phi - \Phi_\mathrm{F}\right) \left(v - v_\mathrm{F}\right) \mathrm{d}S \ . \tag{3.14}$$

The right-hand side of the weak form (Eq. (3.3)) is augmented by

$$\int_{\Gamma_\mathrm{F}} J_\mathrm{F} v_\mathrm{F} \mathrm{d}S \ . \tag{3.15}$$

Then, the matrix does not have saddle point like characteristics (i.e., the zero block of Eq. (3.13) is filled with non-zero entries [208]).

3.1.3 Numerical solution of the resulting linear systems

The crucial step to obtain the FEM solution is to solve a linear system of equations. In principle, it is sufficient to determine the inverse matrix $\mathbf{A}^{-1}$ and apply it on Eq. (3.8) to obtain

$$\mathbf{x} = \mathbf{A}^{-1}\mathbf{b} \ . \tag{3.16}$$

This approach is taken when a direct solver is chosen. Even though specialised algorithms exploiting the sparsity pattern of the FEM matrices exist to reduce the computational cost [209], direct solvers become prohibitively expensive in terms of memory consumption and computational time for large problems. As a rule of thumb, problems with more than 10^6 DOFs should not be solved using a direct solver on a powerful workstation. On laptops or standard personal computers, only problems with much less DOFs might be solvable with a direct solver.

To overcome the limitations of direct solvers, iterative solvers are used [210]. The basic idea is to choose an initial solution guess $\mathbf{x}_0$, which gives the initial residual $\mathbf{r}_0 = \mathbf{b} - \mathbf{A}\mathbf{x}_0$. Subsequently, the initial solution is improved and the norm of the residual minimised until it reached a certain threshold. To improve the convergence of the solution, usually a preconditioner is used. The preconditioner should lead to a better eigenvalue spectrum of the matrix. This corresponds to a reduced condition number, which, for example, positively influences the convergence of the conjugate gradient (CG) solver [210]. There exist a multitude of available methods and algorithms that are summarised in textbooks [210, 211] or manuals of linear algebra software libraries like *PETSc* [212–214]. For the sake of brevity, I will give a summary of best practices:

- Symmetric positive-definite matrices can be solved by the CG method with a suitable preconditioner (e.g., incomplete LU factorization (ILU) or multgrid techniques). CG is more memory-efficient than other iterative methods and has

a well-understood convergence behaviour. Thus, it should be paid attention to have the required matrix properties (see also Sec. 3.1.2) to successfully use CG.

- Complex symmetric matrices can be solved, for example, by biconjugate gradient stabilized method (BiCGSTAB), generalized minimal residual method (GMRES) or transpose-free quasi-minimal residual method (TFQMR) with a suitable preconditioner (e.g., ILU or multgrid techniques).
- Saddle-point problems arising when floating conductors are present (Eq. (3.13)) require special approaches, which are summarised in [215]. An example for floating conductors can also be found in [207].

Particularly multigrid preconditioners are efficient [216, 217]. They can be broadly distinguished into geometric and algebraic multigrid preconditioners. While geometric multigrid (GMG) requires a mesh hierarchy, algebraic multigrid (AMG) uses the matrix to construct the preconditioner. AMG is thus a black box approach and can be used for most of the problems discussed in this work. It is particularly suitable for complex geometries, for which no mesh hierarchy can be easily constructed and also robust for heterogeneous material parameters [217]. However, it requires a setup phase that is not required by GMG. In *NGSolve*, AMG can be combined with the BDDC (balanced domain decomposition by constraints) preconditioner [218], which is particularly suitable for higher-order methods. Unless stated otherwise, I used this preconditioner.

3.1.4 Post-processing

The FEM solution for the potential can be post-processed to obtain relevant observables. In general, the equations given in Sec. 2.3.4 can be straightforwardly used in the FEM approach.

However, for numerical reasons it is recommended to compute observables such as the current by volume integrals (Eq. (2.31)) rather than by surface integrals (Eq. (2.29)) [183]. Thus, I will report, unless otherwise stated, the result of the volume integration and have used the results obtained from surface integration only to double-check the solution. For the thin layer approximation (see Sec. 2.3.1), a term accounting for the power dissipation in the volume of the thin layer has to be added. This term is constructed by assuming the parallel-plate capacitor approximation (Eq. (2.23)) for the current density J_l and electric field E_l in the layer. Note that these quantities are scalars here as the field in an ideal parallel-plate capacitor is assumed to be homogeneous. The volume integral from Eq. (2.29) is substituted by a surface integral

$$P = d_\mathrm{l} \int\limits_{\partial\Gamma_\mathrm{l}} J_\mathrm{l}^* E_\mathrm{l} \mathrm{d}S = \int\limits_{\partial\Gamma_\mathrm{l}} \frac{\hat{\sigma}_\mathrm{l}^*}{d_\mathrm{l}} (\Phi_\mathrm{o} - \Phi_\mathrm{i})^* (\Phi_\mathrm{o} - \Phi_\mathrm{i}) \mathrm{d}S \ . \tag{3.17}$$

The layer conductivity $\hat{\sigma}_\mathrm{l}$ divided by the layer thickness d_l can be substituted by the specific layer admittance (see Eq. (2.22)).

One numerical reason for the better performance of the volume integrals might be singularities of the solution, which can occur at, for example, electrode corners, sharp edges or material transitions. In this case, the solution does not converge with optimal order and the error is greater around the singularity. To cope with singularities, adaptive mesh refinement is employed, which will be introduced in the following.

Adaptive mesh refinement

The goal of adaptive mesh refinement is to refine the mesh, where the numerical error is large. For that, an error estimate needs to be established to obtain the error associated with the i-th element η_i. Then, all elements with an error η_i above a certain threshold are marked and refined. In this work, I exclusively used the Zienkiewicz-Zhu error estimator [219]. A broader overview can be found in textbooks on adaptive mesh refinement [220, 221].

The Zienkiewicz-Zhu estimator can be understood from a physics point of view: The FEM solution Φ_FEM of the EQS field equation, which is in H^1, has a gradient that is by construction discontinuous between the elements. The flux is computed by multiplying this gradient with the respective material properties. However, it is known from Eq. (2.18) that the normal component of the flux must be continuous. In other words, the flux must be $H(\mathrm{div})$-conforming. Thus, the flux computed from the FEM solution can be interpolated onto an $H(\mathrm{div})$-conforming function to obtain a better approximation of the flux $G(\Phi_\mathrm{FEM})$.

Then the error estimator is

$$\eta = ||G(\Phi_\mathrm{FEM}) - \hat{\sigma}\nabla\Phi_\mathrm{FEM}||_{L^2} = \sum_i \eta_i \ , \tag{3.18}$$

where the η_i are evaluated for each element by element-wise numerical integration.

The error estimator is called efficient if there is a constant ratio between the estimated and the true error for all refinement steps. It is called reliable if it is an upper bound for the true error. The error estimator is asymptotically exact if it converges to the true error. Zienkiewicz-Zhu type error estimators are efficient and reliable, but not asymptotically exact [222]. In a comparative study of error estimators of different types, the Zienkiewicz-Zhu estimator performed well and can easily deal with jumps in the material properties [222]. I checked the implementation in *NGSolve* by solving the Fichera corner benchmark problem [223] for different polynomial orders using adaptive mesh refinement as well as global refinement. As expected [183], the optimal convergence rate with respect to the number of elements could be restored by adaptive mesh refinement (not shown).

3.1.5 Software packages

The aforementioned theoretical considerations can be used to formulate essential requirements for a suitable FEM software:

- Availability of different types of higher-order elements (at least H^1- and $H(\mathrm{div})$-conforming).
- Support of restricting function spaces to sub-domains to implement, for example, jump interface conditions or local constraints via Lagrange multipliers.
- Smooth interaction with mesh generators and the possibility to use higher-order geometry representations for curved elements.
- Interface to an efficient and versatile linear algebra library to solve the arising linear system by suitable, scalable and fast solvers.

Another desirable feature is the availability of complex arithmetic. Even though the complex-valued formulation can be converted into a real-valued formulation by separating real and imaginary part, it then requires special treatment by customised preconditioners [211, 224], which might not be straightforward to implement.

Initially, I experimented with *FEniCS* [198], which takes the weak form from Eq. (3.3) and automates the matrix assembly and linear algebra step. However, it does not feature complex arithmetic, does not offer curved elements and does not straightforwardly support the restriction of function spaces to sub-domains. Most of these features will be available in a new version of the *FEniCS* library, which is currently developed and had not been released early enough to be considered in this work. Instead, I used *NGSolve* [199], which is built on top of the mesh generator *Netgen* [225]. Its programming interface is similar to *FEniCS* but *NGSolve/Netgen* comes with a computer-aided design (CAD) kernel and can thus import, adapt and create 3D geometries to be used in the numerical computations. This is an important feature as it permits to refine meshes, curve the mesh again after the refinement and optimise the mesh with respect to the geometry. Hence, the geometrical error can be reduced because the surfaces of the geometry are better approximated. From a historical perspective, this feature had been lacking in many FEM codes used in industry, which led to the development of isogeometric analysis [226].

A detailed documentation of *NGSolve* can be found online[2]. Exemplarily, the implementation of the aforementioned basic FEM problem based on Eq. (3.3) is shown in Listing A.1. The implementation and use of the thin layer approximation will be discussed in Sec. 6.1, while floating electrodes will be discussed in Sec. 5.2.4 and Appendix A.2.

Among others, the commercial software package *COMSOL Multiphysics*® (in the following briefly called *COMSOL*) can be used to solve the EQS field equation

[2] `https://ngsolve.org/`

with the above-mentioned boundary conditions. They are included in the "electric currents" interface of the AC/DC module and are referred to as "contact impedance" and "floating potential". However, it remains unclear how exactly the conditions are implemented.

In recent years, other solutions to similar problems utilising open-source finite element software have been published [227–229]. They have focussed on the time-domain formulation of Eq. (2.16). Thus, they did not utilise complex numbers, which are required to solve the problem described here and could thus not be used.

3.2 Uncertainty Quantification

In the conventional modelling approach, a set of input parameters (e.g., dielectric properties) is chosen and the problem is solved for this set of parameters. Nevertheless, it is inevitable to account for the uncertainties of the model parameters including also geometrical parameters. Particularly with regard to experimental validation, it is important to be able to decide if a measured observable lies within the prediction interval and does thus validate the model. At the same time, the impact of an individual input parameter on the observable is of interest. It is measured in sensitivity analysis approaches. The UQ approach in a nutshell involves (see also Fig. 3.3 for a visual explanation):

1. The choice of appropriate probability distributions for uncertain input parameters.

2. The propagation of the uncertainty of the input parameters through the model.

3. Computation of model observables and their uncertainties as well as computation of sensitivity measures to estimate the impact of each input parameter on the observable.

The above-mentioned UQ approach is referred to as *forward UQ approach* as it starts with the model parameters and yields information about observables. There exists also an *inverse UQ approach*, where experimentally obtained observables are used to infer the probability distributions of the input parameters. In this work, the focus lied on the forward approach.

In practice, the forward approach requires the uncertain model solution to be dependent on the uncertain input parameters. For that, different numerical approaches exist that can be broadly distinguished into intrusive and non-intrusive methods [230]. In intrusive methods, the UQ approach is integrated into the solver. That means that the linear system of equations, for example of the original FEM approach, is extended to account for the parameters uncertainty. Thus, intrusive approaches require special software (e.g., the FEM package HiFlow^3 [231]) and the development of appropriate

solution techniques while potentially offering improved performance [230]. Consequently, intrusive methods cannot be used with existing black-box solvers such as *COMSOL* or existing implementations in *NGSolve* or *FEniCS*. Thus, I exclusively used non-intrusive methods. Non-intrusive methods rely on solving the model multiple times to generate samples from which statistical properties are calculated. In Monte Carlo approaches, samples are drawn from the probability distributions. They require tens of thousands of model runs to yield converged uncertainty estimates [232]. Hence, they are not suitable to perform a UQ analysis of detailed 3D models.

Instead, more efficient but approximate polynomial chaos methods are used. In this approach, a polynomial representation based on the probability distributions of the input parameters, a so-called surrogate model, is constructed [233]. The polynomials are chosen with respect to the probability distributions of the input parameters. The coefficients of the polynomial expansion, which constitutes the surrogate model, are calculated from the solutions computed for different sets of input parameters. There exist different methods to choose the sets of input parameters. I used the point collocation method, which is more robust than pseudo-spectral approaches and has thus been recommended [234]. At the collocation points, the polynomials (i.e. the surrogate model) are forced to yield the same result as the numerical model. In contrast to Monte Carlo methods, this means that the surrogate model does not necessarily have to be equal to the model solution at all sampling points but only at the collocation points.

The introduced methods have been implemented in the open-source *Python* package *UncertainPy* [234], which I used for all polynomial chaos analyses in a modified version[3]. For d uncertain input parameters, the number of expansion coefficients N_p for a polynomial of order p is

$$N_p = \binom{d+p}{p} \ . \tag{3.19}$$

Unless otherwise stated, the polynomial order was set to four (as recommended in [235]). *UncertainPy* generates sets of input parameters at $2(N_p + 1)$ collocation points, for which the model is solved. The UQ of a model with, for example, five uncertain parameters requires 254 individual model runs while ten uncertain parameters require already 2004 runs. Hence, the number of uncertain parameters should be kept as small as possible.

Statistical metrics such as the mean or the variance can be directly computed from the polynomial chaos expansion. Similarly, Sobol indices, which are measures of the parameter sensitivity, can be directly computed. To obtain the 5^{th} and 95^{th} percentile, which are the bound of the 90%-prediction interval, samples are drawn from the surrogate model. This task is computationally inexpensive and thus 10^4 and 10^5 samples were drawn to ensure convergence.

[3] `https://github.com/j-zimmermann/uncertainpy/tree/1.2.0.1`

I modified *UncertainPy* with respect to an application in an high-performance computing (HPC) environment. My modification exploits that only the probability distributions of the input parameters have to be known to create the input parameter sets for the individual model runs. The model runs can be performed in parallel and without any communication between them, writing the simulation results to an individual file. Once all runs are done, *UncertainPy* reads in the individual files to compute the polynomial chaos coefficients and finally the statistical metrics. Thus, the performance of the modified version depends mainly on the availability of computing nodes on an HPC cluster.

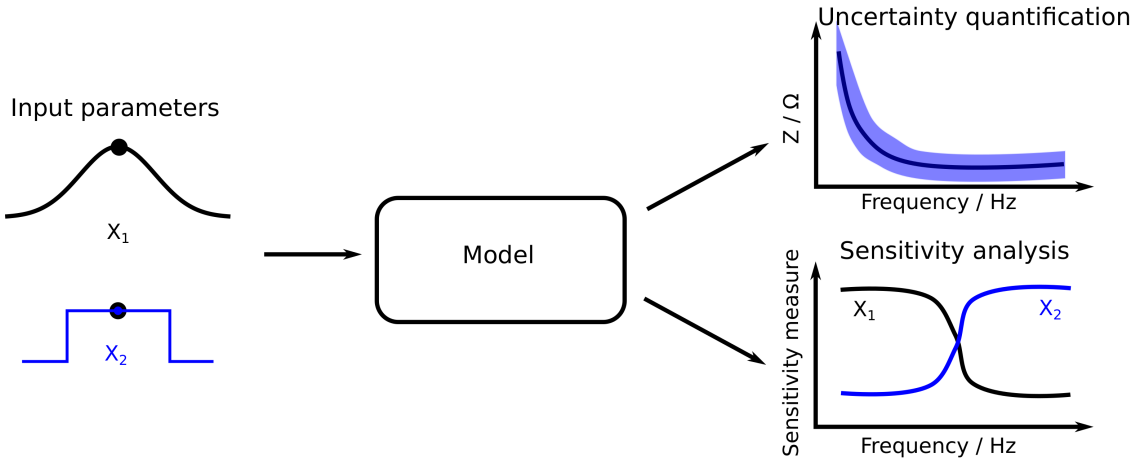

Figure 3.3: A visual summary of the UQ approach, inspired by [234]. The input parameters are described by probability distributions (here, X_1 by a normal and X_2 by a uniform distribution). In the conventional approach only one parameter value is considered. In the UQ approach, the information about the parameter distributions is propagated through the model. An observable, here the frequency-dependent impedance Z, is computed and its mean value (black line) and prediction interval are reported (blue area). This part of the approach is the actual uncertainty quantification. Simultaneously, the sensitivity of the observable with respect to the input parameters can be estimated by a sensitivity measure (usually Sobol indices). This aspect of the UQ approach is referred to as sensitivity analysis.

4 Experimental methods

In the following chapter, I will introduce the experimental methods used in the scope of this work. Due to the complexity of the sample handling in the lab, I often performed the measurements together with collaborators. Nevertheless, I contributed significantly to the design and implementation of the experiments and the data acquisition. The data evaluation was done exclusively by me for all results shown in this thesis.

4.1 Voltage and current measurements

The voltage and current measurements are used to record time-dependent signals as occurring during active stimulation. Multimeters are the simplest and most affordable devices for voltage and current measurements. They are particularly suitable for DC measurements. For AC measurements, the device specifications have to match the measurement range. We, for example, used a digital multimeter (Voltcraft VC850) that has a frequency range of 45 to 400 Hz. Thus, it is not suitable for measurements at many frequencies, which are relevant for cartilage stimulation. Instead, we used an oscilloscope for AC measurements. Then, a shunt resistor was added to the circuit for low-side current sensing (i.e., measuring the voltage drop across the shunt resistor). Because we used multiple devices, they are not listed here but will be introduced later.

4.2 Electrochemical impedance spectroscopy

The impedance is recorded over a wide frequency range in EIS and serves to assess the electrochemical properties of the system. EIS is not used during stimulation but rather before and after. The accuracy of the measurement can be derived from the accuracy contour plot [112]. For each frequency, the supported impedance range can be extracted from the plot. Thus, an estimate of the impedance should be extracted before measuring to use a device, which is capable of measuring the expected impedance accurately. Again, the employed devices will be introduced later but sufficient accuracy has always been ensured. I also used literature data in Sec. 7.2. The theoretical concepts to post-process impedance spectra will be introduced in the following. The text follows closely the paper [236] to which I contributed as a first author.

4.2.1 Relation between impedance and dielectric properties

The dielectric properties, relative permittivity ε_r and conductivity σ, can be extracted from impedance spectra for a known unit capacitance C_0 of an electrode [237][1]. The unit capacitance corresponds to the capacitance in air. The measured impedance Z and the dielectric properties are related by

$$Z = \frac{1}{j\omega\hat{\varepsilon}C_0} \text{ with } \hat{\varepsilon} = \varepsilon_r - \frac{j\sigma}{\omega\varepsilon_0} \ . \tag{4.1}$$

In this formulation, the unit capacitance is assumed to be a frequency-independent constant, while the dielectric properties are in general frequency-dependent. The unit capacitance can be experimentally determined from EIS data of samples with well-known dielectric properties such as air, distilled water or conductivity calibration solutions [238]. Note that this approach requires a fixed electrode geometry during and between measurements to ensure comparability. Furthermore, the electrode positioning and sample dimensions should be chosen appropriately such that only the sample properties are reflected in the EIS data. In practice, this means that an influence of the volume surrounding the sample (e.g., air, plastic dish or sample holder) on the impedance spectrum should be negligibly small. If this is not considered, the unit capacitance or the dielectric properties of an unknown sample will be computed wrongly using Eq. (4.1). In this work, I assumed that all considered data fulfil these requirements (i.e., that only the sample properties have been measured, which hence can be described by Eq. (4.1)). To identify data that might not fulfil these criteria, validity tests can be performed, which will be introduced in the following.

4.2.2 Validity test

The goal of EIS is to study the linear and causal response of a stable system [102]. Measured EIS data, which fulfil these requirements (linearity, causality and stability), must satisfy the Kramers-Kronig relations. Furthermore, the dielectric properties of (biological) tissues are related by the Kramers-Kronig relations (see Eqs. (2.26) and (2.27)) [194] and should thus be computed from valid EIS spectra that fulfil the Kramers-Kronig relations. A violation of the Kramers-Kronig relations can have various reasons such as instrumentation errors, temperature changes during the measurement, nonlinear electrode effects or other time-dependent errors.

The accordance of the EIS data with the Kramers-Kronig relations can be tested by fitting to a general equivalent circuit model comprising an ohmic resistor in series with a number of RC elements with a fixed time constant and, if applicable, a capacitor and an inductance [239, 240]. This approach is referred to as Lin-KK test.

[1] It is also common to speak of the cell constant K, which can be straightforwardly converted in the unit capacitance by $C_0 = \varepsilon_0/K$.

Another method to test the EIS data relies on the numerical evaluation of the Kramers-Kronig relations, which are integral transforms [241]. Theoretically, EIS data covering the entire frequency range from zero to infinity must be available to accurately evaluate the integrals.

4.2.3 Parameter estimation

Complex nonlinear least-squares techniques can be used to estimate the parameters of equivalent circuit models (e.g., Fig. 2.1) or dielectric relaxation models (e.g., Eq. (2.24)) from EIS data [102].

During the work on this thesis, I (supported by Leonard Thiele) wrote the software library *ImpedanceFitter* [242] that can generate arbitrary equivalent circuit models. Dielectric relaxation models are converted to circuit elements using their impedance computed by Eq. (4.1) for a known unit capacitance. All equivalent circuit models in this work were generated using *ImpedanceFitter*.

The models are fitted to experimental data using *LMFIT* [243], which is a library for complex nonlinear least-squares. *LMFIT* features a broad range of local and global minimizers and permits the user to customise the fitting routine. Moreover, the aforementioned Lin-KK test as presented in [240] and the numerical evaluation of the Kramers-Kronig relations were implemented.

A main reason for implementing an own software library was that many devices come with their own proprietary software, which does not allow one to use or implement novel algorithms as the Lin-KK test from [240]. Moreover, dielectric relaxation models are usually not supported. In my opinion, compared to self-written scripts, which are the status quo, an entire software library supports better versioning and thus better reproducibility. In the meantime, other researchers have identified a similar need for an open-source impedance fitting software and have written the software package *impedance.py* [244]. It is focussed on other aspects of EIS and thus can in its current state not perform the same analysis as *ImpedanceFitter*.

5 Numerical simulations of electrical stimulation devices

As outlined in Sec. 2.1, the documentation of electrical stimulation experiments is not always detailed enough to ensure replicability. At the same time, the lack of thorough documentation hampers the translation of in vitro research to in vivo applications (i.e., the translation from a cell culture of chondrocytes to the application of an electrically active implant in the knee joint). A crucial point is the dosimetry of the applied stimulation, that is the electric field and current density the cells are locally exposed to. Unfortunately, the local electric field and current density cannot be measured directly, but only be inferred from measurements of the local voltage or the global current [195]. Thus, numerical simulations can bridge the gap between theory and experiment and help to shed light on the prevailing electrical properties. Nevertheless, numerical simulations always rely on assumptions and need to be scrutinised [86]. Code verification is usually performed in the test suites of, for example, FEM software such as *NGSolve*. Thus, model validation (i.e., checking if the model describes reality) and UQ remain as open tasks for every numerical model of electrical stimulation. In the following, two electrical stimulation devices using different electrode materials, waveforms and amplitudes are investigated in detail and a workflow to establish a digital twin of these devices is presented. Eventually, documentation guidelines to overcome the replicability problem are suggested. Biological aspects of the electrical stimulation will not be explicitly addressed.

5.1 A workflow to create a digital twin of a stimulation chamber

This section is based on the publication "Using a digital twin of an electrical stimulation device to monitor and control the electrical stimulation of cells in vitro", which appeared in Frontiers in Bioengineering in Biotechnology [245][1].

The first subject of investigation is an in vitro stimulation chamber similar to the one introduced for DC stimulation in [246, 247]. The chamber (Fig. 5.1) has been, for example, used to study osteogenic differentiation of rat mesenchymal stem cells [247, 248], human mesenchymal stem cells [249] and preosteoblasts [250]. However, it is in principle suitable to study the effect of electrical stimulation on chondrocytes or the

[1] I conceptualised this study, carried out all simulations and the data analysis, prepared the figures and the initial draft of the manuscript. All experiments were conducted together with Kai Budde and Nils Arbeiter. Francia Molina performed the cell experiments in close collaboration with Kai Budde. Alexander Storch, Adelinde Uhrmacher, and Ursula van Rienen supervised the project, acquired the funding and provided all resources. The datasets generated for this study can be found online (`dx.doi.org/10.5281/zenodo.5189258`).

chondrogenic differentiation of mesenchymal stem cells thanks to its general design.

Nevertheless, in this work the focus is only laid on the relation between stimulation methods and their simultaneous potential to serve electrochemical characterisation irrespective of the type of cells stimulated. Techniques to feed data, which can be recorded in situ, into the theoretical models are introduced. In this work, we aimed at deriving impedance spectra from the recorded stimulation pulses and thus at gaining information about the systems while it is actively stimulated.

An essential step to build a reliable model is the integration of electrochemical processes at the electrode surface into the model. The augmented model can be tested by comparing predicted to recorded waveforms. If the results agree well, local electric field strengths become accessible. Furthermore, a controlled stimulation setting is defined. The first step on the way to a reliable model is the definition of the geometrical model.

5.1.1 Geometrical aspects

The stimulation chamber has initially been described in [246, 247]. Detailed instructions to replicate the chamber have been published in [248]. The chamber consists of a standard 6-well culture plate (Greiner Bio-One, Frickenhausen, Germany) with a modified lid (Fig. 5.1A). In each well, two platinum wires bent into L-shapes are connected to the lid and placed 25 mm apart. The upper part of the platinum wire is 18 mm long while the bottom part is 22 mm long. The wire has a cylindrical shape with a radius of 0.5 mm.

The electrodes are connected through insulation-displacement connectors and a planar multi-wire cable to a circuit board. The electrode pairs can be connected in series, in parallel, or in any other manner depending on the concrete circuit board used for connecting the electrodes to the power supply. This also permits only one electrode (pair) to be connected at a time. The circuit board is placed outside of the incubator, where the stimulation chamber is usually placed for in vitro experiments. Photos of the chamber and a technical drawing are shown in Fig. 5.1.

I prepared a parametrised 3D geometry of an electrode pair in a well using the open-source CAD tool *SALOME*[2] (Fig. 5.2). The cell culture medium is modelled as a cylinder with a modified top surface. Due to the capillary action in the Petri dish, the culture medium surface follows a meniscus-shaped profile (Fig. 5.2). The height of the meniscus has been empirically found to follow [251]

$$h(r) = h_0 \left(e^{-\frac{R-r}{c}} + e^{-\frac{R+r}{c}} \right) \quad , \tag{5.1}$$

where r is the radial distance from the centre of the well, R is the radius of the well, h_0 is the maximum height of the meniscus relative to the height at $r = 0\,\text{mm}$, and c is a parameter describing the decay of the meniscus. In preliminary measurements,

[2] `https://www.salome-platform.org/`

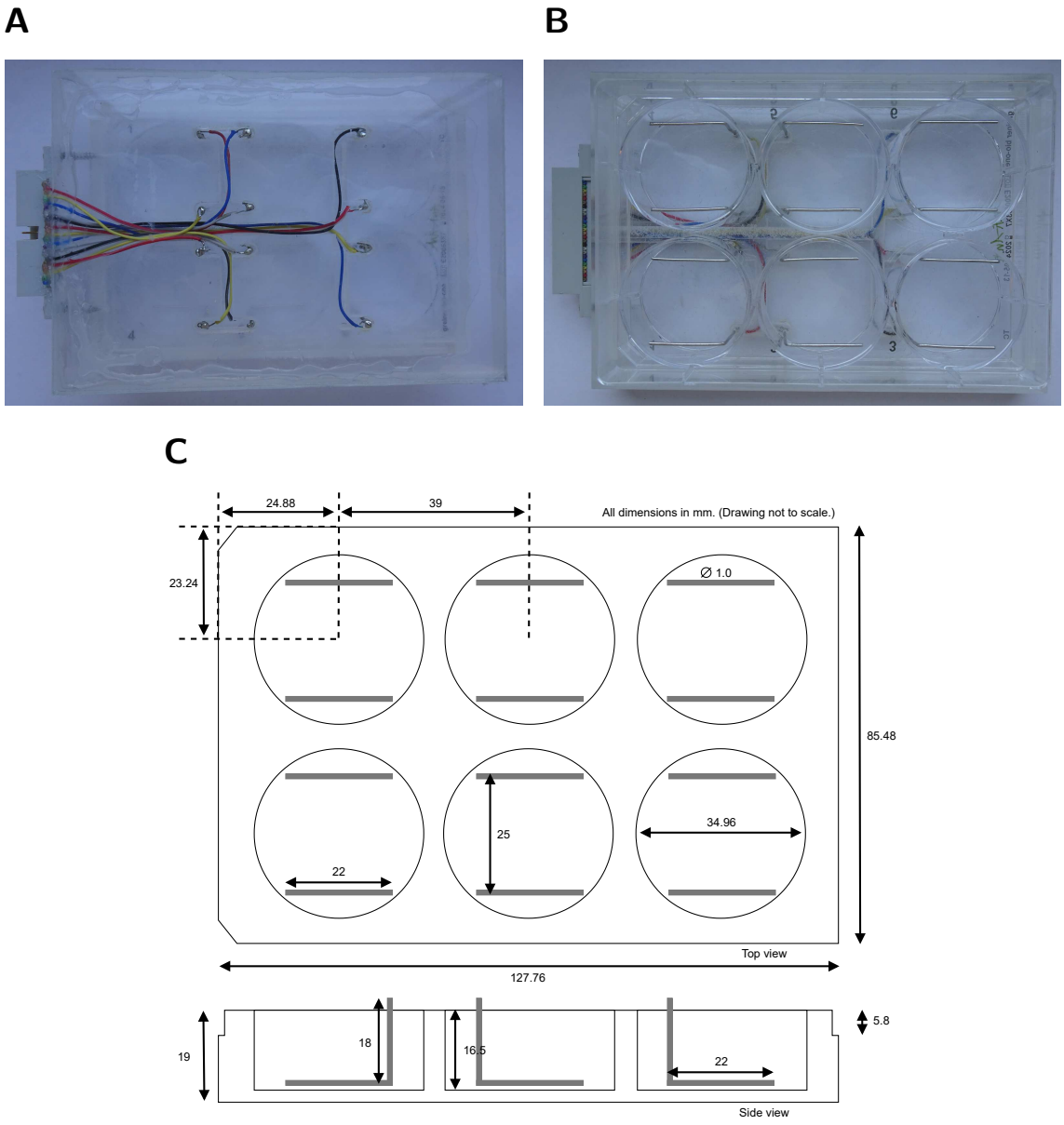

Figure 5.1: Images of the stimulation chamber (6-well lid with platinum electrodes) designed for flexible stimulation applications (top view **A** and bottom view **B**) as well as a drawing of the device (**C**). The figure was taken from the supplementary material of [245] and was prepared by Kai Budde.

we observed a maximum height of about 2 mm, which is about 0.4 to 0.5 mm less than previously reported [251]. However, the dish used in this work has a slightly larger radius than the dishes used in [251]. We did not measure the parameter c and assumed its value to be 2 mm as determined by [251]. I will address the uncertainties due to these choices later in the UQ approach. The height of the cell culture medium in the CAD model at $r = 0$ mm was determined using a bisection algorithm, which ensured a geometricl model with a volume of the cell culture medium having an error of less than 0.1 µL.

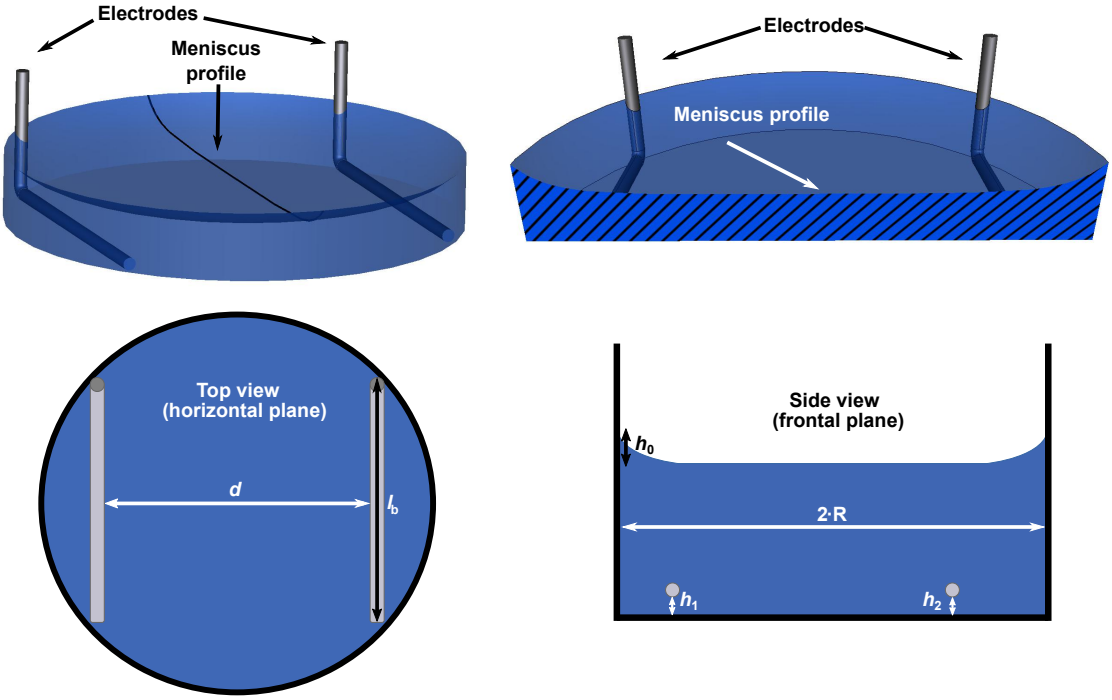

Figure 5.2: A 3D model of one well with two electrodes is shown (upper row). The radial profile of the meniscus was constructed using Eq. (5.1). The meniscus profile is highlighted in a cross-section through the centre of the well. Possible parameter choices for the UQ studies are indicated in sketches of the top and side view of the chamber (lower row): spacing between the electrodes d, length of the bottom part of electrode l_b, height of the electrode with respect to the bottom of the well (h_1, h_2) and height of the meniscus h_0. They account for horizontal or vertical movement of the electrode or variation of the meniscus height in Eq. (5.1). For more details on the choice of the modelling parameters see also Table 5.1. The figure was taken from [245].

5.1.2 Electrical aspects

The electrical stimulation chamber can be approximately described by an equivalent circuit (Fig. 2.1). As the electrodes are rather large, the impedances of the wires

and the electrodes themselves can be omitted as their magnitude is expected to be negligibly small. The dominant contributions to the system's impedance, which characterises the system's response to the applied stimulation, stem from the EEIs and the resistance of the cell culture medium. The EEI impedances comprise, as introduced in Sec. 2.1.1, a resistive (usually related to faradaic reactions) and a capacitive part (due to charging of the double layer).

The diffusion layer around the electrode in which the charge neutrality is not preserved is assumed to be small in comparison to the dimension of the cell culture well. Hence, it is neglected in the modelling approach. Then, a numerically efficient linear model can be solved, instead of an involved non-linear multiphysics model that explicitly models the interaction between applied electrical stimulation and ion dynamics [103].

5.1.3 Numerical methods

I performed electrostatic simulations (i.e., solving Laplace's equation) as described in greater detail in Sec. 3.1. In previous work, we found that the electric field is almost homogeneous in the centre of the well, where the cells are located [252]. This means that the electric field approximately has the same magnitude and direction at all points in this region. Hence, I only evaluated and reported the field strength (the magnitude of the field vector) at the centre of the well.

For all numerical experiments, the imposed voltage difference U was 1 V and the conductivity σ was $1\,\mathrm{S\,m^{-1}}$. Thus, a reference value for the current (and resistance) was obtained, which can be easily adjusted by proper scaling to match the respective experimental reality.

I performed adaptive mesh refinement using a Zienkiewicz-Zhu error estimator for the base geometry described in the previous sections. From a numerical point of view, the aforementioned base geometry can be considered as the worst case. The reason for this is that this configuration features the smallest possible distance of the electrode to the dish. Thus, small elements are needed to discretise the geometry around the electrode. These elements contain a comparably large error and might need additional refinement. For other geometrical configurations, the distance of the electrode to the dish is larger and thus the numerical error is expected to be smaller. Different meshing hypotheses can be used and will eventually influence the mesh quality [225]. The adaptive mesh refinement strategy on a mesh that was generated using a hypothesis to generate a very fine mesh led to a change of the current and field strength of less than 0.01%. The deviation from benchmark results, which were obtained using *COMSOL* V5.5, were equally small. Because I expected this numerical error to be much smaller than the possible uncertainty obtained in a UQ study, I did not perform adaptive mesh refinement for every configuration but used instead the above-mentioned meshing hypothesis for all computations.

Uncertainty quantification

The UQ was performed as introduced in Sec. 3.2. To speed up the computations, the model runs were performed in parallel on the HAUMEA high-performance computing cluster of the University of Rostock (each computing node equipped with 2 Intel Xeon Gold 6248 CPUs with in total 40 cores and 192 GB RAM).

The assumed hypotheses for the UQ computations are summarised in Table 5.1 (for a graphical representation see Fig. 5.2). Note that the effect of the cell culture was not considered because the focus in this work was on applications involving cells seeded in 2D culture. In 2D culture, the cells adhere to the bottom of the well in a very thin layer, which is a few micrometres thick. Such a thin layer is not expected to have any influence on the current through the chamber or the impedance, which are of interest in this work. Moreover, I considered only uniform distributions. This reflects the current knowledge of the uncertainties of the individual parameters. I would like to mention that the presented approach can be straightforwardly used with all probability distributions that are implemented in *Chaospy* (and thus *UncertainPy*) including, for example, the normal distribution [253].

5.1.4 Experiments

Direct current signals

Chronoamperometric DC measurements were performed using cell neurobasal medium inside an incubator at 37 °C. The details of the cell medium composition are not relevant for the theoretical analysis and thus the interested reader is referred for more details to the original publication [245]. Only one electrode pair in one well was used. The potential was applied using a laboratory power supply (Voltcraft PS 405 Pro). A digital multimeter (Voltcraft VC 404) was used to ensure a constant voltage throughout the entire experiment. We used a digital multimeter (Voltcraft VC 850) together with a Bluetooth device (Voltcraft VC 810) to record the current. The sampling interval was 1 s. We applied the current for about 10 minutes, then short-circuited the two electrodes until the discharging current became zero and then reversed the polarity. The current was recorded for three voltages: 1 V, 1.25 V and 1.5 V (in this order). We used different stimulation chambers for the AC and DC experiments because DC stimulation caused surface oxidation, which could have caused reduced replicability of AC experiments. During all measurements inside the incubator, the temperature was recorded with a thermometer. Furthermore, the temperature inside the cell culture medium was estimated by placing a temperature sensor (DrDaq, temperature sensor DD100, PicoLog 6, Pico Technology) in an adjacent well filled with the same amount of medium.

Table 5.1: Assumptions for the uncertainty quantification calculations. $\mathcal{U}$ stands for uniform distribution. We distinguish between geometrical and handling uncertainties. The geometrical uncertainties are due to manufacturing inaccuracies or the limited knowledge of the exact geometry. We estimated the geometrical uncertainties of the electrodes based on a measurement of the chamber used in this work. In contrast, the handling uncertainties are introduced by the experimenter.

Parameter	Distribution	Reasoning
Geometrical uncertainties		
Height of electrode h_1 or h_2 in mm	$\mathcal{U}(0.01, 1.5)$	Misalignment of electrodes
Length of bottom part l_b in mm	$\mathcal{U}(21, 22.3)$	Misshaping of electrodes
Spacing of electrodes d in mm	$\mathcal{U}(23, 25)$	Misalignment of electrodes
Decay of meniscus profile c in mm	$\mathcal{U}(1.95, 2.05)$	Estimate based on [251]
Height of meniscus profile h_0 in mm	$\mathcal{U}(1.8, 2.5)$	Estimate based on [251]
Handling uncertainties		
Cell culture medium V in mL	$\mathcal{U}(3.4, 3.6)$	Pipetting inaccuracies

Electrochemical impedance spectroscopy

Impedance spectra were recorded using a Gamry Reference 600+ potentiostat[3] . The input amplitudes were set to 25 mV. In preliminary numerical experiments, we also used 50 mV and did not observe a visible difference, which indicates that the selected amplitude was chosen sufficiently small to exclude electrochemical reactions at the EEI. Unless stated otherwise, the spectra were recorded from 1 Hz to 5 MHz. The EIS measurements were carried out in a two-electrode configuration (i.e., no reference electrode was used). The EIS spectra were analysed using *ImpedanceFitter*. By applying the Lin-KK test (see Sec. 4.2.2), it was checked, which part of the spectrum could be successfully fitted to an equivalent circuit. Usually, only points at high frequencies greater than 1 MHz and at very low frequencies below 10 Hz had to be excluded from the analysis.

For the EIS experiments, we used both an aqueous KCl solution of known conductivity (HI7030, Hanna Instruments) and the cell culture medium for the characterisation of the chamber. The KCl solution was used at ambient conditions (25 °C) and the cell culture medium as described in Sec. 5.1.4. The conductivity of the KCl solution at 25 °C is $1.288\,\mathrm{S\,m^{-1}}$. The conductivity of the cell proliferation medium was measured with a handheld conductivity meter (LF 325-A, Wissenschaftlich Technische Werkstätten, Weilheim, Germany) and was $1.38 \pm 0.05\,\mathrm{S\,m^{-1}}$ at 37 °C.

To check if the results obtained with one electrode pair can be also used for six electrode pairs, we performed EIS measurements also using six filled wells with each

[3] I would like to thank Sylvia Speller's group, in particular Ingo Barke and Regina Lange, for providing the potentiostat.

3.5 mL medium. When using six wells connected in series, the measured impedance is

$$Z = \sum_{i=1}^{6} Z_i \approx 6Z_1 \ , \tag{5.2}$$

where Z_i is the impedance of a single well and the Z_i are expected to be similar to the previously measured impedance of a single well Z_1. Likewise, the impedance of six wells connected in parallel is expected to be

$$Z = \left(\sum_{i=1}^{6} \frac{1}{Z_i} \right)^{-1} \approx \frac{Z_1}{6} \ . \tag{5.3}$$

Rectangular wave stimulation — Broadband impedance spectroscopy

We investigated the current and voltage response to pulses with a frequency of 130 Hz, which is commonly used in DBS [60]. The pulse width was chosen as 60 µs, 200 µs, or 600 µs. Both monophasic and biphasic pulses without an interphase gap were investigated. The voltage signal was supplied by the ISO-STIM 01D unit (NPI electronics). The current signal was measured using a 1 Ω shunt resistor and amplified using a custom-built amplifier with a gain of 10. Both signals were recorded using an oscilloscope (RTB2004, Rohde&Schwarz). Note that because of the shunt resistor, not the entire input voltage drops across the stimulation chamber. To keep the influence of the shunt resistor negligible, we chose its resistance to be much smaller than the smallest expected impedance of the stimulation chamber in the relevant frequency range.

The voltage and current responses were Fourier transformed using the fast Fourier transform (FFT) method of the *NumPy* package [254]. The impedance was estimated by dividing the Fourier-transformed voltage signal by the current signal. This technique is also known as broadband impedance spectroscopy [255]. The applied voltages were chosen to be 1, 1.5 and 2 V such that the current amplitude was between 1 and 10 mA. In the current-controlled mode, the current amplitude was kept fixed at 6.5 mA.

Cell experiments

The stimulation chamber was tested with adult neural stem cells. As these cells are not related to cartilage tissue engineering, the reader is referred for a detailed description of the cell culture to the original publication [245].

Different stimulation protocols were assessed: short-term stimulation (current-controlled stimulation for 30 minutes, one hour, two hours; voltage-controlled stimulation for 24 hours) and long-term stimulation (current-controlled stimulation for 12 hours per day for 4 days (in proliferation phase) or 10 days (4 days in proliferation and 6 days in differentiation phase)). In the current-controlled mode, symmetric

biphasic pulses with 6.5 mA, 130 Hz and pulse width of 60 µs were used to simulate in vivo deep brain stimulation conditions [60] and the wells were connected in series. In the voltage-controlled mode, the same waveforms were used but with an amplitude of 1.5 V and the wells were connected in parallel.

Cell viability was tested by visual inspection in short-term stimulation conditions and by quantitative cell counting in long-term stimulation experiments using DAPI staining of cell nuclei for reliable counting. During the cell experiments, the voltages and/or currents were monitored using a RIGOL DS1000Z oscilloscope. The recordings were controlled and the data saved to a laptop using the VISA interface and a self-written *Python* script[4].

5.1.5 Results

The workflow can be subdivided into four steps:

- Predicting the resistance / electric current for a fixed voltage and a known conductivity under consideration of uncertainties.
- Performing measurements of the voltage and current or impedance to compare the prediction to the experimental reality.
- Augmenting and refining the model to be able to make reliable predictions.
- Testing the model and updating its parameters during the stimulation based on recordings of the stimulation signals. This step eventually establishes the digital twin.

The results associated with the individual steps will be presented in the following.

Numerical predictions of the simulation model — a prerequisite for the digital twin

Because the numerical FEM problem is linear, the relevant observables (i.e., electric field and current) depend linearly on the imposed voltage difference U. Let I_0 be the current that is computed for an imposed voltage difference of $U_0 = 1\,\mathrm{V}$ and a conductivity of $\sigma_0 = 1\,\mathrm{S\,m^{-1}}$, then the expected current I at voltage U and (in general temperature-dependent) conductivity $\sigma(T)$ is

$$I = \frac{\sigma(T)}{\sigma_0}\frac{U}{U_0}I_0 \ . \tag{5.4}$$

[4] `https://github.com/j-zimmermann/PyVISAScope`

Thus, the computed resistance of the cell culture medium is independent of U but depends on the temperature-dependent conductivity of the cell culture medium

$$R = \frac{U}{I} = \frac{\sigma_0}{\sigma(T)} \frac{U_0}{I_0} \ . \tag{5.5}$$

Because the UQ assumptions (Table 5.1) are all uniform distributions, it is sensible to consider the 90% prediction interval as an error estimate. This means that I will establish a lower and an upper bound for each observable. To account for the uncertainty in the conductivity, I multiplied the 5^{th} percentile with the lowest possible conductivity and the 95^{th} percentile with the highest possible conductivity. To estimate the lowest and highest possible conductivity, we assumed a temperature fluctuation of $\pm 1\,^{\circ}\text{C}$ together with a change of the conductivity value of $2\,\%/^{\circ}\text{C}$. This estimate was based on the manufacturer information and is similar to values reported for cell culture media [193].

First, I ran the UQ analysis only with the geometrical uncertainties (six parameters in total) to assess the uncertainty arising from the manufacturing process. With six parameters, 422 runs were required (a formula to compute the number of runs for a given polynomial order and number of uncertain parameters can be found in [234]). These runs were usually done within a few hours thanks to a high degree of parallelism. It turned out that the meniscus decay had almost zero influence. Thus, it was omitted from the further analysis.

Then, I considered the uncertainty of the volume due to pipetting inaccuracies. Changes in the volume appeared to have an influence on the current but not on the field strength (Fig. 5.3). The error of the spacing (about 4%) is almost linearly propagated through the model for the electric field strength. This is also highlighted in the probability distributions of the samples drawn from the surrogate model (Fig. 5.4). The distribution of the field strength appears to be almost uniform, thus indicating that the assumed probability distribution for the electrode spacing is dominantly influencing the uncertainty of the predicted field. In contrast, the distribution of the current is widened and more bell-shaped, which highlights the additional influence of the volume uncertainty. Eventually, I used only the three parameters, which influenced the current the most (d, l_b, V), to reduce the number of required simulation runs to 72. The uncertainty estimate did then not deviate notably from the previous results, while the UQ analysis takes considerably less time.

In Table 5.2, the 90% prediction interval of the resistances R is reported as well as the prediction intervals multiplied with the uncertainty interval of the conductivity. The unit capacitance of the electrode can be computed from the resistance as $C_0 = \varepsilon_0/(\sigma R)$. It is about 38 fF for a volume of 3.5 mL. The prediction intervals for the field strength in $\text{V}\,\text{m}^{-1}$ were $[37.56, 40.67]$ for 3.5 mL, $[36.87, 39.85]$ for 4 mL and $[35.58, 38.45]$ for 5 mL. These results suggest a slight decrease in the field strength with increasing volume.

Table 5.2: Comparison between predicted resistance of the medium R_{medium} and R_{medium} as extracted from fits to experimental data (more details in Sec. 5.1.5). The values are reported in Ω. The fitted and measured impedance deviated on the order of the accuracy of the potentiostat (1%) indicating the high quality of the fit. We did not investigate the experimental error in greater detail and thus estimate it to be 1% for all reported values. The predicted values (between the 5^{th} and 95^{th} percentile) are entirely based on the UQ analysis. The uncertainty of the conductivity σ was assumed to be ±2% of the expected value ($1.288\,\text{S}\,\text{m}^{-1}$ for KCl at 25 °C, $1.38\,\text{S}\,\text{m}^{-1}$ for cell culture medium at 37 °C). The values for parallel and series connections were estimated using Eqs. (5.2) and (5.3).

Electrolytic solution	Volume	Experimental value in Ω	Predicted value in Ω	Predicted value with uncertainty of σ in Ω
KCl	3.5 mL	183.84	[177.97, 197.18]	[174.48, 201.21]
KCl	4.0 mL	167.26	[157.42, 173.39]	[154.34, 176.93]
KCl	5.0 mL	138.40	[129.58, 141.96]	[127.04, 144.85]
Medium (1-well)	3.5 mL	166.56	[166.11, 184.04]	[162.85, 187.79]
Medium (6-well)	3.5 mL, ∥	29.02	[27.69, 30.67]	[27.14, 31.29]
Medium (6-well)	3.5 mL, series	1075.25	[996.66, 1104.24]	[977.10, 1126.74]

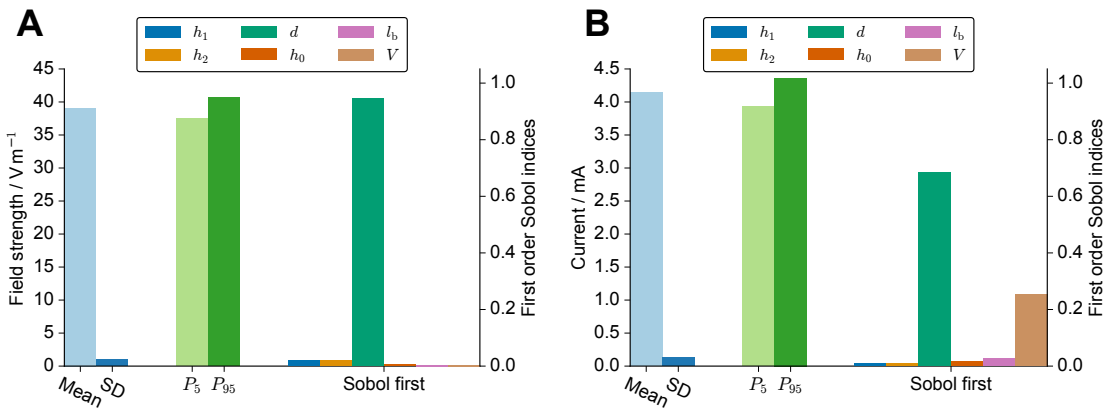

Figure 5.3: UQ results for the electric field strength (**A**) and the current (**B**). The mean, standard deviation, 5$^{\text{th}}$ and 95$^{\text{th}}$ percentile are shown together with the first-order Sobol indices, which indicate the individual influence of the respective parameter on the simulation result. The varied parameters were the height of the meniscus profile h_0, the height of the left and right electrodes h_1/h_2, the spacing of the electrodes d, the length of the horizontal part of the electrode l_b, and the volume of the cell culture medium V. These parameters and their probability distributions are explained in greater detail in Table 5.1. The simulations were run for an imposed voltage difference of 1 V and a conductivity of 1 S m^{-1}. The figure was taken from [245].

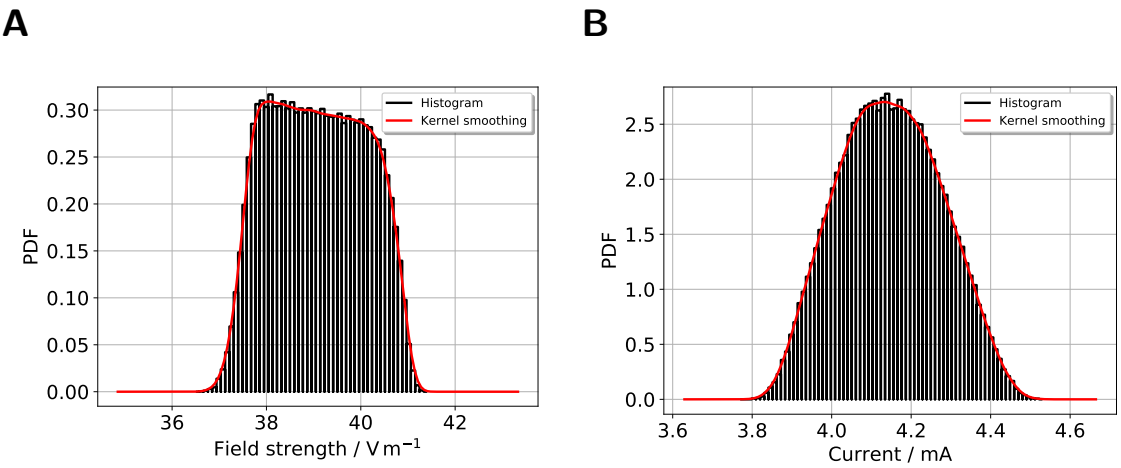

Figure 5.4: Comparison of probability distributions sampled from surrogate UQ models for field (**A**) and current (**B**). Note that this figure corresponds to the UQ results presented in Fig. 5.3 . The figure was taken from the supplementary material of [245].

In the following, experimental approaches to augment the model by an EEI impedance and assess its predictive power will be introduced. In particular, it will be assessed if the corresponding experimental observations lie within the aforementioned prediction intervals.

Stimulation methods for characterising the stimulation chamber and augmenting the simulation models — constructing the digital twin

Direct current stimulation — Chronoamperometry Initially, the chamber was tested for its original purpose: DC stimulation. We observed that the measured current did not grow linearly with the applied voltage. This would have been the expected behaviour for a circuit dominated by the ohmic resistance of the cell culture medium. Instead, the current drastically decreased with increased stimulation time. Even after about ten minutes, the currents did not converge to a steady value. I could describe the recorded current response I by a function of the following form

$$I(t) = \frac{a}{\sqrt{t}} + be^{-t/c} \ , \tag{5.6}$$

where a, b, and c are positive constants and t is the time. Equation (5.6) was fitted to the experimental data using a nonlinear least-squares method from *LMFIT*. The fitted current was in good agreement with the measured current for all voltages (see, for example, Fig. 5.5, other figures can be found in the supplementary material of [245]).

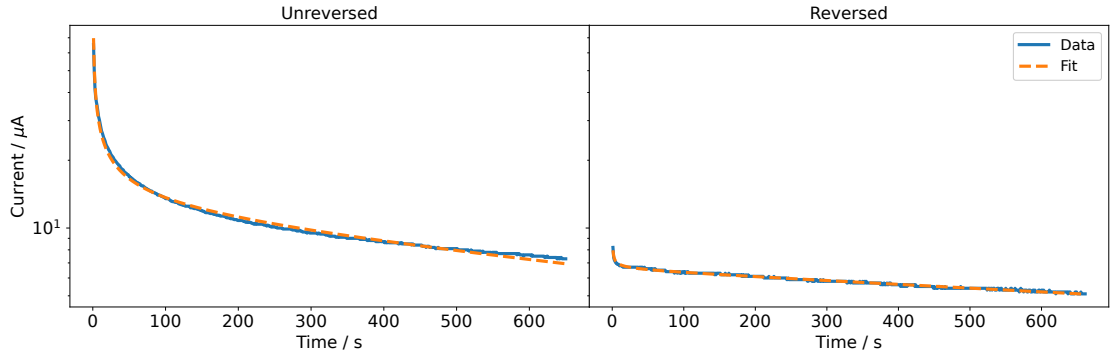

Figure 5.5: Recorded and fitted currents through the cell culture medium at a DC voltage of 1 V. Note that the ordinate is log-scaled because the current decreases sharply with time. The figure was taken from [245].

The equation for the current response could describe a superposition of a faradaic, diffusion-limited current inversely proportional to $\sqrt{t}$ and nonfaradaic, capacitive current decaying with $\exp(-t)$ [98]. The nonfaradaic current can, for example, be interpreted in terms of a charging of the double layer or the pseudocapacitance at the

electrode surface [92, 99]. However, more advanced measurements would be required to unambiguously explain the observed behaviour. The behaviour of platinum during electrical stimulation is still subject of ongoing research [256]. Importantly, one cannot establish a direct relation between Eq. (5.6) and the cell culture medium resistance, which can be computed from the FEM solution. Thus, the current recorded at a fixed voltage cannot be used to validate numerical simulations based only on Eq. (2.28). Instead, local potential recordings would be required [195].

Studying the two parts of Eq. (5.6) individually revealed that before reversing the polarity, the faradaic and nonfaradaic currents are on the same order of magnitude. The nonfaradaic current is almost constant at all times. During the measurement period, the current did not converge to this constant value. After reversing the polarity, the influence of the faradaic current is considerably smaller. It even seems as if the current after polarity reversal was a continuation of the current before polarity reversal. Because we short-circuited the electrodes and thus there should be no residual charge stored in the system before reversing the currents this observation is surprising. The result suggests an electrochemical memory of the system. This could mean that both electrodes are continuously changed during the experiment and that the state of the electrodes is not reversed when changing polarity. There might also be other reasons for the irreversibility; for example, depletion of reactive species around the electrodes [93]. Then, the composition of the medium around the electrodes could have changed and a diffusion layer, which I did not include in the simulation model, could be present. When using the stimulation chamber in cell experiments, we observed a change of the colour of the anode, most likely showing oxidation (PtO_2). Thus, we cleaned the electrodes electrochemically after each DC stimulation application by applying a higher voltage of $U = 5\,\mathrm{V}$ for 5 minutes in NaCl. For the cell experiments, this ensured replicable stimulation currents.

Electrochemical impedance spectroscopy The general equivalent circuit shown in Fig. 2.1 distinguishes between the two EEIs. However, the EEIs are in practice indistinguishable unless a reference electrode is used. Hence, the EEIs are often described by one circuit comprising a CPE in parallel with a charge-transfer resistance [90]. I found that this equivalent circuit did not describe the EIS spectra well. Instead, I used a circuit that had been developed to describe platinum surface oxidation (Fig. 5.6) [257]. More general explanations on the involved elements and identification of suitable equivalent circuits are given in the Appendix B.

The fitted impedance values deviated usually less than 1% from the experimental data (an example is shown in Fig. 5.7). For some configurations, an additional lead inductance improved the fit results (compare also Fig. 2.1). This was particularly the case for the 6-well configuration. The ohmic resistance R_{medium} can be directly compared to the numerical simulations (Table 5.2). All measured values lie within the prediction intervals of the numerical simulation, which validates the chosen

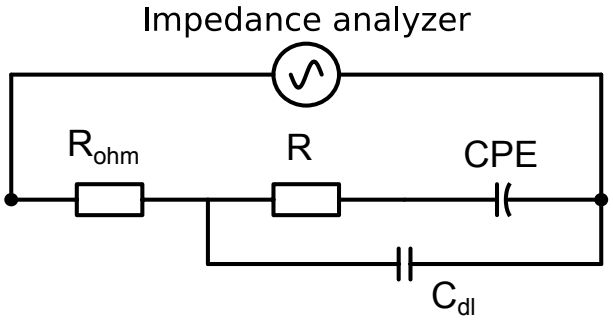

Figure 5.6: Equivalent circuit model as described in [257]. One part of the interface impedance is modelled by a constant-phase element (CPE) in series with a resistor (R). The other part is modelled by a capacitor (C_{dl}), which is meant to account for the ionic double layer. The ohmic resistance of the electrolyte (R_{ohm}) is connected in series with the interface element. To highlight the source of the ohmic resistance, we also refer to it as R_{medium}. If applicable, a lead inductance can be connected in series with the ohmic resistance. The figure was taken from the supplementary material of [245].

model. Using different volumes of the KCl solution showed that the liquid could be modelled entirely as a resistor: the measured imaginary part did not depend on the volume, which would have been expected if the imaginary part would not be exclusively due to the EEI (Fig. 5.8). The cutoff frequency where the impedance changes from capacitive to resistive behaviour can be estimated to lie between 1 kHz and 10 kHz. A more rigorous definition of the cutoff frequency can be found in [93]. The impact of this quantity on the current and voltage transients will be shown later. In sum, these results show that the numerical simulations can reliably predict the ohmic resistance of the culture medium while the EEI properties can only be inferred from EIS measurements.

To assess the nonlinear behaviour of the EEI impedance, we measured the impedance at the fundamental frequency (130 Hz) for increasing voltage amplitudes. Indeed, we could observe nonlinear behaviour (Fig. 5.9). The impedance did not change notably at amplitudes lower than 250 mV. Hence, this voltage amplitude can be used as an estimate for the limit of linearity.

Rectangular wave stimulation — Broadband impedance spectroscopy

Rectangular waves can be described in the frequency domain by Fourier series (see also Appendix C). To obtain the frequency-domain representation of the signals, there exist two popular approaches: fast Fourier transform (FFT) of time-domain signals [258] or the use of the analytically available expressions for the Fourier series [259]. The main difference in the frequency spectra of the waveforms considered in this work is that the biphasic pulse has its main contribution at higher frequencies than the monophasic pulse (Figs. C.1–C.3). The amplitudes of the

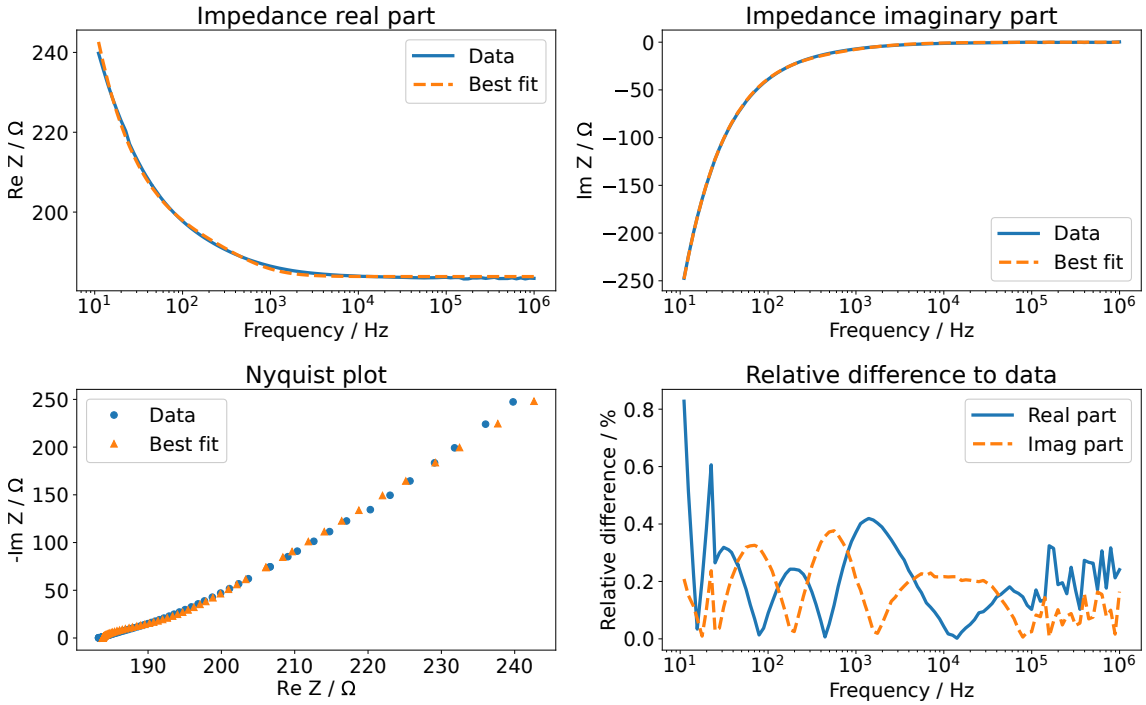

Figure 5.7: EIS measurement of aqueous KCl solution (3.5 mL). The real part and imaginary part of the measured data are compared to the best fit results using the impedance model of [257]. The relative difference is given with respect to the absolute value of the impedance. As the relative difference does not exceed the measurement accuracy of 1% at al frequencies, it can be assumed that the fit is accurate. The figure was taken from [245].

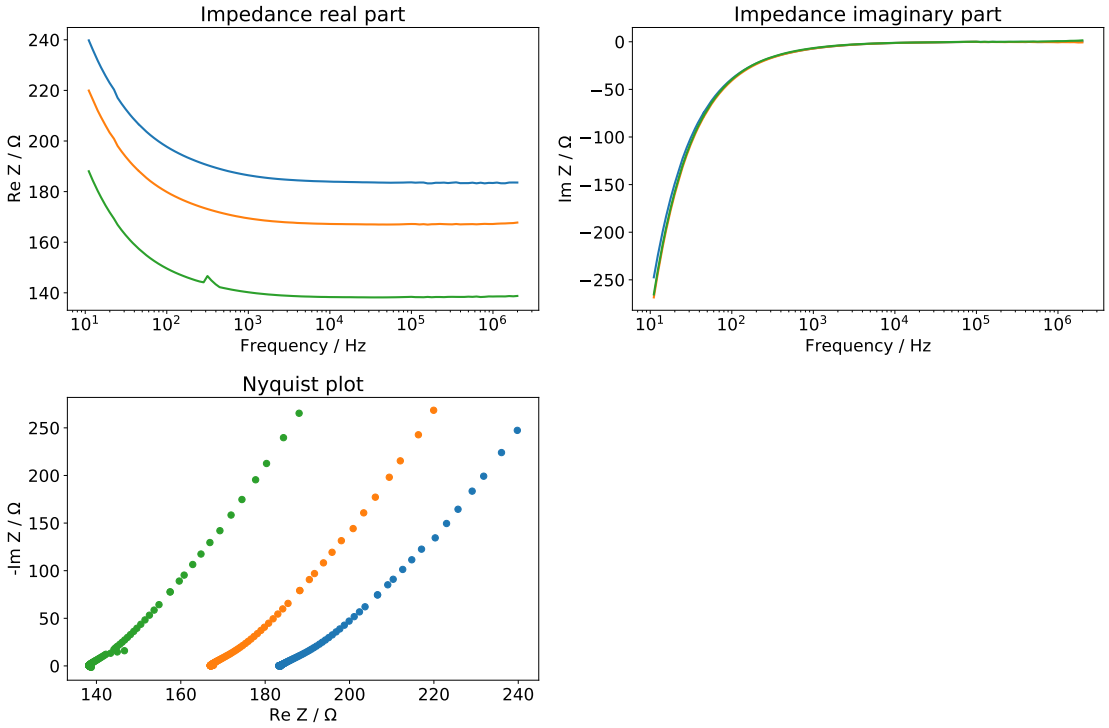

Figure 5.8: Impedance spectra of KCl solution with 3.5 mL (blue curves), 4 mL (orange curves), and 5 mL (green curves). The figure was taken from the supplementary material of [245].

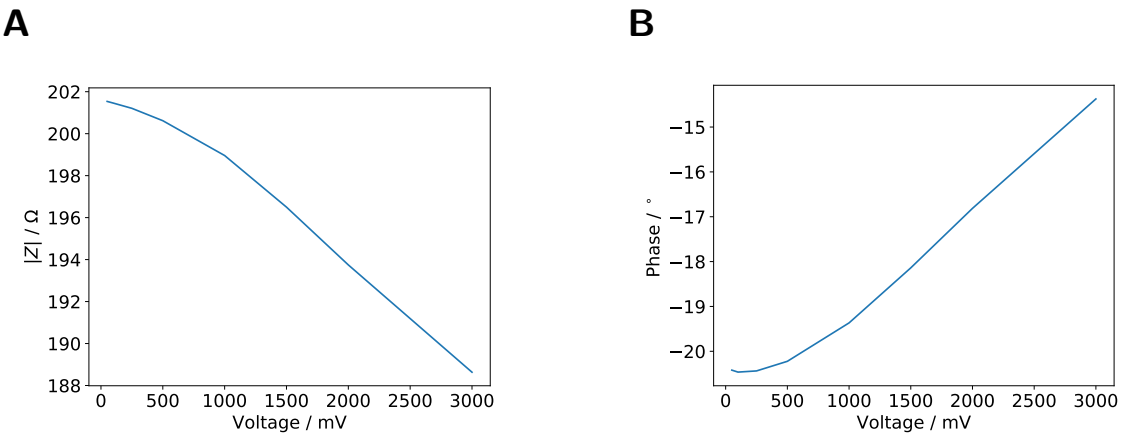

Figure 5.9: Impedance at 130 Hz for different voltage amplitudes. The impedance magnitude (**A**) and the phase (**B**) are shown. The figure was taken from the supplementary material of [245].

individual frequency components of the different waveforms did not exceed the aforementioned limit of linearity for an overall pulse amplitude of 1 V. Amplitudes greater than or equal to 2 V would lead to frequency amplitudes greater than 250 mV and thus potentially non-linear responses at low frequencies. I used 2500 harmonics (i.e., including harmonics up to a frequency of 325 kHz) to compute the signals unless otherwise stated. This number of harmonics covers the relevant part of the frequency spectrum for all considered signals and reduced oscillations caused by high-frequency contributions. High-frequency oscillations occurred only for current-controlled stimulation in the predicted signals but were not measured. Aside of possibly being a numerical artefact, it could be that high-frequency oscillations are filtered by the stimulator, the employed amplifier or the oscilloscope, which was used for recording. Importantly, the general signal shape of the predicted and measured signals always agreed well.

I used the FFT approach to estimate EIS spectra from time-domain data. The impedance is given by

$$Z(\omega) = \frac{U(\omega)}{I(\omega)} \tag{5.7}$$

with ω the angular frequency, Z the impedance, U the potential and I the current in the frequency domain. The impedance computed by the FFT is known at equally spaced frequencies. The frequency resolution (i.e., the frequency spacing) depends on the length of the time signal. I found that recording about 10 periods, which corresponds to a frequency resolution of about 10 Hz, yielded a sufficient resolution. I used a truncation method to reduce noise in the FFT spectra: only data points with a current amplitude that is at least 10% of the maximum current amplitude were considered. This approach has also been proven to be effective for numerical simulations [260].

To construct time-domain signals under consideration of the measured EIS spectra, I used the analytical Fourier series approach. Note that charge-balancing signals such as symmetric biphasic, biphasic with delay etc. can be straightforwardly computed as the superposition of time-shifted monophasic rectangular waves.

In preliminary experiments, we found that the current-controlled monophasic waveform with KCl showed a problem of a large DC voltage offset (Fig. 5.10). Moreover, the EIS spectra changed after using such a waveform, which indicated a possible change of the electrodes as previously mentioned (data not shown). Hence, we did not further consider current-controlled monophasic waveforms because potentially harmful electrochemical reactions cannot be excluded. Simple reasoning for this DC offset, which has also been reported elsewhere [261], can be given based on the results presented in Sec. 5.1.5. The employed monophasic pulse with an amplitude of 6.5 mA, a pulse width of 60 µs, and a frequency of 130 Hz has a DC component of 50.7 µA. We found that a DC voltage of about 1 V caused a current of only about 10 µA decaying with time (Fig. 5.5). This explains why the current-controlled

monophasic waveform required a voltage DC offset greater than 1 V.

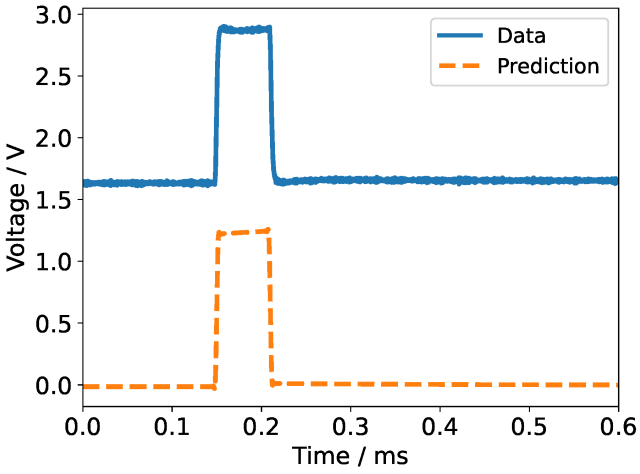

Figure 5.10: Measured and expected voltage transient for KCl solution with 3.5 mL stimulated with a current-controlled pulse (6.5 mA, 130 Hz, 60 µs). The figure was taken from the supplementary material of [245].

The impedance data obtained using the FFT algorithm (Fig. 5.11) could be well explained using the EIS results from Sec. 5.1.5. Nevertheless, the impedance deviated slightly from the impedance measured by EIS. Thus, the impedance was fitted again to update the parameter values of the impedance model (Fig. 5.6). Considering a change in all variables turned out to be an inappropriate approach. Some waveforms contain information only in a limited frequency range (Figs. C.1–C.3). In this case, not all parameters of the impedance model could be unambiguously determined. Some fit parameters were linearly correlated. In consequence, this caused a wrong estimate of the ohmic resistance. Instead, I found that permitting changes in (i) inductance, (ii) ohmic resistance and (iii) double-layer capacitance sufficed to accurately describe the measured data. The increased lead inductance (evidenced by the positive phase of the measured data in Fig. 5.11) is most likely caused by the long and unshielded wires connecting the stimulator and the stimulation chamber. Because the conductivity of the medium depends on the temperature, the deviation of the expected and observed ohmic resistance can be, for example, explained by the uncertainty of the incubator's temperature control. The change in the double-layer capacitance was usually only a few per cent. It could be caused by an electrochemical reaction at the electrode surface [257], which occurs due to the applied electrical stimulation. With this result, a means to update the model (Fig. 5.6) based on evolving data was established, as required for a digital twin [87]. Furthermore, it permits to identify (undesired) changes in the stimulation system with increasing stimulation time.

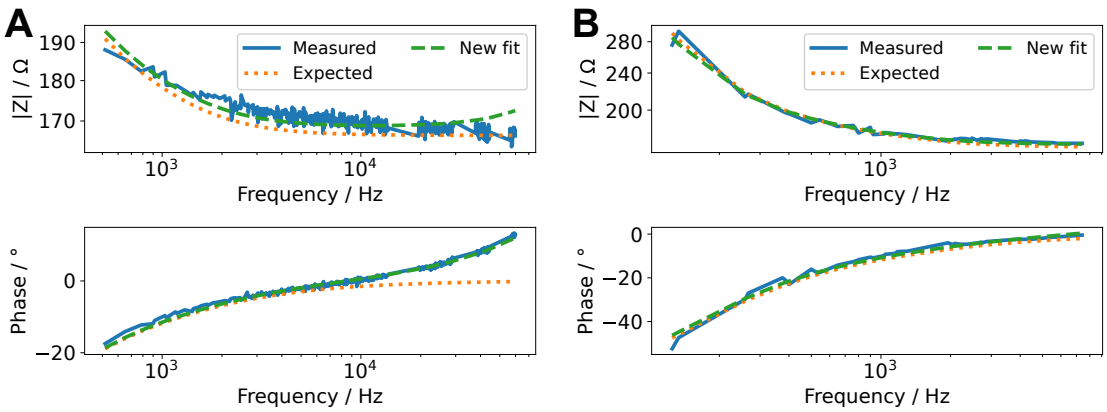

Figure 5.11: Bode plot of the impedance computed from FFT of voltage and current pulse for a pulse width of 60 µs (left) and 600 µs (right) and an amplitude of 2 V (*measured*). Note that we omitted Fourier components with small magnitude to reduce noise at higher frequencies. The measured impedance is compared to the impedance expected after EIS measurements (*expected*). A new fit to the measured impedance was made by varying only the lead inductance, ohmic resistance of the cell culture medium and double-layer capacitance (*new fit*). Note that both abscissa and ordinate differ between the figures because the signals comprise different frequency contributions. The ordinate is log-scaled. The figure was taken from [245].

The (re-)construction of the stimulation signals is possible for both voltage- and current-controlled stimulation. For the sake of brevity, I will focus here on the voltage-controlled stimulation, which sufficiently describes the approach. The interested reader is referred to our original publication for current-controlled results [245]. Having the parameter values to compute the impedance at hand, the expected current for a given voltage can be estimated using the Fourier series representation of the voltage and Eq. (5.7). A very good agreement between theory and experiment can be observed (Fig. 5.13). The measured currents show the influence of the cutoff frequency, which is deemed to be one important characteristic of a stimulation electrode [93]. The signals with dominant contributions at frequencies greater than the cutoff frequency (Fig. 5.13a) yield a more rectangular current than the signals with a longer pulse width and thus more dominant low-frequency components.

We observed a negative DC current offset for voltage-controlled monophasic pulses. This was most evident when using KCl solution (Fig. 5.12). This DC current offset was in good agreement with the theoretical prediction (Fig. 5.12). The impedance predicted by the model (Fig. 5.6) tends to infinity when the frequency tends to zero (i.e., to the DC limit). Then, the (positive) DC current component is blocked by an infinitely large DC impedance (see Eq. (5.7)). Because the DC current component does not contribute to the current signal, a significant (negative) DC offset can be observed. In terms of electrochemistry, the DC offset indicates an infinitely large

charge transfer resistance, which suggests that no significant faradaic electrochemical reactions occur [90]. Due to the blocking effect, the cells would be exposed to a small field in the negative direction even when no signal is actively applied (i.e., when the input voltage is zero). For this reason, current-controlled pulses are often preferred over voltage-controlled pulses because the applied stimulation field strength is proportional to the current density but not to the applied voltage. Nevertheless, many approaches in cartilage tissue engineering use voltage-controlled electrical stimulation (see Sec. 2.1).

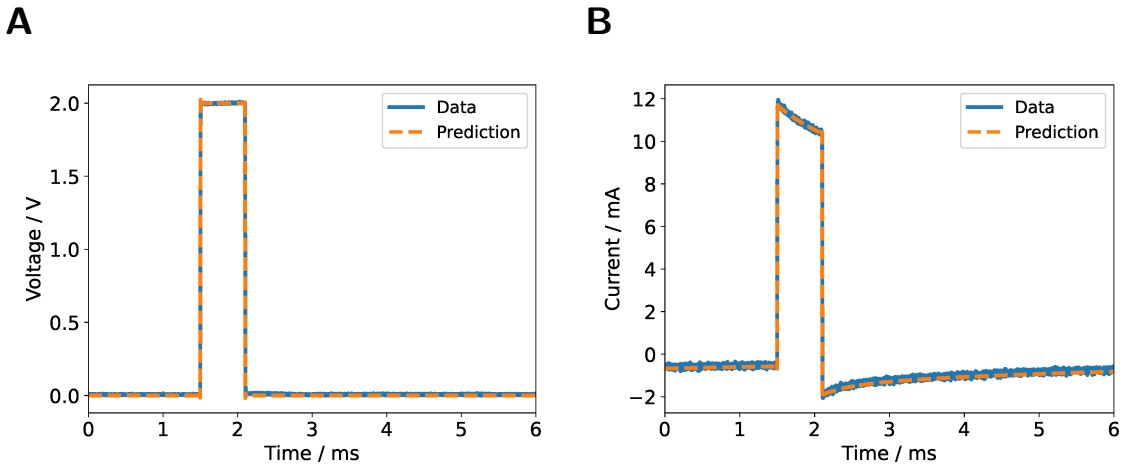

Figure 5.12: Measured and expected voltage (**A**) and current transient (**B**) for KCl solution with 4 mL stimulated with a voltage-controlled pulse (600 µs, 2 V, 130 Hz). A negative DC offset in the current is evident. The figure was taken from the supplementary material of [245].

In the case of the parallel connection, it turned out that the waveform slightly deviated from the expected waveform (not shown). The impedance of the 6-well system connected in parallel is only about 30 Ω. Hence, the total current through the system becomes large (about 60 mA) and might negatively affect the performance of the stimulator [67]. This result highlights the importance of a digital twin for the performance assurance of the electrical stimulation device. Still, the agreement between prediction and the measured current was good. By integrating the shunt resistor (1 Ω) into the equivalent circuit model (Fig. 5.6) and repeating the analysis, we could study its influence. At this point, the shunt resistor did not significantly change the results, but we will discuss later a case, where the shunt resistor has to be modelled explicitly.

When connecting the six wells in series, we did not observe similar behaviour as for the parallel connection (data not shown). This indicates that the observed deviations are indeed explained by the small load impedance of the parallel connection. In general, the good agreement between predicted and measured current transients

for the parallel and series connection is highly important because it suggests that there is no significant difference between the individual electrode pairs with respect to their electrochemical behaviour.

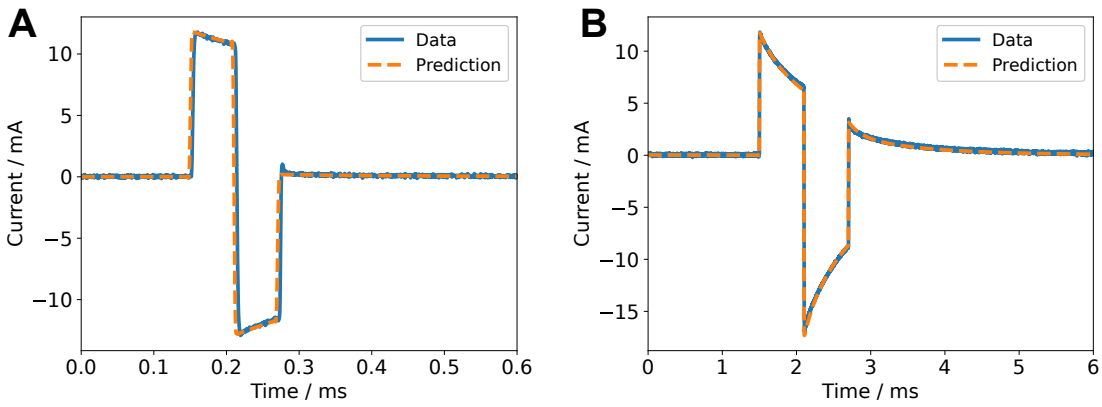

Figure 5.13: Current response for a biphasic pulse in voltage-controlled regime (2 V amplitude) with a pulse width of 60 µs (**A**) and 600 µs (**B**) for a single electrode pair. The experimental data is compared to the prediction based on the impedance model. The figure was taken from [245].

Validating the FEM simulations enabled us to establish a connection between macroscopic quantities (voltage, current) and local quantities (potential, electric field strength). This permits estimating the field strengths to which the cells are exposed from the current transients. For that, the voltage drop across the medium U (i.e., the boundary condition of the simulation) is computed by multiplying the measured current I and the computed resistance R (known from Eq. (5.5) for a known conductivity σ). We use the UQ bounds for the resistance R (Table 5.2) to obtain error bounds for the voltage drop U. For each U, the prediction interval for the field strength is known (see Sec. 5.1.5). Because this approach requires knowledge of the current I and the conductivity σ, it is termed current-conductivity method.

There is a second way to estimate the field strength inside the cell culture medium through the estimation of the voltage drop across the cell culture medium U_{medium}. This approach requires exact knowledge of the impedance of the medium Z_{medium} to apply the voltage divider formula

$$U_{\text{medium}}(\omega) = \frac{Z_{\text{medium}}(\omega)}{Z(\omega)} U_{\text{in}}(\omega) \ . \tag{5.8}$$

The total impedance Z is known from the fitted EIS spectra and/or fits to the Fourier-transformed voltage/current transients. This approach, which is referred to as the voltage-divider approach, has one advantage over the previously presented current-conductivity approach: the error of the conductivity does not need to be considered and thus the field estimates are more accurate (Fig. 5.14).

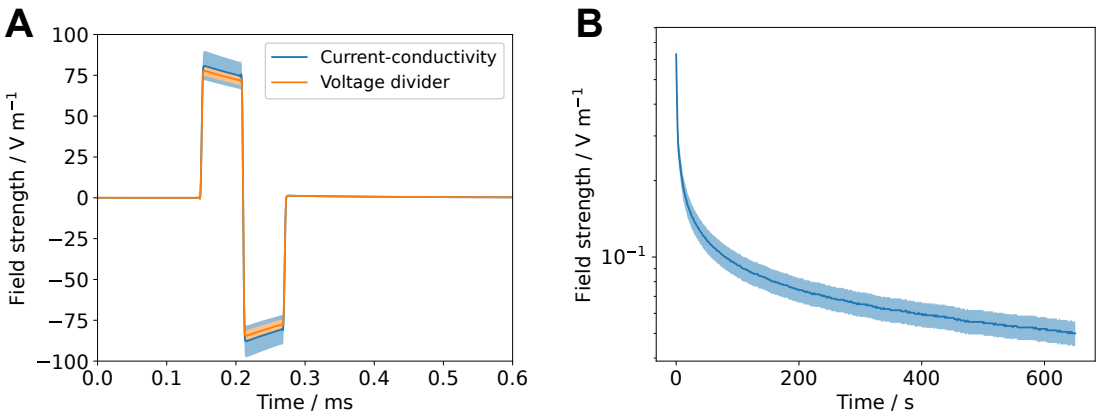

Figure 5.14: The estimated field strengths using the current-conductivity method (based on Eq. (5.5) and Table 5.2) and the voltage-divider approach based on an equivalent circuit scheme (Fig. 5.6) are compared. The mean value is shown (solid line) with the prediction interval (shaded). (**A**) corresponds to Fig. 5.13A and (**B**) to Fig. 5.5. Note that for the DC result (**B**), there is no possibility to estimate the field through the voltage-divider approach because no suitable equivalent circuit model is available. The figure was taken from [245].

The same field estimate procedure can be applied for wells connected in series or parallel. However, then the error estimates are less reliable because the computation is done using the approximation that all electrode pairs share the same impedance (see Eqs. (5.2) and 5.3). I attempted to account for this by a worst-case assumption: the lower bound for the impedance is computed under the assumption that all wells have the minimal impedance computed for one well. Vice versa, the maximum impedance of one well was used to estimate the upper bound for the impedance. For the voltage-divider approach, I did not include an additional error estimate and used the error bounds for the field strength determined for one well. This approach probably underestimates the error.

The presented approach for estimating the electric field strength based on an equivalent circuit model is usually referred to as lumped-element approach. Other examples of this approach can be found in [96, 110]. Alternatively, distributed impedance models can be considered [109], which rely on the thin layer approximation of the electrochemical surface layer (see Sec. 2.3.1). Thus, they require simulation runs for each EEI impedance. Furthermore, they suffer from the problem that the EEI impedance of the individual electrodes is not unambiguously known. For the chamber studied here and the EEI impedances for the considered frequency range, there was no significant difference between the lumped and distributed approach (Fig. 5.15), which suggests that the field estimates by the lumped-element approach are reliable. Figure 5.15 shows also the homogeneity of the electric field.

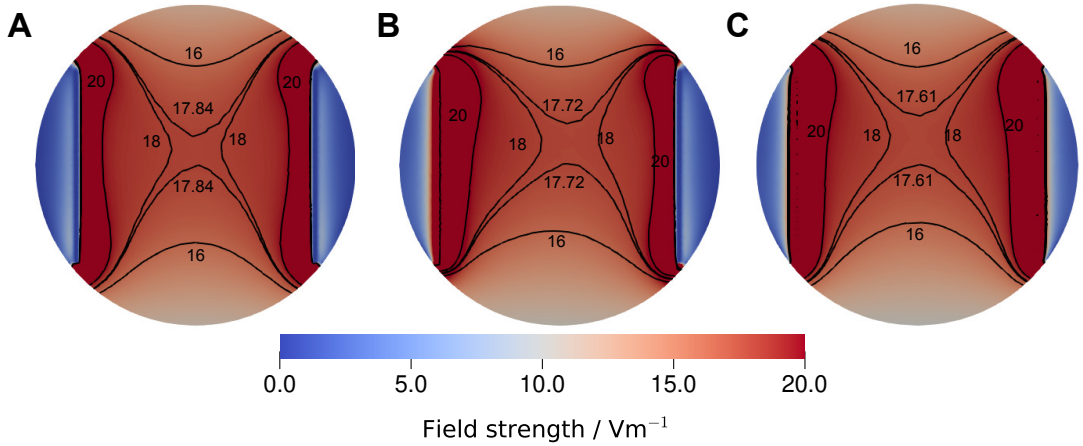

Figure 5.15: Comparison of the electric field strength at the bottom of the well for the largest experimentally determined EEI impedance at 130 Hz, which was 195.33 Ω, a medium conductivity of 1.38 S m^{-1}, a volume of 3.5 mL and a stimulation voltage of 1 V. Three different configurations were considered: (**A**) the voltage-divider approach, where the voltage drop across the medium has been computed for the given impedance, (B) the asymmetric distributed configuration, where the Robin boundary condition (Eq. (2.20)) was applied only on the left electrode using the full impedance and (C) the symmetric distributed configuration, where the EEI impedance was divided by two and applied on both electrodes. The reference voltage Φ_{ref} was equal to the voltages chosen for the Dirichlet boundary conditions. For the sake of comparability, the isolines for 16 V m^{-1}, 18 V m^{-1} and 20 V m^{-1} are shown together with the isoline for the field strength at the centre of the well that we reported throughout this manuscript. Evidently, the three modelling approaches yield only slightly different results. Thus, I concluded that the lumped approach, which permits to estimate the field strength without repeat simulations, delivers a sufficiently good estimate of the field strength. The figure was taken from [245].

Observations during the stimulation of adult neural stem cells — digital twin at work We tested the predictions of our model against data recorded during in vitro stimulation of adult neural stem cells. We found very good agreement of theory and experiment for both voltage- and current-controlled stimulation over a period of 12 hours and 24 hours, respectively. The comparison can be nicely visualised using animations, which can be found in the supplementary material of our original publication [245]. These results indicate that the stimulation system is electrochemically stable over the course of the stimulation and that the stimulation does not induce a temperature increase. For the voltage-controlled stimulation, six wells were connected in parallel. To increase the load impedance, a 100 Ω shunt resistor was added, which stabilised the signal. Because the shunt impedance is greater than the impedance of the wells, it needed to be explicitly included in the model. The good agreement of theory and experiment shows that this can be done straightforwardly without harming the predictive power of the model. Naturally, the shunt resistor has to be considered when estimating the field strengths using the voltage-divider approach. A pleasant effect of a larger shunt resistor is the increased voltage drop, which makes it possible to record the current without an amplifier.

Visual inspection of cell cultures after short-term stimulation revealed no differences in cell counts and morphology between stimulated and non-stimulated cultures. Hence, a negative effect of the stimulation can be excluded. During the short-term experiments, we made an unexpected observation: when the system was not thermally equilibrated (i.e., the electrodes were kept at room temperature prior to the stimulation and were inserted into freshly changed medium just before the stimulation), the measured signals deviated from the predicted signals (Fig. 5.16). The peak-to-peak voltage decreased about 15% from approximately 7.5 V to 6.5 V over a time course of about 2 hours (Fig. 5.16).

Because the signal with a pulse width of 60 µs is dominated by the ohmic resistance of the cell culture medium, we can assume that the resistance of each well also changed by about 15%. Using the aforementioned change of the conductivity of about 2%/°C, we can estimate under the assumption of a spatially homogeneous temperature distribution that the temperature in the well was initially decreased by approximately 7.5 °C. Estimating the mixture temperature (see Supplementary Material of [245]) does not support the hypothesis that the temperature drop could have been caused by the electrodes alone, which were kept at room temperature. Instead, it is likely that the temperature of the pre-heated cell culture medium was below 37 °C. Additionally, the ambient temperature in the incubator dropped during the handling. Even though the measured relaxation time seems to be surprisingly large, it appears to be credible. We observed in the validation experiments that it takes about 30 minutes to re-equilibrate the temperature of the cell culture medium after handling it outside the incubator (data not shown). For example, when the stimulation chamber was handled at room temperature for a few minutes, the temperature of the medium decreased from 37 °C to about 33 °C.

Of course, the temperature estimate needs to be refined because we only considered the average but not the local temperature, which could be inhomogeneous. The results show that the thermal equilibration of fresh cell culture medium takes a considerable amount of time. In contrast, heating of the medium due to the applied electrical stimulation can be ruled out and does not need to be modelled because the stimulation voltage did not change within 24 hours of stimulation of a thermally equilibrated system (Fig. 5.16).

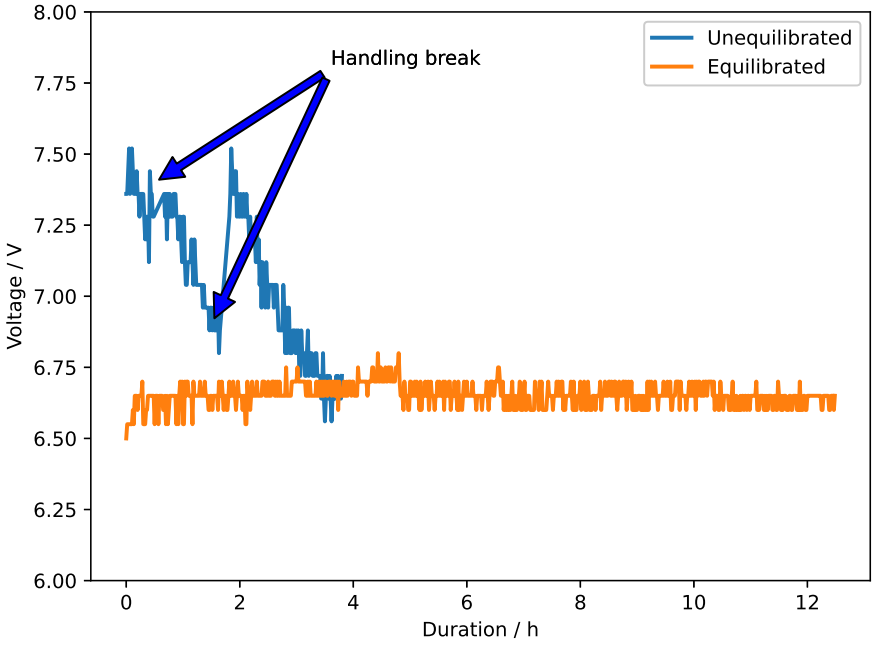

Figure 5.16: Comparison of stimulation voltages (peak-to-peak) for current-controlled stimulation (6.5 mA amplitude, 130 Hz, 60 µs) when the system was used directly after handling without thermal equilibration (blue) or after thermal equilibration took place (i.e., at 37 °C) (orange). The stimulation was performed with three (out of six) filled wells in series (without thermal equilibration) or six filled wells (with thermal equilibration). For the sake of comparison, the results for the thermally equilibrated system were divided by two to account for the additional wells. Because we could show that the wells are equal from an electrochemical point of view, this approach is feasible and does not introduce an error. When the thermally unequilibrated system was used, three 6-well plates, containing fresh cell culture medium, were stimulated successively either for 30 minutes, 60 minutes, or 120 minutes including short handling breaks in between. During these handling breaks, the lid was cleaned and kept at room temperature and the ambient temperature in the incubator dropped by a few degrees Celsius. The stimulation of the thermally unequilibrated system was completed after 4 hours. The stimulation of the thermally equilibrated system was continuously applied for 12 hours. The figure was taken from the supplementary material of [245].

A change in temperature leads to altered stimulation conditions. For example, at lower temperatures, an increased voltage is required to drive the preset current, and this increased voltage, in turn, temporarily causes a higher stimulation field strength. In addition, a decreased temperature has an impact on the activity of excitable cells [262]. Again, this result highlights the possibilities of performance assurance using a digital twin while suggesting its extension in the direction of multiphysics modelling for future research.

5.1.6 Summary

The results presented in the previous section demonstrate how a digital twin of an electrical stimulation device can be established. In this particular example, the digital twin comprises an in silico model of the stimulation chamber, which is calibrated by prior electrochemical characterisation, and can be updated dynamically through analysis of the stimulation waveforms, which can be recorded in situ. Eventually, this approach aims at enabling performance assurance and replicable research. Particularly the *in silico* modelling extends the guideline for stimulation experiments suggested by Boehler *et al.* [93], which focussed on the experimental performance assessment of stimulation electrodes.

In summary, the main insights and limitations regarding the effectively delivered electrical stimulation can be formulated:

1. The naive estimate of the field strength is: $E = U/d$. In this approach, the geometry of the well and the electrodes is mostly neglected and the field is assumed to be spatially homogeneous, which is a valid estimate only for parallel-plate capacitor geometries with sufficiently large electrodes. Moreover, it is often assumed that the voltage drop across the medium U is equal to the voltage delivered by the stimulator. For the chamber considered here, the field strength estimated by the naive approach ranges between $40\,\mathrm{V\,m^{-1}}$ and $43.5\,\mathrm{V\,m^{-1}}$ for $1\,\mathrm{V}$ (and thus $80\,\mathrm{V\,m^{-1}}$ to $87\,\mathrm{V\,m^{-1}}$ for an amplitude of $2\,\mathrm{V}$). Because this approach does not require information on the impedance of the system and/or on the voltage and current transients, it may lead to insufficient documentation of the stimulation experiment and wrongly estimated field strength.

2. By acquiring more information on the geometry, studying the dielectric properties of the system and monitoring both the voltage and current transients, a validated and comprehensible simulation model can be built. The validated simulation yields a spatially-dependent field strength. For the part of the well where the cells are located, the field strength can be estimated to lie in an prediction interval between about $65\,\mathrm{V\,m^{-1}}$ and $90\,\mathrm{V\,m^{-1}}$ for a rectangular pulse of $2\,\mathrm{V}$ amplitude, a frequency of $130\,\mathrm{Hz}$ and a pulse width of $60\,\mu\mathrm{s}$ when using a medium volume of $3.5\,\mathrm{mL}$ (based on the current-conductivity method). Due to the EEI impedance, the time course of the field strength depends

strongly on the frequency and pulse width. For the DC stimulation at 1.5 V, the current (and thus the field) decays rapidly over time and the asymptotic field strength can be approximated as about $0.05\,\mathrm{V\,m^{-1}}$. With the voltage-divider method, the field cannot be estimated for the DC stimulation because no impedance model is available. For the stimulation using rectangular pulses, the voltage-divider method is applicable and yields a field ranging between about $70\,\mathrm{V\,m^{-1}}$ and $80\,\mathrm{V\,m^{-1}}$, which is a more accurate estimate than obtained by the current-conductivity method. These results can be straightforwardly updated if a different medium volume is used or the frequency and/or pulse width are changed.

3. Still, the model leaves room for improvement. Local recordings of the voltage would be ideal to corroborate the results. For that, microelectrode arrays could be integrated into the well. For systems, where, unlike in this work, the simulation results for the electric field indicate a significant difference between the lumped and distributed modelling approach, such local measurements are inevitable. Such a system will be discussed later in Sec. 5.2. Local pH measurements would be important to identify electrochemical processes [263]. We assumed the influence of possible ion movements, cell layers and cell volume fraction to be negligible. Local field/impedance measurements would be required to refine the models regarding effects on the cellular scale (for example, by employing optical methods [146, 264]). Also, local temperature fluctuations have not yet been studied by us.

A main result is that a linear model described the experimental data well when rectangular pulses are used. This indicates that no strong electrochemical reactions occurred for the tested configurations as they would have led to a non-linear response that could not be described by a linear model. For applications of electrical stimulation for cartilage tissue engineering, the linear behaviour of the stimulation system has to be verified.

The quantities needed for the model (EEI impedance, conductivity) could be determined accurately prior to the actual stimulation experiment and can, in principle, be monitored and updated in situ. The model can be used to predict voltage and current transients. With this information, properties such as the charge per phase, which can be used to design safe stimulation protocols [92, 265], can be estimated prior to the stimulation experiment. Hence, the number of experiments could possibly be reduced by identifying unsafe stimulation parameters at an early stage. However, the limits for the charge per phase have been mostly found empirically for neural stimulation applications. For cartilage tissue engineering applications, such limits have yet to be established.

At the current stage, I could not find a predictive model for DC stimulation. Thus, there currently exist no means to predict the electric field reliably for future DC experiments. Our experimental results for DC stimulation indicate that different

electrochemical processes can be expected to occur and that the observed current is dominated by processes at the electrode surface but not by the bulk volume, which is most relevant to estimate the effect of the stimulation. To build a meaningful model of DC stimulation I expect to require at least a non-linear formulation, which depends on the overpotential [109] and describes the secondary current distribution. Probably even models considering the individual ion concentrations and their temporal dynamics could be required [103]. For models also considering secondary current densities stemming from non-linear faradaic electrochemical reactions, kinetic reaction parameters need to be known. For the chamber discussed here, such an approach has been presented in [249] to model DC stimulation. The model considering secondary current densities has relied on empirical data and could not predict measurement results. We measured time-dependent currents for DC stimulation, which has not been considered in the model presented in [249]. In contrast, the time course of the rectangular pulses could be accurately described by a well-understood model that comprises both identifiable contributions from the EEI and the bulk volume.

Thanks to the digital twin, possible variations of the voltage/current transients can be related to different processes. As we demonstrated, temperature changes of the cell culture medium could be detected. Even though the temperature of a cell culture should be ideally kept constant, this aspect has not been mentioned in previous works using the chamber considered here [246, 247, 250]. To use the ohmic resistance as a temperature sensor, the temperature dependence of the conductivity of the cell culture medium has to be known well. To date, only limited data are available [193]. A database with high-accuracy data for different cell culture media should be established. Furthermore, changes in the ohmic resistance could serve as an indicator for medium contamination (growth of bacteria) or a change in the chemical constitution (ion concentrations). On the other hand, the digital twin of the stimulation chamber could be used to infer the (unknown) conductivity of cell culture media via Eq. (5.4). However, the resolution of the inferred conductivity is currently limited by the geometrical uncertainties. The results of the UQ analysis indicate possible improvements of the experimental setup. The chamber considered here should be improved with respect to the accuracy of the electrode spacing. When preparing the experiments, attention should be paid to the volume of the medium in each well to ensure well-interpretable current measurements.

Changes in the double-layer capacitance could indicate electrochemical reactions at the electrode surface [257]. It has been argued that elevated primary current densities at higher frequencies could benefit corrosion [109]. The use of biphasic pulses prevents corrosion because the electrochemical reactions are reversed. Moreover, we would expect to observe a significant change of the EEI impedance if the surface corrodes [102]. Thus, the digital twin approach might also serve as an early indicator for an electrode replacement. This aspect will also be discussed in Sec. 5.2. Furthermore, we would expect to not be able to describe the signals anymore by the linear impedance model upon corrosion [266]. I am not aware of any research

relating the (non-)linearity of the EEI impedance to biologically relevant quantities such as the pH value. This will be subject of future research. DC stimulation has been shown to increase the hydrogen peroxide level in the cell culture medium [249]. A raised hydrogen peroxide concentration benefits corrosion [93]. Thus, monitoring and reporting of both stimulation voltage and current is imperative to ensure the replicability of DC stimulation studies. In our lab, we found better replicability of AC stimulation in comparison to DC stimulation because of the aforementioned oxidation of the electrodes in the DC regime.

For a general electrode system, a comparison between the lumped-element approach and the distributed-impedance approach is necessary to quantify the effect of the EEI impedance on the electric field. A change in the EEI impedance would then necessitate new simulations. Hence, it is recommended to choose stimulation signals with dominant contributions at frequencies greater than the cutoff frequency, from which the EEI impedance has almost no effect. In this work, this applies to biphasic pulses with a pulse width of 60 µs. Vice versa, the stimulation electrode should be chosen such that it has a low cutoff frequency (as already argued by Boehler *et al.* [93]) to gain flexibility with regard to the stimulation signals.

The presented approach has relevance also if the sample contains more than one phase (e.g., hydrogel or tissue in cell culture medium). Measurements of rectangular voltage and current pulses (i.e., similar to stimulation pulses) have been used as an in situ method to infer the impedance of the porcine brain *post mortem* [267].

For the use of rectangular stimulation pulses for cartilage tissue engineering, it is advisable to start with in vitro analyses. Full tissue models are prone to large uncertainties not only regarding the geometry but also the material properties (more details will be given in Chapter 7). Electrically conductive hydrogels have been identified as a tool for tissue engineering combined with electrical stimulation due to their tuneable physical properties [268]. The role of hydrogels for application in cartilage tissue engineering will be discussed in greater detail in Sec. 6.3.5. The electrical stability of electrically conductive hydrogels has been assessed using rectangular pulses [269]. Again, the digital twin approach can be straightforwardly applied. The employed *a posteriori* estimator for the FEM simulations is reliable in the context of many materials [222] and thus a high accuracy of the simulations can be verified. In the UQ analysis, the influence of positioning and dielectric properties of the hydrogel could be tested. The UQ results of this work revealed the influence of the cell culture medium volume on the observed current. Thus, in future studies using hydrogels of potentially uncertain volume, a volume control should be established to enable accurate modelling of the system. Eventually, changes in the system could be detected by in situ monitoring.

The results presented in this section were obtained for a general stimulation system used with rectangular pulses. In the next section, a different electrode designed for cartilage tissue engineering with low-frequency sine waves will be investigated. Particularly, local potential measurements will be considered.

5.2 Applying the workflow to an electrode for cartilage tissue engineering

This section is based on the publication "Experimental and numerical methods to ensure comprehensible and replicable electrical stimulation experiments", which is yet unpublished but has been submitted for review. [5]

The stimulation electrode considered in the previous section appeared to be electrochemically stable. It generated an almost homogeneous electric field. Thus, a second electrode made of a different material and leading to an inhomogeneous field shall be investigated. The electrode had been used for cartilage tissue engineering [95] and a similar design has been considered for in vivo application to foster bone growth [96]. Even though numerical simulations to estimate the electric field around the electrode have been performed, experimental validation has remained an open question. This question is to be answered in the following.

5.2.1 Geometrical and electrical aspects of the stimulation device

The considered electrical stimulation device (see Fig. 5.17) consists of two titanium pieces separated by an insulator. It has been developed to study the interaction of an electrical stimulation implant with chondrocytes and mesenchymal stem cells using standard 6-well plates [95]. An earlier version of the stimulation device had been used to study the effect of electrical stimulation on bone cells and bacteria but had required custom-built chambers [97]. Considered frequencies have ranged between 20 Hz and 60 kHz. Stimulation voltages up to 1 V have been employed. The electric field has been estimated using FEM [95] and has been found to be inhomogeneous. Observables have not been computed and experimental validation of the simulations has not been performed. Similar steps as in Sec. 5.1 are taken to obtain a detailed understanding of the stimulation system and eventually prepare a digital twin.

I used the technical drawing of the electrode geometry, which was provided as a CAD file and is published in the dataset for this study to ensure reproducibility. A fixed voltage was applied on the electrode surfaces by Dirichlet BCs. The full model of the device comprised the polyether ether ketone (PEEK) insulator separating the two electrodes and the cell culture medium. In the reduced model, the PEEK insulator was cut out and on its surface an insulating Neumann BC applied. The electrode

[5] I conceptualised this study, carried out all simulations and the data analysis, prepared the figures and the initial draft of the manuscript. All experiments were conducted together with Franziska Sahm, Nils Arbeiter, Henning Bathel and Zezhong Song. Rainer Bader, Anika Jonitz-Heincke, and Ursula van Rienen supervised the project, acquired the funding and provided all resources. The datasets generated for this study can be found online (`dx.doi.org/10.5281/zenodo.6937096`).

can be placed in two configurations in the culture well: the 'high' configuration corresponds to a spacing of 3 mm between the well bottom and the electrode, and the 'low' configuration to a spacing of 1 mm between the well bottom and the electrode.

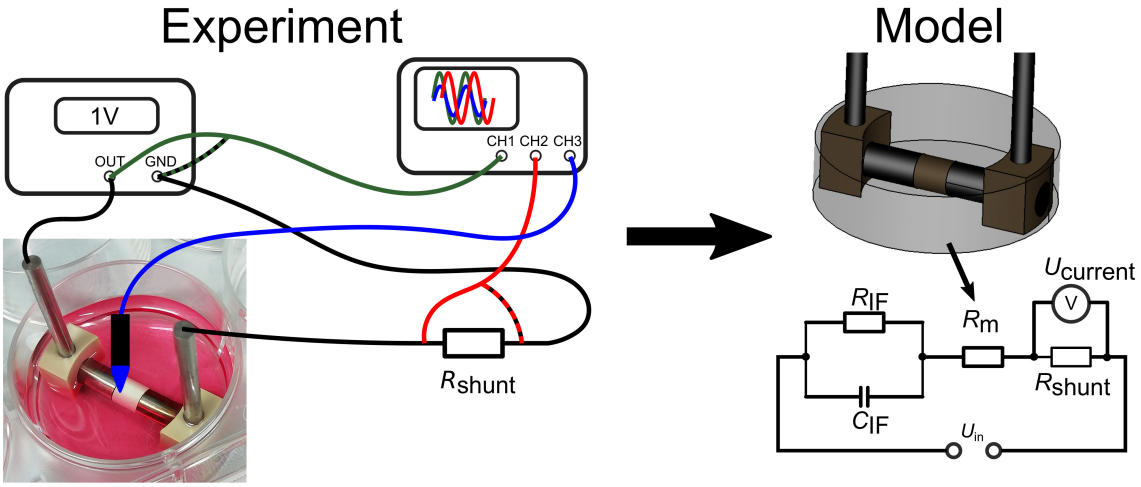

Figure 5.17: Experimental part: The electrode (two titanium bars separated by a PEEK insulator and supported by PEEK electrode holders) is placed in a cell culture well filled with cell culture medium. The electrode is connected to a signal generator (or the output of a power amplifier that stabilises the signal provided by the signal generator). The stimulation input signal is recorded by an oscilloscope (green line, CH1). At the low side of the stimulation electrode, a shunt resistor R_{shunt} is placed for current measurement. Please note that the term 'low side' here is not related to the low configuration geometry but refers to the side of the stimulation device that is connected to the ground. The voltage drop across the shunt resistor is recorded (red line, CH2) and the current can be computed by dividing the recorded voltage by R_{shunt}. Both the input signal and the current are measured with respect to a common ground (GND), which is indicated by the broken lines. Hence, the total impedance can be computed from the amplitudes and phase shift of the signals. A reference electrode (depicted in blue and black) is used to measure the local voltage in the cell culture medium (blue line, CH3). Modelling part: A geometrical model of the entire stimulation setup is prepared and used to compute the resistance of the cell culture medium R_{m}. Moreover, the electric field for a given voltage drop across the medium is computed. An equivalent circuit model is suggested. It contains the shunt resistor, the cell culture medium resistance and a part with interface resistance R_{IF} and capacitance R_{IF}. The interface impedance is idealised and a potentially more suitable equivalent circuit representation to describe the experimental data has to be determined. For that, frequency sweeps to obtain the impedance over a broad frequency range have to be performed. This can also be done by a frequency response analyser.

As in the previous example, there was a meniscus of the cell culture medium visible. However, due to the electrode holder and also the electrode placement, it appeared to be impossible to estimate the shape of the meniscus reliably for the conditions used in the cell experiment. A volume of 5 mL was used for the in vitro experiments. With this volume, the medium barely covered the electrode and did not cover the electrode holder. Microscope images of the electrode immersed in liquid did not help to create a better geometry model. Hence, the cell culture medium was modelled as a cylinder. Only for volumes greater than 10 mL, which covered the entire electrode and the holder, the meniscus was modelled. Then, the parameters $c = 2.0\,\text{mm}$ and $h_0 = 2.0\,\text{mm}$ of Eq. (5.1) were chosen. The height of the cylinder was chosen according to the height of the medium in the centre of the well. For 10 mL, it was about 11 mm to 12 mm. A volume of about 7 mL marks a special case as the height of the medium is then approximately equal to the height of the electrode holders.

The same numerical approach as in Sec. 5.1 was used and adaptive mesh refinement was performed using a Zienkiewicz-Zhu error estimator. Instead of *SALOME*, I used the Open CASCADE Technology (OCCT)[6] kernel in *NGSolve* for CAD modelling. This feature has been available since the *NGSolve* release v6.2.2105 and offers the same functionality as *SALOME* while making the modelling approach more concise. Furthermore, *SALOME* does not have to be installed and the entire modelling workflow can be realised in *NGSolve*, which reduces dependencies and thus is more user-friendly. Because the geometry of the model cannot be straightforwardly modified and the electrode is manufactured in an industrial process, unlike the platinum electrodes of Sec. 5.1, I did not perform a UQ analysis. Nevertheless, I will later briefly discuss the influence of the uncertainty of the medium volume.

To experimentally characterise the device, again KCl solution (Hanna Instruments) and the cell culture medium (DMEM, without calcium, containing 10% fetal calf serum (PAN-Biotech, Aidenbach, Germany), 1% amphotericin B, 1% penicillin-streptomycin, and 1% HEPES buffer (Sigma-Aldrich, Munich, Germany)) were used. The conductivity of the cell culture medium was $1.84\,\text{S}\,\text{m}^{-1}$ at 37 °C (measured with the handheld conductivity meter LF 325-A, Wissenschaftlich Technische Werkstätten, Weilheim, Germany). The voltage and current signals were measured as specified in Fig. 5.17. The impedance was measured by a Gamry Reference 600+ potentiostat over a broad frequency range (usually 1 Hz to 5 MHz) using a sufficiently small voltage amplitude of 25 mV or 50 mV. In preliminary experiments, no difference between the impedance measured with the two different voltages was found. Hence, it can be assumed that only the linear impedance response was recorded.

[6] `https://www.opencascade.com/open-cascade-technology/`

5.2.2 Initial numerical analysis

Initially, the measured value of the cell culture medium conductivity was used with a relative permittivity of 80. The PEEK pieces were modelled as perfect insulators with a relative permittivity of 2. To estimate if the full EQS equation has to be solved, the upper frequency limit of the impedance analysis, 5 MHz, was considered. Particularly, it is of interest if the PEEK separating the metal pieces acts similar to a dielectric in a capacitor and influences the expected impedance. The analysis was performed for all electrode configurations with 5 mL, 7 mL and 10 mL of medium. As the matrix is complex symmetric for the full EQS model, preconditioned GMRES was used while for the reduced model preconditioned CG could be used as only Laplace's equation is to be solved in this case.

When using 5 mL, a spherical domain representing air was added. With this, it was accounted for the fact that the electrode was not fully covered by medium. The full model for the low configuration after adaptive mesh refinement had 2,764,910 DOFs. The computed impedance had a magnitude of 56.258 Ω and a phase of 0.013°. The reduced model had 532,348 DOFs and the computed resistance was 56.259 Ω. For the high configuration, similar results could be obtained. The full model yielded an impedance magnitude of 65.637 Ω with a phase of 0.013° having 2,913,918 DOFs, while the reduced model yielded an impedance magnitude of 65.646 Ω with a phase of 0.013° having 432,204 DOFs. Evidently, the system behaves mainly as a resistor and is fully characterised by its resistance. A similar result was obtained for the other volumes.

For a volume of 7 mL, both the low and the high configuration yielded a resistance of 38.57 Ω. This was to be expected as both configurations are geometrically equal if the meniscus is neglected. For a volume of 10 mL, the low configuration yielded a resistance of 33.35 Ω. Using the same volume but the high configuration yielded a resistance of 31.7 Ω (i.e., about 5% less than for the low configuration). To put it in a nutshell, the electric field in the cell culture medium can be modelled using Laplace's equation as in Sec. 5.1. Hence, the number of DOFs can be reduced significantly compared to the full EQS model. Moreover, the fast and reliable preconditioned CG solver can be used.

An example of the electric field distribution at relevant cut planes for a volume of 10 mL is shown in Fig. 5.18. The electric field is highest in the area below the insulator, which separates the electrodes, and can reach values up about 150 $\mathrm{V\,m^{-1}}$. For the low configuration, electric field strengths of similar order can be reached at the bottom of the well, where usually the cells are located. In contrast, the field is only about 100 $\mathrm{V\,m^{-1}}$ at the bottom in the high configuration. Please note that the values for the electric field were computed for a voltage drop across the well of 1 V. Nevertheless, the electric field can be scaled linearly to estimate the values for other voltage drops. The electric field below the electrode did not significantly depend on the volume, which is in line with the UQ results of the previous section (Fig. 5.3).

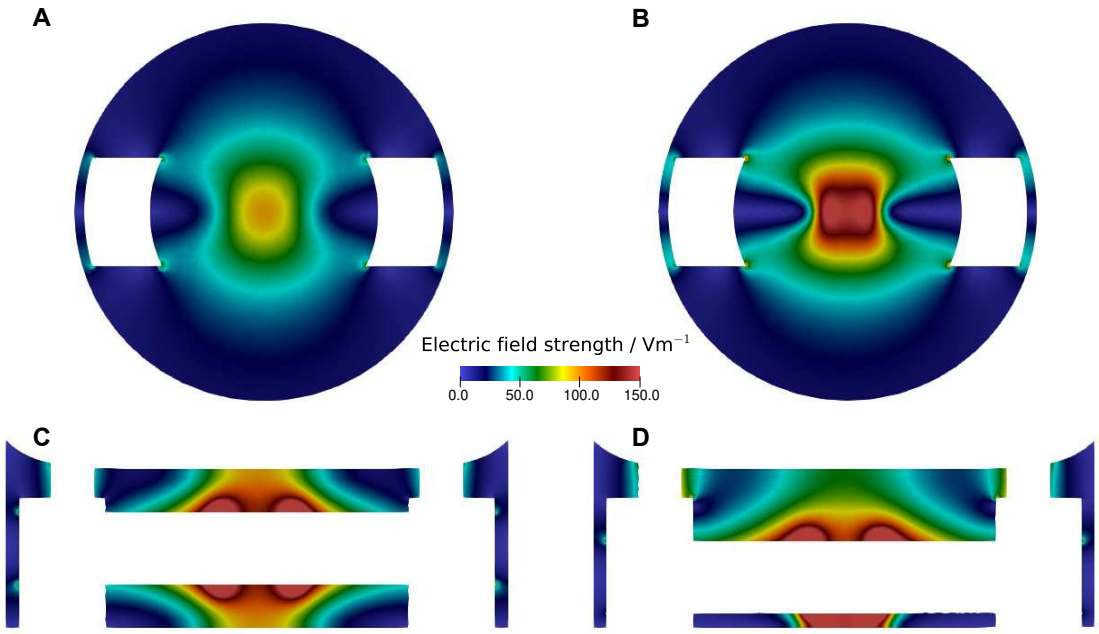

Figure 5.18: The electric field strength is compared at the bottom plane of the well for high (**A**) and low (**B**) configuration with a volume of 10 mL. Furthermore, the field is shown on the center plane for high (**C**) and low (**D**) configuration. In **C** and **D**, the electrode is cut out to support the identification of the center plane from Fig. 5.17.

In addition, the resistance of the cell culture medium can be easily scaled according to the medium conductivity using Eq. (5.5) without re-running the simulations. For EIS measurements, this result means that a real-valued impedance is predicted. As it can be expected that an EEI impedance will also be present for this electrode, a real-valued impedance is to be expected at frequencies greater than the cutoff frequency. The cutoff frequency is to be determined by EIS. Moreover, there should not be a significant difference between the high and low configurations if a volume of 10 mL is used. For smaller volumes (e.g., 5 mL) a notable difference should be measured because it can be expected that the current and thus the resistance dependi on the volume as for the previously studied electrode configuration (Fig. 5.3) . However, it must be mentioned that the impedance of the configurations with a small volume strongly depends on the height of the medium. As mentioned before, it was not possible to accurately measure the height of the medium and thus no UQ analysis to quantify the variation of the impedance was performed.

5.2.3 Initial impedance measurements

Initially, the goal was to validate the setup for the volume used in the in vitro experiments (i.e., 5 mL). During these investigations, a fresh electrode was compared

to an electrode that had been in use multiple times. The impedance measurements revealed significant differences between the two electrodes (data not shown), which motivated the research presented in the following.

Corrosion detection

The simulations predict a purely resistive impedance at high frequencies. However, we observed unexpected capacitive behaviour in the MHz-range (Fig. 5.19). An elemental analysis of the electrode surface using energy dispersive x-ray analysis (EDX)[7] revealed that a layer of calcium and phosphorus covered the electrode surface. We speculated that a layer of calcium phosphate must have built on the titanium surface; most likely due to corrosive processes. It is known that titanium implants in aqueous environment corrode [270] and that calcium phosphate forms on titanium in electrolyte solution [271]. This process can potentially be enhanced by active electrical stimulation as titanium can be coated by calcium phosphate by electrochemical deposition [272]. However, the focus did not lie on the determination of the exact mechanism behind the corrosion. Instead, the removal of the calcium phosphate layer was paramount to regenerate the electrical properties of the electrode. For that, 10% acetic acid was employed successfully (Fig. 5.19)[8]. Hence, the experimental lab protocol could be successfully updated to ensure replicable stimulation conditions. Most importantly, the corrosion of the electrode could not be easily identified by visual inspection as the calcium phosphate layer is probably only a few hundred nm thick. Instead of thinking of corrosion, we first assumed that the electrode surface was scratched. Evidently, the electrode corrosion could not have been detected without the numerical prediction.

Validation measurements

We measured the impedance of the two configurations using liquids of different conductivity (Table 5.3). The relative error between the predicted and fitted resistance was usually below 5%. This indicates a very good agreement between theory and experiment. The uncertainty of the numerical prediction due to the assumed conductivity can be estimated to about 2% (see details in Sec. 5.1). Two different electrodes were compared using 7 mL (Fig. 5.19). The fitted impedance deviated by less than 1 Ω. This deviation corresponds to a relative error of about 1.4%, which is close to the accuracy of the potentiostat (1%). Thus, the manufacturing uncertainty was assumed to be negligibly small. Furthermore, this result permits to define a reference state for performance assurance. Every manufactured electrode can be

[7]Support by Regina Lange who performed the measurements and provided the results of the elemental analysis is gratefully acknowledged.
[8]The experiments were performed by Nils Arbeiter whose support I gratefully acknowledge.

tested using the presented experimental approach. If, for example, the fitted resistance or measured impedance at high frequencies significantly deviates (e.g., more than 5%) from the expected value, the electrode should not be used for stimulation experiments until the reason for the deviation has been found and eliminated.

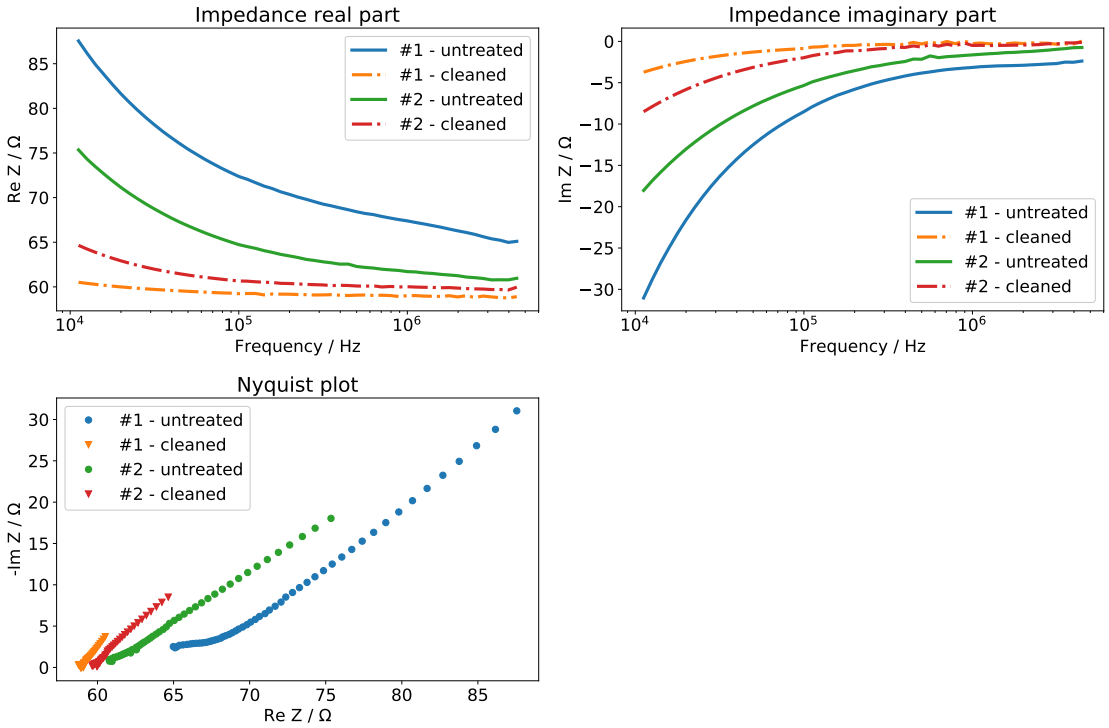

Figure 5.19: Comparison of two electrodes before and after cleaning treatment with 10% acetic acid. The impedance was measured for the low configuration using 7 mL KCl conductivity standard at 19 °C with a conductivity of 1.143 S m^{-1}. To highlight the high-frequency behaviour, the impedance is shown only for frequencies above 10 kHz. The electrodes were used in stimulation experiments before the treatment. Evidently, the untreated electrodes show capacitive behaviour (i.e., a non-zero imaginary part) up to very high frequencies. This stands in contrast with the simulation result that predicted purely resistive behaviour (i.e., an imaginary part tending to zero) at high frequencies. After the cleaning treatment, both electrodes show resistive behaviour at high frequencies. By fitting a CPE in series with a resistor, the resistance at high frequencies could be determined. The resistance of electrode #1 was estimated to be 58.9 Ω, while electrode #2 had a resistance of 59.7 Ω. For the setup here, the simulations predicted 62.1 Ω. This is in good agreement with the measured values (deviation not significantly greater than 5%) particularly given the fact that the meniscus was ignored.

Aside from the manufacturing uncertainty the height of the medium can be expected to be the main source of uncertainty. Particularly at low volumes (5 mL and 7 mL) it cannot be extracted accurately and the meniscus was therefore not

included. At a volume of 10 mL, we could estimate its height using an uncertainty of about 1 mm with a median height of 11 mm. Moreover, the meniscus was modelled. Changing the height from the assumed 11 mm to 12 mm, yielded a resistance of 31.67 Ω, which deviates about 5% from the predicted value. Furthermore, it yields a value closer to the measured resistance of 31.92 Ω. In sum, this rough estimate of the uncertainty of the numerical prediction demonstrates the agreement of measured and predicted values. Hence, the chosen geometrical model appeared to be valid.

Yet, the influence of the EEI has to be considered. In principle, it can be modelled by an equivalent circuit as, for example, done in the fitting of the resistance. However, the electrode has been used only for stimulation at a single frequency. Thus, no information on the frequency-dependent behaviour of the impedance can be extracted from the stimulation signal. Instead, only the impedance magnitude and phase at one frequency can be obtained from the stimulation voltage and resulting current signals. To extract the impedance of the EEI at this frequency, the cell culture medium resistance is subtracted from the measured impedance. By monitoring the impedance over time, electrochemical changes and temperature changes can be detected. Unlike in the previous example using rectangular pulses, they cannot be distinguished. For that, EIS measurements would have to be conducted regularly as in [273]. Instead, I want to explore in this work if the numerical simulations can be validated by local voltage measurements.

Table 5.3: Comparison of the fitted resistance from EIS measurements (see Fig. 5.19 for more details) and the resistance predicted by numerical simulations. To reduce the fitting error, the impedance was considered at frequencies greater than 1 kHz. In this range, a CPE in series with a resistor yielded a relative difference of usually less than 2% between the fitted resistance and the measured impedance modulus (which at high frequencies is equal to the resistance). Different geometrical configurations were compared. One medium was DMEM used at 37 °C and its conductivity of 1.84 $\mathrm{S\,m^{-1}}$ was measured at this temperature. The other medium was a KCl solution at room temperature. The varying conductivities of the KCl solution are due to different ambient temperatures.

Configuration	Conductivity in $\mathrm{S\,m^{-1}}$	Fitted resistance in Ω	Predicted resistance in Ω	Relative difference in %
5 mL, low	1.84	55.20	56.26	1.9
5 mL, low	1.191	88.1	86.99	1.3
5 mL, high	1.264	91.29	95.56	4.5
7 mL, low	1.143	58.90	62.09	5.1
7 mL, low	1.143	59.70	62.09	3.9
10 mL, low	1.84	31.92	33.35	4.3

5.2.4 Local voltage measurements

For the validation of the numerical simulations by local voltage measurements, three frequencies shall be considered:

1. 20 Hz as it marks the lowest considered frequency for electrical stimulation with this device. At this frequency, the EEI impedance dominates.

2. 1 kHz as it has been considered for the stimulation of chondrocytes and mesenchymal stem cells [95]. The EEI impedance is significantly smaller than the resistance of the medium.

3. 60 kHz as it has been used in capacitive coupling of chondrocytes and it corresponds approximately to the cutoff frequency (compare Fig. 5.19). Thus, it is expected that the impedance at this frequency is equal to the predicted resistance and that the numerical solution is in very good agreement with the measured values.

To achieve the posed goal, a measurement electrode is inserted in the cell culture medium. Hence, the numerical models have to be updated to include the measurement electrode.

Preliminary numerical considerations

To gain an understanding of the system with a measurement electrode, an approximate model of a cannula (a needle) is used. It had been considered by collaborators as it is available in every medical laboratory and is easy to handle. The geometry is standardised. For a typical cannula type 21G, the diameter is 0.8 mm and it has a sharp tip. To avoid numerical artefacts, I modelled the cannula by a cylinder of matching diameter with a semi-sphere of the same diameter as the measurement tip. Then, different configurations of the cannula-like probe were considered: straight, tilted in one direction (tilted #1) and tilted in two directions (tilted #2) as well as a mirror of this configuration (tilted #3, see Fig. 5.20).

In a second step, the shaft of the probe was insulated and only the tip was left floating. Subsequently, a thinner probe with a diameter of 0.2 mm was considered. All these simulations were performed for the a medium height of 5 mL. The measurement points were chosen along a line in x-direction at the bottom of the well (0.5 mm distance between the tip and the bottom (see Fig. 5.20). This setup aimed at resembling the manual measurement of local voltages during a cell culture experiment.

The floating part of the electrode was also modelled using a surface impedance (see Sec. 3.1.2). As the exact value of the surface impedance is not known, I chose two numerical values that represent an intermediate ($10^3\,\Omega\text{mm}^2$) and a large surface ($10^6\,\Omega\text{mm}^2$) impedance.

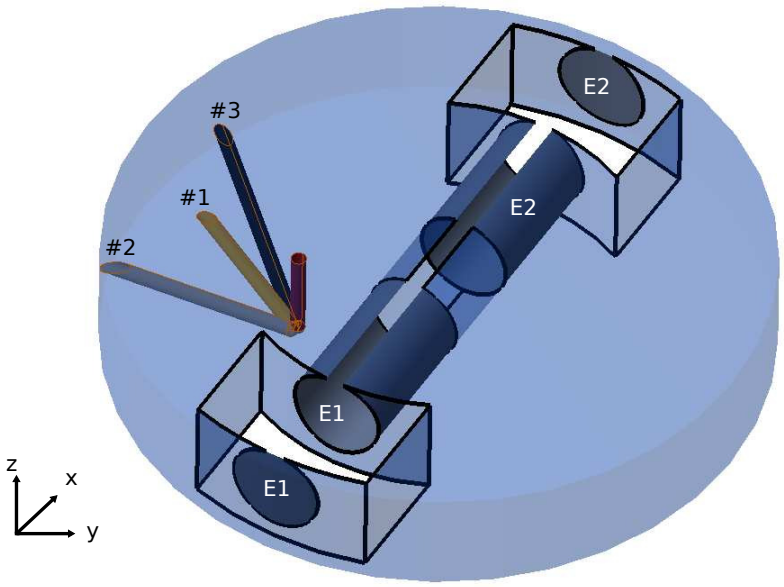

Figure 5.20: Positioning of the measurement probe in the cell culture medium (blue, transparent). The active electrodes are shown in grey and labelled E1 and E2. Four configurations of the measurement electrode were considered: a straight probe (named straigth, brown), tilted in one direction (named tilted #1, golden), tilted in two directions (named tilted #2, light grey) and a mirror of tilted #2 (named tilted #3, dark grey). The measurement probe was moved along the x-axis at fixed y- and z-positions.

The arising linear system was solved using the direct solver *MUMPS* [274] available in *NGSolve* and the *FieldSplit* block preconditioner [275] together with the flexible GMRES solver, both implemented in *PETSc* [212–214] and available in *NGSolve* through the *ngs-petsc* interface[9]. When considering the surface impedance, CG with an AMG preconditioner was used as an iterative solver.

The simulations revealed that the electrode positioning is the most crucial parameter if the shaft of the measurement probe is not insulated (Fig. 5.21). If the probe is not kept straight, the measured value can deviate significantly (i.e., up to about 50%) from the expected benchmark value. This means that the numerical simulations could not be validated correctly using this approach. However, when the probe was kept straight, the relative deviation between benchmark and measured value were below 1.2% at all measurement points. Even without simulations, it may be possible to detect the deviation introduced by the measurement probe. Introducing a blank metal probe leads to a change in the total current under the assumption that there is no surface impedance on the electrode (Fig. 5.22). As this change is position-

[9] `https://github.com/NGSolve/ngs-petsc`

dependent for configurations that lead to a perturbed measurement result, recording the current during experiment can help to detect this unwanted influence of the measurement probe. Unfortunately, the change did not exceed 1.6%, which suggests a high-resolution current measurement to be required for successful detection. Nevertheless, the straight configuration led to a small change in the current of not more than 0.2%, which is most likely not detectable in a real experiment. If a surface impedance was considered, the current did not deviate significantly (Fig. 5.22).

These first results could be improved by insulating the shaft of the electrode, which led to a deviation of less than 1.5% for all configurations. The accuracy could be further improved by reducing the diameter of the electrode.

In sum, the measurement probe should be widely insulated and only the tip should be left uninsulated to sense the local voltage. Then, the positioning of the electrode has a negligible influence and instead of running multiple simulations for the different probe locations, the expected measurement value can be extracted from the benchmark simulation. Nevertheless, a straight positioning is expected to yield the most accurate measurement results. The surface impedance of the measurement probe is in general unknown but luckily did not appear to influence the expected measurement value. Thus, it does not have to be determined a priori for the chosen probe geometry.

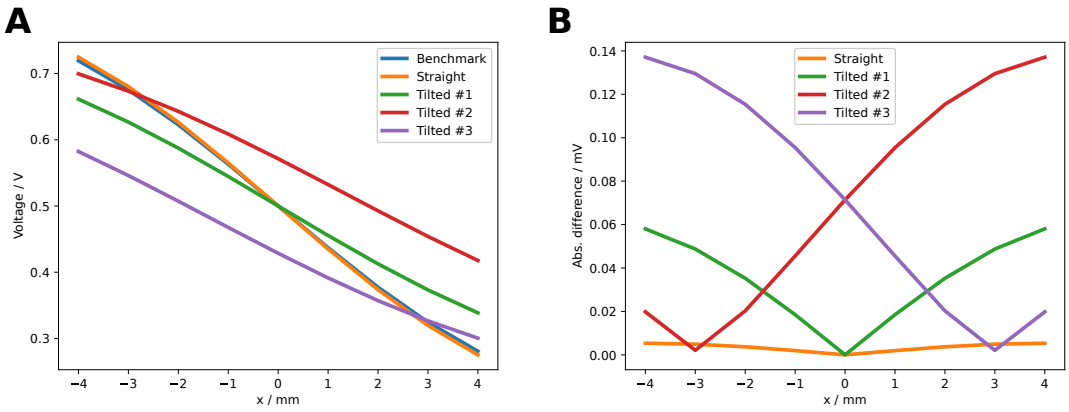

Figure 5.21: Comparison of the benchmark values derived from a simulation without inserted measurement probe and simulation results for different configurations of a floating measurement probe. In **A**, the measured voltage extracted from the simulations is compared. In **B**, the deviation between measured and expected benchmark values is shown. For more details regarding the naming, please see Fig. 5.20.

The validation of the simulation results shown in Fig. 5.18 requires scanning the local voltage at many points to successfully resolve the inhomogeneity of the field. The negative gradient of the recorded local voltage serves as an estimate of the electric field. As the area under the electrode is not easily accessible, a small probe shall be used to scan the area above the electrode using a volume of 10 mL. A grid

was constructed using 330 points with a spacing of 1 mm in x- and y-direction at two planes 1 mm and 3 mm above the electrode. The probe was moved to the grid points in straight configuration. As for the previous example (Fig. 5.20), the measurement probe could successfully reproduce the benchmark simulation without significant differences.

When modelling the probe configurations, the iterative solver failed for 4 out of the 330 configurations while the direct solver could always solve the problem. It is unclear why this happened and it did not happen with any other tested configuration. In future research, it is desirable to use a projection-based preconditioner such that the indefinite linear system can also be solved by CG [207].

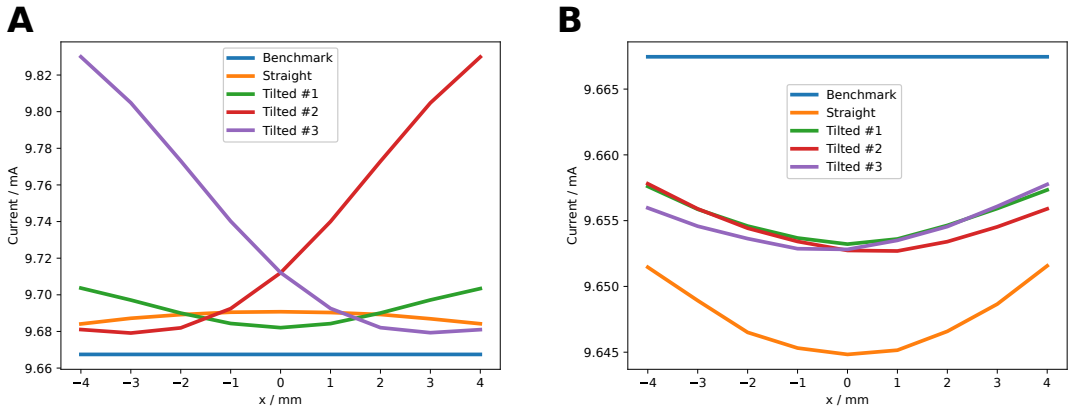

Figure 5.22: Comparison of the computed current through a well with and without measurement probe. Different configurations of a floating measurement probe were studied. For more details regarding the naming, please see Fig. 5.20. In **A**, a perfectly conducting probe without a surface impedance was considered, while in **B** a surface impedance of $10^3\,\Omega\text{mm}^2$ was considered. Note that the scales are different for the sake of better comparability between the benchmark and the results for different probe configurations.

Data analysis workflow

From the preliminary numerical configurations, a near-optimal experimental setup could be derived. A 3D printer (Monoprice MP Select Mini Pro) was purchased and modified such that a small measurement probe (Microprobes, PI2PT33.0B10) with a diameter of 370 µm and a few µm of the metal tip uninsulated could be moved along defined grid points. As an influence of the measurement probe is not to be expected from the preliminary numerical investigations, the experimental data will be compared to the benchmark simulation.

I developed the following workflow to automate data acquisition and analysis:

1. Measure the height of the medium in the centre of the well. Switch on the

stimulation voltage and move down the electrode until a sinusoidal signal with the stimulation frequency appears on the oscilloscope screen.

2. Prepare the geometry model. Load the standard electrode geometry and add a cylinder with the radius of the well and the measured height. Reshape the cylinder to account for the meniscus using Eq. (5.1).

3. Compute the expected current or impedance and estimate the voltage drop across the shunt resistor. Choose the dimensions of the shunt resistor such that the voltage drop is within the measurement range of the oscilloscope.

4. Choose the measurement grid along which the measurement probe should be moved.

5. Apply the stimulation voltage and scan the voltage distribution inside the medium. The measurement result at each point is written to a YAML-file. *Python* scripts for synchronising the 3D printer movements and the oscilloscope readings can be found on *GitHub*[10].

6. Use automated *Python* scripts to extract the input amplitude, current and measured voltage from fits to sine functions.

7. The expected voltage is computed from the benchmark simulation results by shifting and scaling. To account for the shunt resistor, a voltage divider equation is used to compute the effective voltage drop across the chamber. For that, the absolute value of the impedance of the entire system Z is computed by dividing the voltage amplitude by the current. Then, the voltage at the low side of the chamber is computed by $U_{\mathrm{low}} = U_{\mathrm{in}} \frac{R_{\mathrm{shunt}}}{Z}$. The benchmark simulation result is scaled by the voltage drop across the chamber $U_{\mathrm{in}} - U_{\mathrm{low}}$ and shifted by adding U_{low}.

8. The expected voltage is evaluated at the measurement points. Both expected and measured voltage are interpolated on a triangulation of the grid and their interpolated values are compared (e.g., by computing and visualising the absolute and relative difference).

Results and Discussion

As expected, the measurement results at 60 kHz were in good agreement with the simulation results (Fig. 5.23). The relative difference was below 10% for most of the measurement points (Fig. 5.24). However, it is evident that the positioning by the 3D printer might not be sufficiently accurate as fluctuations were visible in the recorded values. Sometimes the positioning failed and there occurred shifts in the

[10] `https://github.com/j-zimmermann/PyVISAScope/tree/master/examples/3DPrinter`

recorded voltages. Hence, currently it is investigated how to make the experimental approach more reliable.

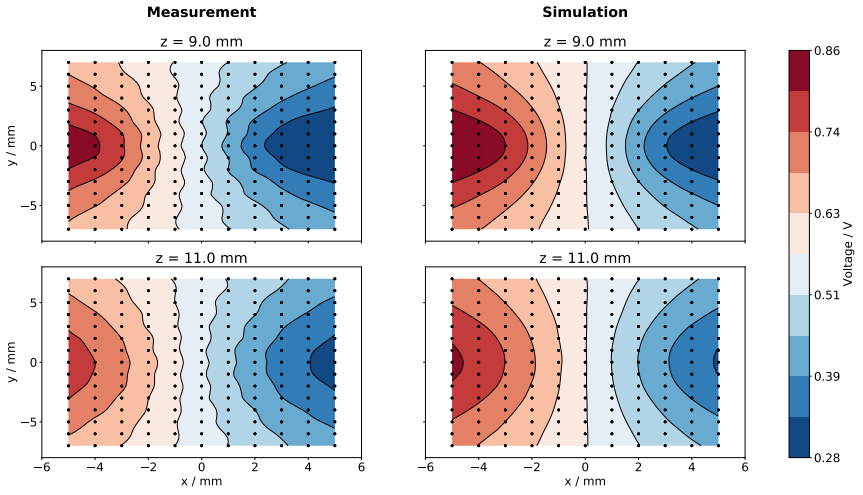

Figure 5.23: Local voltage recording in cell culture medium at 60 kHz and 37 °C for the high configuration and 1 V input voltage amplitude. The left side shows the measured values at two different heights relative to the well bottom. The black dots indicate the measurement points. The measured values were interpolated to generate a heatmap. The right side shows the corresponding expected values, which were numerically computed. The relative difference between measured and expected values is shown in Fig. 5.24

The electric field can be estimated from the local voltage distribution (Fig. 5.25) by taking the gradient of the voltage. The general field distribution is in agreement with the numerical predictions. Nevertheless, the uncertainty of the positioning propagates. Hence, the field distribution is, for example, not symmetric as predicted and to be expected due the symmetric setup but fluctuates. Nevertheless, the expected and measured field strengths agree well.

It takes about 30 minutes to scan the voltage distribution in the well. In contrast, global properties such as the current can be measured in a couple of seconds. At 60 kHz, the measured current has a phase shift of about 1° (±1°) with respect to the stimulation voltage and deviates less than 5% from the expected current. This result was expected and indicates that it is sufficient to record the current (both amplitude and phase shift) to validate the numerical simulations. Moreover, current recordings throughout a stimulation experiment can be used to monitor the status of the stimulation electrodes. Hence, for high frequencies such as 60 kHz, a digital twin was successfully established for the considered stimulation setup.

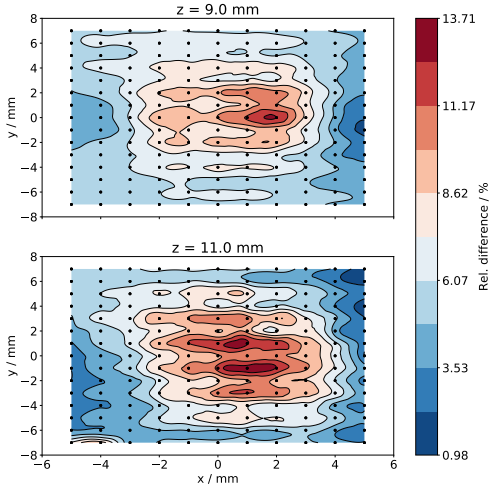

Figure 5.24: The relative difference between measured and expected values at two different heights relative to the well bottom. The measured and expected values are shown in Fig. 5.23. The measurements were performed in cell culture medium at 60 kHz and 37 °C for the high configuration and 1 V input voltage amplitude. The corresponding absolute difference between measured and expected values is in the range of a few mV.

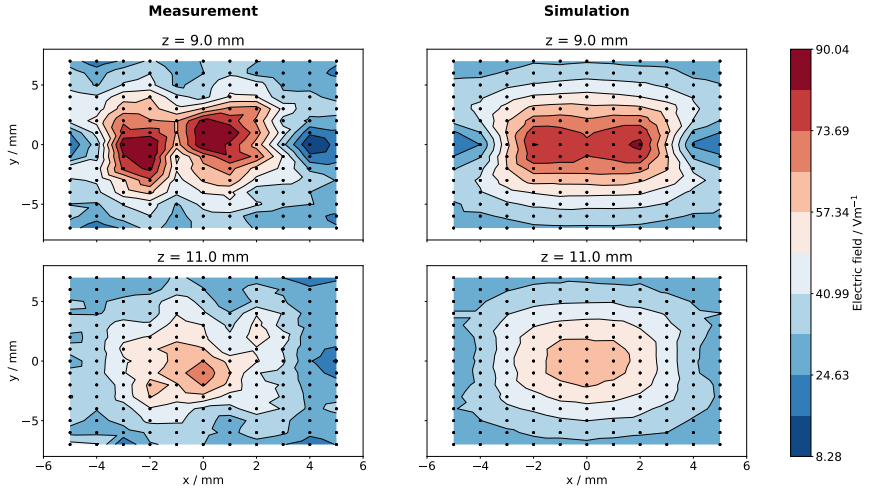

Figure 5.25: The electric field strength was estimated from the voltages recorded in cell culture medium at 60 kHz and 37 °C (shown in Fig. 5.23) by computing the gradient. Again, the measured values are shown on the left for two different heights relative to the well bottom. On the right, the expected electric field is shown.

In contrast, the results at 20 Hz and 1 kHz were less promising. At 20 Hz, the voltage drop across the medium was only about 30 mV, which is close to the measurement resolution. To demonstrate the general approach, I will only show the results at 1 kHz for the high configuration and cell culture medium. At this frequency, the general shape of the recorded local voltage looks similar to the expected result (Fig. 5.26). However, the voltage drop across the medium is smaller than expected. Moreover, the measured current has a phase shift of about 22° and is also about 21.5% smaller than expected.

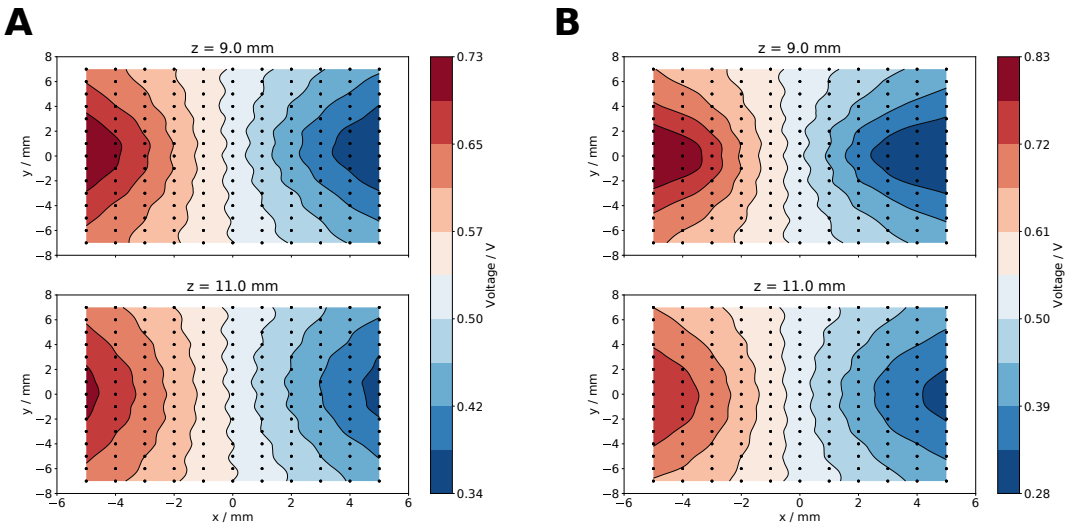

Figure 5.26: Local voltage recording in cell culture medium at 1 kHz and 37 °C for the high configuration and 1 V input voltage amplitude (**A**). The voltage was measured at two different heights relative to the well bottom. For comparison, the voltage distribution at 60 kHz is shown in **B**. Please note the different voltage scales, which arise due to the EEI impedance present at 1 kHz.

Instead of the expected impedance of about 31.1 Ω, an impedance of about 42.6 Ω was measured after subtracting the shunt resistor. This suggests that the EEI impedance is about 11.5 Ω. With this information, the EEI can be taken into account. In the lumped-element approach, the benchmark result is scaled to match the voltage drop across the medium that is estimated using the EEI impedance. In the distributed-element approach, the EEI impedance is distributed across the electrode surface. For the considered configuration, the approach has to be tested for more than one configuration (as in Sec. 5.1.5) because it is not clear how the impedance is distributed across the two electrodes. I considered again the symmetrically and asymmetrically distributed impedance (compare Fig. 5.15).

It must be noted that the computed current using the distributed-element approach deviates slightly from the measured value, which was used as an input parameter.

Instead of the expected 17.87 mA, the computed current was 16.38 mA (symmetrically distributed impedance) and 16.85 mA (asymmetrically distributed impedance). A possible reason for this observations could be the assumption that the surface impedance z_s equals the global EEI impedance Z multiplied by the surface area A. However, the global impedance is in general related to the surface integral of the local impedance [102]

$$Z = \left(\int_S \frac{1}{z_\mathrm{s}(\mathbf{x})} \mathrm{d}S \right)^{-1} \quad , \tag{5.9}$$

where S is the electrode surface and $z_\mathrm{s}(x)$ the position-dependent local impedance. Evidently, the surface impedance z_s can be computed reliably from the global impedance Z only under the assumption that the surface impedance is not position-dependent. This assumption is not justified in general. Indeed, I observed a position-dependent phase shift between the recorded local voltage and the stimulation voltage when the EEI impedance had a significant influence (Fig. 5.27). This result was also confirmed using a different reference electrode made of Ag/AgCl (not shown).

At 60 kHz, where the EEI impedance has no significant effect, a position-dependent phase could not be observed (not shown). This result suggests that the choice of a fixed surface impedance is not perfectly reflecting reality. Nevertheless, the predicted and observed field distributions agree well. By visual inspection, the asymmetric distributed-element approach yielded the best agreement between measurement and simulation (Fig. 5.28). Still, the symmetric distributed-element approach did not deviate considerably. The lumped-element approach overestimated the field. Moreover, there was no constant ratio between the measured and the expected voltage (not shown). This result suggests that the lumped-element approach based on a voltage divider is not applicable as it would employ a linear scaling of the voltage drop across the medium. In comparison to the electric field strength predicted without the influence of the EEI, the maximum observed field strength is about 30% smaller.

5.2.5 Summary

For the second electrical stimulation (ES) electrode considered in this section, the establishment of a digital twin does not appear straightforward. In agreement with the results shown in the previous section Sec. 5.1, the numerical models are only predictive at frequencies above the cutoff frequency. Corrosive processes could be clearly identified by changes of the impedance and thus the cutoff frequency. The numerical models helped to unambiguously identify these processes.

At frequencies below the cutoff frequency, the EEI has to be considered and integrated into the numerical model. The local voltage recordings reveal that this is not straightforward as assumptions on the surface impedance have to be made. It has to remain subject of future research to identify practical and economic solutions. Probably, empirical nonlinear models could help to contribute [109].

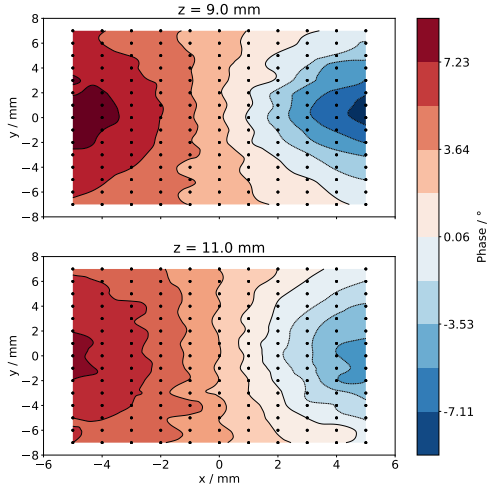

Figure 5.27: Phase shift between the local voltage recorded in cell culture medium at 1 kHz and 37 °C for the high configuration (shown in Fig. 5.26) and the applied input voltage of 1 V amplitude. The voltage was recorded at two different heights relative to the well bottom.

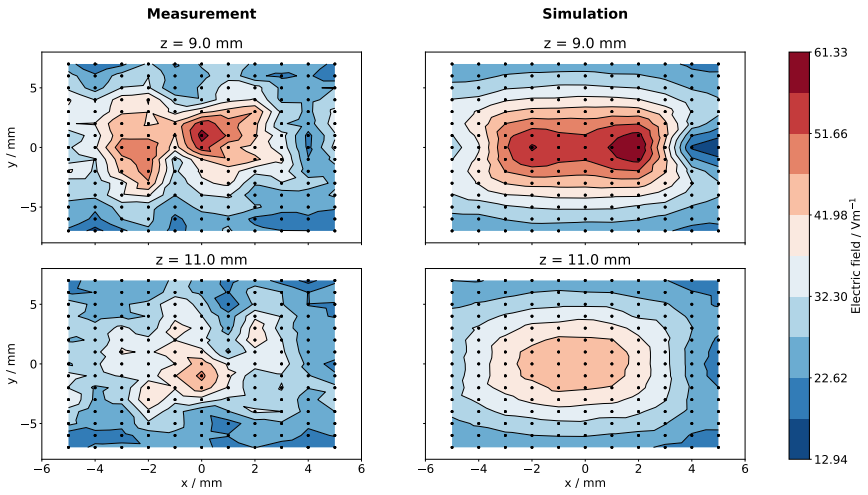

Figure 5.28: The electric field strength was estimated from the voltage recorded in cell culture medium at 1 kHz and 37 °C for the high configuration (shown in Fig. 5.26) by computing the gradient. The measured values are shown on the left for two different heights relative to the well bottom. On the right, the expected electric field is shown computed using the asymmetric distributed-element approach.

Moreover, the results highlight the importance to choose the measurement points such that effective voltage differences in the measurement range of the used instrumentation can be expected. For example, the results in the center of the well (at $x = 0\,\mathrm{mm}$) are always about $0.5\,\mathrm{V}$ for the considered stimulation voltage of $1\,\mathrm{V}$ (compare Figs. 5.23 and 5.26) irrespective of the frequency and height of the measurement probe. This is mostly for geometrical reasons. If one measured only along this line at $x = 0\,\mathrm{mm}$, one will find very good agreement between simulation and experiment. Nevertheless, this is not sufficient for validation as the measurement at different x-positions would reveal frequency-dependent deviations and also the current would not match the expectations for certain frequencies. Furthermore, the EEI impedance at $20\,\mathrm{Hz}$ was so large that the voltage drop across the medium became so small that it could not be well resolved with the used oscilloscope. Advanced instrumentation has to be considered for this case. Still, combining known values of the applied voltage, measured current and electric conductivity with geometrical information permits a relatively good estimate of the actually prevailing electrical stimulation. In the following, the gained knowledge shall be compiled into recommendations to enhance documentation standards.

5.3 Enhancing documentation standards

The status quo of performing numerical simulations to quantify electrical stimulation has been to build a geometrical model and choose material properties as well as ESI impedances based on literature data. In this chapter, the concept of a digital twin of electrical stimulation devices has been introduced. The results can be used to formulate documentation standards that ensure reliability of both experiment and numerical simulation.

Community standards for documentation are required to ensure replicability [76, 276]. In the context of electrical stimulation, thorough documentation is required to enable researchers to translate in vitro findings to clinical therapies. The stimulation chamber considered in Sec. 5.1 exemplarily highlights this need: a field strength of $100\,\mathrm{V\,m^{-1}}$ at a stimulation amplitude of $2.2\,\mathrm{V}$ (DC) has been promised [246]. In subsequent experimental studies, the focus has been laid on the field strength [247, 250] and thus the reported values have made it into literature reviews [71, 73]. Albeit, the computed current density of $0.5\,\mathrm{A/m^2}$ by Srirussamee *et al.* [249] and our research indicates that a much smaller field strength must have prevailed. The aforementioned current density corresponds to a field strength of only $0.33\,\mathrm{V\,m^{-1}}$ for the reported conductivity of $1.5\,\mathrm{S\,m^{-1}}$. The field strength that we found in the DC setting is even smaller. We could reach field strengths close to the promised $100\,\mathrm{V\,m^{-1}}$ only when using short rectangular pulses. Likewise, other researches have concluded that many field strengths in the literature appear to be overestimated [81]. This poses a serious challenge for the reliability and replicability of electrical stimulation studies.

I did not focus on biological aspects of electrical stimulation of cell cultures. The interested reader can find more details on replicability aspects from a biological point of view in [277]. Instead, I introduced theoretical and experimental approaches to advance the characterisation of electrical stimulation devices and make them more comparable and comprehensible for translational research. One could argue that the approach presented here is too detailed and too cumbersome to enter laboratory practice. To highlight the importance of the presented approach, I would like to compare the electrical stimulation approach to a therapeutic intervention using a drug. If only simulations based entirely on geometric information and material properties were used, the field could be overestimated by about 30% (AC stimulation presented in Sec. 5.2.4) or even by a factor of 300 (DC stimulation presented in Sec. 5.1). That means: if one wanted to investigate the influence of 1 g of a drug, in reality one would have used only 0.7 g or even just 0.003 g. But this would never happen in laboratory reality as the weight is usually measured before an experiment. Nothing else than this unquestioned standard procedure was presented for an electrical stimulation experiment in this chapter. Instead of a balance, numerical simulations, impedance measurements, current/voltage recordings and local voltage measurements are used to determine the 'weight' of the stimulation signal. Only when the documentation of an experiment contains all these ingredients, reliable goal functions for the electrical stimulation application can be derived. All in all, this brings us to a summary of this chapter and a vision for future research.

5.4 A vision for future research

I demonstrated the general approach for relatively simple model system. Nevertheless, the approach can be readily adapted because it is

- easy to implement
- relies exclusively on free and open-source software
- uses relatively affordable hardware that can be in total purchased for less than 5000 EUR.

In future research, even cheaper, smaller and more portable hardware solutions should be developed. Potentially, the approach can be integrated into implantable stimulators such as presented in [261]. Recently, it has been demonstrated that neural implants [278] and cochlear implant electrodes [279] can be used as in situ electrochemical sensors by employing time-domain electrochemistry analysis. Probably, the frequency-domain approach presented here can be combined with the time-domain approach to obtain a maximum of information about the electrochemical state during stimulation. In comparison to the approach that has been recently suggested by

Abasi *et al.* [273], the approach in this work does not necessarily require an impedance analyser as the monitoring unit but could be realised with only a shunt resistor connected to an amplifier and an oscilloscope. Still, an impedance analyser can greatly contribute to assess the electrochemical state of the stimulation electrodes. Most impedance analysers perform a frequency sweep. Alternatively, time-domain signals can be used for impedance spectroscopy (as in Sec. 5.1.5). Instead of rectangular pulses, optimised pulses could be used regularly to perform fast and accurate impedance spectroscopy [255, 280].

The approaches presented in this chapter are closely related to data-driven models. In this context, inverse methods could be employed. Use cases are the estimation of dielectric properties or the ESI impedance. For cartilage tissue engineering applications, this is of particular interest for hydrogels with dielectric properties changing over time [269] or biological tissues with highly uncertain dielectric properties [236].

Regarding research software, it is paramount to develop reliable and easy-to-use approaches. Ideally, simulations can be automatically generated based upon an experiment description. To this end, an abstraction of numerical models is required. Within the SFB 1270 ELAINE, first ideas towards workflow descriptions and simulation schemas have been developed that will hopefully pave the way for automated validity checks and numerical experiment generation [281, 282]. For the data documentation, electronic lab notebooks (ELNs) have been identified as the potential link between laboratory and numerical simulation. In cooperation with Kai Budde, we suggested to extend a guideline for documenting cellular assays [252]. To this end, we developed an ELN template that contains the minimal information required for the documentation of an electrical stimulation experiment. An overview of the full workflow involving in vitro experiments, ELN documentation and numerical simulations is given in Fig. 5.29. The individual steps leading to a sufficient documentation of a reliable electrical stimulation experiment are summarised in Fig. 5.30.

Once the numerical models of the stimulation chambers are validated, it becomes feasible to develop reliable models of the effect of electrical stimulation. In the following chapter, the change in the transmembrane potential will be considered as an example. However, all results presented in the following are purely theoretical and are not experimentally validated. Thus, they should be treated rather as hypotheses than as recommendations for electrical stimulation applications for cartilage tissue engineering.

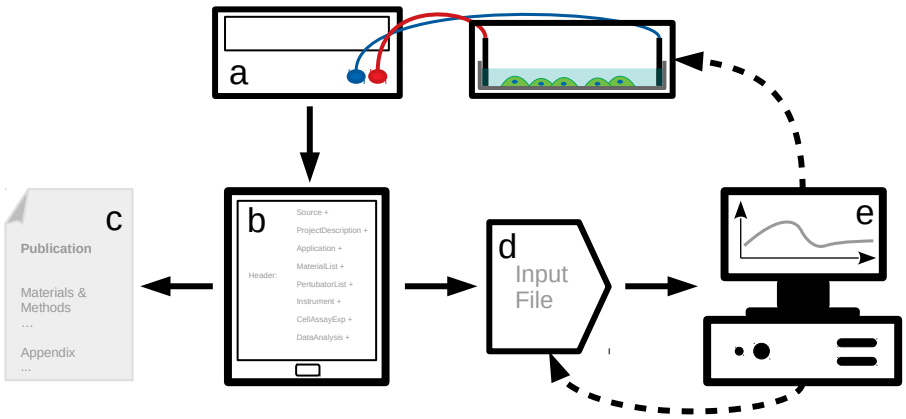

Figure 5.29: Workflow for executing in vitro and in silico experiments with the support of ELNs. An electrical stimulation experiment (a) is documented with the help of an ELN template (b). The documentation may be extracted from an ELN and directly put into a publication (c). The documentation may also be filtered for information required to complete an input file (d) that is used for executing a computer simulation (e). The input file may need to be completed with simulation-specific information. The simulation results may then inform researchers about parameters to be tested in vitro. The figure was taken from [252] and printed with permission from IEEE.

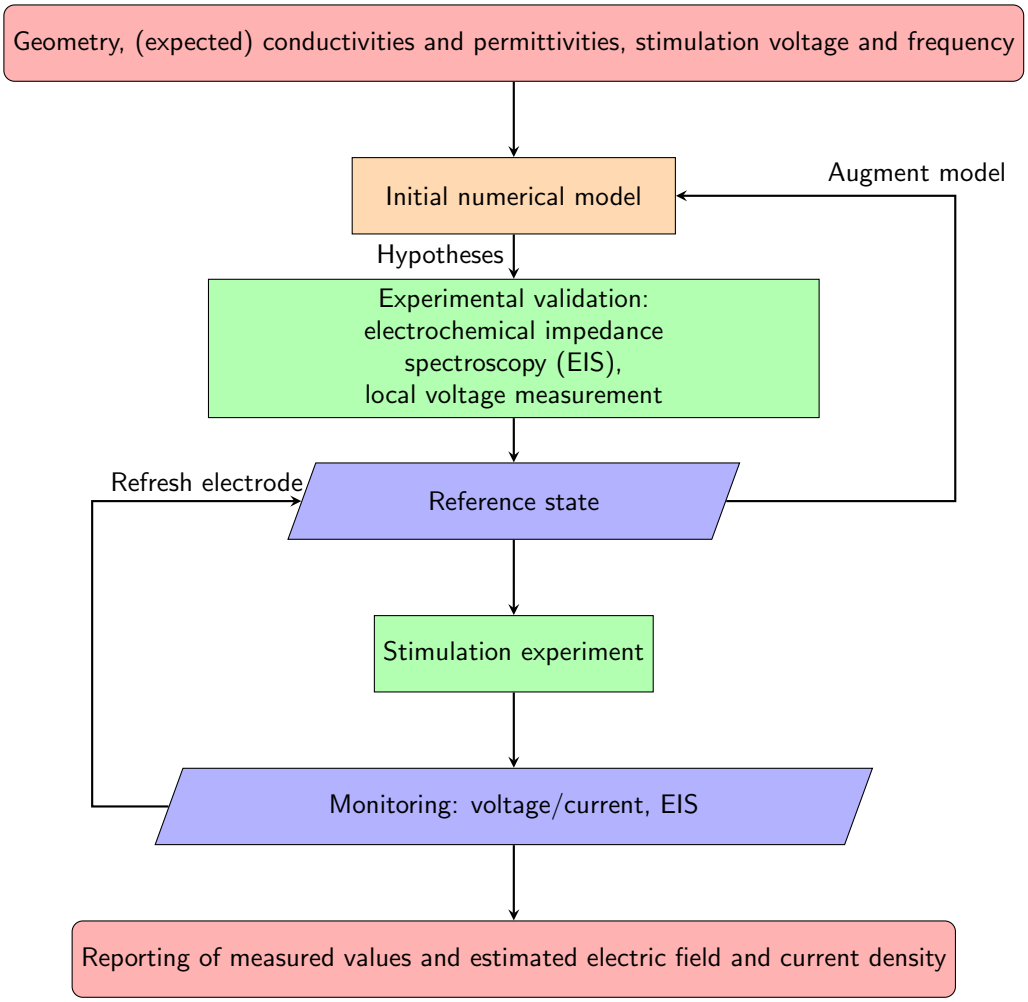

Figure 5.30: Suggested workflow to obtain a controlled and monitored electrical stimulation experiment with reliable electric field and current density estimates. Sufficient information about the geometry, dielectric properties and stimulation protocol is required to build an initial model. The initial model is validated and calibrated by experimental measurements to define a reference state of the stimulation system. The reference state is particularly important as it defines the initial point for the electrical stimulation experiment. Starting from that, it can be assessed if there occurred any changes during the stimulation experiment (e.g., chemical or thermal changes). To detect these changes, monitoring of the voltage and current and ideally also the impedance is required. Eventually, reliable dosimetry data are available that can readily be reported.

6 Numerical studies on the mechanism of interaction

A research focus of electrical stimulation for cartilage tissue engineering has been laid on capacitive coupling. This stimulation approach can be used to circumvent the electrochemical effects at the electrode surface. Thus, it can be expected that a simulation model that relies only on the geometry and the material properties is sufficient to describe the electrical stimulation based on capacitive coupling. In particular, empirical interface impedance models should not be required. Even though capacitive coupling has been often considered for cartilage tissue engineering, its mechanism of interaction is not well understood (i.e., the underlying biological mechanism that is triggered by the electrical stimulation). As experimental findings could be related to voltage-gated channels (see Sec. 2.2), a means to estimate the biological effect could be the induced transmembrane potential. In the following chapter, methods to cope with the integration of the thin cell membrane into a model of a stimulation chamber are presented to eventually obtain a reliable estimate of the induced transmembrane potential.

Models ranging from a basic 2D or 2.5D representation to realistic experimental situations are considered. To understand the influence of the dielectric properties on the modelling outcome, uncertainty quantification techniques are employed. The goal is to provide guidance for future experimental studies.

Parts of this chapter have been published in the paper "Numerical study on the effect of capacitively coupled electrical stimulation on biological cells considering model uncertainties", which appeared in Scientific Reports [91][1] and in the paper "Numerical Simulations as Means for Tailoring Electrically Conductive Hydrogels Towards Cartilage Tissue Engineering by Electrical Stimulation", which appeared in Molecules [283][2]. The two works were reformulated and combined for this chapter.

6.1 Numerical methods

The challenge when including the cell membrane is the thickness of the membrane. It is about a thousand times smaller than the cell radius. Hence, instead of modelling it explicitly, it can be accounted for by a thin layer interface condition. These types

[1] I conceptualised this study and carried out the simulations together with Richard Altenkirch. I performed the data analysis, prepared the figures and wrote the initial draft of the manuscript. Ursula van Rienen supervised the project, acquired the funding and provided all resources.

[2] I conceptualised this study and carried out the simulations, performed the data analysis, prepared the figures and wrote the initial draft of the manuscript. Thomas Distler contributed to the conceptualisation and chemical description of hydrogels. Aldo Boccaccini and Ursula van Rienen supervised the project, acquired the funding and provided all resources.

of interface conditions are also common in heat transfer problems, where they are referred to as contact resistance problems [204].

Two types of methods can be used to cope with the discontinuity of the solution at the interface (see also Sec. 2.3.1): H^1-conforming subspaces overlapping on the interface (see Sec. 3.1.2) or mixed methods [204, 284]. As mixed methods involve the electric field, which means an increased number of DOFs, and lead to an indefinite linear system, I will focus only on the method using overlapping subspaces. This approach is similar to the mortar method [285] but in comparison the resulting linear system of equations is definite because it relies on matching meshes. To prove that the FEM implementation matches the theoretically expected order of convergence, I studied a benchmark problem described in [204] using *NGSolve* (see Appendix A.3).

I did not perform the entire convergence study in *COMSOL*. Instead, I compared the results obtained with *COMSOL* and *NGSolve* for selected configurations. There was no difference and so I concluded that both software packages use a correct implementation of the underlying theory. As the implementation in *NGSolve* was not ready at the time the results were generated, the results shown in this chapter were all generated using *COMSOL*, V5.3a. All computations in this chapter were performed on a workstation with 24 physical Intel® Xeon® CPU Gold 6136, 3.00 GHz cores and 256 GB RAM.

6.2 Studying single cells under capacitive coupling

From a model of a stimulation chamber, which has been validated following the instructions presented in the previous chapter, the electric field acting on the cells is known. This permits to estimate the induced transmembrane potential using, for example, Schwan's equation (Eq. (2.3)). However, such an estimate is valid only for a single spherical cell in a homogeneous field. Numerical models are required to treat the more general case. In particular, they may pave the way for the modelling of tissue-specific cell geometries and distributions.

In this chapter, the focus is on capacitive coupling stimulation, which has received attention for application in cartilage tissue engineering. Even though stimulation chambers using capacitive coupling have been developed in the SFB 1270 ELAINE [23, 44], experimental validation and characterisation has not yet been performed. Nevertheless, I believe that impedance and local voltage measurement can be used similarly as in the previous chapter to perform experimental validation.

For capacitive coupling stimulation, typically a single cell placed directly on the insulating layer separating the electrodes from the cell culture has been considered [121, 286]. Due to the high aspect ratio between the cell membrane and the general setup, these computations have been mostly carried out for 2D or 2.5D models. Axisymmetric geometries can be represented in 2D and are then referred to as 2.5D models as the 3D result can be reconstructed from the 2D solution.

The previous works investigating stimulation of single cells by capacitive coupling have fully discretised the membrane [121, 286] (in the following also called full-fidelity method). Instead, I aimed at using the thin layer approximation approach. In the capacitive coupling case, the cell membrane is close to a good insulator. Previously, the validity of the thin layer approximation has been shown for direct-contact configurations, where the cell is entirely surrounded by conductive cell culture medium [146]. Thus, first a basic problem is considered using the thin layer approximation and the full-fidelity method to validate the approximate approach for capacitive coupling stimulation. Then, a more advanced geometry, which has already been considered for cartilage tissue engineering, is studied and compared to the basic model.

6.2.1 Modelling of capacitive coupling chambers

As the chambers developed in the SFB 1270 ELAINE had not been ready at the time when this work was performed, example geometries from the literature were considered. First, the geometry considered by Taghian *et al.* [121] was used (in the following called Taghian geometry). It is a 2D domain of 50 µm height and 100 µm width with an abstract cell model (Fig. 6.1). The capacitive coupling in this model can be understood in terms of an equivalent circuit model. Two capacitors (1 µm thick insulation covering the electrodes) are connected in series with a parallel RC circuit (48 µm thick cell culture medium filling the space between the electrodes) [121]. The Taghian geometry is used in this work to assess the validity of the thin layer approximation because benchmark results for this geometry have been published and could be used to check the correctness of the results presented here.

As a second chamber, I tried to recreate the original geometry of the device suggested by the Brighton group [39, 40] (in the following called Brighton model). This device has been used for cartilage tissue engineering and, to the least of my knowledge, has not been considered in FEM simulations that also include single cells. The geometrical model is shown in Fig. 6.2. Again, a 2.5D representation of the geometry was chosen. Furthermore, I did not model the electrodes explicitly. Instead, a fixed value of the potential was assigned to the sides of the cover slips that are not in contact with the cell culture medium. Thereby, capacitive coupling is achieved because there is no direct current flow from the electrodes into the medium.

To model the geometry, I assumed for the cover slips a thickness of $d_{\mathrm{cs}} = 0.15\,\mathrm{mm}$ and a radius $r_{\mathrm{cs}} = 16.5\,\mathrm{mm}$. The medium had a thickness $d_{\mathrm{buf}} = 1.415\,\mathrm{mm}$. Furthermore, I assumed it to have a radius $r_{\mathrm{buf}} = r_{\mathrm{cs}}$. To account for a hydrogel as the scaffold material for cartilage tissue engineering, I added a domain with 1 mm radius and 1 mm height at the symmetry axis on the bottom cover slip. The Brighton geometry (shown in Fig. 6.2) can be reduced to a parallel-plate-capacitor geometry similar to the Taghian geometry. Hence, it can also be described by an equivalent circuit. For that, only certain parts of the geometry were considered, which are highlighted in Fig. 6.2.

The aforementioned equivalent circuit model comprises impedances of cylindrical lossy dielectrics, which are given by

$$Z_i = \frac{d_i}{j\omega\hat{\varepsilon}_i\pi r_i^2} \ . \tag{6.1}$$

Here, d_i is the thickness of the cylinder, r_i its radius and $\hat{\varepsilon}_i$ its complex permittivity. Knowing the total and individual impedances, the electric field inside the cell culture medium can be estimated considering a voltage divider. The voltage drop across the medium is

$$U_{\mathrm{buf}} = U_0 \frac{Z_{\mathrm{buf}}}{Z_{\mathrm{total}}} \ . \tag{6.2}$$

Then, the field is (assuming a parallel plate capacitor)

$$E_s = \frac{U_{\mathrm{buf}}}{d_{\mathrm{buf}}} \ . \tag{6.3}$$

Here, U_0 is the amplitude of the initially applied voltage.

6.2.2 Integration of single cells into the model

In the existing models of capacitive coupling using the Taghian geometry, the cell membrane had a thickness of 5 nm and was meshed explicitly [121, 286]. To compare to these models, I also meshed the membrane (Fig. 6.3) using the Taghian geometry. Due to the aspect ratio between the scales, the meshing is a numerically expensive and error-prone task [287] if not performed with great care. To obtain an accurate result, I discretised the membrane such that it is represented by at least four layers of triangular elements. The mesh was additionally refined at the triple point where membrane, medium and insulator meet. This yielded 1,390,530 DOFs with quadratic Lagrange elements. Usually, such a large number of DOFs is more characteristic of 3D problems. It took about 8 min to solve the system at all considered frequencies for the same dielectric properties as in [121]. Please note that the runtime is just an estimate and is only meant to give an impression of the performance of the respective numerical method. The runtime may depend on the occupation of the workstation (e.g., by background processes) and the chosen dielectric properties as they can influence the condition number of the system matrix. Moreover, 3D simulations can probably be sped up by reusing the solution at a previous frequency as an initial guess for the iterative solver. Such a speed-up is impossible for 2D and 2.5D solutions, for which a direct solver is usually chosen.

Note that a full discretization of the membrane appeared to be infeasible for the 3D case on the employed workstation. When making use of the thin layer approximation, the distance of the nodes on the membrane was set to be less than 0.1 µm. In addition, the edges where the cell is in contact with the substrate were refined such that the

results converged well. This yielded 31,713 DOFs, which took a runtime of about 15 s to solve the system at all frequencies. A 3D representation of the same system required 4,575,090 DOFs and a runtime of about 10 min per frequency. The same meshing hypothesis was used for cells added to the Brighton geometry. This yielded a similar amount of DOFs as for the Taghian geometry.

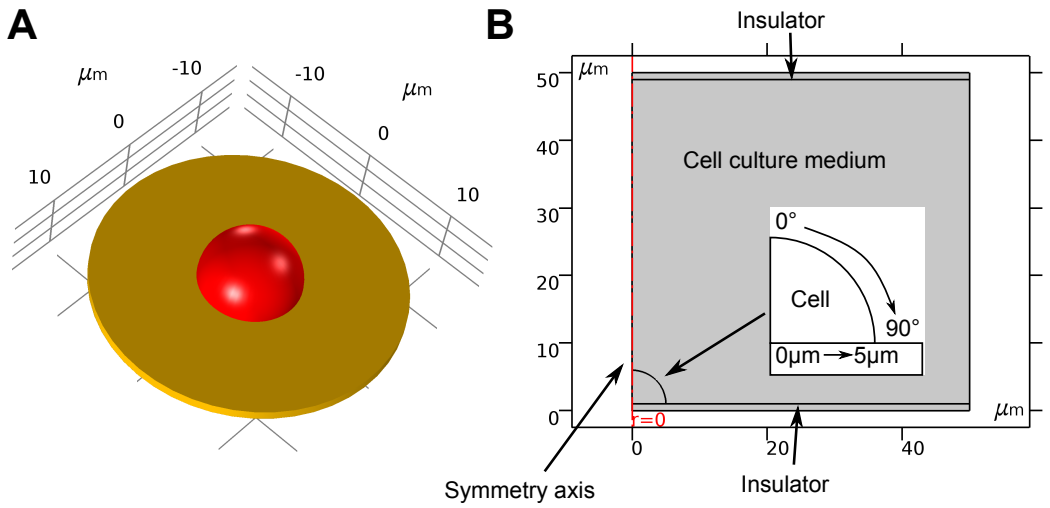

Figure 6.1: 2.5D model of a cell on a substrate exposed to capacitively coupled fields (Taghian geometry) [121]. The 3D equivalent of the 2.5D model (zoomed-in) is shown in **A**. The cell (red) adheres to a substrate (yellow) which is a plastic insulator with a thickness of 1 µm. The cell has a radius of 5 µm and its membrane a thickness of 5 nm. The 2D view of the 2.5D model is shown in **B**. On the top and bottom boundaries of the domain, Dirichlet boundary conditions are applied to impose a net voltage difference. The boundary conditions mimic the electrodes, which are not explicitly modelled. Note that the electrodes are not in direct contact with the medium because they are covered by insulators. The other boundaries are electrically insulating. Material parameters for the cell cytoplasm and the culture medium are assigned as stated in Table 6.3. Different locations along the curved part of the cell membrane are denoted by the angle with the symmetry axis. Positions along the bottom part are denoted by the distance to the cell centre. The figure was taken from [91] and adapted.

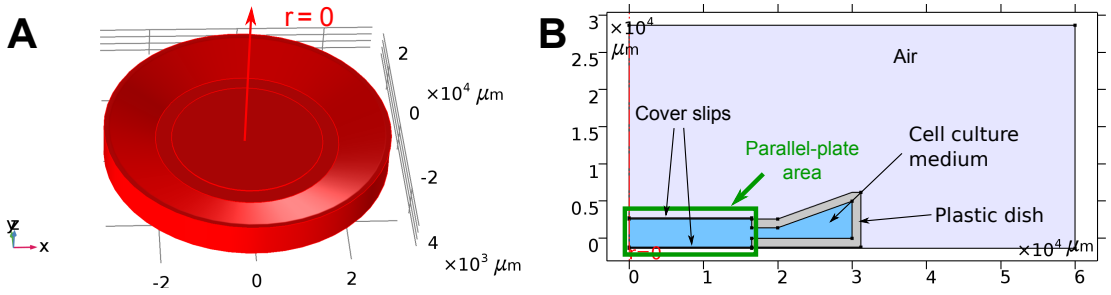

Figure 6.2: General geometry of the Brighton model. 3D representation of the axisymmetric setup (**A**), consisting of (**B**) air, culture medium/buffer (blue), plastic dish (grey), and symmetry axis (red). The voltage is applied between the top side of the upper cover slip and the bottom side of the lower cover slip. The area highlighted in green is the area for which the parallel-plate capacitor approximation was applied. The figure was taken from [283] and adapted.

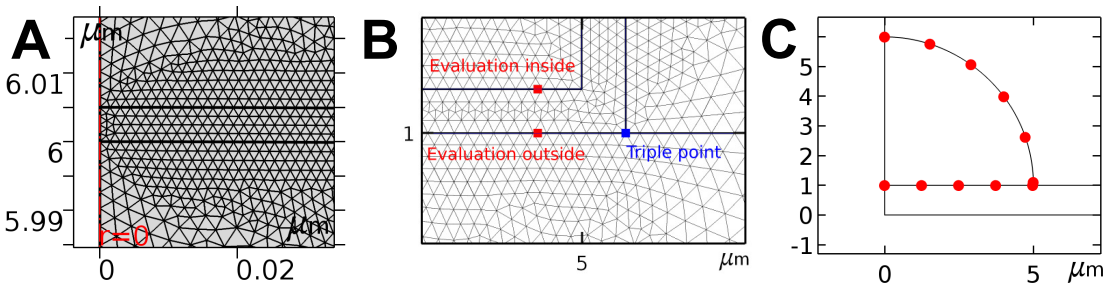

Figure 6.3: Discretization of the cell membrane (between 6 and 6.005 µm) at the cell's apex (**A**). The symmetry axis is shown in red. Discretization of the cell membrane at the cell's right corner close to the triple point (**B**). The evaluation along the membrane is presented for one of the evaluation points shown in **C**. All points for evaluation of the transmembrane potential are shown in **C**. Note that in this illustration, the triple point is covered by two points, one on the circular and one on the bottom line part of the cell membrane. The figure was taken from the supplementary material of [91] and adapted.

Dielectric properties for single cell models

Initially, a UQ analysis of the models suggested in [121, 286] (Taghian geometry) shall be conducted. Therefore, I chose probability distributions containing the values used in these works. The assumptions for the UQ analysis are summarised in Table 6.1. As the dielectric properties of the cell culture medium can be measured with high accuracy [193] and thus do not carry a large uncertainty, I kept them fixed in the analysis. Moreover, the dielectric properties of the insulating coating can be measured well, but the permittivity might change depending on the thickness of the coating [185]. Hence, I included the permittivity of the coating in the UQ analysis

while assuming its conductivity to be negligibly small. For the measurement of the cellular parameters, only less accurate methods such as electrorotation, patch clamp or impedance spectroscopy are available [288]. Some of the parameters have also been covered in a previous study by Taghian *et al.* [121]. In this work, I intend to highlight the influence of the membrane conductivity; an aspect that has not been studied before. I probed conductivities from $0\,\mathrm{S\,m^{-1}}$ (idealised case) to $10^{-3}\,\mathrm{S\,m^{-1}}$ (extreme case, probably perforated membrane).

As the abovementioned dielectric properties are not linked to a specific cell type, experimental values of the dielectric properties of chondrocytes [289] are considered for the specific application in cartilage tissue engineering. I used the reported values and errors for membrane conductivity, membrane permittivity, and cytoplasm conductivity of the PC5 cell line together with the reported average cell radius of 4.1 µm to study the effect of capacitive coupling for the Taghian geometry. Furthermore, the membrane thickness of 7 nm was used to be consistent with [289]. The assumed probability distributions are summarised in Table 6.2. Note that the relatively large conductivity is supported by other experimental findings reporting a large permeability of the chondrocyte membrane at rest for certain ions [134, 135]. Again, polynomial chaos is used for the UQ with fourth-order polynomials.

All conductivities and permittivities of the subdomains of the model were assumed to be constant. Moreover, the frequency dependence of the individual dielectric properties was neglected, which for materials similar to the ones considered here is a valid assumption for frequencies of up to about 100 MHz (see Sec. 2.3.2 and Fig. 2.5). Nevertheless, at high frequencies in the upper MHz-range, the dielectric properties of the membrane can become frequency-dependent [290]. I did not account for this relaxation, which has a characteristic relaxation frequency of about 180 MHz, because it affects only the upper frequency range. Moreover, I was not aware of any research on the dielectric properties of chondrocytes in this frequency range. In sum, frequencies ranging from 10 Hz to 100 MHz were considered to also explore frequencies aside the 60 kHz often used in capacitive coupling stimulation of chondrocytes [23, 114, 291].

Table 6.1: Parameters for the UQ study of the numerical model as reported in [121, 286] using cell-unspecific values. $\mathcal{U}$ stands for uniform distribution.

Domain	Quantity	Value	Explanation
Cytoplasm	Conductivity in $\mathrm{S\,m^{-1}}$	$\mathcal{U}(1, 1.5)$	Guess
	Relative permittivity	$\mathcal{U}(60, 80)$	Assumptions from [289] and [121]
Cell membrane	Conductivity in $\mathrm{S\,m^{-1}}$	$\mathcal{U}(0, 10^{-5})$	Possible range
	Relative permittivity	$\mathcal{U}(9.9, 12.1)$	10% variation
Coating	Conductivity in $\mathrm{S\,m^{-1}}$	0	
	Relative permittivity	$\mathcal{U}(2.4, 2.8)$	Guess based on [185]

Table 6.2: Parameters for the UQ study of the numerical model as reported in [121, 286] applied to chondrocytes (values based on [289]). $\mathcal{N}$ stands for normal distribution. Note that the cytoplasm permittivity was kept fixed in the analysis in [289].

Domain	Quantity	Value
Cytoplasm	Conductivity in $\mathrm{S\,m^{-1}}$	$\mathcal{N}(0.12, 0.02)$
	Relative permittivity	60
Cell membrane	Conductivity in $\mathrm{S\,m^{-1}}$	$\mathcal{N}(6.895 \times 10^{-5}, 1.77 \times 10^{-5})$
	Relative permittivity	$\mathcal{N}(59.06, 12.88)$
Coating	Conductivity in $\mathrm{S\,m^{-1}}$	0
	Relative permittivity	$\mathcal{U}(2.4, 2.8)$

6.3 Results

6.3.1 Validation of the numerical model of the stimulation chamber

As shown in the previous chapter, EIS is a suitable method to validate the numerical models. The impedance has already been used to validate the Taghian geometry [121]. I replicated the study and could find very good agreement of the numerically computed impedance and the expected impedance based on equivalent circuit analysis (not shown). Consequently, also the expected and the computed electric field were in good agreement. At 60 kHz, the electric field strength is about $28.9\,\mathrm{V\,m^{-1}}$. The field was computed for a supplied voltage U_0 of 10 V to be in line with [121, 286]. Please note that the system is again linear and the solution for a different supplied voltage can be obtained straightforwardly by scaling the voltage.

As a novel aspect, I performed a UQ analysis of the Brighton geometry without a cell. In contrast to the Taghian geometry, U_0 (the supplied voltage) was set as 44.81 V to be in line with the works of the Brighton group [40]. At 60 kHz, the field strength was found to be $1.33\,\mathrm{V\,m^{-1}}$, which is 1.5 times smaller as reported earlier [39, 41, 42, 116, 123, 124]. The deviation can be mainly attributed to incomplete documentation of how the expected $2\,\mathrm{V\,m^{-1}}$ were determined before [39, 41, 42, 116, 123, 124], as well as limited knowledge of the actually used geometry.

I found that the numerical model of the simplified geometry (compare Fig. 6.2) of the here investigated electrical stimulation chamber agrees very well with the analytical equivalent circuit expression (based on Eqs. (6.1) and (6.3), data not shown). Moreover, the FEM for the full geometrical model leads to similar results. The impedance deviates less than 1% between the numerical FEM solution and the analytical solution based on equivalent circuits (data not shown). If one takes only the part of the chamber, where a spatially uniform field exists (i.e., up to a

radius of about 10 mm), the electric field strength deviates less than 1% (data not shown). Thus, the macroscopic electric behaviour of the stimulation device can be characterised solely by equivalent circuits without using FEM. In addition, this result validates the numerical simulation approach demonstrated here. Furthermore, it indicates that the simple Taghian geometry is not overly simplistic as it resembles the capacitive coupling approach for cartilage tissue engineering suggested by the Brighton group.

Because each variation of geometrical parameters would require the generation of a new mesh in the FEM, I investigated the effect of geometrical parameters solely for the analytical equivalent circuit model. For the UQ analysis, I assumed a uniform variation of 10% around the mean value. The analysis revealed that the absolute value of the impedance scales linearly with the frequency (see Fig. 6.4a), which is characteristic of capacitors. Its mean is centred in the 90% prediction interval for all frequencies. The phase of the impedance is mostly $-90°$, which indicates the strong capacitive behaviour of the circuit (see Fig. 6.4b). Only at frequencies greater than 1 MHz the phase increases slightly. The field also scales linearly with the frequency (not shown).

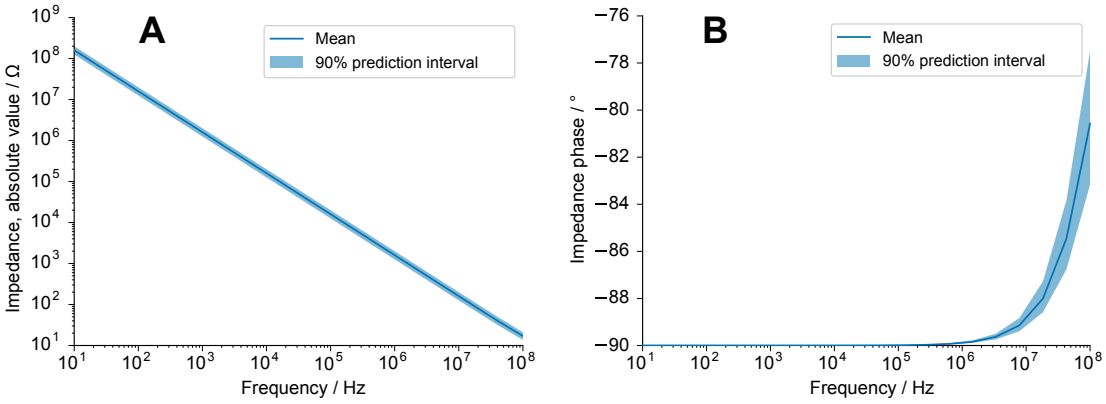

Figure 6.4: Uncertainty quantification (UQ) result for the absolute value (**A**) and the phase (**B**) of the impedance of the equivalent circuit describing the Brighton chamber (Fig. 6.2). The mean value is shown together with 90% prediction interval for a broad frequency range. The figure was taken from [283] and adapted.

The first-order Sobol indices do not change with the frequency for the made assumptions (not shown). Hence, I only report the frequency-averaged Sobol indices (Fig. 6.5). For the impedance, the geometric parameters of the cover slips (radius and thickness) as well as the permittivity of the cover slips strongly influence the impedance value (Fig. 6.5a). In contrast, the electric field in the buffer medium is also influenced by the radius of the buffer as well as its conductivity (Fig. 6.5b). The uncertainty of the permittivity of the buffer does not play a significant role (Fig. 6.5).

For future experiments with electrically conductive hydrogels and capacitive-coupling stimulation, my findings imply that the dimensions and permittivity of the cover slips should be precisely known as they influence the electric field in the medium and thus the effect of the electrical stimulation. The results indicate that again EIS can be a tool for the experimental validation of the theoretical model. The use of EIS as a measurement tool is complicated by the impedance of the cover slips, which is much greater than the impedance of the cell buffer. This effectively leads to an important limitation: the conductivity of the sample (e.g., the cell culture medium) cannot be monitored in situ. This excludes a digital twin approach as presented in the previous section. In addition, the electric field strength cannot be estimated reliably upon impedance measurement. That is because the field depends on the conductivity of the medium, which does not significantly influence the impedance. In contrast, the conductivity of the medium had a significant impact on the impedance measured in direct contact configurations (see previous chapter), which permitted a reliable field estimate. Furthermore, local voltage measurements are hampered by the high impedance of the cover slips. The voltage drop across the cell culture medium can be estimated using Eq. (6.3) to be about

$$U_{\mathrm{buf}} = E_{\mathrm{s}} d_{\mathrm{buf}} = 1.33\,\mathrm{V\,m^{-1}} \cdot 3.785\,\mathrm{mm} \approx 5\,\mathrm{mV} \quad . \tag{6.4}$$

This means that the local voltage measurement should have a resolution of, for example, 1 mV or even finer to be able to resolve the change in the local voltage. As demonstrated in Sec. 5.2.4, such a fine resolution is not straightforward to achieve in experiments.

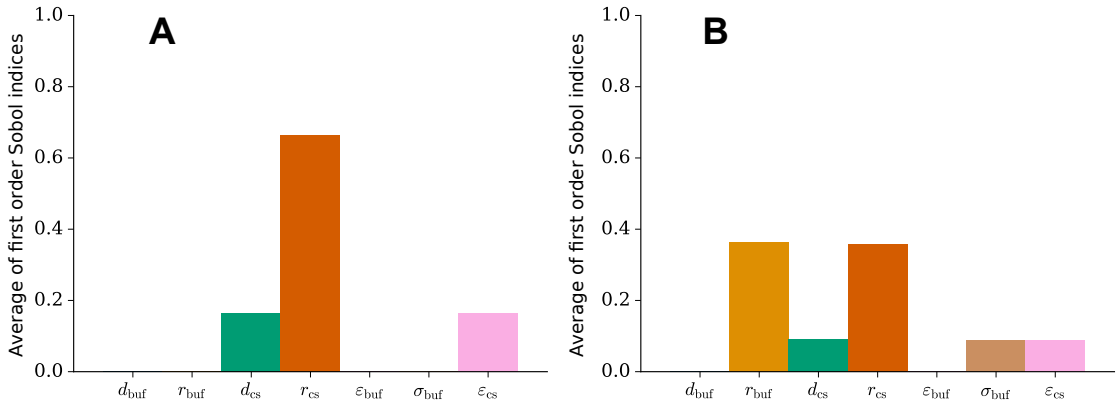

Figure 6.5: First order Sobol indices for (**A**) the absolute value of the impedance of the equivalent circuit describing the Brighton chamber (Fig. 6.2) and (**B**) for the electric field in the buffer medium. The figure was taken from [283] and adapted.

The considerations and analysis tools presented here could be helpful for the design of a novel device which can stimulate and measure the impedance simultaneously.

The results indicate that the impedance of the electrode insulation (i.e., the cover slips) has to be substantially decreased by decreasing the thickness of the insulation, increasing its area, or using a high-permittivity material. The latter would also increase the field strength in the medium substantially while requiring a smaller input voltage, which would make the capacitive coupling approach more energy-efficient and safer [120, 252]. A potential material for this task could be high-permittivity ceramics, which were already suggested in 1984 [292], but have not yet been used for electrical stimulation in cartilage tissue engineering.

6.3.2 Studying the influence of the membrane conductivity

After having analysed the impedance of the capacitive coupling chambers, single cells shall be considered. A hemispherical cell situated on the culture well bottom of the Taghian geometry (Fig. 6.1) was considered. The hemispherical cell is an abstract model, which has been considered in previous works [121]. Due to the symmetry of the hemispherical cell geometry, it can be described by a 2D geometry with corresponding symmetry boundary conditions (i.e., a 2.5D model). To check the applicability of the thin layer approximation for the cell model, the results generated using the thin layer approximation were compared against the results obtained by the so-far employed full-fidelity approach at prominent points along the cell membrane. The transmembrane potential in the electro-quasistatic formulation is a phasor. Thus, its absolute value and phase were computed and compared. Apart from this comparison, I generally report the absolute value of the transmembrane potential as this is the property of interest in therapeutic applications.

Firstly, the transmembrane potential was computed for the same dielectric parameters as in previous studies [121, 286] (see Table 6.3) using the full-fidelity as well as the approximate model. The results obtained by the approximate and the full-fidelity method did not deviate significantly (data not shown). Furthermore, I observed that the accuracy of the thin layer approximation does not deteriorate when a conductivity greater than $0\,\mathrm{S\,m^{-1}}$ was chosen. Hence, I concluded that the thin layer approximation works reliably in a capacitive coupling setting when the cell is not only surrounded by conductive cell culture medium but also in close contact with an insulator. Consequently, only the results generated using the thin layer approximation are reported in the following.

In previous studies [121, 286] the idealised case of a membrane conductivity of $0\,\mathrm{S\,m^{-1}}$ was assumed. Realistic values of the membrane conductivity are in the range of $10^{-5}\,\mathrm{S\,m^{-1}}$ to $10^{-8}\,\mathrm{S\,m^{-1}}$ as the membrane is not a perfect insulator and permits a leakage current [144, 289, 293]. It turns out that changes in the membrane conductivity strongly influence the results (Figs. 6.6 and 6.7). Upon alteration of the membrane conductivity, a high-pass-filter effect was observed. In the idealised case of $0\,\mathrm{S\,m^{-1}}$, the transmembrane potential is constant and non-zero over a broad frequency range. This would indicate an effective stimulation already at very low frequencies approach-

Table 6.3: Dielectric properties for the numerical benchmark model (Taghian geometry) as reported in [121, 286].

Domain	Conductivity in $\mathrm{S\,m^{-1}}$	Rel. permittivity
Insulator	0	2.6
Culture medium	1.5	80
Cytoplasm	1.5	80
Cell membrane	0	11.3

ing the static limit of 0 Hz. The results using a non-zero membrane conductivity suggest, that the transmembrane potential is close to zero for low frequencies before it starts to approach the constant value that was predicted previously. Nevertheless, this constant value, which is usually approached between 1 kHz and 1 MHz, is independent of the conductivity if the transmembrane potential rises at a sufficiently low frequency. Evidently, Schwan's equation (Eq. (2.3)) cannot be used in the context of capacitive coupling to estimate the transmembrane potential because it would predict a value that increases linearly with the frequency. The greater the membrane conductivity, the higher becomes the frequency, from which on the transmembrane potential rises. In the high-frequency limit, the values again coincide irrespective of the membrane conductivity. Later, it will be shown that the transmembrane potential in this frequency region is mainly influenced by the membrane permittivity, which explains the aforementioned observation.

The absolute value of the transmembrane potential depends on the location on the membrane for frequencies above about 1 MHz. Figure 6.6 shows that at the membrane apex (denoted by the blue line corresponding to an angle of 0°) the transmembrane potential increases from about 1 MHz and peaks at about 10 MHz before it decreases. A special point on the membrane is the triple point, where membrane, medium and insulator meet (see also Fig. 6.3B). This point is a result of the geometrical modeling, in which the cell builds a relatively sharp corner with the insulator and the medium. Such a corner is most likely not present in reality. On the circular part, the triple point is located at an angle of 90°. Close to this point, the transmembrane potential drops continuously from about 1 MHz on and does not peak. These results are mostly caused due to the geometrical modeling, so this behaviour probably has numerical reasons. The transmembrane potential at these points should not be considered representative of the electrical stimulation.

When the transmembrane potential along the bottom line is considered, qualitatively similar observations could be made (data not shown). The higher the membrane conductivity is, the higher frequencies are needed to induce a non-zero transmembrane potential. The transmembrane potential along the bottom is roughly 1.9 times larger than that along the circular part. It does not depend much on the location on the cell membrane except for points close the triple point.

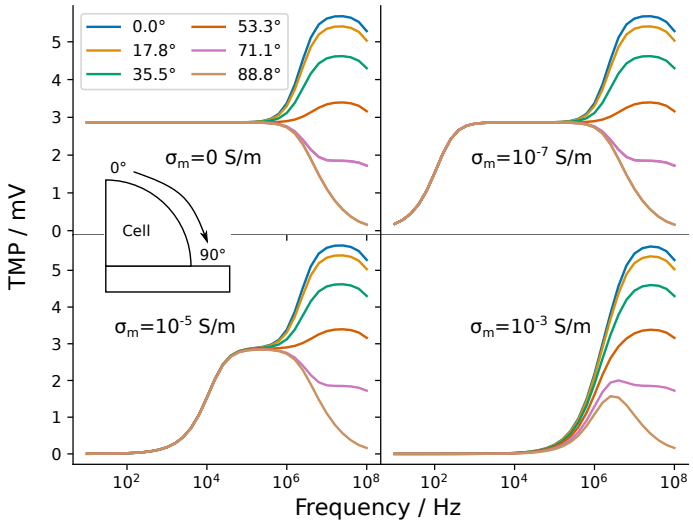

Figure 6.6: Transmembrane potential along the curved part of the cell membrane for different membrane conductivities of $0\,\mathrm{S\,m^{-1}}$, $1 \times 10^{-7}\,\mathrm{S\,m^{-1}}$, $1 \times 10^{-5}\,\mathrm{S\,m^{-1}}$ and $1 \times 10^{-3}\,\mathrm{S\,m^{-1}}$. The results were generated using the thin layer approximation. The figure was taken from [91] and adapted.

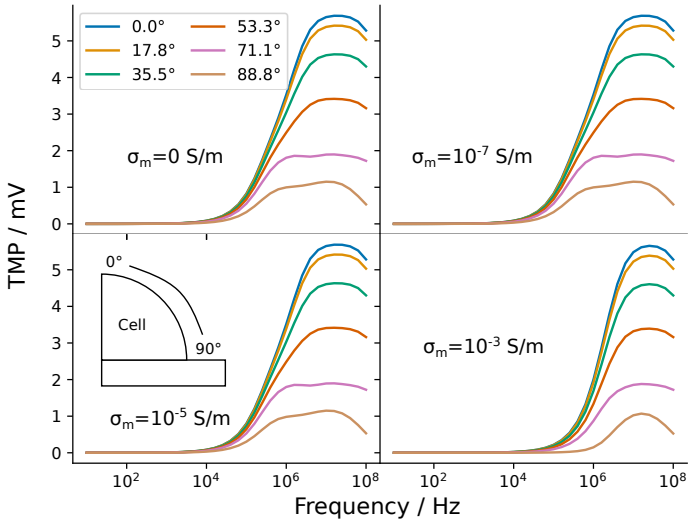

Figure 6.7: Transmembrane potential along the curved part of the cell membrane for different membrane conductivities of $0\,\mathrm{S\,m^{-1}}$, $1 \times 10^{-7}\,\mathrm{S\,m^{-1}}$, $1 \times 10^{-5}\,\mathrm{S\,m^{-1}}$ and $1 \times 10^{-3}\,\mathrm{S\,m^{-1}}$ when the cell was separated from the well bottom by a gap of 100 nm. The results were generated using the thin layer approximation. The figure was taken from [91] and adapted.

The numerical results of the studied benchmark model are in good agreement with previously published results [121]. Note that the electric field across the membrane (which other publications [121, 286] focussed on) can be calculated by dividing the transmembrane potential by the membrane thickness. Likewise, the transmembrane potential of about 3 mV for a hemispherical cell with idealised membrane conductivity corresponds to an electric field strength of $0.6\,\mathrm{MV\,m^{-1}}$ for a membrane of 5 nm thickness. This result of the 2.5D simulation is about $0.2\,\mathrm{MV\,m^{-1}}$ less than reported for the pure 2D case [121]. Hence, it shows how important the axisymmetric assumption is to account for the real 3D geometry.

In recent years, the numerical simulation models of capacitive-coupling stimulation have assumed that cells are in direct contact with the insulator on the electrode [121, 286]. However, it has been found in experiments that there exists a gap between the cell membrane and the substrate. For neurons, the gap is homogeneous (i.e., has an almost constant thickness between 60 nm and about 100 nm [294]). The gap is most likely filled with a conductive electrolyte with at least the same conductivity as the cell culture medium [295]. I am not aware of a study investigating the adhesion of, for example, chondrocytes or osteoblasts at such a fine scale. Thus, I included a gap of 100 nm filled with cell culture medium in the aforementioned 2.5D model. The results of this model are shown in Fig. 6.7 and can be directly compared to the results shown in Fig. 6.6 (i.e., the case without a gap). The shape of the transmembrane potential curves of the model without (Fig. 6.6) and with the gap (Fig. 6.7) are very similar at very high frequencies greater than about 1 MHz for most of the points on the membrane. The transmembrane potential is mostly zero at lower frequencies for all membrane conductivities if the gap is considered. The frequency from which on the transmembrane potential becomes non-zero only slightly increases with increasing membrane conductivity. Evidently, the gap has a similar effect as the highest membrane conductivity in the model without a gap. In the following, I will not further consider the gap to keep the modelling approach comparable to previous studies [121, 286] and due to a lack of reliable experimental data to be used in a UQ approach.

6.3.3 Preliminary uncertainty quantification of a reduced model

To understand the influence of all parameters at the same time, I performed a UQ analysis using probability distributions for the parameters based on prior knowledge (see Table 6.1). The result of the UQ analysis for the simple cell model (Fig. 6.1) is shown in Fig. 6.8. Here, the focus was laid on the transmembrane potential value at the cell apex (i.e., the highest point of the cell where the transmembrane potential becomes maximum on the circular part of the membrane). There was no significant difference between first-order and total Sobol indices in regions where

the transmembrane potential was considerably larger than zero. This indicates no significant interaction between the input parameters. Consequently, only first-order indices are reported in the following.

The mean value of the transmembrane potential behaves similarly, as previously shown in Fig. 6.6 for non-zero membrane conductivity. Its 90% prediction interval is not broader than 1 mV for all frequencies. It highlights the possible range in which the transmembrane potential value can be expected. Thanks to the first-order Sobol indices, the possible deviation from the mean transmembrane potential can be attributed to the different parameters. In the range up to about 10 kHz, the membrane conductivity σ_{m} plays a crucial role. From 10 kHz to 1 MHz, the transmembrane potential is most sensitive to changes of the membrane permittivity ε_{m}. In addition, the permittivity of the coating $\varepsilon_{\mathrm{coat}}$ plays a significant role. For higher frequencies, membrane permittivity, coating permittivity, and cytoplasm conductivity σ_{cyt} contribute to a change of the transmembrane potential with their uncertainty. Furthermore, the cytoplasm permittivity $\varepsilon_{\mathrm{cyt}}$ does not have any influence over the entire frequency range. I also investigated the transmembrane potential at the centre point at the bottom of the cell (i.e., where the cell is in direct contact with the insulator). The main difference to the result at the cell apex is that the cytoplasm conductivity does not influence the transmembrane potential at higher frequencies (data not shown). As mentioned previously, the transmembrane potential is greater at the cell bottom and does not further increase at frequencies above 1 MHz. Because changes of the cytoplasm permittivity did not reveal any influence on the modelling outcome, I did not further consider it.

In the previous paragraph, assumptions were made on the probability distributions of the uncertain parameters. The range of the parameters was chosen to include the values of previous numerical studies [121, 286]. A more realistic result of the UQ was gained by using probability distributions based on experimental data and their reported uncertainties [289] (Table 6.2). The experimentally determined dielectric properties of chondrocytes differ in two aspects from the previously chosen parameters: their probability distributions are normal distributions instead of uniform distributions and the expectation values for the cytoplasm conductivity as well as membrane permittivity are outside the previously tested interval. At this point, I would like to mention that the cytoplasm conductivity chosen in previous numerical studies of capacitive coupling stimulation [121, 286] is relatively large compared to the expected values for eukaryotic cells [293]. In contrast, the experimentally determined values for chondrocytes [289] are in the expected range.

The results using the dielectric properties of chondrocytes are shown in Fig. 6.8B. It is evident that the transmembrane potential is considerably smaller when using the experimentally determined parameter values. Moreover, the shape of the 90% prediction interval and the course of the mean value of the frequency-dependent transmembrane potential differ from the previous results using guessed properties (Fig. 6.8A). The mean value peaks between 30 kHz and 90 kHz. At the same frequen-

cies, the prediction interval covers the highest possible transmembrane potential values. Close to the maximum frequency of 100 MHz, the transmembrane potential increases again. Below 10 kHz, the transmembrane potential value tends to zero with high probability.

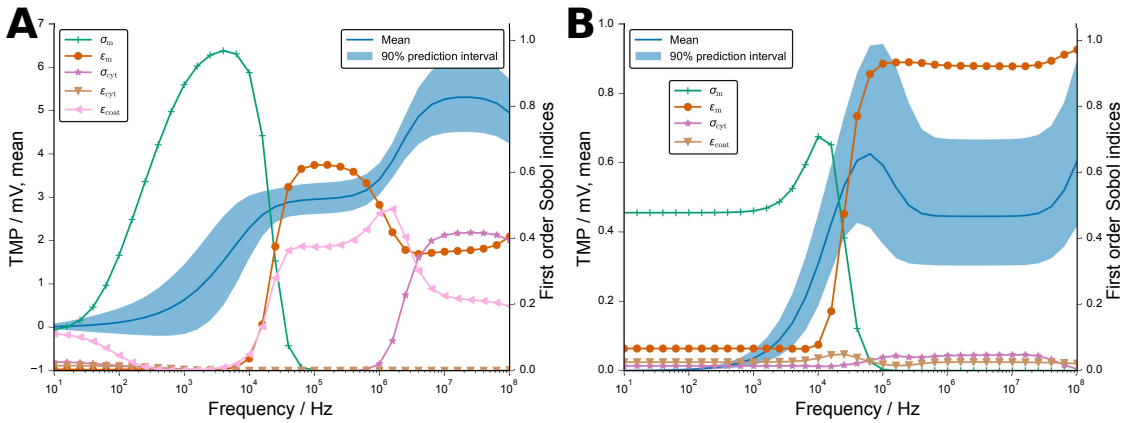

Figure 6.8: Comparison of the UQ analyses for the basic model shown in Fig. 6.1 considering different assumptions on the dielectric properties. In **A**, guessed parameter ranges were considered (Table 6.1). The mean and 90% prediction interval of the absolute value of the transmembrane potential at the cell apex (left axis) are shown together with the first order Sobol indices for each uncertain parameter (i.e., the conductivity (dark green) and permittivity (orange) of the membrane, the conductivity (purple) and permittivity (brown) of the cytoplasm, and the permittivity of the coating (pink)). In **B**, the dielectric properties of chondrocytes were considered (Table 6.2). Hence, the uncertain parameters were the conductivity (dark green) and permittivity (orange) of the membrane, the conductivity (pink) of the cytoplasm, and the permittivity of the coating (brown), respectively. Please note that the ordinates differ between the figures. The figure was generated using figures from [91].

As presented in the previous paragraph, the membrane conductivity plays a dominant role in the low-frequency range, whereas the membrane permittivity influences the results most in the high-frequency range. Interestingly, the comparatively small error of the cytoplasm conductivity also leads to a decreased influence of this parameter. The same holds true for the coating permittivity. The result at the cell bottom resembles the result at the cell apex (data not shown). A significant difference is that the transmembrane potential does not peak, but instead remains almost constant from about 60 kHz onwards. Furthermore, the transmembrane potential value is larger and the influence of the cytoplasm conductivity is even smaller.

6.3.4 Studying realistic 3D models

To validate the possibility and physical correctness of the modelling of a 3D geometry using the thin layer approximation, I compared the 2.5D model shown in Fig. 6.1 to its 3D representation. The comparison showed good agreement between the two models with deviations of a few percent or less or a very small absolute error. The results deviated notably only close to the triple point.

As a more realistic model of adherent cells, I considered the model shown in Fig. 6.9. It comprises two semi-ellipsoidal cells because the semi-ellipsoidal cell shape has been shown to approximately represent adherent cells [146]. The two semi-ellipsoidal cells cannot be described by a 2.5D model and are thus modelled in 3D. For a setup with one cell, 3,576,601 DOFs were required and for one with two cells 6,393,262 DOFs. The runtime of the models is in the range of a few minutes per frequency. The large number of DOFs is caused by the fine resolution of the cell membrane, which was controlled by a meshing parameter. Adaptive mesh refinement techniques could be explored in future research to reduce the number of DOFs.

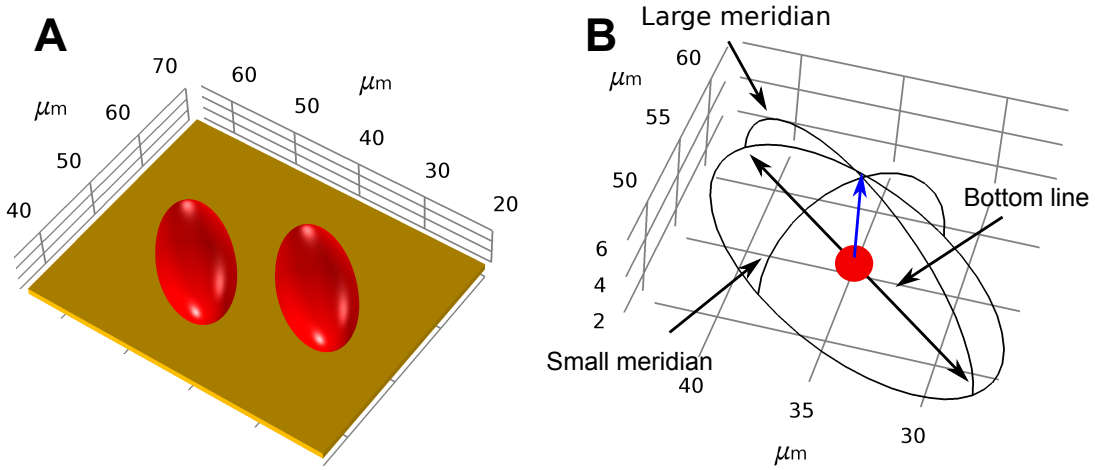

Figure 6.9: In 3D, cells with a semi-ellipsoidal shape were used to simulate the case of adherent cells. The model of two cells with a minimal distance of about 5 µm (zoomed-in) is shown in (**A**). The wireframe view of a single cell and the definition of lines along which the solution was evaluated are shown in (**B**). Points located on the small and large meridian were characterised by the angle between the reference vector (blue arrow) and the vector from the origin (red point) to the point on the membrane. The points along the bottom line were characterised by the distance to the centre point. The figure was taken from [91] and adapted.

As an evaluation of the model over the same frequency range as in the previous section becomes prohibitively expensive even on well-equipped workstations, I

focussed on one frequency[3]. I chose 60 kHz due to its wide application in cartilage tissue engineering approaches. UQ was performed on this model using the experimentally determined parameters for chondrocytes (Table 6.2). Based on the results of the reduced model (Fig. 6.8B), I omitted the cytoplasm conductivity and the coating permittivity to further reduce the complexity of the UQ analysis.

To better understand the stimulation of the two cells, the electric field strength around the cells and the transmembrane potential on the cell surface are considered (Fig. 6.10a). The observables were computed for the expectation values of the model parameters. It turns out that the field is mostly homogeneous around the cells and changes only in close proximity to the individual cells. It is in agreement with this observation that the transmembrane potential appears to be identical on both cells. Consequently, I only report the results for one cell because there was no significant numerical deviation between the results for each of the two cells. In comparison to the results at 60 kHz using the previously assumed dielectric properties (Fig. 6.6), the transmembrane potential changes on the curved part of the cell surface (Fig. 6.10a). It increases with decreased distance to the cell bottom (i.e., it does not assume its maximum value at the cell apex). Instead, the transmembrane potential close to the triple point is about 25% greater than at the cell apex. However, on the cell bottom it remains constant (not shown), which was also the case in the previous analysis of the reduced model. I could attribute the change in the spatial dependency of the transmembrane potential on the curved part of the membrane solely to the change of the chosen dielectric properties. The validity and accuracy of the thin layer approximation was not influenced when choosing the chondrocyte dielectric properties instead of the previously assumed properties.

When analysing the influence of the modelling outcome in a UQ setting, deviations of the transmembrane potential with respect to the membrane properties could be observed (Figs. 6.10b). Again, changes of the membrane permittivity influence the transmembrane potential strongly while the membrane conductivity plays a subordinate role, given the uncertainty of the experimental data. The 90% prediction interval of the transmembrane potential is rather wide and can extend to values that are 40% larger than the mean transmembrane potential. As I used homogeneous (i.e., spatially independent) dielectric properties on the cell membrane, the width of the prediction interval does not depend on the specific location on the cell membrane. However, the aforementioned spatial dependency along the curved part of the membrane is reflected in both the mean transmembrane potential and the prediction interval (Fig. 6.10b). Accordingly, the mean transmembrane potential and prediction interval along the cell bottom are not spatially dependent (not shown).

[3]With the approach used in the previous chapter, it becomes feasible to run multiple simulations simultaneously on an HPC cluster. However, commercial software such as *COMSOL* cannot straightforwardly be used this way as first appropriate licences must be purchased. This aspect was another motivation to develop an open-source alternative, which will be presented in the next chapter.

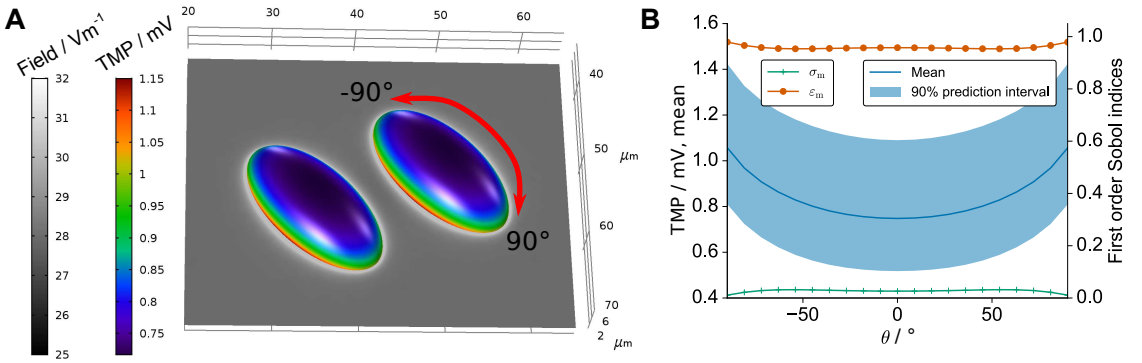

Figure 6.10: **A**: The electric field strength around the cells and the transmembrane potential on the cell surface are shown for the expectation values of the cell dielectric properties (Table 6.1). **B**: Left axis: Mean and 90% prediction interval of the absolute value of the transmembrane potential at the cell apex for the ellipsoid cell model shown in Fig. 6.9. Right axis: First order Sobol indices for each uncertain parameter (i.e., the conductivity (dark green) and permittivity (orange) of the membrane). The results were evaluated along the large meridian using the angle with the central normal vector as an indicator for the location (as indicated by the red arrow in **A**). The results along the small meridian deviated only slightly and are not reported. The figure was taken from [91] and adapted.

6.3.5 The influence of the scaffold

To enhance the outcome of electrical stimulation on the cellular response, electroactive hydrogels represent a promising potential strategy. The design of such hydrogels comprises the choice of the scaffold material and conductivity tuning by appropriate electroactive materials [296, 297] or by initially using hydrogels solely consisting of conductive polymers [298]. Such conductive polymer composites have been shown to be suitable for biomedical applications [296].

Aspects as the chemical composition or mechanical properties shall not be discussed here and the reader is referred to the literature overview in [28, 283]. To fabricate hydrogels that mimic the complexity of articular cartilage, 3D printing techniques have been identified as a promising route [299, 300]. Furthermore, recent research has demonstrated the 3D printing of electroactive hydrogels with tuneable conductivity [30, 300]. This might pave the way for patient-specific solutions.

The Taghian geometry was considered to validate the numerical approach based on the thin layer approximation for capacitive coupling stimulation. Subsequently, I considered the Brighton model to study the influence of a hydrogel under realistic conditions. As mentioned before, both geometries are very similar and only quantitative differences between the results are to be expected.

In contrast to the cell culture medium, which is considered in models without hydrogels, the relative permittivity of the hydrogel is not known. For cartilage, the

relative permittivity can easily increase up to 10^3 [237]. Thus, I considered a broad span from the cell culture medium case to the cartilage case in the UQ analysis of the hydrogel model (see Table 6.4).

Table 6.4: Assumptions for the dielectric properties of electrically conductive hydrogels with an exemplary single cell model [121]. The uniform distribution is denoted by $\mathcal{U}$.

Domain (subscript)	Conductivity in $\mathrm{S\,m^{-1}}$	Rel. permittivity
Hydrogel (*hydro*)	$\mathcal{U}(0.1, 2.0)$	$\mathcal{U}(60, 1 \times 10^3)$
Buffer medium (*buf*)	$\mathcal{U}(0.5, 1.5)$	$\mathcal{U}(60, 80)$ (benchmark) or 80
Membrane (m)	$\mathcal{U}(0, 5 \times 10^{-5})$	$\mathcal{U}(5, 15)$
Cytoplasm (*cyt*)	$\mathcal{U}(0.1, 1.0)$	60

I observed the following behaviour in our simulations when including a hydrogel with variable conductivity. Regarding different relations of hydrogel conductivity (σ_{hydro}) and conductivity of the surrounding cell culture medium (σ_{buf}), there are three possible outcomes of the electrical stimulation, which are represented by the electric field inside (E_i) and outside (E_o) the scaffold:

1. $\sigma_{\mathrm{hydro}} > \sigma_{\mathrm{buf}} \Rightarrow E_i < E_o$.
2. $\sigma_{\mathrm{hydro}} < \sigma_{\mathrm{buf}} \Rightarrow E_i > E_o$.
3. $\sigma_{\mathrm{hydro}} = \sigma_{\mathrm{buf}} \Rightarrow E_i = E_o$.

This behaviour is in agreement with the current conservation law underlying the modelling approach (Eq. (2.18)). As the normal component of the current density has to be continuous at the material interface, a higher conductivity of the hydrogel has to lead to a smaller normal component of the electric field at the hydrogel surface and vice versa. Regarding the influence of the individual parameters, the field depends on the hydrogel conductivity for a wide frequency range (not shown). Solely at high frequencies, the field is influenced by the hydrogel permittivity and the buffer conductivity. This influence becomes visible by slight changes in the field strength at the edges of the hydrogel, where it is in direct contact with the surrounding medium. I do not expect any influence of this comparably small effect on the cell stimulation. The total impedance of the stimulation chamber is unaffected by a changing hydrogel conductivity or permittivity (not shown). In turn, this means that a possible change of the dielectric properties of the hydrogel cannot be monitored in situ. This is the same result as for the case without a hydrogel (Sec. 6.3.1).

To quantify the influence of the hydrogel properties at different stages of the experiment, I analysed the induced transmembrane potential of a single cell for three different configurations (see Fig. 6.11):

- an elongated, flat cell corresponding to initial cell adhesion to the hydrogel [301],
- the transition to spherical cell shape (half grown-in),
- a fully embedded spherical cell, which is the desired shape supporting chondrogenesis [176].

The latter configuration corresponds to either an encapsulated cell shown in direct cell printing or to cells migrated into the hydrogel. The geometry used in this model corresponds to a 3D cell culture, which mimics the conditions inside the native tissue better.

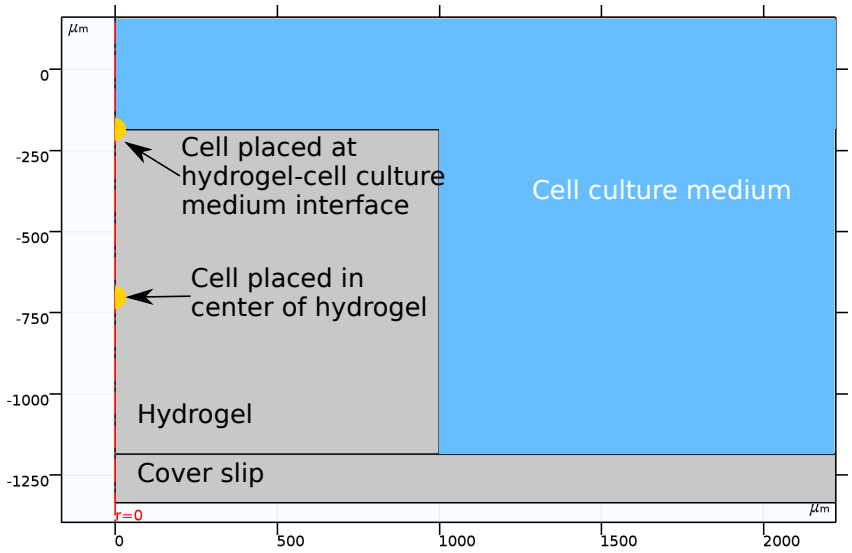

Figure 6.11: Segment of the Brighton model geometry with a hydrogel placed on the bottom of the well. The different locations of single cells placed in the model are indicated. An elongated, flat cell and the half grown-in spherical cell were placed at the hydrogel-medium interface to model initial adhesion and ingrowth. A fully embedded spherical cell was placed in the center of the hydrogel. The figure was taken from the supplementary material of [91] and adapted.

I found only slight differences of the induced transmembrane potential with respect to the cell shape and location. Thus, I show here only the result for a spherical cell centred in the hydrogel (see Fig. 6.12). The results indicate that a cell seeded on or placed inside the hydrogel will be stimulated less with increasing hydrogel conductivity (Fig. 6.12a). For all cell geometries, the transmembrane potential appears to increase significantly only for frequencies above 100 kHz. The UQ analysis reveals that only the conductivity of the hydrogel has an impact on the transmembrane potential up to about 100 kHz (Fig. 6.12b). From 100 kHz on, the 90% prediction interval becomes very broad and extends up to 0.4 mV for a mean value of about

0.2 mV. In the regions where the prediction interval is broad, the variance of the transmembrane potential is mainly caused by the cellular dielectric properties.

Nevertheless, there are slight differences between the different cellular configurations. As could be expected, the membrane region exposed to the cell culture medium is influenced more by the conductivity of the culture medium than by the hydrogel conductivity. Geometrically, this applies to the adherent, elliptical cell and the half grown-in spherical cell. The cytoplasm conductivity, which has an influence at frequencies greater than 100 kHz for the spherical embedded cell, does not impact the transmembrane potential of an adherent elliptical cell at these high frequencies. Instead, only the membrane permittivity plays a role. In general, both sides of the elliptical cell experience a similar change in the transmembrane potential. Once the cell is partially immersed in the hydrogel, the cytoplasm conductivity plays a role (i.e., for the half grown-in spherical cell). I found that the transmembrane potential of a cell close to the hydrogel-medium interface resembles the transmembrane potential of a cell centred in the hydrogel. As the half grown-in cell and the adherent elliptical cell are rather artificial configurations, the embedded spherical cell is probably the most realistic configuration. Thus, the results shown in Fig. 6.12 can be understood as representative.

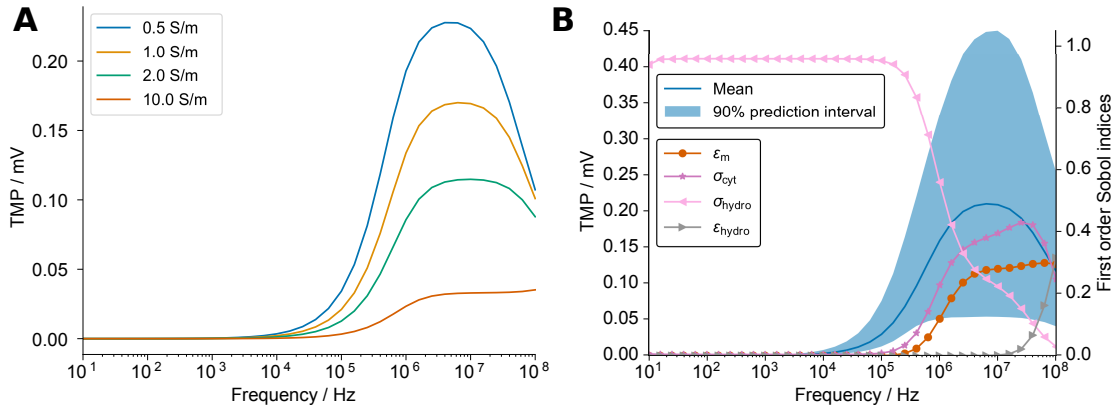

Figure 6.12: In **A**, the transmembrane potential is shown for a varying hydrogel conductivity. In **B**, the mean value and 90% prediction interval for the transmembrane potential (TMP) is shown together with the Sobol indices for the scanned parameters of the Brighton model with the cell located at the center of the hydrogel. While the hydrogel conductivity σ_{hydro} has a large influence for frequencies below 1 MHz, at higher frequencies, cytoplasm conductivity σ_{cyt} and membrane permittivity ε_{m}) contribute substantially. The hydrogel permittivity ($\varepsilon_{\mathrm{hydro}}$) has an impact only at very high frequencies. Tested parameters whose Sobol index does not exceed 0.1 over the entire frequency range are not shown for the convenience of the reader. The figure was generated from figures taken from [91].

The individual influence of the hydrogel conductivity on the transmembrane potential is highlighted in Fig. 6.12A. A conductivity of $10\,\mathrm{S\,m^{-1}}$ was considered as

a boundary case, which would correspond to a hydrogel conductivity about ten times greater than the bovine articular cartilage conductivity [302]. The simulation result implies that only in a narrow high-frequency region above 1 MHz the hydrogel conductivity substantially affects the transmembrane potential when subjected to the capacitive electrical stimulation investigated in this work. As expected from the dependence of the electric field on the hydrogel conductivity, the transmembrane potential decreases with increasing hydrogel conductivity.

In comparison to the benchmark of a single adherent cell (compare Fig. 6.8B), it becomes evident that the transmembrane potential of a cell on/in a hydrogel can reach a similar magnitude in the mV-range. However, this magnitude is only reached at higher frequencies greater than 100 kHz. For an adherent cell, the transmembrane potential is mostly influenced by the dielectric properties (see previous section, Fig. 6.8B). Hence, it cannot directly be influenced by varying the conductivity of the cell culture medium. Using electrically conductive hydrogels, it becomes feasible to optimise the effect of the electrical stimulation for cells seeded on or embedded in the hydrogel. Altering the electrical conductivity of the hydrogel to values lower than the surrounding medium could be a tool to increase the transmembrane potential while higher conductivity values would cause a decrease of the transmembrane potential.

6.3.6 Theoretical considerations regarding cellular organisation

I investigated the effect of the hydrogel properties on the real part of the Clausius–Mossotti factor (Eq. (2.5)), which is a measure of the dielectrophoretic force on the cell. For spherical cells, there exists an analytical formula to compute the complex permittivity of the cell $\hat{\varepsilon}_2$. Limits of the model parameters for eukaryotic cells are known from the literature [293]. These limits (Tables 6.5 and 6.6) served as the input of the UQ study.

The Clausius–Mossotti factor can be understood as a relative force, the sign of which indicates whether a cell would experience a force in direction of lower (negative sign) or higher (positive sign) field strengths. It has been argued that cell deformation would also follow this force [172, 303, 304]. However, recent research has suggested that the eventual cell shape upon deformation cannot be entirely predicted by only the Clausius–Mossotti factor [175, 177].

Considering the theoretically possible values for eukaryotic cells [293], which includes chondrocytes but also others such as mesenchymal stem cells, and the desired values for hydrogels (see Table 6.4), I found that the mean value of the real part of the Clausius–Mossotti factor remains negative for most of the frequencies (see Fig. 6.13). Only between 1 MHz and 100 MHz, the probability that it assumes a positive value is largely increased as its value may become greater than zero. In this frequency window, the permittivity of the membrane and the conductivities of

the hydrogel and the cytoplasm need to be known precisely to determine the sign of the Clausius–Mossotti factor reliably.

Table 6.5: Assumptions for the dielectric properties of eukaryotic cells as reported in [293]. The uniform distribution is denoted by $\mathcal{U}$.

Domain (subscript)	Conductivity in $\mathrm{S\,m^{-1}}$	Rel. permittivity
Membrane (m)	$\mathcal{U}(8 \times 10^{-8}, 5.6 \times 10^{-5})$	$\mathcal{U}(1.4, 16.8)$
Cytoplasm (cyt)	$\mathcal{U}(0.033, 1.1)$	$\mathcal{U}(60, 77)$
Nuclear envelope (ne)	$\mathcal{U}(8.3 \times 10^{-5}, 7 \times 10^{-3})$	$\mathcal{U}(6.8, 100)$
Nucleoplasm (np)	$\mathcal{U}(0.25, 2.2)$	$\mathcal{U}(32, 300)$

Table 6.6: Assumptions for the geometric properties of eukaryotic cells as reported in [293]. Note that instead of the explicit nucleus radius R_n, a scale parameter was introduced such that $R_\mathrm{n} = \mathrm{scale} \cdot R_\mathrm{c}$. This ensures that the nucleus radius is always less than the cell radius. The uniform distribution is denoted by $\mathcal{U}$.

Parameter	Symbol	Probability distribution
Cell radius	R_c	$\mathcal{U}(3.5, 10.5)$ µm
Membrane thickness	d_m	$\mathcal{U}(3.5, 10.5)$ nm
Scale	scale	$\mathcal{U}(0.28, 0.84)$
Nuclear envelope thickness	d_n	$\mathcal{U}(20, 60)$ nm

The negative real part of the Clausius–Mossotti factor indicates that it is very likely for eukaryotic cells immersed in electrically conductive hydrogels to be attracted by regions of lower field strengths. As highlighted in the previous section, hydrogels, which have a conductivity less than the surrounding cell culture medium, will be regions of higher field strengths. Hence, cells seeded on the top side of the hydrogel might experience a repelling force that prevents them from growing into the scaffold. Cells inside the scaffold might also be guided to certain regions of the hydrogel if the externally applied field is non-uniform. Devices delivering non-uniform fields have been developed in the SFB 1270 ELAINE [44].

In the Taghian and the Brighton geometry, the electric field is uniform. Cells can be deformed but not moved in uniform electric fields. Aranda *et al.* have suggested a morphological diagram of lipid vesicles exposed to AC fields [175]. Depending on the conductivity ratio between cytoplasm and external conductivity (e.g., the hydrogel or cell culture medium) and the frequency, different vesicle shapes are to be expected. Lipid vesicles can be understood as a model system for cells. Translating the results for lipid vesicles to the case of cells embedded in a hydrogel means that a hydrogel conductivity similar to the usual cell culture medium or even greater could

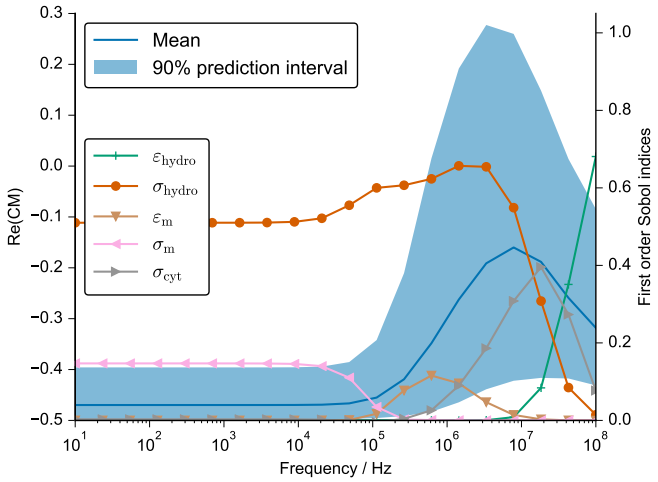

Figure 6.13: Mean value and 90% prediction interval for the real part of the Clausius–Mossotti factor, Re CM (left axis), shown together with the Sobol indices for the parameters, which were considered in the UQ analysis (see Tables 6.5 and 6.6). The figure was taken from the supplementary material of [91] and adapted.

lead to a mechanical deformation perpendicular to the field for frequencies roughly between 10 kHz and 10 MHz. This translation relies on the assumption that the expected conductivity of the cytoplasm is at least three times (for general eukaryotic cells [293]) to ten times (for chondrocytes, see Table 6.2) smaller than the usual conductivity of the cell culture medium, which is about $1.5\,\mathrm{S\,m^{-1}}$. The deformation could result in a round cell shape because it counteracts adhesion to the hydrogel fibres that are aligned along the field vector for the considered chambers. This hypothesis is supported by the observation that capacitive coupling stimulation leads to rounder cell shapes [43]. Moreover, the deformation could lead to the activation of stretch-activated channels, as observed in electrical stimulation experiments with physiological inhibitors [71, 305]. Future experimental research is needed to analyse if the force due to the external field is sufficiently large to substantially affect the cells (i.e., if cell migration or deformation occur). The main differences of the stimulation chamber considered here and setups to rapidly organize cells is the exposure time and field strength. While the cellular organisation [170] or deformation [303, 304] takes place in a few minutes and uses field strengths in the range of $\mathrm{kV\,m^{-1}}$ or even higher, the stimulation of cell cultures usually happens for considerably longer period of times and is applied repeatedly at field strengths of $\mathrm{V\,m^{-1}}$ [41, 43, 116]. Thus, the forces are expected to be at least one order of magnitude smaller but act continuously. To obtain a better understanding of the interaction between the cells and the hydrogel, mechanical models are required. They should explain, for example, why and how a certain channel size in printed scaffolds influences the cell

shape [306]. Due to the rather complex microstructure of the hydrogels and the biological interaction of the cells with the hydrogel fibres, this task currently seems to not be accomplishable with the existing models. A first approach could be to use numerical implementations of models relying on electrohydrodynamics or mechanical membrane models [177] assuming cells in an isotropic medium.

6.3.7 Discussion

The goal of this chapter was to find an accurate numerical method to estimate the effect of capacitive coupling stimulation on individual cells. The thin layer approximation is suitable to estimate the induced transmembrane potential not only when the cells are surrounded by conductive liquid [146] but also when they are in close contact with a substrate. Thus, an accurate but computationally efficient approach is available to estimate the effect of capacitive coupling stimulation. Furthermore, simulations of realistic 3D geometries are feasible. The thin layer approximation reduces the computational cost so that a sensitivity analysis of the model by UQ techniques becomes easily feasible. UQ techniques require a frequent repetition of the simulation run to sample the parameter space. Nevertheless, the total runtime of the UQ study with the approximate model was eventually of the same order as the runtime of the full-fidelity model. During the numerical experiments another advantage appeared. If the membrane is fully discretised, the ratio between the small elements of the discretised membrane and the larger elements in the rest of the domain makes the system hard to solve for low frequencies [287]. In particular, ill-shaped triangles may occur, which increase the condition number of the system matrix and hence negatively affect the employed solver. In *COMSOL*, this was indicated by a refinement warning. This warning was not raised with the thin layer approximation, which in this sense appears to be numerically more stable. The exact implementation in *COMSOL* and thus accuracy of the underlying numerical method is not known. However, the use of second-order Lagrange finite elements in *COMSOL* suggests that a third-order accurate computation of the transmembrane potential for sufficiently smooth solutions can be expected [204, 229, 284] (compare also Appendix A.3). Thus, I would expect the thin layer approximation to be theoretically more accurate than finite differences approaches [307] or first-order FEM approaches [308, 309].

To identify how accurate the considered FEM approach can represent the experimental situation, experimental validation is required. Impedance spectroscopy is a tool that permits the determination of the linear electric properties of the entire system. By comparing the computed and the measured capacitance of the capacitive coupling stimulation chamber, validation of the numerical model becomes feasible. In this sense, the capacitance corresponds to the resistance that has been identified as the characteristic property of direct contact stimulation chambers in Chapter 5. However, the UQ analysis of the impedance and the corresponding electric field

revealed that a measurement of the impedance is not sufficient to reliably monitor the applied electric field. Hence, the currently used capacitive coupling stimulation chambers cannot be used with the digital twin approach, which was introduced in the previous chapter. Other experimental approaches are required to overcome this limitation and to eventually monitor the applied electric field and its effect.

For example, fluorescence microscopy with the help of potentiometric dyes could be used to measure the induced transmembrane potential. For direct contact stimulation with much larger field strengths as used in capacitive coupling, numerical simulations could be validated by fluorescence spectroscopy experiments [146]. Moreover, this experimental approach permits to assess the spatial dependency of the transmembrane potential. The numerical results suggest that the spatial dependency of the transmembrane potential depends on the dielectric properties of the cell membrane and cell cytoplasm. Furthermore, measurements of the transmembrane potential at low frequencies in the Hz range could answer if the cutoff effect due to the finite membrane conductivity exists. Based on the results of my simulations, no significant transmembrane potential should be induced at these frequencies upon external stimulation. In contrast, previous numerical studies [121, 286] have predicted an induced transmembrane potential even for frequencies approaching 0 Hz because they used the idealised assumption of a perfectly insulating membrane. Upon varying the membrane conductivity, it seems that there exists a cutoff frequency that depends on the membrane conductivity. Through a UQ analysis the sensitivity of the computed transmembrane potential with respect to multiple parameters could be identified. This improves a previous approach [121], where the influence of one parameter at a time but not the combined influence of many input parameters has been studied. Thus, measuring the transmembrane potential could also be used to infer dielectric properties or detect changes in the physiological state of the cells, which manifest themselves in changes of the dielectric properties. Besides the small field strengths and thus small transmembrane potential values, the high frequencies of the capacitive coupling fields in the kHz range pose a challenge for such optical validation approaches. An alternative experimental approach could be local impedance measurement. Recently, impedance measurements of single cells at 2 Hz using optical methods have been demonstrated [264]. The experimental results could qualitatively be explained by numerical simulations. With progress in this field, experimental validation of numerical models also at higher frequencies could become feasible. The common cell models for capacitive coupling stimulation [121, 286] rely on the assumption that the cell membrane is in direct contact with the insulator. Introducing a small gap between the cell and the electrode had a similar effect as increasing the membrane conductivity. Hence, I speculate that an adhesion gap between cells and the insulator, which is filled with a conductive electrolyte, also leads to a cutoff effect. Due to limited availability of experimental data, I did not further investigate the model with the gap and the influence of its geometrical and dielectric properties on the model result. For future experimental validation approaches, it should be

kept in mind that the gap might play a significant role and thus should be carefully quantified. Moreover, it is to be clarified if and how the measurements are possible when hydrogels are involved. Similar to the adhesion gap, electrically conductive hydrogels lead to a rather high cutoff frequency in the range of 100 kHz.

From a theoretical point of view, the UQ analysis can be simplified as presented here. By studying a simple, reduced system such as the 2.5D model of a hemispherical cell, the influence of multiple parameters can be studied. Eventually, individual parameters can be omitted in UQ analyses of more complicated and computationally expensive models if they do not reveal a significant influence on the reduced, cheaper model. However, this choice cannot be generalised but must be made dependent on the known or assumed parameter uncertainties. In the case of parameter uncertainties chosen in accordance with previous works (see Table 6.1), the cytoplasm conductivity and coating permittivity had a significant influence in certain frequency regions. In contrast, both parameters had no influence in the case of uncertainties inferred from experimental parameters (see Table 6.2). Thus, the choice of which particular parameters to omit in the analysis of a more sophisticated model cannot be answered in general.

The magnitude of the transmembrane potential changed significantly when the assumptions on the material properties were altered. In any case, it was in the mV range that is assumed to possibly have a biological effect [141, 310]. In the case of chondrocytes and related stem cells, the biological effect corresponds to a reduced de-differentiation [23, 41] and enhanced chondrogenic differentiation [71]. It is to be investigated if the induced transmembrane potential is sufficiently large to trigger voltage-gated channels in chondrocytes, which have been identified as crucial for signal transduction in chondrocytes stimulated by capacitively coupled fields [116]. Patch-clamp recordings could be used during the stimulation to detect the excitation of voltage-gated channels [311]. However, it has to be ensured that the stimulus signal does not overlay the patch-clamp recordings. Ideally, reliable transmembrane potential thresholds can be determined such that validated numerical simulations can be used to tailor the stimulation regarding the experimental reality (i.e., geometry, bio/electro/chemical environment).

When a leaky membrane (i.e., a membrane that permits a leakage current due to a non-zero conductivity) is considered there exists the aforementioned cutoff frequency below which the transmembrane potential tends to zero. Above this frequency, the transmembrane potential assumes a value that could be physiologically relevant. Thus, I speculate that the electrical stimulation should not be effective below the cutoff frequency. Indeed, finding a suitable stimulation protocol is a frequent research objective [23, 41, 118]. The approach considered here could facilitate the choice of the right frequency. For a cell membrane conductivity of down to $10^{-7}\,\mathrm{S\,m^{-1}}$, the stimulation frequency should be above 1 kHz (Fig. 6.6). For chondrocytes, a frequency above 10 kHz but not exceeding 100 kHz could be most efficient (Fig. 6.8B). This conclusion is in good agreement with the experimental findings [41] justifying the

establishment of 60 kHz as the stimulation frequency in capacitive coupling electrical stimulation. Furthermore, a decrease of the transmembrane potential with increased membrane conductivity could be found experimentally for DC stimulation [312]. The membrane permittivity does not contribute to the cutoff effect. It only leads to a change of the transmembrane potential value. When the cells are in contact with an electrically conductive hydrogel, an effect on cells inside a hydrogel due to a change in the transmembrane potential seems unlikely based on the numerical results. Frequencies in the MHz-range, for which I found the transmembrane potential to reach biologically relevant values in the mV range, have yet not been considered in cartilage tissue engineering. They could be tried in the future when conducting experiments with electrically conductive hydrogels. A frequency of about 5 MHz could be optimal to verify the hypothesis that an induced change in the transmembrane potential causes the biological effect. Nevertheless, I would like to mention that a technical realisation of a stimulation system with a frequency in MHz-range might be complicated by stray capacitances and other undesired influences. Moreover, it might be necessary at high frequencies to add, for example, the cell nucleus to the model. Most likely, the cell nucleus can be treated in a similar fashion as the cell (i.e., the nucleus membrane can be described by the thin layer approximation).

A 3D model of two hemiellipsoids in close proximity, which approximately represents adherent cells [146], could shed light on the interaction of cells in a capacitive coupling setting. As there was no difference in the induced transmembrane potential between the two cells, they evidently do not seem to influence each other during the stimulation. Nevertheless, I only chose the frequency that has often been used in capacitive coupling experiments. Furthermore, only the conductivity and permittivity of the cell membrane as key parameters for estimating the transmembrane potential were considered in the UQ analysis. These two simplifications reduce the complexity of the UQ analysis considerably and make it possible to tackle such a complex model. There was no preference of a meridian and in general no strong dependence of the transmembrane potential on the location on the cell membrane (Fig. 6.10). Unlike in the case of spherical cells in an external field [146], this transmembrane potential does not have poles where it becomes zero. I assume that this is due to the difference in stimulation and the direct contact of the cells with the insulating coating layer. For all configurations studied in this work, the transmembrane potential was greater along the cell bottom than at the top side of the cell. Without experimental evidence it remains unclear whether this can be related to the biological effect of the electrical stimulation. The relative permittivity of the cell membrane strongly influences the transmembrane potential at the relevant frequency of 60 kHz. A comparison of different cell types with different membrane permittivities would be an interesting subject for further research in order to demonstrate whether the stimulation effect can be related to this parameter. The 3D model describes the case of rather freshly seeded cells that have not yet grown into a monolayer. For such cases, different models have to be built based on imaging data. Subsequent tests

will then demonstrate whether the observation also holds true for different distances between the cells and multiple, irregularly shaped cells potentially interacting with each other.

A limitation of the thin layer approximation is the simplification of the cell membrane. In the models presented here, the cell membrane is a perfectly smooth thin layer with a fixed conductivity. At high frequencies in the upper MHz-range, the dielectric properties of the membrane can become frequency-dependent [290]. I did not account for this relaxation, which has a characteristic relaxation frequency of about 180 MHz. The dielectric properties of chondrocytes have not been measured at such high frequencies to the best of my knowledge. In future works, the membrane relaxation can be straightforwardly integrated into the FEM approach by using frequency-dependent membrane conductivity and permittivity described by a relaxation model (e.g., the Debye model [290]). For the UQ analysis, the uncertainty of the parameters of the relaxation model can be considered. A nonlinear, transmembrane potential-dependent description of the membrane conductivity is common to model electroporation [313]. Then, the conductivity would become time-dependent. I do not expect electroporation during capacitively coupled stimulation. Thus, I did not use a nonlinear conductivity. In principle, the structure of Eq. (2.21) permits to assign position-dependent conductivity, permittivity or thickness values on the membrane. This could be exploited to account for stochastic fluctuations of the dielectric and geometric properties of the membrane. Alternatively, models using a rough membrane could be considered. Such models could, for example, contain membrane protrusions [314] or an oscillating membrane thickness [315].

Furthermore, optical measurements could clarify if there is a mechanical deformation or interaction between the cells. This would support the development of mechanical models, which could for example be used to tune stimulation parameters such that a beneficial cell shape is fostered by electrical stimulation. Furthermore, models are needed for the dynamic behaviour of the membrane as constituents of the membrane can rearrange under the influence of the external field [160, 316]. The development of theoretical multiphysics models requires the performance of experimental studies on the mechanisms of interaction. A great contribution would be a clarification of the question whether voltage-gated [116] or other channels are involved in the signal transduction. This could lead to multiphysics models including, for example, ion dynamics [317] or the mechanical behavior of the membrane [318, 319]. Furthermore, the adhesion of chondrocytes and resulting gaps between cell membrane and insulator should be investigated to provide reliable geometric models of cells in capacitive coupling stimulation chambers. Another possible effect of the electric field could be heating. The frequency of 60 kHz falls into the radiofrequency range. Frequencies in this range (however usually about 500 kHz) are used for thermal tissue ablation [320]. The thermal effect of the electric field in this frequency range is mainly influenced by the conductivity [321]. Considering the conductivity of the cell culture medium, its volume and the reported field strength, the applied power is

in the range of a few µW. This is far below the usually applied power of considerably more than 1 W [320, 321]. Thus, no significant thermal effect of the electric field is to be expected. This result is in line with the results for direct stimulation shown in Sec. 5.1, where no temperature change due to the electrical stimulation could be recorded.

An additional possibility to improve certain aspects of the electrical stimulation are hydrogels with a tailored conductivity. The conductivity of the hydrogels can be chosen to yield, for example, a higher field strength in the vicinity of the cells or to induce a defined deformation. The numerical results suggest that a conductivity less than the cell culture medium conductivity could beneficially contribute to an increased change in the transmembrane potential. In contrast, the mechanical effect could be promoted by hydrogels with a conductivity greater than the cell culture medium conductivity. Nevertheless, the interaction of the hydrogels with the chondrocytes depends on the structure of the hydrogel. For example, in the case of fibrous collagen scaffolds, the scaffold fibres should have a smaller diameter than the cells to ensure a spherical cell shape [322] that is beneficial for chondrogenesis [176]. Spherical chondrocytes have occurred dominantly in sponge-like collagen scaffolds [322]. As the hydrogel conductivity is achieved by adding a dopant or a conductive filler to the basic hydrogel [268, 323, 324], the chemical cell–hydrogel interaction should be taken into account. Furthermore, increasing the conductivity of the hydrogel might lead to a changed osmolarity that is caused by an increased fixed charge density in the hydrogel [103]. Chondrocytes react to changes in osmolarity [325], which might mask the effect of the electrical stimulation, and may give in combination with electrical stimulation an exciting field for future research of cartilage tissue engineering assisted by electrical stimulation using electroactive hydrogels. An aspect that should not be neglected is the change of the hydrogel conductivity in aqueous solution with time [269]. To be able to detect these changes, a digital twin of the capacitive coupling stimulation chambers should be found. For that, the impedance of the electrode insulation, which is used in the currently considered chambers, has to be drastically reduced to gain access to the dielectric properties of the cell culture medium and hydrogel.

Simplistic computational cell models such as the models considered here are commonly used across different communities [121, 146, 286, 307, 309, 326, 327]. More sophisticated models including a large number of cells require large high-performance-computing facilities [328]. For types of tissue such as cartilage, where the volume fraction of the cells is small and the distance between the cells is rather large [329, 330], models including few or only one cell might be sufficient. This topic is addressed by detailed 3D models that will be presented in the following chapter.

7 Modelling of cartilage tissue at multiple scales

7.1 The status quo

The dielectric properties of cartilage have not been widely investigated in the frequency range below 1 MHz, which is relevant for cartilage tissue engineering. However, the conductivity at low frequencies and for DC has been investigated [302, 331, 332]. It has been shown that the conductivity of articular cartilage is about $0.6\,\mathrm{S\,m^{-1}}$ to $1.0\,\mathrm{S\,m^{-1}}$ at 1 kHz when the tissue had been equilibrated in Ringer's solution [331]. In contrast, the conductivity depended on the fixed charge density when the tissue had been immersed in distilled water. Binette *et al.* have found that the conductivities of bovine cartilage tissues are frequency-independent between 10 Hz and 1 kHz and are about $0.88\,\mathrm{S\,m^{-1}}$ to $1.14\,\mathrm{S\,m^{-1}}$ [302]. Gu *et al.* have investigated the dependence of the DC conductivity on the water content [332]. They have found a linear relationship with values ranging between $0.5\,\mathrm{S\,m^{-1}}$ to $1.1\,\mathrm{S\,m^{-1}}$. In the aforementioned works, the relative permittivity has not been considered. As the conductivity is similar to cell culture media, it can be assumed that cartilage behaves as a resistor at low frequencies. Thus, the permittivity is not necessarily required to build a model if the imaginary part $\omega\varepsilon$ is small compared to the conductivity (see Secs. 2.3.3 and 5.1).

Nevertheless, other resources suggest the existence of a so-called α-dispersion, which manifests itself by a huge low-frequency permittivity. For example, the popular parametric model by Gabriel *et al.* [333] predicts a notable α-dispersion for a large number of tissues including cartilage (see Fig. 7.1). However, the conductivity predicted by the Gabriel model is not in agreement with the aforementioned conductivity measurements (Fig. 7.1). In addition, there exist other reasons to reassess the Gabriel model. Before returning to cartilage tissue, I will re-analyse the Gabriel data to address in particular the low-frequency dielectric properties of biological tissue in general. To develop reliable numerical models for electrical stimulation approaches in regenerative medicine, an unambiguous understanding of the dielectric properties at the considered low frequencies (usually below 100 kHz) is required.

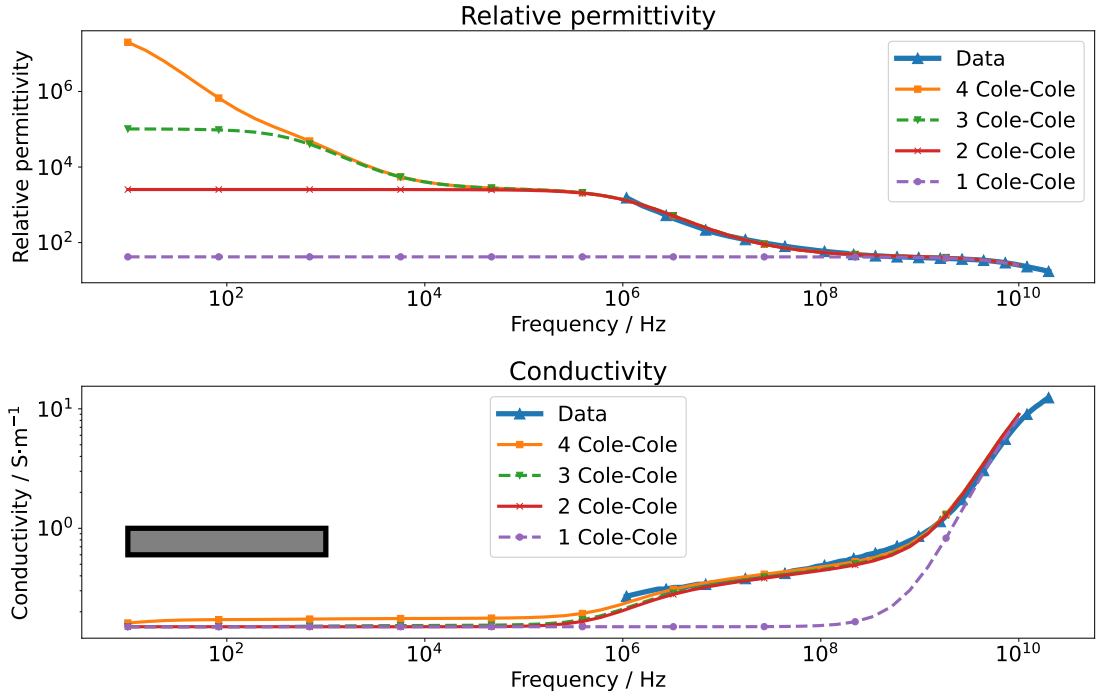

Figure 7.1: The dielectric properties data of cartilage measured by Gabriel *et al.* [334] are compared to different Cole-Cole models using the parametric Gabriel model [333]. While the cartilage data were only recorded from 1 MHz to 20 GHz, the parametric model is formulated for the entire frequency range originally considered for experiments by Gabriel *et al.* [237]. In the original publication, it has been explained that the sample size of cartilage had not been sufficient to be measured at low frequencies. To highlight the individual contribution of each dispersion, the Cole-Cole model is evaluated for four (original Gabriel model), three, two and only one dispersion (see Eq. (7.1)) using the parameters from [333]. The dispersion at the lowest frequencies (i.e., the 'fourth' dispersion, which is most evident in the relative permittivity) is often referred to as α-dispersion. The successive dispersions are accordingly called β-, γ-, δ-dispersions. For comparison, the conductivity range of cartilage recorded at low frequencies is shown (grey rectangle with black frame) [302, 331].

7.2 Reassessing the Gabriel database

The following section is based on the paper "Ambiguity in the interpretation of the low-frequency dielectric properties of biological tissues", which appeared in Bioelectrochemistry [236][1].

[1] I conceptualised the study, developed the software, analysed the data, prepared all figures and wrote the original draft. Ursula van Rienen acquired the funding, supervised the project, provided all resources, and contributed to the final manuscript.

In 1996, Gabriel *et al.* laid the foundations for the current state of knowledge on dielectric properties for a large number of tissues with an initial literature survey [335] and subsequent experimental studies [237, 334]. The authors performed EIS to characterise excised tissues, which were mainly ovine. Based on the literature and experimental data, they developed a parametric model of the dielectric properties of biological tissues over a wide frequency range from 10 Hz to 100 GHz [333]. This model is still in use and serves, for example, as the basis for the IT'IS database of dielectric properties [336]. The parametric model for cartilage and other tissues relied only on literature data in the low-frequency range. Hence, Gabriel *et al.* published a study on the low-frequency conductivity of various tissues in 2009 to update their previous study from 1996 [337]. Cartilage was not considered in this update and the permittivities of the tissues were not reassessed. In any case, a key observation in the parametric model of Gabriel *et al.* is that the majority of the tissues exhibit a large dispersion at very low frequencies ($< 1\,\mathrm{kHz}$), which manifests itself in a large permittivity and a decreased conductivity [333].

For some tissues (e.g., cartilage and brain tissue), this contrasts other studies that have reported a frequency-independent conductivity at low frequencies [302, 331, 338]. From a technical point of view, the low-frequency conductivity measurements have been carried out using a four-electrode setup while Gabriel *et al.* have used a two-electrode setup. For example, in vivo measurements of brain tissue using a four-electrode setup could not confirm a significant frequency dependence of the conductivity in the low-frequency range [338]. From a theoretical point of view, Bédard and Destexhe have criticised the experiments of Gabriel *et al.* for not only measuring the passive tissue properties but also the effects of ionic diffusion and electric polarisation, which arise due to charge accumulation at the ETI [339]. The criticism is based on a comparison of different biophysical models to Gabriel *et al.*'s parametric model of brain tissue (specifically grey matter) [333]. The biophysical models describe both a frequency-independent passive conductivity and a frequency-dependent conductivity due to ionic effects. As a result, it has been argued that the measurement electrodes employed by Gabriel *et al.* influenced the measured dielectric properties due to the aforementioned effects at the ETI. The four-electrode setup excludes such effects by construction.

Thus, I hypothesised that the Gabriel data could be analysed in a similar manner as the EIS data of the stimulation electrodes in Chapter 5. To test the hypothesis, an equivalent circuit that comprises an element to describe the ETI (e.g., a CPE) and an element that describes the tissue (e.g., a Cole-Cole model) could be considered. If there is an influence of the ETI, the CPE should have similar properties for all tissues because all tissues were measured with the same electrode. If not, the low-frequency dispersion would correspond most likely to the α-dispersion, which has been found in some tissues [194, 340–344]. However, there exists no clear understanding of its origin and it is often inaccessible because it is overlaid by the ETI impedance. To the best of my knowledge, there exists no experimental evidence of the α-dispersion in

cartilage. It has been reported that for some tissues the α-dispersion overlaps with the β-dispersion [343, 344] or is effectively hidden in the β-dispersion [341, 342]. In a study using a two-electrode setup as in the original work by Gabriel *et al.* together with an explicit correction of the ETI impedance, no low-frequency dispersion has been observed in excised human breast tissue starting from 40 Hz [345]. Gabriel *et al.* reported that features arising from effects at the ETI have been removed from the original experimental data [237, 333]. Nevertheless, they concluded in the original study that "it is possible that the dielectric parameters below 1 kHz may be undercorrected" [237]. In a graphical representation of the original experimental data of ovine grey matter [334] and the corresponding impedance data (Fig. 7.2), I found a low-frequency feature resembling a CPE, which is characteristic of electrode polarisation [102, 346] (compare also Chapter 5, for example Fig. 5.8 for a similar EIS spectrum). Moreover, the experimental impedance data are badly fit by the parametric model in the low-frequency range. All in all, the existing knowledge of tissue dielectric properties has to be revisited to close the knowledge gap for cartilage.

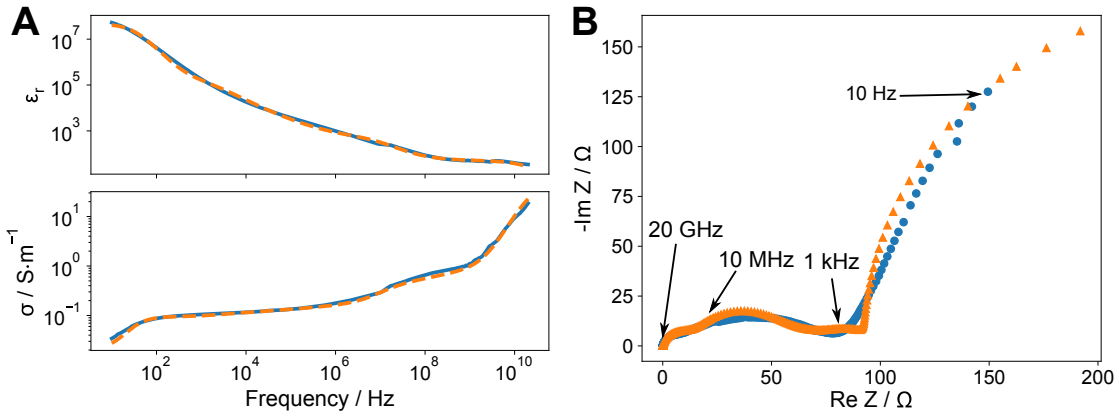

Figure 7.2: Graphical representation of Gabriel *et al.*'s experimental data and the corresponding parametric model for grey matter. (**A**) The experimentally obtained dielectric properties (relative permittivity ε_r and conductivity σ, blue solid lines) [334] are shown together with the corresponding parametric model data [333] (orange broken lines) over a wide frequency range. (**B**) The Nyquist plot of the respective impedance, which was computed assuming a unit capacitance of 1 pF (data – blue dots, model – orange triangles), with characteristic frequencies of the experimental data: characteristic CPE behaviour [102, 346] is evident in the very low-frequency range (1 kHz $> f >$ 10 Hz), while Cole-Cole dispersions can be identified at frequencies greater than 1 kHz. The parametric model describes the very low-frequency range by another Cole-Cole dispersion, which evidently does not fit the data well. The figure was taken from [236].

7.2.1 The Gabriel model

Gabriel *et al.* [333] suggested a parametric model for the complex permittivity $\hat{\varepsilon}$ consisting of four Cole-Cole dispersions describing dielectric relaxation and the static (ionic) conductivity σ_{DC} of the tissue

$$\hat{\varepsilon} = \varepsilon_\infty + \sum_{n=1}^{4} \frac{\Delta\varepsilon_n}{1 + (j\omega\tau_n)^{a_n}} + \frac{\sigma_{\mathrm{DC}}}{j\omega\varepsilon_0} \ , \tag{7.1}$$

where ε_∞ is the high-frequency limit of the relative permittivity, τ_n is the mean relaxation time of the n-th dispersion, $\Delta\varepsilon_n$ is the magnitude of the n-th dispersion and $a_n \in [0, 1]$ is a distribution parameter, which is related to a broadening of the dispersion.

7.2.2 Data analysis

The data of the original work by Gabriel *et al.*, which is used in this work, are available online and provide the frequency-dependent values of ε_r and σ [334]. For now, tissue data not covering the low-frequency range (i.e., also cartilage) are excluded from the analysis. More details of the tissues considered by Gabriel *et al.* can be found in the supplementary material of [236]. For the sake of brevity, I will show here only the results for ovine grey matter.

Under the assumption of an electrode with a unit capacitance of $C_0 = 1\,\mathrm{pF}$, the corresponding impedance was computed using Eq. (4.1) (Fig. 7.2). This capacitance is not related to a specific device. Nevertheless, it is a realistic value for bioimpedance electrodes because it could, for example, correspond to a parallel-plate capacitor of 1 cm diameter and 0.7 mm electrode spacing.

The data were analysed using the Lin-KK test (see Sec. 4.2.2). To identify frequency regions of valid data, the following criteria were defined: the relative differences should oscillate around 0%, should not become very large or show significantly different behaviour between real and imaginary part. These criteria were used to manually detect regions, where the data could be expected to be valid. After removing parts of the spectrum that did not comply with the aforementioned criteria, a second Lin-KK test was performed to confirm the validity of the EIS data. Only for the colon tissue, no valid range could be determined and it was excluded from the analysis.

The test results indicated tissue-dependent violations of the Kramers-Kronig relations in the low- and high-frequency region (not shown, the interested reader can find more details in [236]). The upper and lower bounds for the valid frequency range were not identical for the different tissues (not shown). For most of the tissues, the EIS data were valid from frequencies below 100 Hz on. Only bone marrow represents a special case with a considerably higher lower bound of 50 kHz. The upper frequency bound was above 100 kHz for all tissues but did not exceed 10 MHz. It must be noted

that for some tissues valid data could also be found if the lower bound was set to frequencies greater than 10 MHz (i.e., when the low-frequency range was entirely disregarded). This result is mostly due to the fact that in the original work three different impedance analysers were used. One device covered the range from 10 Hz to 10 MHz, while the other devices covered the high-frequency region. As this work focuses on the low-frequency region, I did not further consider these data.

7.2.3 Parameter estimation

I found that the tissue data in the valid frequency range can be fitted by a model using only two Cole-Cole dispersions. This can also be seen from the cartilage model (Fig. 7.1) where essentially two dispersions are dominating the dielectric properties at low frequencies. In the following, this model is referred to as '2 CC'. When using the equivalent circuit to account for the ETI, I modelled the tissue by the Havriliak-Negami (HN) model (Eq. (2.24)). In this case, the dielectric properties were computed from Eq. (4.1) after subtracting the interface impedance from the total impedance. When accounting for the ETI, the 2 CC model could have been used instead of the HN model to describe the tissue properties. However, I opted against this option because the 2 CC model has a greater amount of free parameters, which increases the probability of overfitting. The two models fitted both the impedance data and the dielectric properties very well (not shown, please be referred to [236]). Skin tissue was an exception that will not be discussed here.

A comparison of the dielectric properties of grey matter obtained by the two models is shown in Fig. 7.3. It is evident that the two models deviate strongly in the low-frequency region below 10 kHz. For the 2 CC model, the permittivity behaves oppositely to the conductivity: it increases with decreasing frequency. For the HN model, both permittivity and conductivity reach a plateau below a certain frequency. This behaviour could be found for all tissues under investigation (not shown).

Qualitatively, the models can be compared by characteristic parameters such as the high-frequency permittivities, dispersion magnitudes, relaxation times and static conductivities. The 2 CC model yielded a good fit with two dispersions in the µs and ms range. The HN model described only one dispersion in the µs range. The µs dispersion revealed permittivity magnitudes $\Delta\varepsilon_1$ of the same order (10^3) for both models. Regarding the static conductivities σ_{DC} predicted by the models, their values were significantly smaller in the case of the 2 CC model. The high-frequency permittivities ε_∞ were found to be at the same order of magnitudes.

The second dispersion of the 2 CC model, with relaxation times in the ms range and large permittivity magnitudes $\Delta\varepsilon_2$ in the range of 10^6, could be characterised by parameters a_2 close to one for all tissues indicating almost no broadening. In contrast, tissue-dependent broadening could be observed for the other dispersion. Likewise, the HN model predicted tissue-dependent broadening, which was indicated by a values considerably less than one. However, some EIS data could be fitted by

asymmetric, but not broadened dispersions ($a = 1$, $\beta < 1$). Except for lung tissue, the EIS data could be described either by broadened (Cole-Cole case) or asymmetric (Cole-Davidson case) dispersions but no true HN behaviour ($a < 1$, $\beta < 1$) was found.

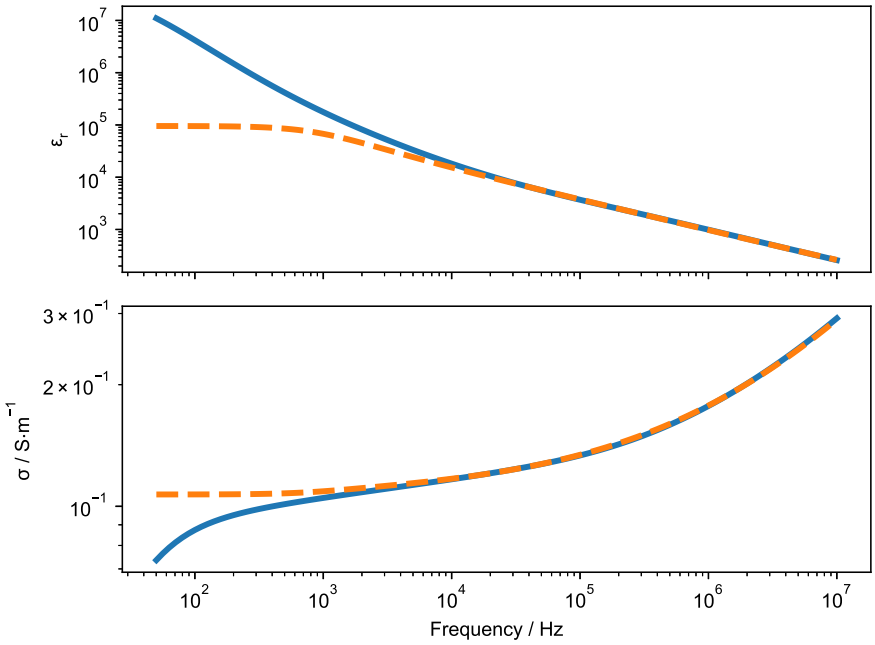

Figure 7.3: Fit results for the dielectric properties of grey matter in the valid data range. The data were fitted to a model using two Cole-Cole dispersions (2 CC model, blue solid lines) and the Havriliak-Negami (HN) model in series with an ETI model, respectively. The HN results (orange broken lines) correspond to the dielectric properties after removing the contribution from the ETI. The figure was taken from [236].

In general, I attempted to minimize the number of free parameters in the fit of the HN model to prevent overfitting. Hence, whenever the fit results suggested Cole-Cole or Cole-Davidson behaviour, I kept the value of a and β, respectively, fixed at 1.0. The same holds true for the charge transfer resistance, which I excluded from the fitting procedure when already the CPE together with the HN model described the data well. The majority of the tissue data could be fitted without taking into account the charge transfer resistance. The CPE exponent α was in the range 0.63 to 0.94 for all tissues whose spectra showed clear CPE behaviour. Half of the tissues could be identified by α between 0.7 and 0.8. The corrected dielectric properties (i.e., after removal of the CPE element) differed from the uncorrected properties at low frequencies in the Hz and kHz range. In this range, the corrected permittivity appeared decreased and the corrected conductivity appeared increased and almost frequency-independent (not shown). For bone marrow as well as wet and dry skin,

the results fell out of range. The reason was either a limited frequency range (bone marrow) or entirely different behaviour compared to the other tissues (skin). As skin is a very good resistor, this result is not surprising. Whenever the charge transfer resistance was required to fit the data, it ranged between 10^2 and $10^4\,\Omega$. Interestingly, this mainly applied to muscular and/or fibrous tissues such as aorta, cervix, muscle or tendon. For most of the tissues, the 2 CC model agreed well with the original Gabriel model (4 CC) for frequencies below 1 MHz. Indeed, Gabriel *et al.* modelled the low-frequency range with mean relaxation times in the ms and µs region [333] (see supplementary material of [236]).

Consequently, I compared the HN model to a modified 4 CC model, where the slowest dispersion in the ms range, which was not found in the HN model, was omitted. Moreover, I set the static conductivity of the modified model to the one of the HN model because the original 4 CC values were significantly smaller than the fitted HN values. This is physically feasible and does not require an adjustment of the relative permittivity according to the Kramers-Kronig relations, because the static conductivity does not depend on the frequency [3]. This modified model is called 3 CC model. An overview of the models considered in this work can be found in Table 7.1.

Table 7.1: Overview of the models considered in this work.

Model	Origin
2 CC	This work, fit to corrected data after Lin-KK test
3 CC	This work, based on original model of Gabriel *et al.* [333] with modified static conductivity and omitted ms dispersion
4 CC	Original model of Gabriel *et al.* [333]
HN	This work, fit to corrected data after Lin-KK test and removal of ETI effects

The comparison of the 3 CC and the HN model dielectric properties (Fig. 7.4A) shows excellent agreement of the conductivity in the frequency range below 1 MHz. However, the permittivity deviates slightly in this range with an overall similar trend. For the frequencies greater than 10 MHz, which were not considered for estimating the HN model parameters, both conductivity and permittivity are not in agreement though following roughly the same trend. In this frequency range, the 3 CC model is considerably more detailed than the HN model. Regarding the impedance (Fig. 7.4B), the models appear to not be in good agreement for frequencies greater than 1 kHz.

7.2.4 Discussion

The aim was to clarify if contributions from the ETI could be found in the EIS data of different biological tissues, which were reported by Gabriel *et al.* [334]. Tabulated

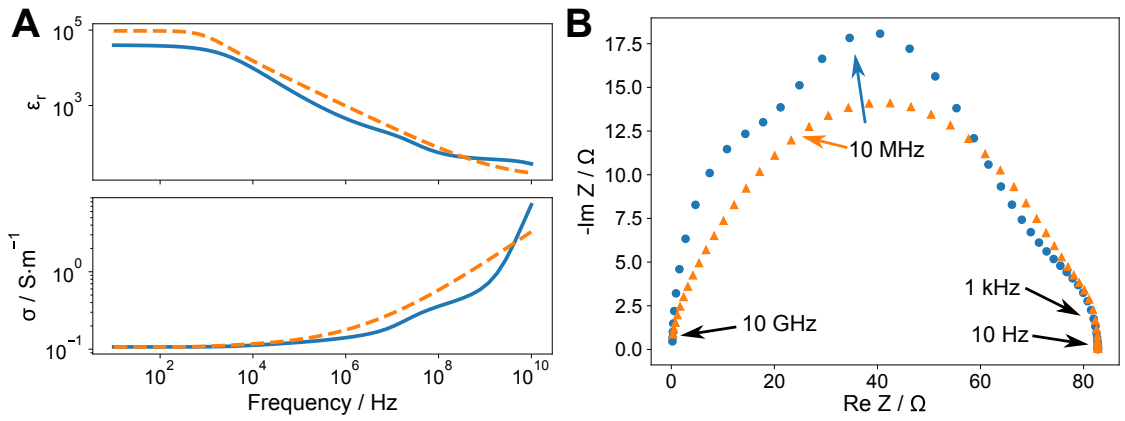

Figure 7.4: Comparison of the modified Cole-Cole (3 CC) and the Havriliak-Negami (HN) model for grey matter. The 3 CC model is based on the original model of Gabriel *et al.* (Eq. (7.1)) [333], which is modified by omitting the slowest dispersion and setting the static conductivity to the value of the HN model. (**A**) The dielectric properties for both models (3 CC – blue solid lines, HN – orange broken lines) are shown over a wide frequency range. (**B**) The Nyquist plot of the respective impedance: the HN model (orange triangles) is represented by a smooth curve resembling a depressed and asymmetric semicircle while the 3 CC model (blue dots) is represented by a superposition of individual depressed semicircles. The figure was taken from [236].

dielectric properties should not contain any contribution from the ETI because it depends on the electrode material and geometry. Instead, the interface impedance can be integrated into theoretical and numerical models using empirical relationships (see, for example, Chapter 5). I identified an ambiguity in the interpretation of the EIS data by Gabriel *et al.* at frequencies below 10 MHz. On the one hand, I could describe the data exclusively by intrinsic tissue properties. On the other hand, an established method to correct the unwanted interface contributions could be successfully applied.

Limitations were given by partial invalidity of the data at extremely low (<100 Hz) and high frequencies (>10 MHz). As a result, different frequency ranges had to be considered for the individual tissues. Nevertheless, most of the tissue data still revealed clearly separable features and the two data interpretations could be formulated. With both employed models, I could identify a dispersion with relaxation times in the µs range for all tissues.

This dispersion can be attributed to the β-dispersion described in the literature [194, 347]. It results from the charging of the biological membranes of cells and other structures inside the tissue (i.e., interfacial polarisation) [347]. The characteristic frequency of this dispersion, which can be computed from the mean relaxation time, is in the kHz to MHz range. As both models describe this dispersion and it has been extensively described in the literature, there exists no doubt that it describes

intrinsic tissue properties.

Another dispersion at frequencies below 1 kHz was well separated by this dispersion (Fig. 7.2). It can be interpreted ambiguously because it may stem from either tissue properties or from the electrode-specific ETI impedance.

On the one hand, this low-frequency dispersion could be described by a Cole-Cole dispersion with relaxation times in the ms range (or characteristic frequencies in the Hz range). In the literature, a dispersion with relaxation times / characteristic frequencies in this range has been referred to as α-dispersion [194, 340–344, 347–351]. It has been speculated for muscle tissue that it arises due to a polarisation of the sarcotubular system and/or counterion polarisation [340]. For heart and liver tissue, the disappearance of the α-dispersion during ischaemia has been linked to closing gap junctions [341]. Theoretical modelling of cells has also attributed the effect to localised charge layers at the cell membrane [350, 351] (i.e., counterion polarisation) or gap junctions connecting the cells [349]. Hence, the low-frequency dispersion that we found could reflect intrinsic tissue properties. It might also be explained by the state of the tissue because Asami has attributed the α-dispersion to perforated cell membranes in a study on erythrocytes [352]. Hence, the α-dispersion might only appear in excised but not in living tissue.

On the other hand, I could describe the ms dispersion by a circuit element, which models electrode polarisation. The latter was not to be expected because the data should not have contained such contributions. A technique to remove electrode polarisation effects, which relies on comparison of the measured tissue data to a NaCl solution of similar low-frequency conductivity, was originally applied before the data were analysed and reported [333, 334]. However, the remark in the original study that "it is possible that the dielectric parameters below 1 kHz may be undercorrected" [237] supports the interpretation that the reported low-frequency data still contained electrode contributions. Note that the measured low-frequency conductivity of electrolyte solutions using a two-electrode setup strongly depends on the electrode material and surface [108, 346]. This can be also seen from the results of Chapter 5.

Indeed, many studies where the electrode contributions have been removed either explicitly or by using a four-electrode setup have not reported a low-frequency dispersion similar to the α-dispersion. Here, I assume that – if not explicitly stated as, for example, by Logothetis *et al.* [338]– all experimenters using a four-electrode setup have investigated possible electrode polarisation effects, which may influence the low-frequency measurement data [101, 337, 353], by reference measurement in, for example, electrolyte solutions.

The data in the low frequency range have initiated discussions in the brain research community [338, 339, 354, 355]. Logothetis *et al.* [338] have found brain tissue to behave like a frequency-independent resistor at frequencies less than 5 kHz using a four-electrode setup, thus contrasting the Gabriel model. Theoretical considerations have been made to compare the approach of Logothetis *et al.* with the approach

of Gabriel *et al.* [339]. As a result, the frequency dependence observed by Gabriel *et al.* has been attributed to diffusion and polarisation effects due to the electrode. My results contribute to this discussion because I analysed the original experimental data and found potential electrode polarisation effects leading to the observed frequency-dependent conductivity. It is important to note that other studies supporting the results by Gabriel *et al.* have applied the same correction technique as used by Gabriel *et al.* [354]. A physically more straightforward approach has been suggested by Stoneman *et al.* [345]. They used – as also presented in this work – an algorithmic correction for the dielectric properties combining a CPE with an empirical dispersion function to model the tissue properties. The CPE exponent has been assumed to depend only on the electrode and is determined from a complex nonlinear least-squares fit to a reference electrolyte solution. The dispersion function used by Stoneman *et al.* is even more general than the HN model [356] and will be hereinafter referred to as universal model. For the analysis presented in this work, the HN model is more suitable because the universal model already includes CPE behaviour and has been applied when either the data have been corrected for electrode polarisation effects beforehand [356] or the CPE exponent describing the electrode polarisation has been determined before measuring the tissue sample [345, 357]. Their correction approach has been applied to excised human breast tissue dielectric properties measured from 40 Hz to 100 MHz [345] and, among others, to rat brain dielectric properties measured in vivo from 2 kHz to 100 MHz [357]. Their results resemble qualitatively the impedance data, which I analysed (Fig. 7.2), and the results of the correction approach (Fig. 7.3) (not shown). This indicates that the algorithmic correction technique is justified. Most notably, their uncompensated impedance spectra and dielectric properties resemble the raw data by Gabriel *et al.* The correction used in [345] leads to decreased permittivities and a constant conductivity at frequencies below 10 kHz (not shown). My results are in accordance with this finding.

The universal model has been designed such that it describes CPE-like asymptotic behaviour of the permittivity, which is not described by, for example, a Cole-Cole model or the HN model [356]. It is worth mentioning that the universal model does not describe a CPE-like asymptotic behaviour of the impedance (i.e., does not reveal a CPE-typical straight line in the complex impedance plane, see supplementary material of [236]). Instead, such asymptotic behaviour of the impedance has been attributed to electrode polarisation effects in [345, 357]. This supports my interpretation of the Gabriel data.

In view of the above-mentioned correction approach, the observed similar CPE exponent for different samples measured by the same electrode suggests that all tissue data (except for the skin tissues) may contain electrode-specific effects. The range of the CPE exponent fits very well to the reported range for platinum electrodes between 0.7 and 0.9 [107, 108]. A possible reason, why the CPE exponents differed between the tissues, could be, for example, modifications of the sputtered platinum electrode surface due to scratches or wear between the measurements.

There is more evidence in the literature that supports the necessity to remove ETI effects from the experimental data. The HN and the 3 CC model, which come without the influence of the potential interface effects, predict an almost frequency-independent conductivity below 1 kHz. This behaviour has not only been observed in the aforementioned conductivity measurements of brain tissue by Logothetis *et al.* [338]. The conductivity of freshly excised rat liver, muscle and skin tissue has not visibly changed between 100 Hz and 1 kHz [358]. The impedance spectrum of rat liver in vivo has been described by a single Cole-Cole dispersion between 1 kHz and 65 kHz [359]. The static conductivity of the Cole-Cole dispersion has been used to detect and distinguish reversible and irreversible electroporation. Similarly, the conductivity of freshly excised human liver tissue has remained constant between 10 Hz and 1 kHz [360]. The impedance of porcine tissues (among others, cardiac muscle, liver, kidney, lung, spleen and muscle) has been characterised by a single Cole-Cole dispersion between 100 Hz and 65 kHz having a distinct low-frequency resistance [343]. Only during ischaemia, another dispersion has appeared at frequencies around 10 kHz. As mentioned before, cartilage also has a fixed conductivity below 10 kHz (Fig. 7.1). All studies mentioned earlier in this paragraph have used the four-electrode technique. In contrast, Raicu *et al.* have measured the dielectric properties of rat liver in vivo starting from 100 Hz using a two-electrode setup and have applied an algorithmic correction of the electrode polarisation. Furthermore, they flushed the surface of the liver with a low-conductivity medium during the measurement, which decreased the static conductivity but did not considerably change the frequency-dependent permittivity and conductivity [361]. This finding is in accordance with the Kramers-Kronig relations [3] and has shown that the measured low-frequency conductivity was dominated by the static conductivity. Moreover, it explains the idea behind the 3 CC model: the dielectric properties of tissues can be described by three dispersions and a static conductivity. Following this interpretation, the fourth dispersion present in the original 4 CC model stems from electrode polarisation effects, while the other dispersions describe the three main dispersions (α, β, γ) described in the literature [194, 347].

Among the three dispersions, the α-dispersion is understood the least. The question arises if the α-dispersion can actually be measured. In a study of ischemic, perfused liver tissue, the dielectric properties have been fitted by two Cole-Cole dispersions [342]. I reproduced the reported permittivity and observed that the α-dispersion is very weak in comparison to the β-dispersion (not shown, see supplementary material of [236]). As the static conductivity has not been reported, I chose a value that matched the reported impedance dispersions but could not reproduce the impedance plots shown in [342]. Instead, the impedance that I computed from the dielectric properties was barely influenced by the α-dispersion; even if I increased the dispersion magnitude. In [341], it has been speculated that gap junctions would cause the α-dispersion. Results of a theoretical study have indeed indicated a relation of the α-dispersion and gap junctions [349]. The α-dispersion appeared only

if gap junctions were modelled. It could be described by a Cole-Cole dispersion with a characteristic frequency of about 6 kHz (i.e., a mean relaxation time of about 26.5 ms). The theoretical model predicts a frequency-independent conductivity and permittivity below 1 kHz. In a Nyquist plot, the semicircle that is related to the α-dispersion impedance is much smaller than the semicircle due to the β-dispersion (not shown, see supplementary material of [236]). In the EIS data of Gabriel *et al.*, the corresponding semicircle is not fully visible, but still much larger than the other arcs related to the tissue impedance (Fig. 7.2B). If the α-dispersion impedance is in reality not considerably separated from the β-dispersion impedance, it might be masked by the ETI impedance and could eventually not be detected.

The charge transfer resistance, which had to be considered for some tissues to generate a good fit, could be an indicator for a tissue-specific α-dispersion. Even though its occurrence due to electrochemical effects at the ETI is not unexpected [107, 362], it is surprising that it occurs only for a few tissues. These tissues are all muscular and/or fibrous. For this type of tissues, the α-dispersion has been described in the literature [194, 340, 344] while its origin is not clear.

Interestingly, the reported α-dispersion of freshly excised muscle tissue [340] can be modelled by the 3 CC model. The α-dispersion in muscle has manifested itself in an increase of the relative permittivity from about 10^5 to up to 10^7 at frequencies below 10 kHz. The conductivity has been reported to remain more or less constant in this frequency range. The original data of Gabriel *et al.* has predicted a drop of the conductivity in this range while the permittivity increases. Interestingly, Gabriel *et al.* modelled muscle tissue by three dispersions in the relevant frequency range with characteristic frequencies at 70 Hz, 500 Hz and 450 kHz. The dispersions were also modelled considerably larger than those of the other tissues. Thus, I found that the 3 CC model, which neglects the slowest ms dispersion, predicts similar α-dispersion behaviour of the dielectric properties of muscle tissue as reported in the literature [340] (not shown, see supplementary material of [236]). Even though the 3 CC model has not been derived from a complex nonlinear least-squares fit, it contains more complete information than the HN model because it has been manually fit to data including also the high-frequency behaviour above 10 MHz [333].

It cannot be excluded that the EIS data of muscular and/or fibrous tissues contained both contributions from the ETI and the α-dispersion. It has been argued that heart muscle tissue possesses such a 'hidden' α-dispersion [341]. Using the 2 CC model together with the ETI element could be a viable way to test this hypothesis. For the existing data, overfitting cannot be ruled out and thus this approach was not tried. For future research, a possibility to achieve this goal would be to find experimental evidence for the ETI effects together with detailed *a priori* characterisation [101, 345]. In addition to the here presented algorithmic correction, the same sample could be measured by electrodes made of different (stable) materials [108] or tissue samples of different thickness could be compared [346].

For non-muscular tissues such as brain tissue, liver or kidney, it is very likely that

these tissues actually behave like resistors with a frequency-independent conductivity below 1 kHz: it is not to be expected that they reveal a change in their conductivity due to an α-dispersion. If this hypothesis can be confirmed, it will have practical implications for the parametric modelling of the dielectric properties. I propose to omit the slowest dispersion and adjust the static conductivity for these types of tissues (i.e., using the 3 CC model). The static conductivities from the IT'IS database [336], which for some tissues differ from the Gabriel results and also my results could be used to construct physically valid, frequency-dependent dielectric properties for tissues that have not yet been characterised down to very low frequencies. This particularly applies to cartilage and could bridge the gap between the existing low-frequency conductivity data and the dielectric properties recorded by Gabriel *et al.* above 1 MHz.

While the conductivity might not be affected, it is likely that the permittivity might change significantly in the low-frequency range due to localised charge layers at the cell membranes [350, 351] or the cellular network [349]. Currently, the 3 CC model might well underestimate the permittivity at very low frequencies. The α-dispersion at these frequencies should be addressed appropriately by, for example, adapting the mean relaxation times and dispersion magnitudes of the 3 CC or 4 CC model or using the universal relaxation model describing the asymptotic low-frequency permittivity. As the α-dispersion appears only at very low frequencies and might be hidden by the ETI impedance, special devices with an extremely low cutoff frequency should be employed [363].

In sum, the ambiguity in the interpretation remains until further experiments on the low-frequency behaviour of biological tissues have been conducted. These experiments should cover a broad frequency range to be able to distinguish between the determined β-dispersion and a possible α-dispersion. For the numerical simulations based on the EQS equation (Eq. (2.16)), the detailed understanding of the low-frequency dielectric properties is decisive for the model complexity. If biological tissue is mostly resistive at low frequencies, the imaginary part of the EQS equation can be ignored (see Sec. 2.3.3 for more details). For FEM simulations, this means that CG can be used as an iterative solver, which has a well-understood convergence behaviour and is more performant in terms of memory consumption the iterative solvers required for the full EQS problem (e.g., GMRES or BiCGSTAB). Moreover, tissues with a low conductivity can possibly be ignored just as the Petri dish and plastic pieces in the models presented in Chapter 5. In the cartilage context, this could, for example, apply to the subchondral bone. Thus, the model complexity can be significantly reduced.

For cartilage, the results presented in this section suggest that a combination of existing low-frequency conductivity information together with the Gabriel model is currently the best possible approximation of the dielectric properties. To overcome this limitation, I will introduce two theories to estimate the cartilage dielectric properties numerically. To this end, cartilage can be understood as a dielectric

mixture. The cells are embedded in an extracellular phase, which is almost liquid, and hence cartilage conceptually resembles a particle suspension. For the description of dielectric mixtures, both analytical and numerical approaches (e.g., based on FEM [364]) exist and will be introduced in the following.

7.3 Suspension models — the analytical approach

When particles suspended in a medium are exposed to a homogeneous electric field, the effective complex permittivity of the particle suspension can be computed analytically. An overview of the derivation, historical development and applications in dielectric spectroscopy of biological systems can be found in the textbook by Raicu *et al.* [1]. Here, I will introduce, based on the aforementioned textbook, the two major suspension models for the dielectric properties of spherical particles in an isotropic medium, which resembles the cartilage structure (overly simplistic: round cells in a jelly-like electrolyte solution). For other cases (e.g., other particle shapes) the interested reader is referred to the literature, for example [1]. Again, I would like to stress that the derivation of the suspension models makes use of the assumption that the external field is homogeneous (e.g., the field in a parallel-plate capacitor).

The simplest theory is the so-called Maxwell-Wagner theory, in which the effective complex permittivity of the suspension $\hat{\varepsilon}_{\mathrm{sus}}$ is given by

$$\hat{\varepsilon}_{\mathrm{sus}} = \hat{\varepsilon}_{\mathrm{med}} \frac{(2\hat{\varepsilon}_{\mathrm{med}} + \hat{\varepsilon}_{\mathrm{p}}) - 2p(\hat{\varepsilon}_{\mathrm{med}} - \hat{\varepsilon}_{\mathrm{p}})}{(2\hat{\varepsilon}_{\mathrm{med}} + \hat{\varepsilon}_{\mathrm{p}}) + p(\hat{\varepsilon}_{\mathrm{med}} - \hat{\varepsilon}_{\mathrm{p}})} \ , \tag{7.2}$$

with p the volume fraction, $\hat{\varepsilon}_{\mathrm{med}}$ being the permittivity of the (liquid) medium and $\hat{\varepsilon}_{\mathrm{p}}$ the permittivity of the suspended particle (e.g., a biological cell). The Maxwell-Wagner theory is valid for dilute suspensions (i.e., for suspensions with a small volume fraction of a few percent). It assumes that the perturbation of the applied homogeneous field introduced by a single particle is so small that the neighbouring particles do not experience it.

For suspensions of higher concentration, the Bruggeman-Hanai approach is chosen. Now, also particle-particle interactions are considered and the Maxwell-Wagner theory is corrected. Nevertheless, both theories assume a random and uniform distribution of the particles in the suspension. The effective complex permittivity of the suspension $\hat{\varepsilon}_{\mathrm{sus}}$ using the Bruggeman-Hanai approach is connected to the particle permittivity $\hat{\varepsilon}_{\mathrm{p}}$ and medium permittivity $\hat{\varepsilon}_{\mathrm{med}}$ for a given volume fraction p via

$$\frac{\hat{\varepsilon}_{\mathrm{sus}} - \hat{\varepsilon}_{\mathrm{p}}}{\hat{\varepsilon}_{\mathrm{med}} - \hat{\varepsilon}_{\mathrm{p}}} \left(\frac{\hat{\varepsilon}_{\mathrm{med}}}{\hat{\varepsilon}_{\mathrm{sus}}} \right)^{1/3} = 1 - p \ . \tag{7.3}$$

While Eq. (7.2) is a regular equation that directly provides the permittivity of the suspension, Eq. (7.3) is a cubic equation and has thus three possible solutions for the

permittivity of the suspension. Only one of them is physical, which can be found by evaluating certain properties of the cubic roots [365]. A general approach to solving cubic equations can be found in [209] and an iterative approach is described in [1]. I implemented both approaches in *ImpedanceFitter*, where the interested reader can also find a more detailed documentation[2].

For the medium permittivity, usually the complex permittivity $\hat{\varepsilon}_{\mathrm{med}} = \varepsilon_{\mathrm{med}} + \mathrm{j}\omega\sigma_{\mathrm{med}}$ is considered. This is also an approximation as the dielectric properties of electrolyte solutions might, for example, be better described by Debye or Cole-Cole relaxations [188]. An important aspect of the suspension models is the particle permittivity $\hat{\varepsilon}_{\mathrm{p}}$. Usually, so-called shell models are considered for biological cells. For example, the single shell model consists of a sphere filled with cytoplasm and having a thin outer shell that mimics the cell membrane. Likewise, the double-shell model also considers the cell nucleus. Moreover, additional layers such as the pericellular matrix can be considered. The analytical expressions for the complex particle permittivity $\hat{\varepsilon}_{\mathrm{p}}$ for the respective model are lengthy and will not be reported here. Again, the interested reader is referred to the literature [1] and the documentation of *ImpedanceFitter*[2].

7.4 Cartilage models — the numerical approach

Besides other analytical approaches such as fractal models, numerical models of biological tissue are a viable option to estimate the dielectric properties [1]. To account for the special structure of articular cartilage with its different zones, the pericellular matrix around the cells, possibly multiple cells connected in one chondron and the varying cell shapes, imaging data of cartilage is required. Moreover, gap junctions [366] or membrane perforations [352] can be integrated into the geometrical models. Evidently, developing a detailed understanding of the cartilage dielectric properties through numerical modelling requires 3D geometries in which extracellular matrix, pericellular matrix, cell membrane and, if possible, the cell nucleus are distinguished. To the best of my knowledge, there exists no detailed database of segmented 3D cartilage geometries derived from medical imaging. Instead, zone-specific cell statistics are known (i.e., the shape of the cells, the mean diameter, the number of cells per chondron, etc. [9]). Moreover, confocal laser scanning microscopy has been used to obtain detailed 3D geometries by fitting ellipsoids to identified cells. Bennetts *et al.* have used this information to generate tissue-specific 3D geometries in an automated manner using open-source software [367]. Here, I make use of their algorithm and their scripts to develop an understanding of the dielectric properties of cartilage tissue. The devised workflow is summarised in Fig. 7.5.

[2] `https://impedancefitter.readthedocs.io/`.

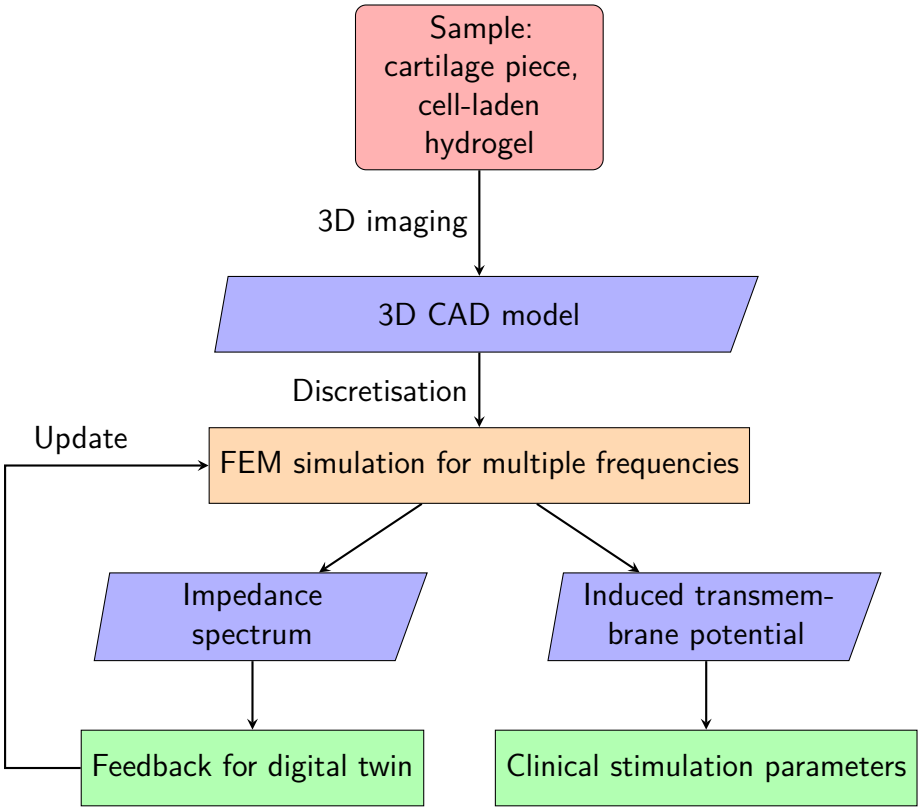

Figure 7.5: Devised workflow to extract information for electrical stimulation experiments from real-world cartilage or cartilage-like samples. The goal is to compute the dielectric properties of cartilage and the effect of electrical stimulation at the same time. For that, 3D CAD models need to be provided. The computed impedance, which permits to estimate the dielectric properties, can also be used in a feedback loop to tailor the electrical stimulation parameters using an approach similar to the digital twin presented in Chapter 5.

7.4.1 Model geometries

To test and verify the implementation in *NGSolve* for multiple cells, the scripts by Bennetts *et al.* [367] were translated from *SALOME* to the OCCT interface in *NGSolve*. All simulations were performed using the at the time most recent version of *NGSolve* (version 6.2.2202) together with the *ngs-petsc* interface for message passing interface (MPI)-parallelised linear algebra operations. To reach a relatively large number of DOFs, 36 cells in a cube with edge length 100 µm were considered that yielded a volume fraction of about 5%. Four different cases were considered:

1. The single shell model with only the cell membrane.
2. The single shell model with a cell wall (i.e., with the pericellular matrix).
3. The double shell model with the cell membrane and the cell nucleus.
4. The double shell model with a cell wall.

The expected impedances for these test cases are known from the suspension theory. The underlying formulae were implemented in *ImpedanceFitter*. When using MPI, adaptive mesh refinement is not yet supported in *NGSolve*. Hence, appropriate meshing hypotheses have to be used to ensure convergence. A maximum mesh size of 1 µm was imposed on the cell wall, cell membrane and the cell nucleus membrane. The maximum mesh size inside the cell was set to 2 µm. In the extracellular matrix (ECM), a maximum mesh size of 5 µm was specified. Furthermore, the meshing hypothesis 'very fine', which is predefined in *Netgen*, was used to generate high-quality elements. The cell surface area and cell volume were compared to the expected values to check the geometrical accuracy of the resulting mesh. A maximum relative error of 1% was chosen. The dielectric properties were taken from [293] (see Table 7.2). The values of dielectric properties of the pericellular matrix are not known. Arbitrary values were chosen but it was ensured that they have a significant impact on the expected dielectric properties.

7.4.2 Results

The modelling workflow for realistic cell-scale models involves using different packages. The geometry is prepared in a CAD tool (e.g., *SALOME* or the OCCT kernel in *Netgen*) and subsequently meshed by, for example, *Netgen*. The mesh is communicated to *NGSolve*, which assembles the linear system to be solved. Then, black-box solvers and preconditioners that are implemented in *NGSolve* or *PETSc* are used to solve the linear system. As realistic tissue models will involve hundreds or thousands of cells, a manual analysis of the model regarding its correctness is impossible. Moreover, the correctness of the underlying implementation of the different employed methods (both for the FEM and the linear algebra solvers) has to be

assumed. Debugging the employed software packages is cumbersome because large models can only be solved using HPC with MPI parallelisation. This means that the mesh is subdivided in multiple sub-meshes that are distributed across the HPC cluster[3]. The distributed linear system is then assembled (i.e., on each sub-mesh associated with a single processor). There is no information on the undistributed global system available. In contrast, there also exists shared-memory parallelisation based on, for example, multithreading. However, this kind of parallelisation is limited to workstations and cannot be used on HPC clusters. Hence, it cannot be expected that it can be used for tissue models that will likely involve many millions or even billions of DOFs.

As a first result, I benchmarked the standard shared-memory FEM implementation against the MPI-parallelised implementation in *NGSolve* to ensure correctness. Initially, the considered method could not be used and I contributed to bug fixes. Furthermore, the *ngs-petsc* interface was improved to conduct frequency sweeps in a memory-efficient way. From a physics point of view, it is sensible to assess the validity of the computed impedance to conclude on the validity of the simulation results. The suggested approach will be introduced in the following.

Table 7.2: Assumptions for the dielectric properties of eukaryotic cells as reported in [293]. In accordance with [293], the radius of the cells was set to 7 µm, the thickness of the membrane to 7 nm, the thickness of the nuclear membrane to 40 nm and the thickness of the cell wall to 2.5 µm. The dielectric properties of the cell wall / pericellular matrix were chosen such that they have a significant impact on the expected dielectric properties.

Domain	Conductivity in $\mathrm{S\,m^{-1}}$	Rel. permittivity
Membrane	8.7×10^{-6}	5.8
Cytoplasm	0.48	60
Nuclear envelope	3×10^{-3}	41
Nucleoplasm	0.95	120
Wall / pericellular matrix	0.01	20

Ensuring valid results

The numerically computed impedance has to fulfil the Kramers-Kronig relations. Thus, the Lin-KK test can be used to assess the validity of the numerical results. To demonstrate this approach, the impedance was on the one hand computed using only the volume integral approach Eq. (2.31). On the other hand, the surface term described in Eq. (3.17), which accounts for the cell membrane, was added

[3]By HPC cluster, I refer to a network of computing nodes that are connected in a local network. In simple terms, this means that multiple computers are connected and one simulation is distributed across the network and solved using the computers in parallel.

to the volume integral. The frequency was swept from 1 kHz to 1 THz using ten logarithmically spaced frequency points per decade. This frequency resolution is often chosen in experimental approaches and can be assumed sufficient for a broadband scan.

As demonstrated in Fig. 7.6, the Lin-KK test successfully detects the wrongly computed impedance. Moreover, it could even contribute to correcting the chosen approach: the error between the best Lin-KK fit and the numerically computed impedance was highest in the MHz-range. This frequency range is typical for the interfacial polarisation (or β-dispersion), which arises due to the cell membrane [347]. Hence, identifying the missing surface term in the impedance computation became straightforward.

Even though I did not observe or test it, I believe that the Lin-KK test should also be able to identify insufficient convergence and other numerical errors, which lead to a wrong numerical result. Most importantly, this means that the validity of any numerically computed impedance can be assessed for realistic geometries (i.e., when there is no analytical solution available).

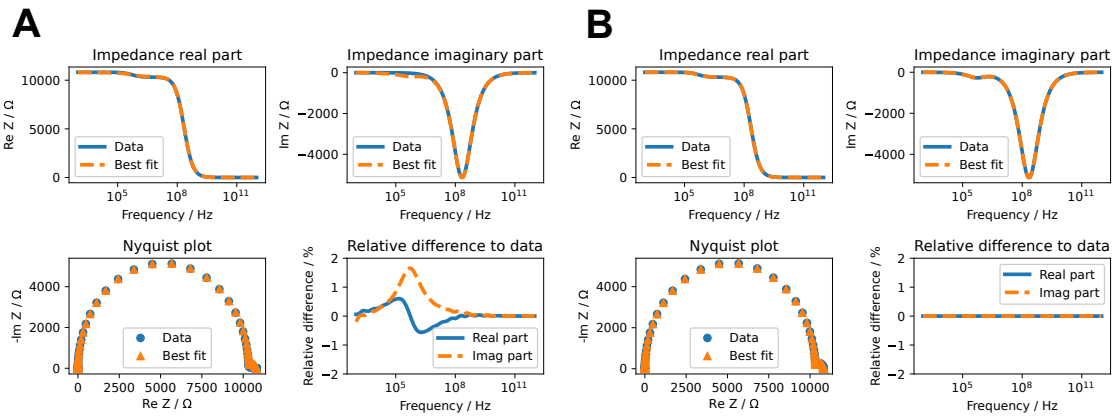

Figure 7.6: Lin-KK evaluation of the computed impedance. **A**: The impedance was computed using Eq. (2.31) (i.e., evaluating only a volume integral). **B**: The contribution of the cell membranes was considered by adding the surface term Eq. (3.17) to the impedance shown in **A**. The parameter c in the Lin-KK test was set to 0.5 to ensure a meaningful result of the test.

Validation case: randomly distributed spherical cells

After having ensured that the impedance is computed correctly, realistic cell geometries shall be studied. The goal was to choose geometries for which an analytical solution is known. Thus, randomly distributed cells with and without a cell nucleus and a cell wall were studied. To get an impression of the numerical performance and requirements, the execution times for meshing the geometry and running the

simulation as well as the number of elements and DOFs are summarised in Table 7.3. Evidently, the meshing takes much more time than the actual solver run (which involves both assembly and solution of the linear system). Particularly if cell nuclei and cell walls are present, the meshing time increases substantially and lasts a few hours. In comparison, the run time of the simulation is only a few minutes. This is problematic for a technical reason. The meshing is parallelised using thread-based parallelism. Thus, it is advantageous to run the meshing in a separate script and save the mesh to a file. The mesh is then loaded into a simulation script, which is MPI-parallelised. To curve the mesh in the simulation script, the geometry has to be loaded again and distributed to every MPI-rank. In comparison to the approach with meshing, curving and simulation in one script, this does not pose a serious challenge and does not increase the computational time significantly.

The impedance deviated usually about by 1% or less (Table 7.3 and Fig. 7.7). As the dielectric properties (Fig. 7.8) are computed from the impedance by Eq. (4.1), their error was always in a similar range (Fig. 7.9). A finer mesh further reduced the error. This result indicates that the used mesh hypothesis is sufficient to ensure an accuracy of at least 1%, which is acceptable as it is on the same scale as the accuracy of experimental approaches. Hence, it can be used in other cell models.

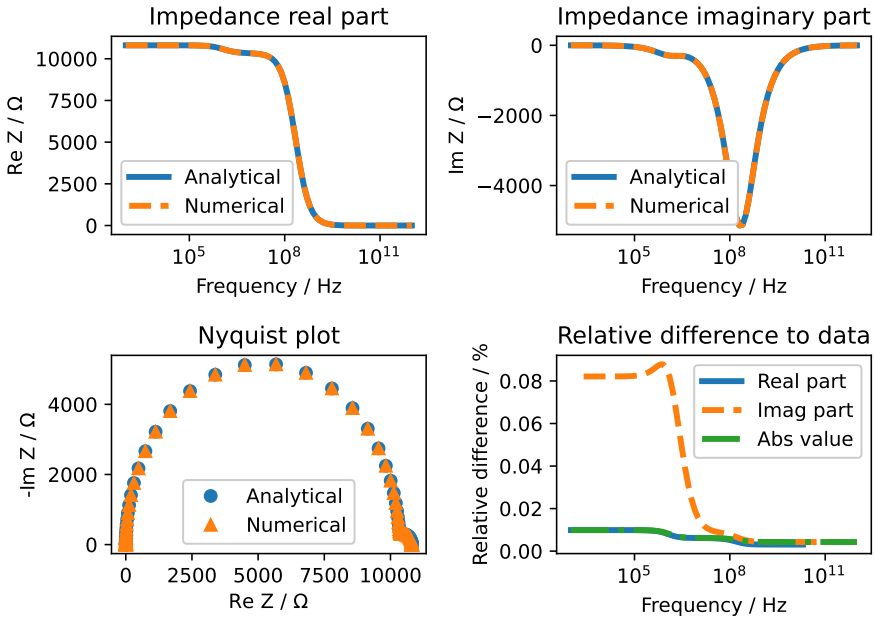

Figure 7.7: Impedance of the numerical model comprising 36 cells compared to the analytical single shell model for the model parameters specified in Table 7.2.

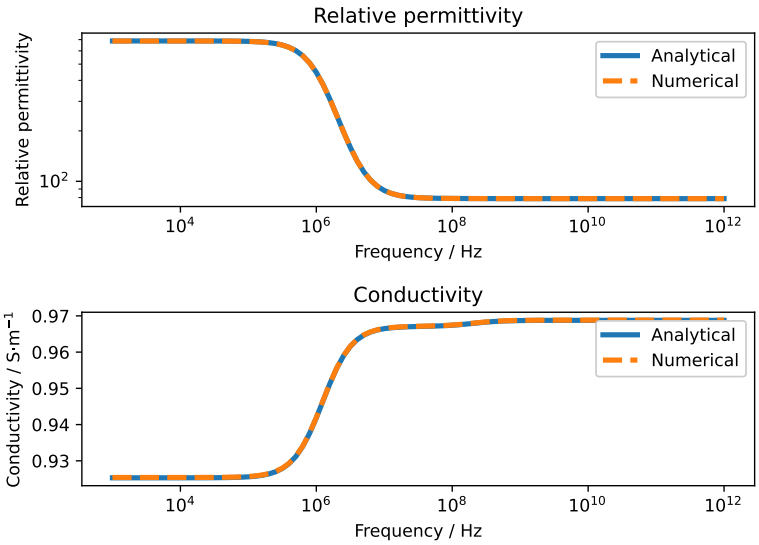

Figure 7.8: Dielectric properties of the numerical model comprising 36 cells compared to the analytical single shell model for the model parameters specified in Table 7.2.

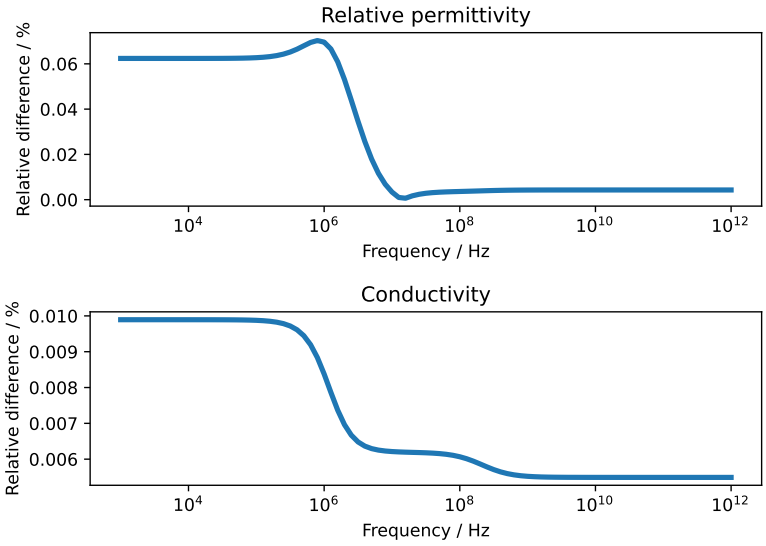

Figure 7.9: Relative error of dielectric properties of the numerical model comprising 36 cells compared to the analytical single shell model (Fig. 7.8) for the model parameters specified in Table 7.2.

Table 7.3: Overview of models: the single shell models are spherical cells without a cell nucleus while the double shell models included a cell nucleus with a radius that was 0.8 times the cell radius. A cell wall of 2.5 µm was added to also check the models for the case of a pericellular matrix. The other model parameters are specified in Table 7.2. The meshing time and run time were rounded and are approximate numbers to give an impression. All computations were performed on the HAUMEA high-performance computing cluster of the University of Rostock (each computing node equipped with two Intel® Xeon® Gold 6248 CPUs with in total 40 cores and 192 GB RAM). The meshing was performed using shared-memory parallelisation on a single node. The simulation runs were performed using distributed-memory parallelisation using four or ten nodes (i.e., 160 (single shell models) or 400 (double shell models) cores). This choice ensured that there were roughly 20×10^3 DOFs per core. The impedance was compared to the Maxwell-Wagner suspension model because the cell volume fraction was about 5% without the cell wall and about 12.9% with the cell wall. Hence, the ratio was always below 20%, which is considered to be the limit from which on the Bruggeman-Hanai model should be used [368]. The maximum relative error of the impedance always refers to the imaginary part, which had a larger error than the real part and the absolute value of the impedance (see Fig. 7.7).

Model	Elements	DOFs	Meshing time	Run time	Max. rel. error of impedance
Single shell	2,013,242	2,807,392	0.3 h	2 min	1%
Single shell w/ wall	2,093,644	2,933,693	1 h	2.3 min	0.17%
Double shell	5,011,319	7,201,475	2.5 h	6.6 min	0.8%
Double shell w/ wall	4,264,575	6,195,322	3.5 h	5 min	0.2%

An important aspect of the chosen approach is the choice of a suitable iterative solver and preconditioner. As the linear system is complex symmetric, I tried the GMRES and BiCGSTAB solvers implemented in *PETSc*. The BiCGSTAB solver appeared more robust and usually converged with fewer iterations (usually less than a few hundred) while GMRES sometimes required a huge number of iterations (a few thousand) or did not converge at all. Perhaps, a better performance of the GMRES solver can be achieved in future research by a suitable restarting protocol. Currently, the performance of the GMRES solver deteriorated with an increasing cell number. Thus, BiCGSTAB became the solver used in all simulations. The chosen residual thresholds for convergence of the iterative solver ensured the aforementioned accuracy of 1%. Possibly, a higher accuracy could be reached by setting lower thresholds, which will lead to more solver iterations. I have not investigated this option as the accuracy appeared sufficient.

For a small cell number, the AMG preconditioner *GAMG* available in *PETSc* worked well. It is to my knowledge the only AMG preconditioner in *PETSc* that can handle complex numbers and working with MPI. However, with a growing number of cells, it did not precondition the matrix well and the iterative solver did not converge

in some cases. A viable alternative were the block Jacobi preconditioner and in particular the additive Schwarz domain decomposition preconditioner. These methods are closely related and particularly suitable for parallel computing [369]. Furthermore, preconditioners based on domain decomposition have been recommended for the more general mortar method [370] and were thus chosen by me.

In my experience, the additive Schwarz preconditioner in *PETSc* performed better and was thus used for all results presented here. Still, even for a refined mesh that yielded about 80×10^6 DOFs, the solver converged in a reasonable time (i.e., about 20 min for the considered frequency sweep using 800 cores). In general, a sufficiently good mesh quality has to be ensured. In preliminary investigations, the solver did not converge when coarse meshes were used. It must be noted that I did not investigate the linear algebra aspects in further detail. Hence, I believe that there probably might be more efficient solvers available. This aspect should be studied in future research.

Realistic cartilage models: an outlook

As the presented solver yields reliable results, it can be applied on realistic cartilage geometries. Thus, a layout file to generate a cartilage geometry with three zones was prepared (see Listing A.5). The layout file was processed using the scripts provided by Bennetts *et al.* [367]. As in their work, similar values reflecting the structure of the individual zones as reported in [9] were used. Eventually, models comprising hundreds to thousands of cells were generated (Fig. 7.10).

As indicated already by the results for 36 cells (Table 7.3), the meshing was the most challenging part. In particular, I experienced meshing issues due to the shape of the cells in the superficial zone. Initially, I experimented with smaller radii of the ellipsoids. Then, the algorithm by Bennetts *et al.* created some ellipsoids with radii of only about 100 nm. Such small structures could not be meshed successfully in a reasonable amount of time. Instead, I chose bigger radii to generate the cells in the superficial zone (see Listing A.5). Unfortunately, only the mean horizontal diameter has been reported in [9]. This information is not sufficient to build a valid ellipsoid. Hence, I chose radii values to generate ellipsoids that are elongated in x-direction and thinner in y- and z-direction. The simulations are meant to get a first impression of the numerical treatment of realistic cartilage samples. A drawback of the statistical description is that it is not perfectly in agreement with its data source, the experimental work by Hunziker *et al.* [9]. The statistical geometrical model has a volume ratio of about 4.5%, which is larger than the actually reported 1.65% [9]. This underlines the necessity to use image-based samples instead of artificially generated samples in future research. Based on the meshing issues, it can be foreseen that cartilage geometries extracted from 3D images have to be pre-processed in a way that small artefacts or very small cells have to be removed to be able to mesh the geometries.

Until now the meshing of more than thousand cells using the desired fine mesh quality with preset maximum mesh sizes per domain has not succeeded. Instead, the *Netgen* meshing hypothesis 'very fine' was used. With this, a model comprising 3218 cells could be built and the resulting mesh led to about 200×10^6 DOFs. Even though the mesh size of the individual structures could not be controlled, the geometry error was reasonably small and below 1%. Given the larger number of cells, this error still appears tolerable and sufficient to compute the impedance with a similar accuracy.

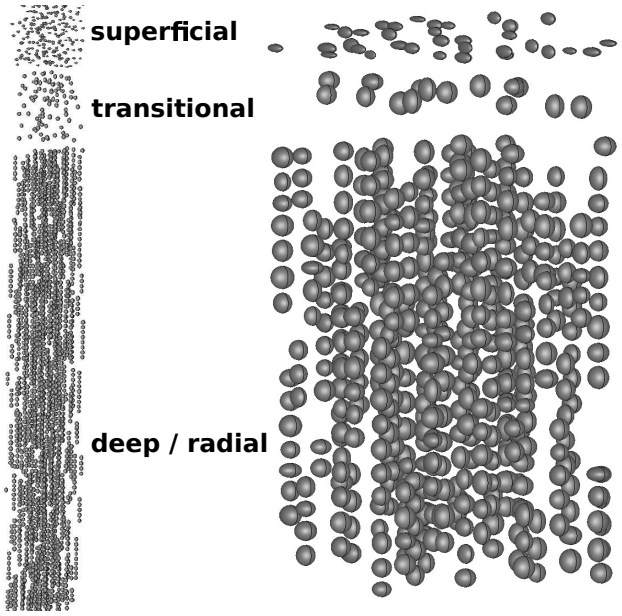

Figure 7.10: Models of cartilage tissue having the three representative cartilage zones (superficial, transitional and deep or radial zone). Please see Fig. 1.2 for a more detailed explanation of the cartilage structure. Left: a model with 3218 cells (cropped at the bottom, generated with the input file shown in Listing A.5). Right: a model comprising 528 cells. The difference between the models is caused by different outer dimensions of the cartilage sample. Nevertheless, the statistical properties of the samples are the same.

The numerically computed dielectric properties of the sample show almost no anisotropy and are very close to the analytical estimate based on the single shell model (Fig. 7.11). The conductivity and permittivity do not change significantly in the sub-MHz range. In a nutshell, these results indicate that cartilage should have frequency-independent dielectric properties in the frequency range that is relevant for cartilage tissue engineering. This hypothesis should be tested in future experiments to close the gap between the low-frequency conductivity measurements, the Gabriel model and the high-frequency Gabriel measurements (Fig. 7.1). Compared to the measurement data by Gabriel *et al.* (Fig. 7.1), it is evident that the β-dispersion, which is approximately centred around 1 MHz, is well captured by the numerical model (Fig. 7.11). Still, the agreement is only qualitative as the assumptions on the

dielectric properties will require more detailed analyses of cartilage tissue. Furthermore, a second and probably third dispersion at frequencies above 100 MHz, which are visible in the measurement data, are not contained in the model results. A possible reason is that the cell nuclei, the cartilage fibre network, and other structures of the cell membrane such as the primary cilium are not yet included in the model.

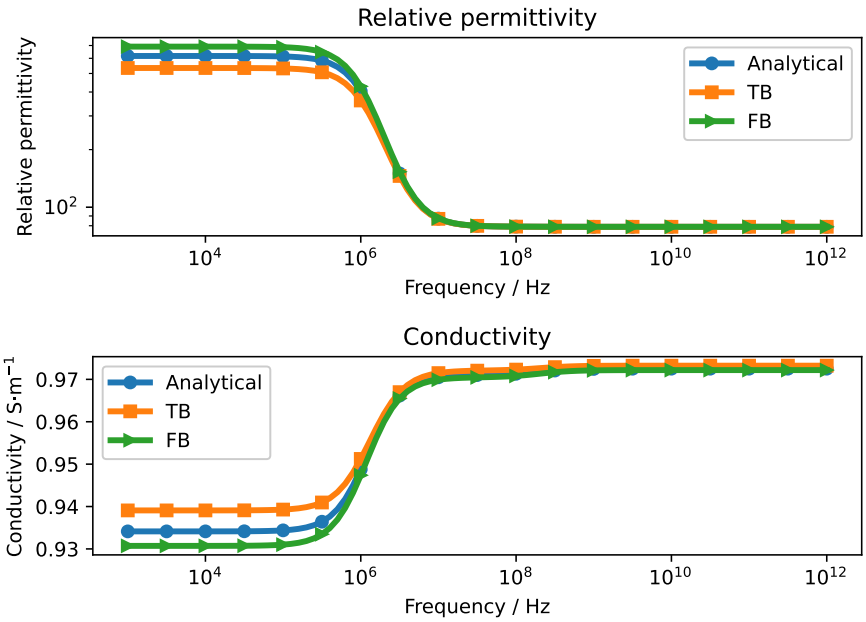

Figure 7.11: Dielectric properties of a cartilage sample comprising 3218 cells (Fig. 7.10). The dielectric properties were computed applying the voltage from the top surface to the bottom surface of the sample (TB) and from the front to the back (FB). The results with a voltage applied from left to right was not distinguishable from the FB result and is thus not shown. The dielectric properties are compared against an analytical estimate using the single shell model for spherical cells. An average cell radius of 7 µm and the computed volume ratio of about 4.5% were used for the analytical estimate together with the other model parameters specified in Table 7.2. While the permittivity deviates by about 15% from the analytical estimate in the sub-MHz range, the conductivity only deviates by about 0.5%. At higher frequencies, no significant deviation could be observed.

The results suggest that analytical models can potentially be used to analyse the dielectric spectra of cartilage. Thus, they could help to identify crucial parameters related to the volume fraction, cell geometry and membrane properties. However, certain parameters have to be known beforehand because some parameters are linearly dependent. For example, the geometrical information and the permittivity of the cytoplasm should be known to determine the cellular and membrane parameters [368]. Vice versa, the cellular and membrane parameters should be known to

extract unknown geometrical parameters. As the approach considered in this work assumes that the geometry of the sample and the contained cells is known, information about the dielectric properties can in principle be inferred from impedance measurements.

I used UQ and sensitivity analysis of the analytical single shell model to understand in which frequency range the measurements have to be performed. The uncertainty of the dielectric properties is propagated through the analytical model under the assumption of known geometrical parameters. For that, I used the uncertainties based on [293], which are summarised in Table 6.5. Furthermore, the conductivity of the extracellular matrix was described by $\mathcal{U}(0.95, 1.05)$ and its permittivity by $\mathcal{U}(70, 80)$. I used the Monte Carlo method with 1×10^5 samples to construct the sampling using Saltelli's method (please be referred to [234] for more details).

A parameter can be expected to be extracted from EIS data if its first-order Sobol index indicates a sufficient sensitivity of the impedance with respect to the individual parameter. The results suggest that the cellular parameters can only be inferred from measurements in the MHz-range (Figs. 7.12 and 7.13). Interestingly, the membrane conductivity seems to influence the measured impedance only at low frequencies, where it leads to relatively small changes of the impedance (Fig. 7.13). This poses a challenge and an opportunity at the same time. On the one hand, it is most likely impossible to infer the membrane conductivity from impedance measurements of a cartilage sample even if the cellular geometries are known. On the other hand, the membrane conductivity does not need to be known precisely to build a valid model of cartilage tissue to estimate the tissue impedance. As computing the impedance involves the transmembrane potential, this applies also for the stimulation effect.

A possibility to clarify if a parameter can be extracted from measurement data is to perform multiple fit runs. In each run, one parameter is kept at a fixed value in an interval around its (expected) best fit value. The fit residuals are then compared. If the fit residual does not assume a clear minimal value for a certain parameter value but is independent of the chosen parameter value, it can be assumed that the parameter cannot be extracted from the measured data. This approach has, for example, been applied in [371]. Additionally, the presented results (Figs. 7.12 and 7.13) suggest that measurements have to be performed for frequencies up to ideally 1 GHz. This is an experimental challenge due to lead inductances, which play a role at high frequencies. A parallel-plate capacitor setup, as considered in this work, has been developed to enable measurements up to 110 MHz [372]. Considering the need for measurements up to high frequencies, the measured dielectric properties of chondrocytes reported in [289] and used, for example, in Chapter 6 should be verified by independent measurements over a broader frequency range. Currently, the dielectric properties reported in [289] rely on measurements from 10 kHz to 10 MHz. Furthermore, the measurements have been performed in low conductivity medium and thus not under conditions found in cartilage tissue.

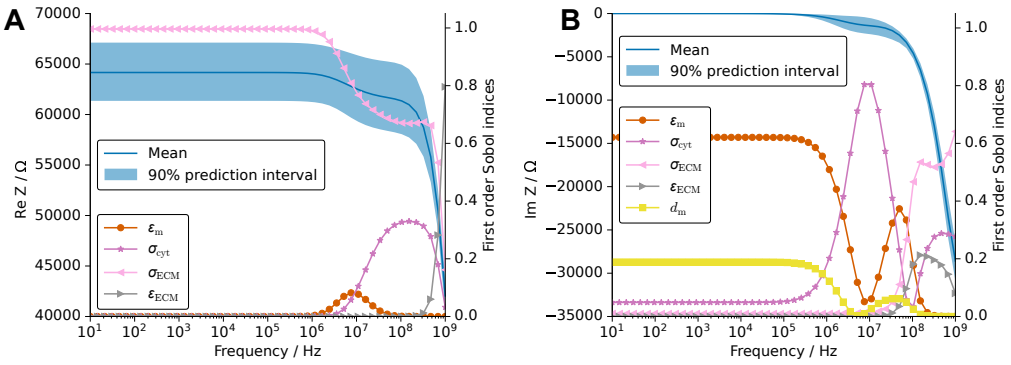

Figure 7.12: The mean value and 90% prediction interval of the real part (**A**) and the imaginary part (**B**) of the impedance are shown over a wide frequency range. Moreover, the frequency-dependent first order Sobol indices are shown for parameters with a Sobol index greater than 0.05. The assumptions for the UQ analysis of the cellular dielectric properties are given in Table 6.5. The conductivity of the extracellular matrix σ_{ECM} was described by $\mathcal{U}(0.95, 1.05)$ and its permittivity ($\varepsilon_{\mathrm{ECM}}$) by $\mathcal{U}(70, 80)$. For these assumptions, only the membrane permittivity ε_{m} and the cytoplasm conductivity σ_{cyt} were cellular parameters with a significant impact. Moreover, the thickness of the membrane d_{m} influences the imaginary part of the membrane. Evidently, the imaginary part of the impedance is close to zero in the sub-MHz range and does not have a significant variance.

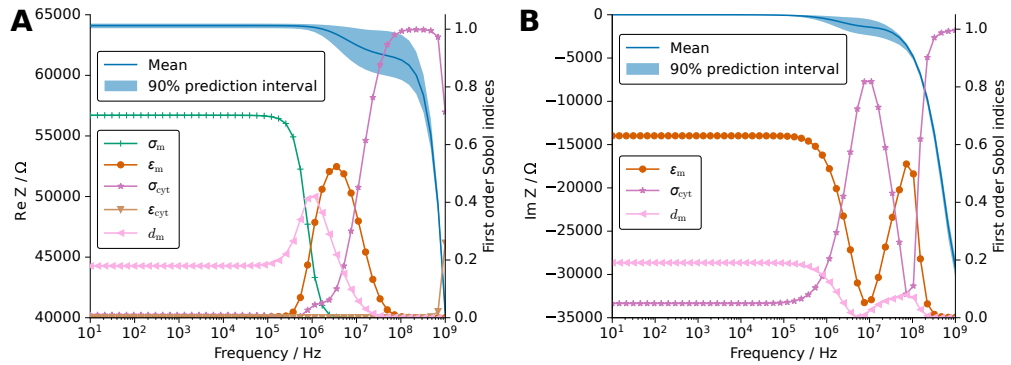

Figure 7.13: The mean value and 90% prediction interval of the real part (**A**) and the imaginary part (**B**) of the impedance are shown over a wide frequency range. Moreover, the frequency-dependent first order Sobol indices are shown for parameters with a Sobol index greater than 0.05. In contrast to the results in Fig. 7.12, the uncertainty of the dielectric properties of the extracellular matrix was neglected and fixed values of $\sigma_{\mathrm{ECM}} = 1\,\mathrm{S\,m^{-1}}$ and $\varepsilon_{\mathrm{ECM}} = 80$ were used. The assumptions for the UQ analysis of the cellular dielectric properties are given in Table 6.5. For these assumptions, the impedance only changes slightly in the sub-MHz range. At higher frequencies, the membrane permittivity ε_{m} and the cytoplasm conductivity σ_{cyt} had a significant impact. Moreover, the thickness of the membrane d_{m} influences the imaginary part of the membrane.

7.4.3 Discussion

This section aimed at establishing a numerical approach to model cartilage at the tissue scale. Leveraging the thin layer approximation, it becomes feasible to describe tissue-specific cell geometries and distributions. In addition, cell nuclei and the pericellular matrix can be modelled. The presented open-source solution is reliable and scalable. However, the preparation of the computational domain, the mesh, is currently a limiting factor. In particular, the generation of the volume mesh is a challenge. A possible solution to this problem could be based on adaptive mesh refinement. Starting from a relatively coarse mesh, a well-resolved mesh could be computed iteratively while at the same time assessing the error of the numerical solution. In distributed memory settings, specialised algorithms and data structures are required to handle mesh adaptation [373]. In *NGSolve*, this functionality is not yet available.

A challenge will be the meshing of detailed 3D images of real cartilage samples. Recently, 3D images of a few thousand chondrocytes in collagen scaffolds have been obtained within the SFB 1270 ELAINE [374]. It has to be clarified if, as in this work, ellipsoids can be used to approximate the cells. Alternatively, the 3D images can be segmented by standard image processing techniques. In any case, a volume mesh has to be generated subsequently.

Another possible numerical method could be the boundary element method (BEM), which requires only surface meshes. In my experience, the generation of surface meshes is less complex than the generation of volume meshes. However, the BEM leads to dense matrices and requires the development of efficient solvers. Recently, the BEM has been considered for detailed geometries and has been shown to be competitive in comparison to FEM approaches [375]. It has to be investigated if this also holds true for the considered thin layer approximation.

Another limitation of the presented work is the focus on cells exposed to homogeneous fields. Nevertheless, the presented approach can be straightforwardly used for arbitrary electrode geometries. The electrode has to be integrated into the geometrical model. Ideally, this can be done based on medical imaging, too.

As the thin layer approximation inherently contains the transmembrane potential, it can be straightforwardly estimated from the computed solution. Here, I do not want to go further into details regarding the stimulation aspect as it is not clear if the transmembrane potential or another quantity is crucial for a biological response. However, the presented computational solution permits to estimate the transmembrane potential for each individual cell. In a second step, a distribution of, for example, the maximum transmembrane potential or an analysis of areas with a decreased transmembrane potential could be identified. Nevertheless, I believe that such simulation results have to be corroborated by experiments, which are currently not available or not feasible.

In the meantime, the presented models can help to improve the understanding

of EIS experiments. Combining imaging and EIS can pave the way for clarifying the ambiguity in the interpretation of the dielectric properties. With the presented numerical solutions, a fine-grained model of tissues can be built and the computed impedance can be compared to measured EIS spectra. As deviations regarding the strength of the dispersions in cartilage were detected in this work, this approach will most likely also require to analyse the different phases of the material independently (i.e., extracellular matrix, pericellular matrix and the cells) to improve the numerical models. Once this approach is established, an application in cartilage tissue engineering could be, for example, the detection of pericellular matrix formation, which takes about four weeks in artificial cartilage constructs (cell-seeded agarose) [376], by impedance spectroscopy. Another possibility is to improve cell tracking based on impedance spectroscopy [377] by linking detailed numerical models to the recorded impedance spectra. It has been shown that osteogenic differentiation of human mesenchymal stem cells can be detected by EIS [378]. A similar approach should be developed for cartilage tissue engineering to closely monitor the proliferation of chondrocytes and chondrogenic differentiation of mesenchymal stem cells by EIS. Numerical simulations can help to understand if the changes in the EIS spectra upon proliferation or differentiation are caused by morphological changes or altered dielectric properties.

As presented in Chapter 5, the EIS measurements can straightforwardly be combined with electrical stimulation. The main advantage of the example considered in this work was that an analytical suspension model provided a good approximation of the impedance spectrum. It has to be clarified if such simple approximations are generally possible. If yes, then they could be employed in, for example, multilevel algorithms for UQ or inverse problems (i.e., parameter estimation) [379]. Hence, they could pave the way for fast, patient-specific solutions. For example, the information provided by cell-scale medical images and impedance spectra of the patient's cartilage could be used to determine the dielectric properties. The dielectric properties are then employed in macroscale models of an electrical stimulation device for cartilage regeneration.

8 Conclusions and Outlook

Cartilage tissue engineering is an open challenge. Its solution is required to tackle health issues such as osteoarthritis, which is increasingly occurring in an ageing society. The low intrinsic healing capacity of cartilage requires external stimuli to be administered. In this work, the focus was laid on electrical stimulation as a biophysical intervention. Combined with other tissue engineering approaches (e.g., hydrogels) it may be a suitable approach for cartilage tissue engineering. To date, the research in this area has focussed on experimental approaches, which are mostly dominated by trial-and-error. Numerical simulations can contribute to an understanding of the interaction of cartilage and its cells with the electric field. Moreover, well-controlled experiments can be developed by exchanging information between numerical models and measurements. On the way to reliable numerical modelling of electrical stimulation for cartilage tissue engineering, three main questions were tackled in this work:

1. What is required to build a reliable numerical model of an electrical stimulation experiment?

2. Which physical markers can be linked to a biological response and how reliably can they be computed?

3. Which numerical methods are capable of describing the interaction of electric fields and realistic, fine-grained tissue geometries?

The first research question was subject of Chapter 5. It was demonstrated how a numerical model of an in vitro electrical stimulation experiment can be built. Experimental strategies to validate the model were presented. A special focus was laid on the possibility to use only macroscopic observables (e.g., current or impedance) to ensure reliable estimation of microscopic quantities (e.g., electric field or current density). Options to integrate relevant electrochemical effects at the ESI into the numerical models were compared and successfully applied. UQ was used to identify the most crucial model parameters and at the same time to permit a meaningful comparison of experimental and numerical results. The resulting workflow was successfully applied to two electrical stimulation setups with potential applications in cartilage tissue engineering. It was demonstrated that electrochemical and thermal processes can be identified under certain conditions by monitoring relevant observables during the stimulation experiment. The numerical models were calibrated using the experimental data. Finally, this permitted to establish a so-called digital twin of the electrical stimulation device. A digital twin bridges the gap between theory and experiment. It integrates the numerical simulations into the experimental reality and provides means to dynamically update the numerical model. In my opinion, it is inevitable to develop a digital twin for every electrical stimulation

device for cartilage tissue engineering for two reasons. Firstly, it helps to ensure that only the effect of the electrical stimulation is studied. For example, temperature changes of the cell culture medium can be detected during the experiment. As the temperature change may have an impact on the biological response of the cells and also on the applied electrical stimulus, the results of such an experiment could be marked as outliers and excluded from the analysis. Secondly, a digital twin offers a way out of the so-called replicability crisis. To date, many reports of electrical stimulation for application in cartilage tissue engineering are incomplete and hence not replicable. As the digital twin involves a validated model and monitoring of the electrical stimulation experiment, it automatically provides a detailed and complete description of the experiment. Two aspects have to be considered in future research if direct contact electrical stimulation is used for cartilage tissue engineering. On the one hand, the stimulation electrodes will most likely corrode the longer they are in contact with the biological sample. This is, for example, known from applications in DBS [380]. Hence, electrochemically stable electrodes have to be employed or strategies to refresh the electrodes have to be developed. On the other hand, the cutoff frequency related to electrochemical effects at the ESI has been identified as a major source of uncertainty regarding the numerically estimated stimulation characteristics (e.g., the electric field). Recent developments have explored modifications of the electrode surface by nanotechnology to reduce the cutoff frequency [381, 382]. Modified electrodes with a cutoff frequency significantly lower than the stimulation frequency should be used. In this case, the numerical simulations become predictive without experimental calibration if the geometry and dielectric properties of the simulation domains are sufficiently well known. An open challenge is the modelling of stimulation with DC signals. Due to complex time-dependent, nonlinear electrochemical processes, it is not yet feasible to develop detailed 3D models.

This work followed a top-down approach. In my opinion, this is the most natural approach as it establishes first a macroscale model of the electrical stimulation device before studying the effects at the cellular scale (and in future probably also molecular scale). In Chapter 6, answers to the second research question have been explored. Often, the transmembrane potential has been considered as a physical marker to be linked to the biological response to electrical stimulation. This had been done, for example, for capacitively coupled electrical stimulation, which is to date a common choice for electrical stimulation in cartilage tissue engineering. In this work, I extended these models from 2D to 3D and investigated different scenarios. Hypotheses for future experiments could be derived from the results. It will be essential to measure the transmembrane potential. In the numerical models, a cutoff effect was observed that suggests a significant induced transmembrane potential only above certain frequencies. This cutoff frequency is increased by an increased membrane conductivity or by a conductive environment around the cell. This hypothesis questions that the observed biological effect (e.g., increased proliferation or re-differentiation) is linked to changes in the transmembrane poten-

tial. Instead, electromechanical effects could play a role. They were not investigated in greater detail and are left for future research. The exact interaction between electric fields and biological structures has been a matter of discussion for decades already. For example, certain animals are capable of sensing extremely small electric fields, which cannot yet be explained by physical theories [383, 384]. A possible solution to this dilemma could be to perform more physical measurements together with biological investigations. The increased amount of data together with computational methods could lead to novel hypotheses as has been argued for other biological fields [385]. Exemplarily, bioinformatics studies of cellular processes could help to link the involved genes to the effect of electrical stimulation. Such an approach has been pursued for epidermal cells [386].

A possibility to develop a detailed understanding of electrical stimulation for cartilage tissue engineering are fine-grained tissue models. As these models involve thousands of cells, suitable numerical methods have to be identified. This aspect, which reflects the third research question, was investigated in Chapter 7. An additional motivation for such detailed models was the uncertainty and ambiguity of the tissue dielectric properties, which were explained in detail therein. Realistic cartilage geometries were generated based on a statistical description. The resulting models had about 10^8 DOFs, which requires HPC solutions. A scalable parallel solver was implemented and tested. In principle, this solver can be reused for an even larger amount of cells. However, it turned out that the mesh generation is error-prone. It has to be improved in future research. Furthermore, cartilage geometries were not directly derived from medical images and only homogeneous fields were applied. Nevertheless, the results suggested that the dielectric properties of cartilage tissue can be described by an analytical cell suspension model. This would reduce the computational complexity drastically. Moreover, a digital twin could be established in future research. For that, more experimental data are required. In particular, impedance spectra and detailed 3D images of the same sample have to be acquired. Subsequently, a large amount of open questions can be tackled by the presented workflow. For example, donor-specific variations of the cell samples are to be investigated with respect to, among others, age and state of the cartilage tissue.

Given that attempts for electrical stimulation for bone and cartilage stimulation have been made since the 1970's [49, 387], the question arises why there are still no clinically approved solutions available while, for example, DBS has made much more progress in roughly the same time. One reason for this status quo is the lack of biophysical information about the electrical stimulation experiments. With this work I hope to have advanced the field by suggesting reliable, reproducible and adaptable numerical models of the electrical stimulation for use in cartilage tissue engineering.

A Implementation of weak forms

A.1 Electroquasistatics

An example of the *NGSolve* implementation of the EQS weak form (Eq. (3.3)) for a simple unit square geometry is given in Listing A.1.

```
# import ngsolve
import ngsolve as ngs
# import Netgen function to generate a unit_square
from netgen.geom2d import unit_square

# mesh the geometry
# it has 4 marked boundaries called:
# 'bottom', 'right', 'top', 'left'
mesh = ngs.Mesh(unit_square.GenerateMesh(maxh=0.4))

# create a complex-valued 1st-order H1-conforming function space
# Dirichlet BCs are assigned to top and bottom
fes = ngs.H1(mesh, order=1, dirichlet="bottom", complex=True)

# get the test and trial functions associated with the
# function space
Phi, v = fes.TnT()

# assign conductivity, Neumann coefficient,
# and surface impedance for Robin BC
# see Eq. 3.3
sigma = ngs.CoefficientFunction(1.0 + 1.0j)
# insulating Neumann
g = ngs.CoefficientFunction(0.0)
# surface admittance on top electrode
p = ngs.CoefficientFunction(1.0 + 1.0j)
# voltage on top electrode
Phi_fixed = ngs.CoefficientFunction(1.0)

# create the bilinear form
a = ngs.BilinearForm(fes)
a += sigma * ngs.grad(Phi) * ngs.grad(v) * ngs.dx
# Robin BC on left boundary
a += p * Phi * v * ngs.ds("top")

# create the linear form
f = ngs.LinearForm(fes)
# Neumann BC on right boundary
f += g * v * ngs.ds("right")
# Robin BC on left boundary
f += p * Phi_fixed * v * ngs.ds("top")

```

```
# assemble linear system
a.Assemble()
f.Assemble()

# create solution vector and assign
# Dirichlet BCs
gfu = ngs.GridFunction(fes)
bndcf = mesh.BoundaryCF({"bottom": 0.0})
gfu.Set(bndcf, ngs.BND)

# solve linear system for free dofs
# and construct full solution under consideration
# of Dirichlet BCs
r = f.vec.CreateVector()
r.data = f.vec - a.mat * gfu.vec
# a direct solver is used
gfu.vec.data += a.mat.Inverse(freedofs=fes.FreeDofs()) * r
# Draw solution
ngs.Draw(gfu)
```

Listing A.1: Example of the FEM implementation in *NGSolve*.

A.2 Floating potential

The implementation for the floating potential conditions described in Sec. 3.1.2 are shown. In Listing A.2, *NGSolve* code for a perfectly conducting electrode without surface impedance is given while Listing A.3 treats the same geometry with a surface impedance. The geometry is a cylinder in an external homogeneous field represented by a 2D domain. The simulation results are shown in Fig. A.1. For comparison, the result of a perfectly insulating cylinder (i.e., with infinitely large surface impedance is shown). Evidently, the surface impedance mediates a behaviour between perfect conductor and perfect insulator while keeping the voltage to be measured accessible.

```
from ngsolve import *
# import Netgen occ module
import netgen.occ as occ

# prepare geometry
unit_square = occ.unit_square_shape
innercircle = occ.Circle(c=(0.5, 0.5), r=0.25).Face()
# name boundaries
for e in innercircle.edges:
    e.name = "Float"
geo = unit_square - innercircle

# FEM order
order = 2

```

```
# mesh the geometry
# it has 5 marked boundaries called:
# 'bottom', 'right', 'top', 'left', 'Float'
occgeo = occ.OCCGeometry(geo, dim=2)
with TaskManager():
    mesh = Mesh(occgeo.GenerateMesh(maxh=0.2))
    mesh.Curve(order)
Draw(mesh)

# set boundary values
cf = mesh.BoundaryCF({"top": 1.0, "bottom": 0.0, "Float": 2.0},
   default=-1)
Draw(cf, mesh, "BND")

# define function spaces
# H1-conforming space
V = H1(mesh, order=order,
       dirichlet="top|bottom")
# Lagrange multiplier on floating electrode
order_lam = order - 1
lm = SurfaceL2(mesh, order=order_lam, definedon=mesh.Boundaries("
   Float"))
# floating potential
Vfixed = NumberSpace(mesh, order=0, definedon=mesh.Boundaries("
   Float"))
# compound space
fes = FESpace([V, Vfixed, lm])
fes = CompressCompound(fes)

# bilinear and linear forms
u, ufix, lam = fes.TrialFunction()
v, vfix, mu = fes.TestFunction()

a = BilinearForm(fes)
a += grad(u) * grad(v) * dx

a += (u * mu + v * lam) * ds("Float")
a += -(ufix * mu + vfix * lam) * ds("Float")

f = LinearForm(fes)
f += 0.0 * v * dx
f += 0.0 * vfix * ds("Float")

# solution function
gfu = GridFunction(fes)

# assemble linear system
with TaskManager():
    a.Assemble()
    f.Assemble()
```

```
    gfu.components[0].Set(cf, BND)

# solve linear system
# the direct solver MUMPS is used
with TaskManager():
    res = f.vec.CreateVector()
    res.data = f.vec - a.mat * gfu.vec
    gfu.vec.data += a.mat.Inverse(fes.FreeDofs(), inverse="mumps")
   * res

# post-processing
sol = gfu.components[0]
Draw(sol)
print("Floating potential: ", gfu.components[1].vec)
field = -grad(sol)
Draw(field, mesh, "field")
```

Listing A.2: Example of the FEM implementation of floating potentials without a surface impedance in *NGSolve*.

```
from ngsolve import *
# import Netgen occ module
import netgen.occ as occ

# surface impedance
zl = 1.0

unit_square = occ.unit_square_shape
innercircle = occ.Circle(c=(0.5, 0.5), r=0.25).Face()
# name boundaries
for e in innercircle.edges:
    e.name = "Float"
geo = unit_square - innercircle

# FEM order
order = 2

# mesh the geometry
# it has 5 marked boundaries called:
# 'bottom', 'right', 'top', 'left', 'Float'
occgeo = occ.OCCGeometry(geo, dim=2)
with TaskManager():
    mesh = Mesh(occgeo.GenerateMesh(maxh=0.2))
    mesh.Curve(order)
Draw(mesh)

# set boundary values
cf = mesh.BoundaryCF({"top": 1.0, "bottom": 0.0, "Float": 2.0},
   default=-1)
Draw(cf, mesh, "BND")

```

```
# define function spaces
# H1-conforming space
V = H1(mesh, order=order,
       dirichlet="top|bottom")
# floating potential
Vfixed = NumberSpace(mesh, order=0, definedon=mesh.Boundaries("
   Float"))
# compound space
fes = FESpace([V, Vfixed])

# bilinear and linear forms
u, ufix = fes.TrialFunction()
v, vfix = fes.TestFunction()

a = BilinearForm(fes)
a += grad(u) * grad(v) * dx
a += 1. / zl * (u - ufix) * (v - vfix) * ds("Float")

f = LinearForm(fes)
f += 0.0 * v * dx
f += 0.0 * vfix * ds("Float")

# solution function
gfu = GridFunction(fes)

# assemble linear system
with TaskManager():
    a.Assemble()
    f.Assemble()
    gfu.components[0].Set(cf, BND)

# solve linear system
# the direct solver MUMPS is used
with TaskManager():
    res = f.vec.CreateVector()
    res.data = f.vec - a.mat * gfu.vec
    gfu.vec.data += a.mat.Inverse(fes.FreeDofs(), inverse="mumps")
   * res

# post-processing
sol = gfu.components[0]
Draw(sol)
print("Floating potential: ", gfu.components[1].vec)
field = -grad(sol)
Draw(field, mesh, "field")
```

Listing A.3: Example of the FEM implementation of floating potentials with a surface impedance in *NGSolve*.

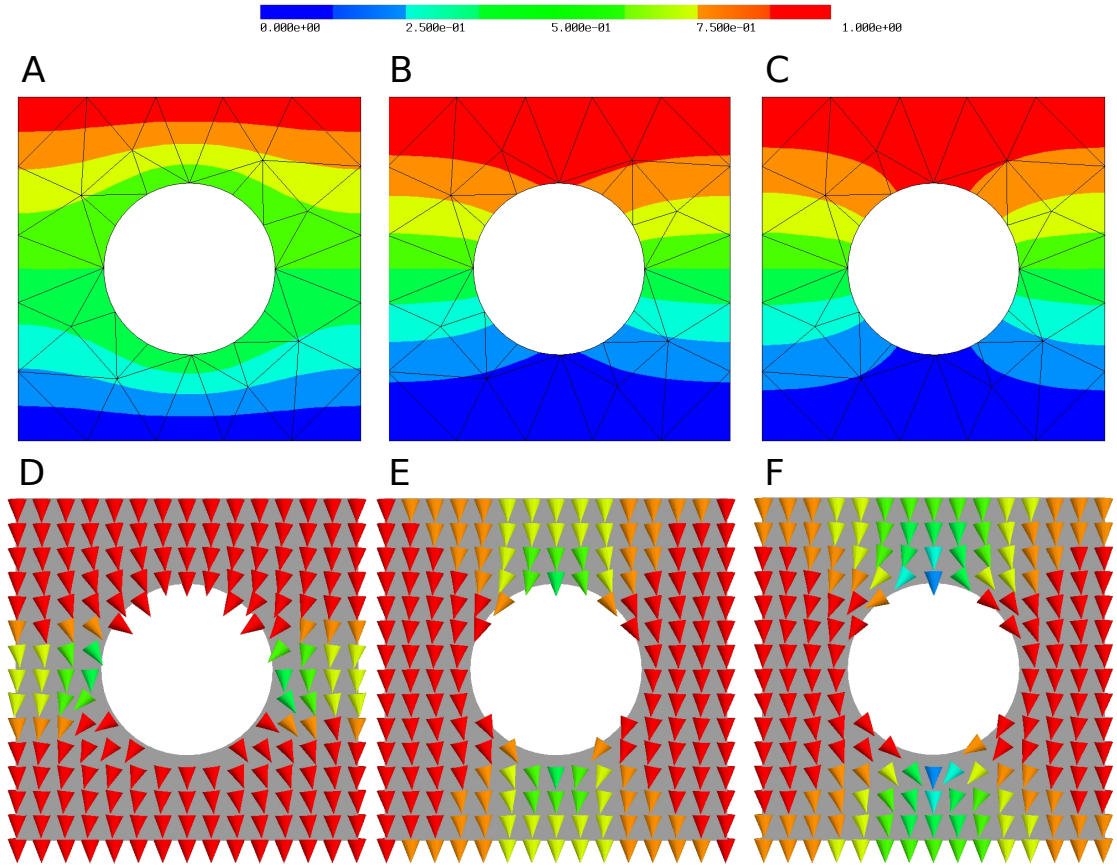

Figure A.1: Comparison of different FEM formulations for a cylinder in an external homogeneous field (mediated by Dirichlet boundary conditions). The potential is shown for a perfect conductor (**A**), a surface impedance of 1 on the cylinder (**B**) and a perfect insulator (**C**). The corresponding electric field is shown in **D**–**F**. Obviously, a perfect conductor bends the field inwards such that the current flows towards the cylinder. On the other hand, a surface impedance or a perfect insulator force the field to go around the cylinder.

A.3 Thin layer approximation

To test the implementation of the thin layer approximation (Eq. (3.9)) in *NGSolve*, a numerical experiment using an analytical solution was conducted. The same example as in [204] was chosen (i.e., a disc of radius 1.5 with the unit circle as the subdomain 1 and the remaining part of the geometry the subdomain 2). The analytical solution reads

$$\Phi_1 = a(x^2 - y^2) \tag{A.1}$$

$$\Phi_2 = (x^2 - y^2)\left(b + \frac{c}{(x^2 + y^2)^2}\right) \tag{A.2}$$

with the Dirichlet BC

$$\Phi_2 = \frac{4}{9}(x^2 - y^2) \quad \text{on} \quad \partial\Omega. \tag{A.3}$$

The conductivities are $\sigma_1 = 1$ and $\sigma_2 = 100$ and the contact impedance is $z_1 = 2$. The coefficients a, b, c of Eq. (A.2) are computed such that the solutions on the subdomains fulfil both the interface condition and the Dirichlet BC. In practice, I used the symbolic computing library *SymPy* to determine the coefficients [388].

The implementation (Listing A.4) was tested for curved H^1-conforming elements up to third order. All simulations were performed using version 6.2.2201 of *NGSolve*.

```
# discretization order (used for FESpace and for geometry approximation):
order = 2

# Creates function spaces
fes_out = H1(mesh, order=order, definedon="out", definedonbound="interface", dirichlet="outer")
fes_in = H1(mesh, order=order, definedon="in", definedonbound="interface")

fes = fes_out * fes_in
fes = CompressCompound(fes)

(u_out, u_in) = fes.TrialFunction()
(v_out, v_in) = fes.TestFunction()

# cofficients for the subdomains
ki = 1.0
ke = 100.
sigvals = {"in": ki, "out": ke}
sig = mesh.MaterialCF(sigvals, default=0)

# interface resistance
R = 0.5

```

```
# Bilinear form:
a = BilinearForm(fes)
a += sig * grad(u_out) * grad(v_out) * dx("out")
a += sig * grad(u_in) * grad(v_in) * dx("in")

# Interface condition
a += 1. / R * (u_out - u_in) * (v_out - v_in) * ds("interface")

# Linear form
f = LinearForm(fes)
f += 0.0 * v_out * dx("out")
f += 0.0 * v_in * dx("in")
```

Listing A.4: Core part of the FEM implementation of the thin layer approximation in *NGSolve*. The example was compared to the analytical solution as described in [204].

The solution is discontinuous at the outer boundary of the inner circle (Fig. A.2). As expected, the optimal order of convergence was observed (Fig. A.3). Furthermore, the importance of the curved elements becomes evident.

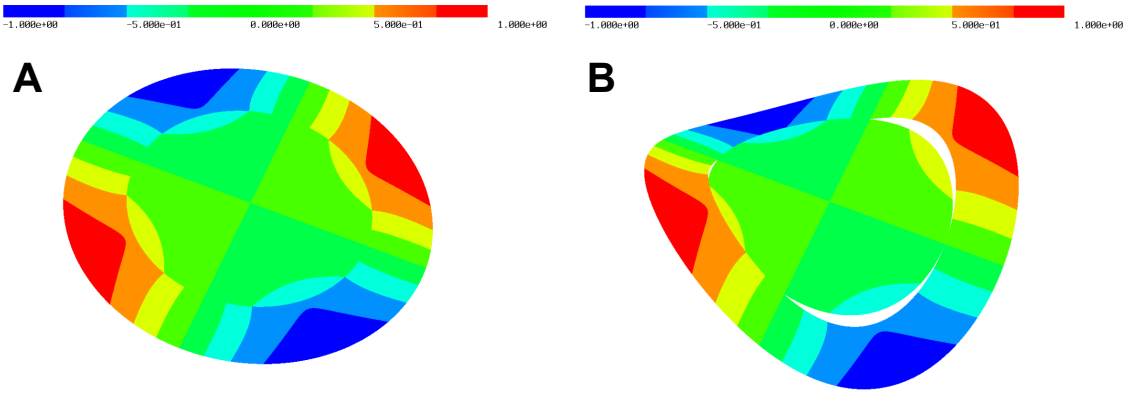

Figure A.2: **A**: Numerical solution of the benchmark problem. **B**: Deformed solution to highlight the discontinuity.

A.3.1 Cell geometries

The analytical solution of Laplace's equation for a spherical cell in an external homogeneous field is, for example, described in [166, 389]. The analytical solution of the boundary value problem of a spherical dielectric in an external homogeneous field is also extensively explained in the textbook by Jackson [3].

For cell geometries, the analytical solution is formulated for all subdomains, for example, the cytoplasm, the cell membrane and the extracellular medium. However, the cell membrane can be accounted for by the interface condition Eq. (2.21) in the analytical solution [166]. Then, the solution does not have to be determined for

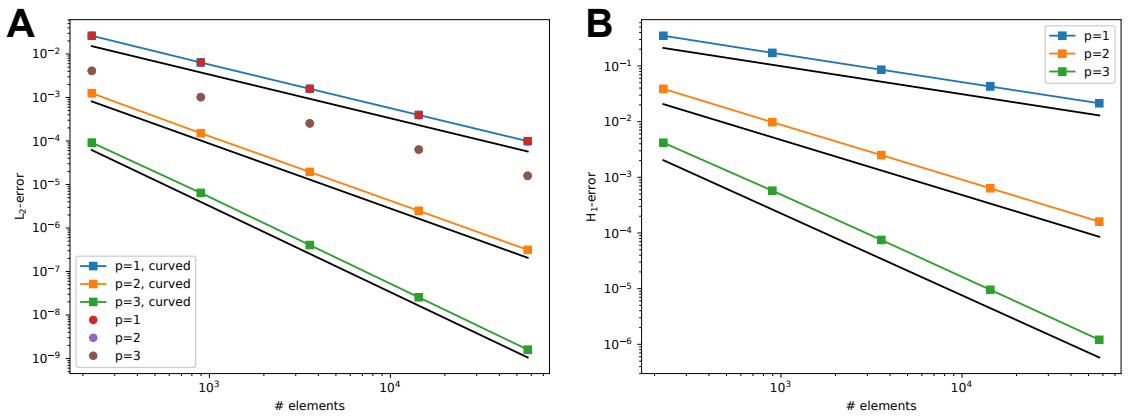

Figure A.3: **A**: Comparison of the L_2-error with curved (filled squares) and uncurved elements (filled circles). **B**: H_1-error with curved elements. The expected optimal order of convergence is indicated by black lines. The chosen polynomial order is indicated by p.

the membrane but only for the cytoplasm and extracellular medium. As this case corresponds to the numerical approach, I used it to verify the implementation in *NGSolve*.

Again, the solutions on the subdomains (inside the cell and outside the cell) feature unknown coefficients as in Eq. (A.2). Given the interface conditions and BCs, these coefficients can be determined from a linear system of equations [389]. I used *SymPy* to solve the linear system of equations. To obtain the analytical solution for a spherical cell with a spherical nucleus or with a cell wall, additional subdomains with respective solutions are introduced and the linear system of equations is constructed according to the interface conditions and BCs.

Because most of the actually implemented solvers assume convergence or focus only on the transmembrane potential, I wanted to check the convergence of the entire solution. I studied the model of a single cell with only the cell membrane in an external homogeneous electric field (also referred to as the single shell model). The cell had a radius of 5 µm and the extracellular space was a cube with edge length 20 µm. The dielectric properties of the cell membrane and cytoplasm were chosen as specified in Table 7.2. The extracellular conductivity was chosen as $1.0\,\mathrm{S\,m^{-1}}$ and the extracellular permittivity as 80. The solution was computed for the steady-state case and a frequency of 10 MHz. The same iterative solver and preconditioner as in Sec. 7.4 was used. In both considered cases, optimal convergence could be observed (Fig. A.4). However, the residual of the iterative solver had to be chosen sufficiently small to ensure an accurate computation.

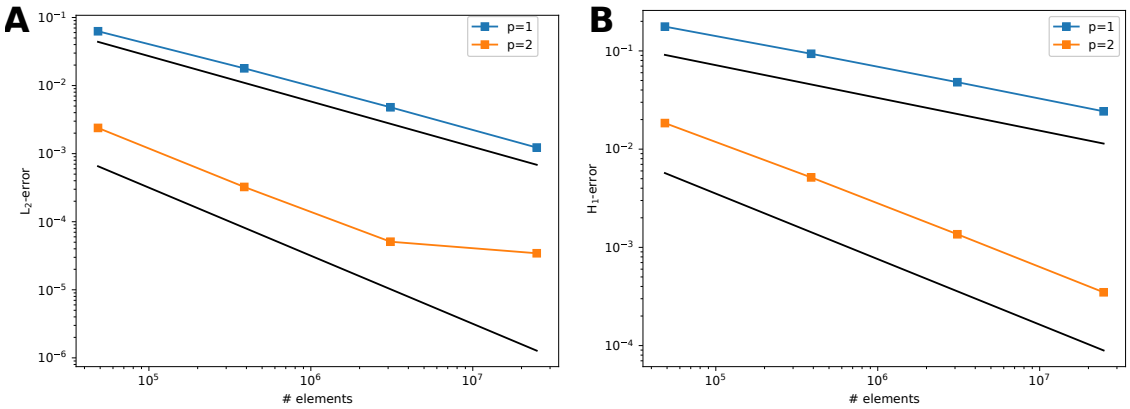

Figure A.4: The convergence of the numerical solution for a single cell with only the cell membrane in an external homogeneous field at steady state was assessed by computing the L_2-error (**A**) and H_1-error (**B**). Curved elements were used when reasonable. The expected optimal order of convergence is indicated by black lines. The chosen polynomial order is indicated by p. Please note that the deviation from optimal order of convergence for the L_2-error at the last refinement stage is most likely due to the accuracy of the employed iterative solver. The frequency-dependent solution did not converge differently and is thus not shown separately.

A.3.2 Generation of cartilage geometries

In Listing A.5, an exemplary layout file to generate a cartilage sample comprising three layers using the scripts provided by Bennetts *et al.* [367].

```
# outer dimensions of sample
200.0 200.0 2400.0
# depth of first zone
0.0 1920.0
# mean chondron density and standard deviation
7000 700
# mean cells per chondron and standard deviation
6 2
# cell radii in x-, y-, z-direction
# and standard deviation
7.0 7.0 7.0 0.75
# PCM thickness and standard deviation
2.5 0.25
# second layer
1920.0 2160.0
10262 466
1 0
7.0 7.0 7.0 0.75
2.5 0.25
# third layer
2160.0 2400.0
```

```
24018 3188
1 0
8.5 3.5 3.5 0.85
2.5 0.25
```

Listing A.5: Example script to create a cartilage geometry with three zones. More details on the implementation can be found in [367].

B Fitting impedance spectra

When fitting impedance spectra, it is important to identify suitable equivalent circuit models. Usually, a combination of capacitive and resistive elements is chosen. If applicable, inductive elements are integrated into the circuit. An overview of typical frequency responses of the basic elements is given in Fig. B.1. The magnitude and phase of the impedance (not shown) can indicate which element to choose. For example, an initially capacitive impedance (i.e., with a phase close $-90°$) turning into a mostly real-valued impedance indicates a capacitor connected in series with a resistor. If the phase becomes positive at higher frequencies, an inductance should be added to the circuit. In (bio-)electrochemistry, models such as the CPE or Cole-Cole models play a role [111]. A typical example of a combination of the two models is given in Fig. B.2. Evidently, the individual contributions can be identified by looking for typical patterns of the respective elements in the Nyquist plot (e.g., a straight line for a CPE or an arc for a Cole-Cole element).

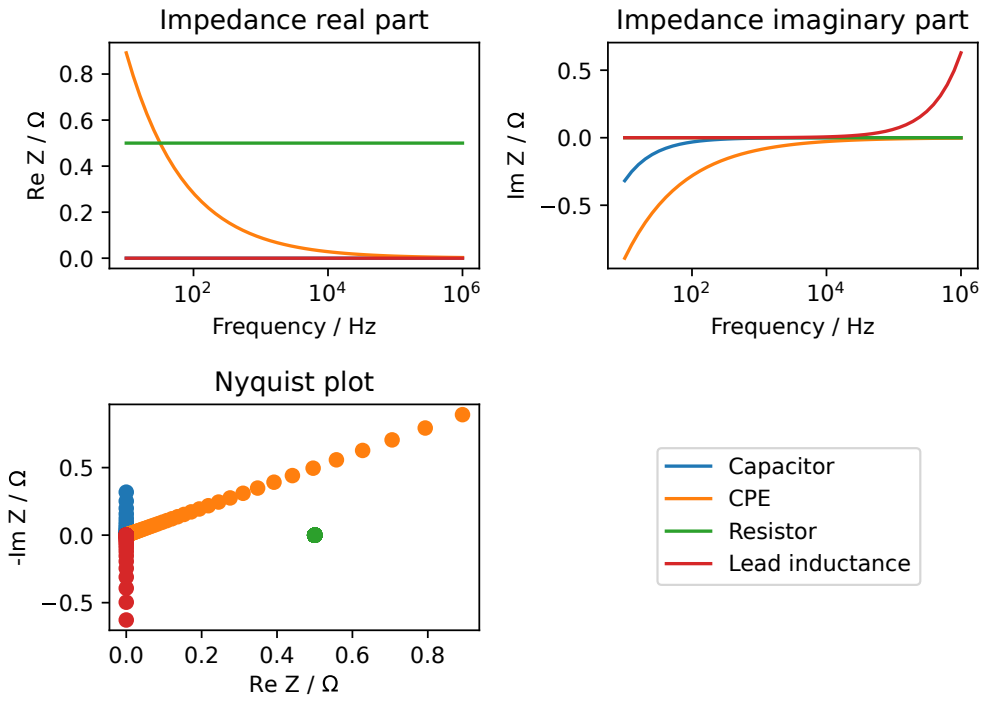

Figure B.1: Exemplary impedance of basic circuit elements over a typical frequency range: a capacitor of 50 mF, a CPE (described by $\kappa(j\omega)^{-\alpha}$) with $\kappa = 10$ and $\alpha = 0.5$, a resistor of 0.5 Ω and a lead inductance of 100 nH. The values were chosen arbitrarily. The capacitor has a complex-valued impedance with zero real part and negative imaginary part, which appears as vertical line in the Nyquist plot. The CPE has a complex-valued impedance with both non-zero real and imaginary part, which appears as a straight line with a fixed slope starting from the origin in the Nyquist plot. The resistor has a real-valued impedance, which appears as a single point in the Nyquist plot. The inductance has a complex-valued impedance with zero real part and positive imaginary part, which appears as vertical line in the Nyquist plot. The impedance response of a real system is given by linear and parallel combinations of these basic elements. This figure was taken from the supplementary material of [245].

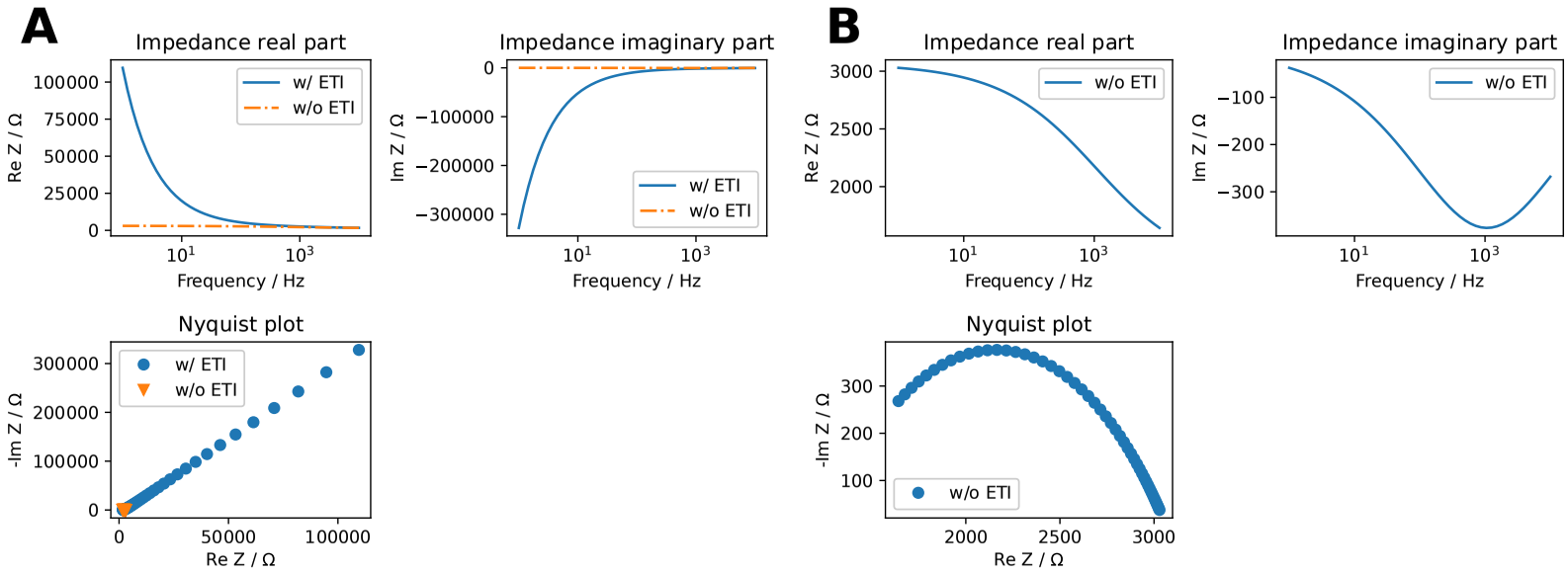

Figure B.2: The model with the respective values reported in [390] was used to plot the impedance of a rhesus macaque's brain one day after DBS implantation. In **A**, the full model comprising a CPE to account for the ETI in series with a Cole-Cole element is compared to the tissue model (i.e., only the Cole-Cole element). As the ETI impedance dominates, the Cole-Cole impedance is shown individually in **B**. There, the characteristic arc shape is revealed in the Nyquist plot, which cannot be identified in **A**.

C Fourier series approach to describe time-domain signals

This section has been published in similar form as part of the Supplementary Material of [245], which is available online[1].

The complex-valued Fourier series of a signal f is given as

$$f(t) = \sum_{k=-\infty}^{\infty} c_k e^{jk\omega_0 t} \ , \tag{C.1}$$

where t is the time, ω_0 the fundamental angular frequency and c_k are the complex-valued Fourier coefficients. The corresponding fundamental frequency is here denoted by f_0.

For a monophasic rectangular pulse of amplitude A and pulse width t_p, the Fourier coefficients read

$$c_k = A t_p f_0 \operatorname{sinc}(k t_p f_0) \ . \tag{C.2}$$

Note that in this particular case, the coefficients c_k are real-valued. A general recipe to compute the coefficients can be found in textbooks (e.g., in [113]). The amplitude of the frequency components A_k, which is relevant to estimate the strength of each harmonic, is given by

$$A_k = 2|c_k| \ \forall \ k > 0 \ \text{ and } \ A_0 = c_0 \ . \tag{C.3}$$

The DC component (c_0) is only determined by the amplitude, pulse width and fundamental frequency

$$c_0 = A t_p f_0 \ . \tag{C.4}$$

In practice, the signal can be constructed using

$$f(t) = c_0 + 2 \sum_{k=1}^{\infty} c_k e^{jk\omega_0 t} \tag{C.5}$$

because the negative k-values would only affect the imaginary part.

Using this information, a biphasic rectangular pulse can be easily constructed as a superposition of two monophasic square waves. The square waves have to be time-shifted and their amplitudes need to have opposite signs. A time shift of the signal by t_s can be achieved by multiplying Eq. (C.2) by $e^{-jk\omega_0 t_s}$. For a biphasic pulse, the time shift has to be equal to the pulse width t_p. Writing the signals as a function $f(t, A, f_0, t_p, t_s)$, the signal of the biphasic rectangular pulse reads

$$f(t, A, f_0, t_p, 0) = f(t, A, f_0, t_p, 0) + f(t, -A, f_0, t_p, t_p) \ . \tag{C.6}$$

[1] `https://www.frontiersin.org/articles/10.3389/fbioe.2021.765516/full#supplementary-material`

The amplitudes at the respective frequencies can then be obtained from Eq. (C.3). Similarly, a biphasic pulse with delay t_D can be constructed by

$$f(t, A, f_0, t_p, 0) = f(t, A, f_0, t_p, 0) + f(t, -A, f_0, t_p, t_p + t_D) \ . \tag{C.7}$$

Obviously, in both pulses the DC component cancels out because it only depends on amplitude and pulse width.

The presented approach is numerically very simple to implement and permits more flexibility than deriving the analytical presentation for each waveform. A drawback of the Fourier series approach are large oscillations that occur at the jumps of the square waves (the so-called Gibbs phenomenon). The oscillations can be attenuated using the Lanczos sigma factor in the summation [391].

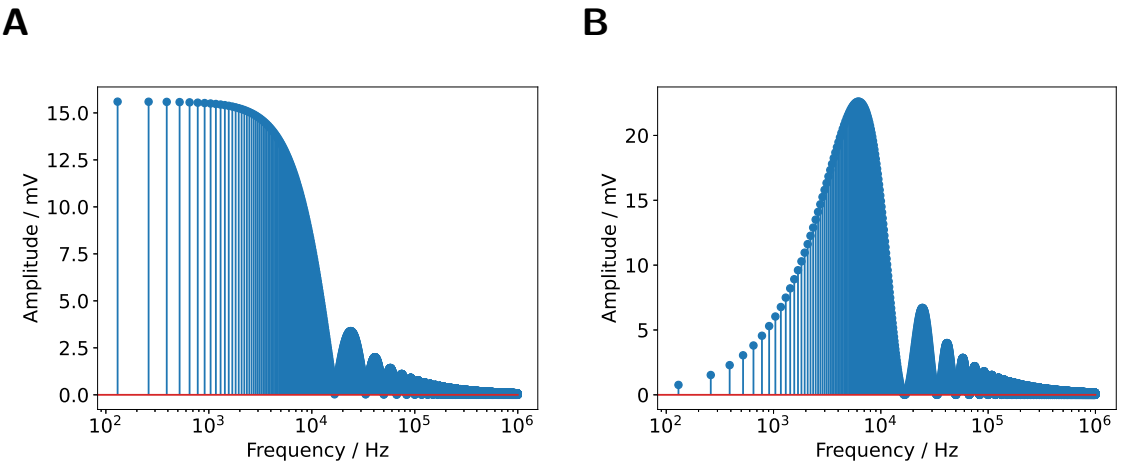

Figure C.1: Fourier coefficients for a pulse width of 60 µs. (**A**): monophasic pulse, (**B**): biphasic pulse. The DC component of the monophasic pulse is 7.8 mV.

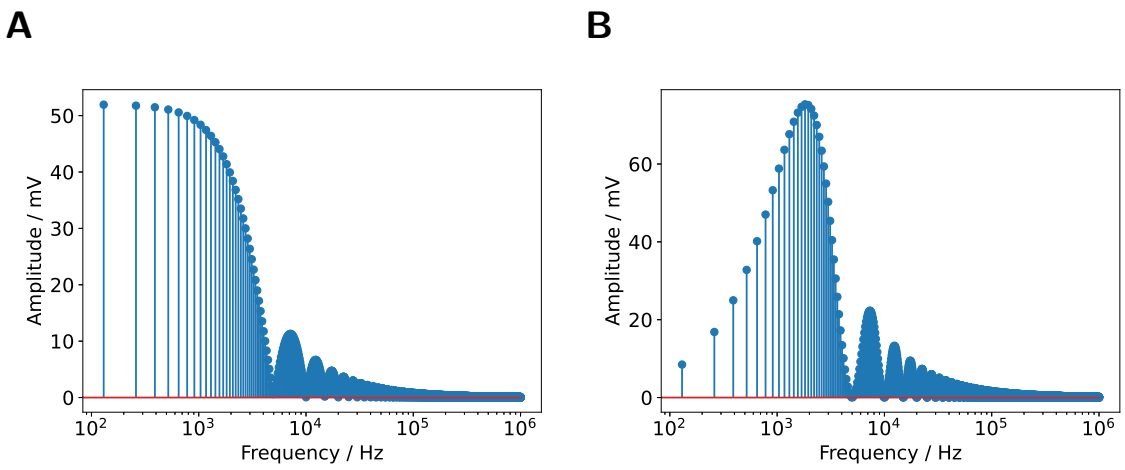

Figure C.2: Fourier coefficients for a pulse width of 200 µs. (**A**): monophasic pulse, (**B**): biphasic pulse. The DC component of the monophasic pulse is 26 mV.

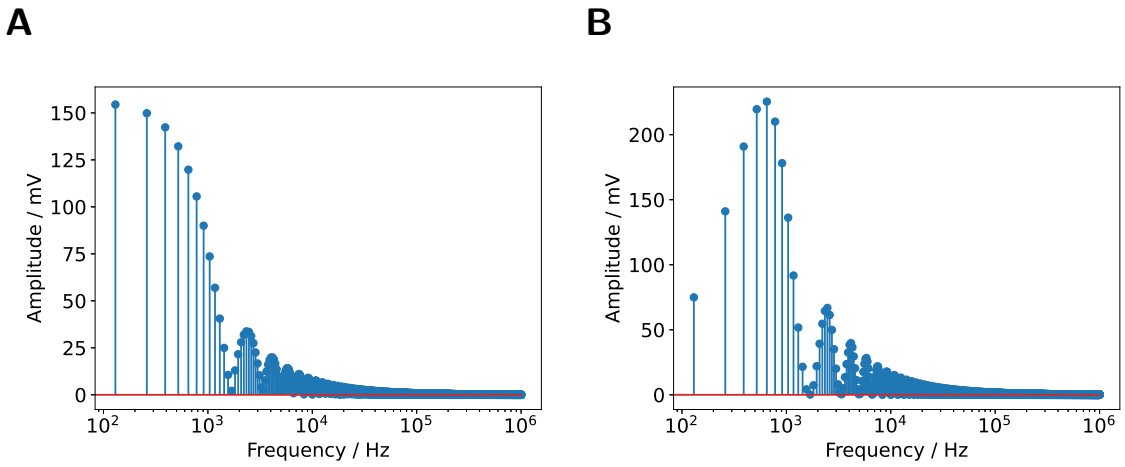

Figure C.3: Fourier coefficients for a pulse width of 600 µs. (**A**): monophasic pulse, (**B**): biphasic pulse. The DC component of the monophasic pulse is 78 mV.

Bibliography

[1] Raicu, V. and Feldman, Y., editors. *Dielectric Relaxation in Biological Systems*. Oxford University Press, Oxford, UK, 2015. doi: 10.1093/acprof:oso/9780199686513.001.0001.

[2] Harrington, R.F. *Time-Harmonic Electromagnetic Fields*. IEEE Press Series on Electromagnetic Wave Theory. IEEE Press: Wiley-Interscience, 2001.

[3] Jackson, J.D. *Classical electrodynamics*. Wiley, New York, NY, 3rd edition, 1999.

[4] Armiento, A.R., Alini, M. and Stoddart, M.J. Articular fibrocartilage - Why does hyaline cartilage fail to repair? *Advanced Drug Delivery Reviews*, 146: 289–305, 2019. doi: 10.1016/j.addr.2018.12.015.

[5] Huey, D.J., Hu, J.C. and Athanasiou, K.A. Unlike Bone, Cartilage Regeneration Remains Elusive. *Science*, 338(6109):917–921, 2012. doi: 10.1126/science.1222454.

[6] Fox, A.J.S., Bedi, A. and Rodeo, S.A. The basic science of articular cartilage: Structure, composition, and function. *Sports Health*, 1(6):461–468, 2009. doi: 10.1177/1941738109350438.

[7] Getgood, A., Bhullar, T.P. and Rushton, N. Current concepts in articular cartilage repair. *Orthopaedics and Trauma*, 23(3):189–200, 2009. doi: 10.1016/j.mporth.2009.05.002.

[8] Farooqi, A.R., Bader, R. and van Rienen, U. Numerical Study on Electromechanics in Cartilage Tissue with Respect to Its Electrical Properties. *Tissue Engineering - Part B: Reviews*, 25(2):152–166, 2019. doi: 10.1089/ten.teb.2018.0214.

[9] Hunziker, E.B., Quinn, T.M. and Häuselmann, H.J. Quantitative structural organization of normal adult human articular cartilage. *Osteoarthr. Cartil.*, 10(7):564–572, 2002. doi: 10.1053/joca.2002.0814.

[10] Choi, J.B. et al. Zonal changes in the three-dimensional morphology of the chondron under compression: The relationship among cellular, pericellular, and extracellular deformation in articular cartilage. *Journal of Biomechanics*, 40(12):2596–2603, 2007. doi: 10.1016/j.jbiomech.2007.01.009.

[11] Poole, C.A. Articular cartilage chondrons: Form, function and failure. *Journal of Anatomy*, 191(1):1–13, 1997. doi: 10.1017/S0021878297002185.

[12] Benninghoff, A. Form und Bau der Gelenkknorpel in ihren Beziehungen zur Funktion - Zweiter Teil: Der Aufbau des Gelenkknorpels in seinen Beziehungen zur Funktion. *Zeitschrift für Zellforschung und Mikroskopische Anatomie*, 2 (5):783–862, 1925. doi: 10.1007/BF00583443.

[13] Julkunen, P. et al. A review of the combination of experimental measurements and fibril-reinforced modeling for investigation of articular cartilage and chondrocyte response to loading. *Computational and Mathematical Methods in Medicine*, 2013:1–23, 2013. doi: 10.1155/2013/326150.

[14] Kwon, H. et al. Surgical and tissue engineering strategies for articular cartilage and meniscus repair. *Nat. Rev. Rheumatol.*, 15(9):550–570, 2019. doi: 10.1038/s41584-019-0255-1.

[15] Schmidt, C.O. et al. Häufigkeiten muskuloskelettaler Symptome und Erkrankungen in der bevölkerungsbezogenen NAKO Gesundheitsstudie. *Bundesgesundheitsblatt - Gesundheitsforsch. - Gesundheitsschutz*, 63(4):415–425, 2020. doi: 10.1007/s00103-020-03110-1.

[16] Makris, E.A., Hadidi, P. and Athanasiou, K.A. The knee meniscus: Structure-function, pathophysiology, current repair techniques, and prospects for regeneration. *Biomaterials*, 32(30):7411–7431, 2011. doi: 10.1016/j.biomaterials.2011.06.037.

[17] Hiligsmann, M. et al. Health economics in the field of osteoarthritis: An Expert's consensus paper from the European Society for Clinical and Economic Aspects of Osteoporosis and Osteoarthritis (ESCEO). *Seminars in Arthritis and Rheumatism*, 43(3):303–313, 2013. doi: 10.1016/j.semarthrit.2013.07.003.

[18] Hunziker, E.B. et al. An educational review of cartilage repair: Precepts & practice - myths & misconceptions - progress & prospects. *Osteoarthr. Cartil.*, 23(3):334–350, 2015. doi: 10.1016/j.joca.2014.12.011.

[19] Angele, P. et al. Chondral and osteochondral operative treatment in early osteoarthritis. *Knee Surgery, Sport. Traumatol. Arthrosc.*, 24(6):1743–1752, 2016. doi: 10.1007/s00167-016-4047-8.

[20] de Girolamo, L. et al. Regenerative approaches for the treatment of early OA. *Knee Surgery, Sport. Traumatol. Arthrosc.*, 24(6):1826–1835, 2016. doi: 10.1007/s00167-016-4125-y.

[21] Caron, M.M. et al. Redifferentiation of dedifferentiated human articular chondrocytes: Comparison of 2D and 3D cultures. *Osteoarthr. Cartil.*, 20(10):1170–1178, 2012. doi: 10.1016/j.joca.2012.06.016.

[22] Makris, E.A. et al. Repair and tissue engineering techniques for articular cartilage. *Nat. Rev. Rheumatol.*, 11(1):21–34, 2015. doi: 10.1038/nrrheum.2014.157.

[23] Krueger, S. et al. Re-Differentiation Capacity of Human Chondrocytes in Vitro Following Electrical Stimulation with Capacitively Coupled Fields. *J. Clin. Med.*, 8(11):1771, 2019. doi: 10.3390/jcm8111771.

[24] Zhao, W. et al. Degradable natural polymer hydrogels for articular cartilage tissue engineering. *J. Chem. Technol. Biotechnol.*, 88(3):327–339, 2013. doi: 10.1002/jctb.3970.

[25] Yang, J. et al. Cell-laden hydrogels for osteochondral and cartilage tissue engineering. *Acta Biomater.*, 57:1–25, 2017. doi: 10.1016/j.actbio.2017.01.036.

[26] Medvedeva, E.V. et al. Repair of damaged articular cartilage: Current approaches and future directions. *Int. J. Mol. Sci.*, 19(8), 2018. doi: 10.3390/ijms19082366.

[27] Ning, C. et al. Electroactive polymers for tissue regeneration: Developments and perspectives. *Prog. Polym. Sci.*, 81:144–162, 2018. doi: 10.1016/j.progpolymsci.2018.01.001.

[28] Armiento, A.R. et al. Biomaterials for articular cartilage tissue engineering: Learning from biology. *Acta Biomaterialia*, 65:1–20, 2018. doi: 10.1016/j.actbio.2017.11.021.

[29] Drury, J.L. and Mooney, D.J. Hydrogels for tissue engineering: Scaffold design variables and applications. *Biomaterials*, 24(24):4337–4351, 2003. doi: 10.1016/S0142-9612(03)00340-5.

[30] Distler, T. and Boccaccini, A.R. 3D printing of electrically conductive hydrogels for tissue engineering and biosensors – A review. *Acta Biomater.*, 101:1–13, 2020. doi: 10.1016/j.actbio.2019.08.044.

[31] U.S. Food and Drug Administration. Guidance for industry: Preparation of IDEs and INDs for products intented to repair or replace knee cartilage, 2011. URL `https://www.regulations.gov/docket/FDA-2007-D-0020`.

[32] Jahr, H., Matta, C. and Mobasheri, A. Physicochemical and Biomechanical Stimuli in Cell-Based Articular Cartilage Repair. *Curr. Rheumatol. Rep.*, 17 (3), 2015. doi: 10.1007/s11926-014-0493-9.

[33] Servin-Vences, M.R. et al. Mechanoelectrical transduction in chondrocytes. *Clin. Exp. Pharmacol. Physiol.*, 45(5):481–488, 2018. doi: 10.1111/1440-1681.12917.

[34] Mow, V.C. and Guo, X.E. Mechano-Electrochemical Properties Of Articular Cartilage: Their Inhomogeneities and Anisotropies. *Annu. Rev. Biomed. Eng.*, 4(1):175–209, 2002. doi: 10.1146/annurev.bioeng.4.110701.120309.

[35] Poillot, P., Le Maitre, C.L. and Huyghe, J.M. The strain-generated electrical potential in cartilaginous tissues: a role for piezoelectricity. *Biophys. Rev.*, 13 (1):91–100, 2021. doi: 10.1007/s12551-021-00779-9.

[36] Misakian, M. et al. Biological, physical, and electrical parameters for in vitro studies with ELF magnetic and electric fields: A primer. *Bioelectromagnetics*, 14(S2):1–73, 1993. doi: 10.1002/bem.2250140703.

[37] Massari, L. et al. Biophysical stimulation of bone and cartilage: state of the art and future perspectives. *Int. Orthop.*, 43(3):539–551, 2019. doi: 10.1007/s00264-018-4274-3.

[38] Stefani, R.M. et al. Pulsed electromagnetic fields promote repair of focal articular cartilage defects with engineered osteochondral constructs. *Biotechnol. Bioeng.*, 117(5):1584–1596, 2020. doi: 10.1002/bit.27287.

[39] Brighton, C.T. et al. Proliferative and synthetic response of bovine growth plate chondrocytes to various capacitively coupled electrical fields. *J. Orthop. Res.*, 7(5):759–65, 1989. doi: 10.1002/jor.1100070519.

[40] Brighton, C.T. et al. In Vitro Bone-Cell Response to a Capacitively Coupled Electrical Field. *Clin. Orthop. Relat. Res.*, 285:255–262, 1992. doi: 10.1097/00003086-199212000-00035.

[41] Wang, W. et al. Up-regulation of chondrocyte matrix genes and products by electric fields. *Clin. Orthop. Relat. Res.*, 427:S163–S173, 2004. doi: 10.1097/01.blo.0000143837.53434.5c.

[42] Brighton, C.T., Wang, W. and Clark, C.C. The effect of electrical fields on gene and protein expression in human osteoarthritic cartilage explants. *J. Bone Joint Surg. Am.*, 90:833–848, 2008. doi: 10.2106/JBJS.F.01437.

[43] Vaca-González, J.J. et al. Effect of electrical stimulation on chondrogenic differentiation of mesenchymal stem cells cultured in hyaluronic acid – Gelatin injectable hydrogels. *Bioelectrochemistry*, 134, 2020. doi: 10.1016/j.bioelechem.2020.107536.

[44] Krueger, S. et al. Establishment of a new device for electrical stimulation of non-degenerative cartilage cells in vitro. *International Journal of Molecular Sciences*, 22(1):1–7, 2021. doi: 10.3390/ijms22010394.

[45] Saghati, S. et al. Tissue Engineering Strategies to Increase Osteochondral Regeneration of Stem Cells; a Close Look at Different Modalities. *Stem Cell Rev. Reports*, 17(4):1294–1311, 2021. doi: 10.1007/s12015-021-10130-0.

[46] Chao, P.H. et al. Chondrocyte translocation response to direct current electric fields. *Journal of biomechanical engineering*, 122(3):261–267, 2000. doi: 10.1115/1.429661.

[47] Kwon, H.J., Lee, G.S. and Chun, H. Electrical stimulation drives chondrogenesis of mesenchymal stem cells in the absence of exogenous growth factors. *Sci. Rep.*, 6(April):1–13, 2016. doi: 10.1038/srep39302.

[48] Zuzzi, D.C. et al. Evaluation of the effects of electrical stimulation on cartilage repair in adult male rats. *Tissue Cell*, 45(4):275–281, 2013. doi: 10.1016/j.tice.2013.02.003.

[49] Lippiello, L., Chakkalakal, D. and Connolly, J.F. Pulsing direct current-induced repair of articular cartilage in rabbit osteochondral defects. *J. Orthop. Res.*, 8(2):266–275, 1990. doi: 10.1002/jor.1100080216.

[50] Hungerford, D.S. et al. Synergistic effect of using a transcutaneous electrical joint stimulator and an unloading brace in treating osteoarthritis of the knee. *Am. J. Orthop. (Belle Mead. NJ).*, 42(10):456–463, 2013.

[51] Garland, D. et al. A 3-month, randomized, double-blind, placebo-controlled study to evaluate the safety and efficacy of a highly optimized, capacitively coupled, pulsed electrical stimulator in patients with osteoarthritis of the knee. *Osteoarthr. Cartil.*, 15(6):630–637, 2007. doi: 10.1016/j.joca.2007.01.004.

[52] Zizic, T.M. et al. The treatment of osteoarthritis of the knee with pulsed electrical stimulation. *J. Rheumatol.*, 22(9):1757–1761, 1995.

[53] Fary, R.E. et al. The effectiveness of pulsed electrical stimulation in the management of osteoarthritis of the knee: Results of a double-blind, randomized, placebo-controlled, repeated-measures trial. *Arthritis Rheum.*, 63(5): 1333–1342, 2011. doi: 10.1002/art.30258.

[54] Vavken, P. et al. Effectiveness of pulsed electromagnetic field therapy in the management of osteoarthritis of the knee: A meta-analysis of randomized controlled trials. *J. Rehabil. Med.*, 41(6):406–411, 2009. doi: 10.2340/16501977-0374.

[55] Negm, A., Lorbergs, A. and MacIntyre, N.J. Efficacy of low frequency pulsed subsensory threshold electrical stimulation vs placebo on pain and physical

function in people with knee osteoarthritis: Systematic review with meta-analysis. *Osteoarthr. Cartil.*, 21(9):1281–1289, 2013. doi: 10.1016/j.joca.2013.06.015.

[56] Li, S. et al. Electromagnetic fields for treating osteoarthritis. *Cochrane Database Syst. Rev.*, (12), 2013. doi: 10.1002/14651858.CD003523.pub2.

[57] Rutjes, A. et al. Transcutaneous electrostimulation for osteoarthritis of the knee. *Cochrane Database Syst. Rev.*, (4), 2009. doi: 10.1002/14651858.CD002823.pub2.

[58] Griffin, X.L. et al. Electromagnetic field stimulation for treating delayed union or non-union of long bone fractures in adults. *Cochrane Database Syst. Rev.*, (4), 2011. doi: 10.1002/14651858.cd008471.pub2.

[59] Schmidt-Rohlfing, B. et al. Elektromagnetische Felder, elektrischer Strom und Knochenheilung: Was ist gesichert? *Zeitschrift fur Orthopadie und Unfallchirurgie*, 149(3):265–270, 2011. doi: 10.1055/s-0030-1250518.

[60] Krauss, J.K. et al. Technology of deep brain stimulation: current status and future directions. *Nat. Rev. Neurol.*, 17(2):75–87, 2021. doi: 10.1038/s41582-020-00426-z.

[61] Lozano, A.M. et al. Deep brain stimulation: current challenges and future directions. *Nat. Rev. Neurol.*, 15(3):148–160, 2019. doi: 10.1038/s41582-018-0128-2.

[62] Balint, R., Cassidy, N.J. and Cartmell, S.H. Electrical Stimulation: A Novel Tool for Tissue Engineering. *Tissue Eng. Part B Rev.*, 19(1):48–57, 2013. doi: 10.1089/ten.teb.2012.0183.

[63] da Silva, L.P. et al. Electric Phenomenon: A Disregarded Tool in Tissue Engineering and Regenerative Medicine. *Trends Biotechnol.*, 38(1):24–49, 2020. doi: 10.1016/j.tibtech.2019.07.002.

[64] Zhao, M. et al. Electrical signals control wound healing through phosphatidylinositol-3-OH kinase-γ and PTEN. *Nature*, 442(7101):457–460, 2006. doi: 10.1038/nature04925.

[65] Zhao, M. Electrical fields in wound healing–An overriding signal that directs cell migration. *Semin. Cell Dev. Biol.*, 20(6):674–682, 2009. doi: 10.1016/j.semcdb.2008.12.009.

[66] Zajdel, T.J., Shim, G. and Cohen, D.J. Come together: On-chip bioelectric wound closure. *Biosens. Bioelectron.*, 192:113479, 2021. doi: 10.1016/j.bios.2021.113479.

[67] Tandon, N. et al. Electrical stimulation systems for cardiac tissue engineering. *Nat. Protoc.*, 4(2):155–173, 2009. doi: 10.1038/nprot.2008.183.

[68] Iwasa, S.N. et al. Novel Electrode Designs for Neurostimulation in Regenerative Medicine: Activation of Stem Cells. *Bioelectricity*, 2(4):348–361, 2020. doi: 10.1089/bioe.2020.0034.

[69] Meng, S., Rouabhia, M. and Zhang, Z. Electrical stimulation modulates osteoblast proliferation and bone protein production through heparin-bioactivated conductive scaffolds. *Bioelectromagnetics*, 34(3):189–199, 2013. doi: 10.1002/bem.21766.

[70] Funk, R.H., Monsees, T. and Özkucur, N. Electromagnetic effects - From cell biology to medicine. *Prog. Histochem. Cytochem.*, 43(4):177–264, 2009. doi: 10.1016/j.proghi.2008.07.001.

[71] Thrivikraman, G., Boda, S.K. and Basu, B. Unraveling the mechanistic effects of electric field stimulation towards directing stem cell fate and function: A tissue engineering perspective. *Biomaterials*, 150:60–86, 2018. doi: 10.1016/j.biomaterials.2017.10.003.

[72] Chen, C. et al. Electrical stimulation as a novel tool for regulating cell behavior in tissue engineering. *Biomater. Res.*, 23(1):1–12, 2019. doi: 10.1186/s40824-019-0176-8.

[73] Ryan, C.N.M., Doulgkeroglou, M.N. and Zeugolis, D.I. Electric field stimulation for tissue engineering applications. *BMC Biomed. Eng.*, 3(1):1, 2021. doi: 10.1186/s42490-020-00046-0.

[74] Zhao, S., Mehta, A.S. and Zhao, M. Biomedical applications of electrical stimulation. *Cellular and Molecular Life Sciences*, 2020. doi: 10.1007/s00018-019-03446-1.

[75] Chalmers, I. et al. How to increase value and reduce waste when research priorities are set. *Lancet*, 383(9912):156–165, 2014. doi: 10.1016/S0140-6736(13)62229-1.

[76] Glasziou, P. et al. Reducing waste from incomplete or unusable reports of biomedical research. *Lancet*, 383(9913):267–276, 2014. doi: 10.1016/S0140-6736(13)62228-X.

[77] Association for Computing Machinery. Artifact Review and Badging Version 1.1, 2022. URL `https://www.acm.org/publications/policies/artifact-review-and-badging-current`.

[78] Ioannidis, J.P.A. et al. Increasing value and reducing waste in research design, conduct, and analysis. *Lancet*, 383(9912):166–175, 2014. doi: 10.1016/S0140-6736(13)62227-8.

[79] Portelli, L.A. et al. Retrospective estimation of the electric and magnetic field exposure conditions in in vitro experimental reports reveal considerable potential for uncertainty. *Bioelectromagnetics*, 39(3):231–243, 2018. doi: 10.1002/bem.22099.

[80] Cemazar, M. et al. Recommendations and requirements for reporting on applications of electric pulse delivery for electroporation of biological samples. *Bioelectrochemistry*, 122:69–76, 2018. doi: 10.1016/j.bioelechem.2018.03.005.

[81] Guette-Marquet, S., Roques, C. and Bergel, A. Theoretical analysis of the electrochemical systems used for the application of direct current/voltage stimuli on cell cultures. *Bioelectrochemistry*, 139:107737, 2021. doi: 10.1016/j.bioelechem.2020.107737.

[82] Simkó, M. et al. Quality matters: Systematic analysis of endpoints related to "cellular life" in vitro data of radiofrequency electromagnetic field exposure. *Int. J. Environ. Res. Public Health*, 13(7):701, 2016. doi: 10.3390/ijerph13070701.

[83] Nicksic, P.J. et al. Electronic Bone Growth Stimulators for Augmentation of Osteogenesis in In Vitro and In Vivo Models: A Narrative Review of Electrical Stimulation Mechanisms and Device Specifications. *Front. Bioeng. Biotechnol.*, 10:793945, 2022. doi: 10.3389/fbioe.2022.793945.

[84] McLeod, K.J. Microelectrode measurements of low frequency electric field effects in cells and tissues. *Bioelectromagnetics*, 13(1):161–178, 1992. doi: 10.1002/bem.2250130716.

[85] Barnes, F.S. Mechanisms for electric and magnetic fields effects on biological cells. *IEEE Trans. Magn.*, 41(11):4219–4224, 2005. doi: 10.1109/TMAG.2005.855480.

[86] Coveney, P.V. and Highfield, R.R. When we can trust computers (and when we can't). *Phil. Trans. R. Soc. A*, 379:20200067, 2021. doi: 10.1098/rsta.2020.0067.

[87] Wright, L. and Davidson, S. How to tell the difference between a model and a digital twin. *Adv. Model. Simul. Eng. Sci.*, 7(1), 2020. doi: 10.1186/s40323-020-00147-4.

[88] Geris, L. et al. The future is digital: In silico tissue engineering. *Curr. Opin. Biomed. Eng.*, 6:92–98, 2018. doi: 10.1016/j.cobme.2018.04.001.

[89] Keysight Technologies. *Impedance Measurement Handbook: A guide to measurement technology and techniques*. 6th edition, 2016. URL `http://literature.cdn.keysight.com/litweb/pdf/5950-3000.pdf`.

[90] Richardot, A. and McAdams, E.T. Harmonic analysis of low-frequency bioelectrode behavior. *IEEE Trans. Med. Imaging*, 21(6):604–612, 2002. doi: 10.1109/TMI.2002.800576.

[91] Zimmermann, J., Altenkirch, R. and van Rienen, U. Numerical study on the effect of capacitively coupled electrical stimulation on biological cells considering model uncertainties. *Sci. Rep.*, 12:4744, 2022. doi: 10.1038/s41598-022-08279-w.

[92] Merrill, D.R., Bikson, M. and Jefferys, J.G. Electrical stimulation of excitable tissue: Design of efficacious and safe protocols. *J. Neurosci. Methods*, 141(2): 171–198, 2005. doi: 10.1016/j.jneumeth.2004.10.020.

[93] Boehler, C. et al. Tutorial: guidelines for standardized performance tests for electrodes intended for neural interfaces and bioelectronics. *Nat. Protoc.*, 15 (11):3557–3578, 2020. doi: 10.1038/s41596-020-0389-2.

[94] Brighton, C.T. et al. Fracture healing in the rabbit fibula when subjected to various capacitively coupled electrical fields. *J. Orthop. Res.*, 3(3):331–340, 1985. doi: 10.1002/jor.1100030310.

[95] Hiemer, B. et al. Effect of electric stimulation on human chondrocytes and mesenchymal stem cells under normoxia and hypoxia. *Mol. Med. Rep.*, 18: 2133–2141, 2018. doi: 10.3892/mmr.2018.9174.

[96] Raben, H. et al. Establishment of a numerical model to design an electro-stimulating system for a porcine mandibular critical size defect. *Appl. Sci.*, 9 (10):2160, 2019. doi: 10.3390/app9102160.

[97] Dauben, T.J. et al. A Novel In Vitro System for Comparative Analyses of Bone Cells and Bacteria under Electrical Stimulation. *Biomed Res. Int.*, 2016: 5178640, 2016. doi: 10.1155/2016/5178640.

[98] Bard, A.J. and Faulkner, L.R. *Electrochemical methods : fundamentals and applications*. Wiley, New York, 2nd edition, 2001.

[99] Lasia, A. Applications of Electrochemical Impedance Spectroscopy to Hydrogen Adsorption, Evolution and Absorption into Metals. In Conway, B. and White, R., editors, *Modern Aspects of Electrochemistry*, volume 35, pages 1–49. Kluwer Academic Publishers, New York, 2005. doi: 10.1007/0-306-47604-5_1.

[100] Auinger, M. et al. Near-surface ion distribution and buffer effects during electrochemical reactions. *Phys. Chem. Chem. Phys.*, 13(36):16384–16394, 2011. doi: 10.1039/c1cp21717h.

[101] Ishai, P.B. et al. Electrode polarization in dielectric measurements: A review. *Meas. Sci. Technol.*, 24(10):102001, 2013. doi: 10.1088/0957-0233/24/10/102001.

[102] Orazem, M.E. and Tribollet, B. *Electrochemical impedance spectroscopy.* The Electrochemical Society series. John Wiley & Sons, Hoboken, New Jersey, 2nd edition, 2017.

[103] Farooqi, A.R. et al. Numerical Simulation of Electroactive Hydrogels for Cartilage–Tissue Engineering. *Materials*, 12(18):2913, 2019. doi: 10.3390/ma12182913.

[104] Schwan, H.P. Linear and nonlinear electrode polarization and biological materials. *Ann. Biomed. Eng.*, 20(3):269–288, 1992. doi: 10.1007/BF02368531.

[105] Moussavi, M., Schwan, H.P. and Sun, H.H. Harmonic distorition caused by electrode polarisation. *Med. Biol. Eng. Comput.*, 32(2):121–125, 1994. doi: 10.1007/BF02518907.

[106] Palanisami, A. et al. Nonlinear impedance of whole cells near an electrode as a probe of mitochondrial activity. *Biosensors*, 1(2):46–57, 2011. doi: 10.3390/bios1020046.

[107] McAdams, E.T. and Jossinet, J. A physical interpretation of Schwan's limit current of linearity. *Ann. Biomed. Eng.*, 20(3):307–319, 1992. doi: 10.1007/BF02368533.

[108] Malleo, D. et al. Note: Characterization of electrode materials for dielectric spectroscopy. *Rev. Sci. Instrum.*, 81(1):016104, 2010. doi: 10.1063/1.3284516.

[109] Cantrell, D.R. et al. Incorporation of the electrode–electrolyte interface into finite-element models of metal microelectrodes. *J. Neural Eng.*, 5(1):54–67, 2008. doi: 10.1088/1741-2560/5/1/006.

[110] Zimmermann, U. et al. Numerical Simulation of Electric Field Distribution around an Instrumented Total Hip Stem. *Appl. Sci.*, 11(15):6677, 2021. doi: 10.3390/app11156677.

[111] Grimnes, S. and Martinsen, Ø.G. *Bioimpedance and Bioelectricity Basics: Third Edition.* Academic Press, Oxford, 3rd edition, 2014.

[112] Wang, S. et al. Electrochemical impedance spectroscopy. *Nat. Rev. Methods Prim.*, 1(1):41, 2021. doi: 10.1038/s43586-021-00039-w.

[113] Oppenheim, A.V., Willsky, A.S. and Nawab, S.H. *Signals & Systems*. Prentice-Hall, Upper Saddle River, NJ, 2nd edition, 1996.

[114] Brighton, T., Wang, W. and Clark, C.C. The effect of electrical fields on gene and protein expression in human osteoarthritic cartilage expiants. *Journal of Bone and Joint Surgery*, 90(4):833–848, 2008.

[115] Vaca-González, J.J. et al. Biophysical Stimuli: A Review of Electrical and Mechanical Stimulation in Hyaline Cartilage. *Cartilage*, 10(2):157–172, 2019. doi: 10.1177/1947603517730637.

[116] Xu, J. et al. Signal transduction in electrically stimulated articular chondrocytes involves translocation of extracellular calcium through voltage-gated channels. *Osteoarthr. Cartil.*, 17(3):397–405, 2009.

[117] Carter, E.L. et al. Field Distributions in Vertebral Bodies of the Rat During Electrical Stimulation: A Parametric Study. *IEEE Trans. Biomed. Eng.*, 36 (3):333–345, 1989. doi: 10.1109/10.19854.

[118] Clark, C.C., Wang, W. and Brighton, C.T. Up-regulation of expression of selected genes in human bone cells with specific capacitively coupled electric fields. *J. Orthop. Res.*, 32(7):894–903, 2014. doi: 10.1002/jor.22595.

[119] Lorich, D.G. et al. Biochemical pathway mediating the response of bone cells to capacitive coupling. *Clin. Orthop. Relat. Res.*, 350:246–256, 1998. doi: 10.1097/00003086-199805000-00033.

[120] Timoshkin, I.V. et al. Transient electrical field across cellular membranes: Pulsed electric field treatment of microbial cells. *J. Phys. D. Appl. Phys.*, 39 (3):596–603, 2006.

[121] Taghian, T., Narmoneva, D.A. and Kogan, A.B. Modulation of cell function by electric field: A high-resolution analysis. *J. R. Soc. Interface*, 12(107): 20150153, 2015. doi: 10.1098/rsif.2015.0153.

[122] Brighton, C.T., Unger, A.S. and Stambough, J.L. In vitro growth of bovine articular cartilage chondrocytes in various capacitively coupled electrical fields. *J. Orthop. Res.*, 2(1):15–22, 1984. doi: 10.1002/jor.1100020104.

[123] Brighton, C.T., Wang, W. and Clark, C.C. Up-regulation of matrix in bovine articular cartilage explants by electric fields. *Biochem. Biophys. Res. Commun.*, 342(2):556–561, 2006. doi: 10.1016/j.bbrc.2006.01.171.

[124] Brighton, C.T. et al. A Spectrophotometric Analysis of Human Osteoarthritic Cartilage Explants Subjected to Specific Capacitively Coupled Electric Fields. *Open J. Biophys.*, 3(2):158–164, 2013. doi: 10.4236/ojbiphy.2013.32019.

[125] Vaca-González, J.J. et al. An In Vitro Chondrocyte Electrical Stimulation Framework: A Methodology to Calculate Electric Fields and Modulate Proliferation, Cell Death and Glycosaminoglycan Synthesis. *Cell. Mol. Bioeng.*, 9 (1):116–126, 2016. doi: 10.1007/s12195-015-0419-2.

[126] Lombardi, M.A. et al. WWVB Radio Controlled Clocks: Recommended Practices for Manufacturers and Consumers. Technical report, National Institute of Standards and Technology, 2009.

[127] Bisceglia, B. et al. Induction of alkaline phosphatase activity by exposure of human cell lines to a low-frequency electric field from apparatuses used in clinical therapies. *Bioelectromagnetics*, 32(2):113–119, 2011. doi: 10.1002/bem.20630.

[128] Couniot, N. et al. Capacitive biosensing of bacterial cells: Analytical model and numerical simulations. *Sens. Actuators B Chem.*, 211:428–438, 2015. doi: 10.1016/j.snb.2015.01.108.

[129] Jiang, Y.D. and Soleimani, M. Capacitively Coupled Electrical Impedance Tomography for Brain Imaging. *IEEE Trans. Med. Imaging*, 38(9):2104–2113, 2019. doi: 10.1109/TMI.2019.2895035.

[130] Kubáň, P. and Hauser, P.C. Contactless conductivity detection for analytical techniques— Developments from 2014 to 2016. *Electrophoresis*, 38(1):95–114, 2017. doi: 10.1002/elps.201600280.

[131] Glaser, R. *Biophysics: An introduction*, volume 9783642252. Springer, Berlin, Heidelberg, 2nd edition, 2012. doi: 10.1007/978-3-642-25212-9.

[132] Kotnik, T. et al. Membrane Electroporation and Electropermeabilization: Mechanisms and Models. *Annu. Rev. Biophys.*, 48:63–91, 2019. doi: 10.1146/annurev-biophys-052118-115451.

[133] Lewis, R., Feetham, C.H. and Barrett-Jolley, R. Cell volume regulation in chondrocytes. *Cell. Physiol. Biochem.*, 28(6):1111–1122, 2011. doi: 10.1159/000335847.

[134] Funabashi, K. et al. Contribution of chloride channel conductance to the regulation of resting membrane potential in chondrocytes. *J. Pharmacol. Sci.*, 113(1):94–99, 2010. doi: 10.1254/jphs.10026SC.

[135] Lewis, R. et al. The role of the membrane potential in chondrocyte volume regulation. *J. Cell. Physiol.*, 226(11):2979–2986, 2011. doi: 10.1002/jcp.22646.

[136] Matta, C., Zákány, R. and Mobasheri, A. Voltage-Dependent Calcium Channels in Chondrocytes: Roles in Health and Disease. *Curr. Rheumatol. Rep.*, 17:43, 2015. doi: 10.1007/s11926-015-0521-4.

[137] Brady, M.A., Waldman, S.D. and Ethier, C.R. The application of multiple biophysical cues to engineer functional neocartilage for treatment of osteoarthritis. Part I: Cellular response. *Tissue Eng. - Part B Rev.*, 21(1):1–19, 2015. doi: 10.1089/ten.teb.2013.0757.

[138] Pall, M.L. Electromagnetic fields act via activation of voltage-gated calcium channels to produce beneficial or adverse effects. *J. Cell. Mol. Med.*, 17(8): 958–965, 2013.

[139] Doering, C.J. and Zamponi, G.W. Molecular Pharmacology of High Voltage-Activated Calcium Channels. *Journal of Bioenergetics and Biomembranes*, 35 (6):491–505, 2003. doi: 10.1023/B:JOBB.0000008022.50702.1a.

[140] Barnes, F.S. Interaction of Direct Current and Extremely Low-Frequency Electric Fields with Biological Materials and Systems. In Barnes, F.S. and Greenebaum, B., editors, *Handbook of Biological Effects of Electromagnetic Fields*, pages 115–156. CRC Press, Boca Raton, 3rd edition, 2007.

[141] Kadir, L.A., Stacey, M. and Barrett-Jolley, R. Emerging roles of the membrane potential: Action beyond the action potential. *Front. Physiol.*, 9:1661, 2018. doi: 10.3389/fphys.2018.01661.

[142] Matsuoka, H. et al. Single-cell imaging of the Ca 2+ influx into bovine endothelial cells occurring in response to an alternating electric stimulus. *Anal. Sci.*, 18(11):1205–1208, 2002. doi: 10.2116/analsci.18.1205.

[143] Grosse, C. and Schwan, H.P. Cellular membrane potentials induced by alternating fields. *Biophys. J.*, 63(6):1632–1642, 1992. doi: 10.1016/S0006-3495(92)81740-X.

[144] Kotnik, T., Bobanović, F. and Miklavčič, D. Sensitivity of transmembrane voltage induced by applied electric fields - A theoretical analysis. *Bioelectrochemistry Bioenerg.*, 43(2):285–291, 1997. doi: 10.1016/S0302-4598(97)00023-8.

[145] Kotnik, T. and Miklavčič, D. Analytical description of transmembrane voltage induced by electric fields on spheroidal cells. *Biophys. J.*, 79(2):670–679, 2000. doi: 10.1016/S0006-3495(00)76325-9.

[146] Pucihar, G. et al. Numerical Determination of Transmembrane Voltage Induced on Irregularly Shaped Cells. *Ann. Biomed. Eng.*, 34(4):642–652, 2006. doi: 10.1007/s10439-005-9076-2.

[147] Kotnik, T., Pucihar, G. and Miklavcic, D. The Cell in the Electric Field. In Kee, S.T., Gehl, J. and Lee, E.W., editors, *Clinical Aspects of Electroporation*, pages 19–29. Springer, New York, 2011. doi: 10.1007/978-1-4419-8363-3.

[148] Tsong, T.Y. et al. Electroconformational coupling (ECC): an electric field induced enzyme oscillation for cellular energy and signal transductions. *J. Electroanal. Chem.*, 275(3):319–331, 1989. doi: 10.1016/0022-0728(89)87232-8.

[149] Woodward, A.M. and Kell, D.B. On the nonlinear dielectric properties of biological systems. Saccharomyces cerevisiae. *J. Electroanal. Chem.*, 299(2): 83–100, 1990. doi: 10.1016/0022-0728(90)87511-H.

[150] Woodward, A.M. and Kell, D.B. Confirmation by using mutant strains that the membrane-bound H+-ATPase is the major source of non-linear dielectricity in Saccharomyces cerevisiae. *FEMS Microbiol. Lett.*, 84(1):91–96, 1991. doi: 10.1111/j.1574-6968.1991.tb04575.x.

[151] Nawarathna, D. et al. Harmonic response of cellular membrane pumps to low frequency electric fields. *Phys. Rev. Lett.*, 95(15):1–4, 2005. doi: 10.1103/PhysRevLett.95.158103.

[152] Nawarathna, D. et al. Nonlinear dielectric spectroscopy of live cells using superconducting quantum interference devices. *Appl. Phys. Lett.*, 86(2):2–5, 2005. doi: 10.1063/1.1844036.

[153] Nawarathna, D. et al. Harmonic generation by yeast cells in response to low-frequency electric fields. *Phys. Rev. E - Stat. Nonlinear, Soft Matter Phys.*, 73(5):1–6, 2006. doi: 10.1103/PhysRevE.73.051914.

[154] Astumian, R.D. Stochastic conformational pumping: A mechanism for free-energy transduction by molecules. *Annu. Rev. Biophys.*, 40(1):289–313, 2011. doi: 10.1146/annurev-biophys-042910-155355.

[155] Montaigne, K. and Pickard, W.F. Offset of the vacuolar potential of Characean cells in response to electromagnetic radiation over the range 250 Hz-250 kHz. *Bioelectromagnetics*, 5(1):31–38, 1984. doi: 10.1002/bem.2250050104.

[156] Treo, E.F. and Felice, C.J. Non-linear dielectric spectroscopy of microbiological suspensions. *Biomed. Eng. Online*, 8:19, 2009. doi: 10.1186/1475-925X-8-19.

[157] Mercier, G.T., Palanisami, A. and Miller, J.H. Nonlinear dielectric spectroscopy for label-free detection of respiratory activity in whole cells. *Biosens. Bioelectron.*, 25(9):2107–2114, 2010. doi: 10.1016/j.bios.2010.02.013.

[158] Mobasheri, A. et al. Na+, K+-ATPase Subunit Composition in a Human Chondrocyte Cell Line; Evidence for the Presence of $\alpha 1$, $\alpha 3$, $\beta 1$, $\beta 2$ and $\beta 3$ Isoforms. *Int. J. Mol. Sci.*, 13(4):5019–5034, 2012. doi: 10.3390/ijms13045019.

[159] Maleckar, M.M. et al. Physiological Effects of the Electrogenic Current Generated by the Na+ /K+ Pump in Mammalian Articular Chondrocytes. *Bioelectricity*, 2(3):258–268, 2020. doi: 10.1089/bioe.2020.0036.

[160] Lin, B.j. et al. Lipid rafts sense and direct electric field-induced migration. *Proc. Natl. Acad. Sci.*, 114(32):8568–8573, 2017. doi: 10.1073/pnas.1702526114.

[161] Lee, R.C. et al. Cell shape-dependent rectification of surface receptor transport in a sinusoidal electric field. *Biophys. J.*, 64(1):44–57, 1993. doi: 10.1016/S0006-3495(93)81339-0.

[162] Ruhlen, R. and Marberry, K. The chondrocyte primary cilium. *Osteoarthr. Cartil.*, 22(8):1071–1076, 2014. doi: 10.1016/j.joca.2014.05.011.

[163] O'Conor, C.J. et al. TRPV4-mediated mechanotransduction regulates the metabolic response of chondrocytes to dynamic loading. *Proc. Natl. Acad. Sci.*, 111(4):1316–1321, 2014. doi: 10.1073/pnas.1319569111.

[164] Lee, W. et al. Synergy between Piezo1 and Piezo2 channels confers high-strain mechanosensitivity to articular cartilage. *Proc. Natl. Acad. Sci.*, 111(47):E5114–E5122, 2014. doi: 10.1073/pnas.1414298111.

[165] Varady, N. and Grodzinsky, A. Osteoarthritis year in review 2015: mechanics. *Osteoarthr. Cartil.*, 24(1):27–35, 2016. doi: 10.1016/j.joca.2015.08.018.

[166] Jones, T.B. *Electromechanics of Particles*. Cambridge University Press, Cambridge, 1995. doi: 10.1017/cbo9780511574498.

[167] Pethig, R. *Dielectrophoresis*. John Wiley & Sons, Chichester, UK, 2017. doi: 10.1002/9781118671443.

[168] Wang, X., Wang, X.B. and Gascoyne, P.R. General expressions for dielectrophoretic force and electrorotational torque derived using the Maxwell stress tensor method. *J. Electrostat.*, 39(4):277–295, 1997. doi: 10.1016/S0304-3886(97)00126-5.

[169] Rey, J.I. et al. Electrostrictive forces on vesicles with compartmentalized permittivity and conductivity conditions. *IEEE Trans. Dielectr. Electr. Insul.*, 16(5):1280–1287, 2009. doi: 10.1109/TDEI.2009.5293939.

[170] Albrecht, D.R. et al. Probing the role of multicellular organization in three-dimensional microenvironments. *Nat. Methods*, 3(5):369–375, 2006. doi: 10.1038/nmeth873.

[171] Sukhorukov, V.L., Mussauer, H. and Zimmermann, U. The effect of electrical deformation forces on the electropermeabilization of erythrocyte membranes in low- and high- conductivity media. *J. Membr. Biol.*, 163(3):235–245, 1998. doi: 10.1007/s002329900387.

[172] MacQueen, L.A., Buschmann, M.D. and Wertheimer, M.R. Mechanical properties of mammalian cells in suspension measured by electro-deformation. *J. Micromechanics Microengineering*, 20(6):65007, 2010. doi: 10.1088/0960-1317/20/6/065007.

[173] Hronik-Tupaj, M. et al. Osteoblastic differentiation and stress response of human mesenchymal stem cells exposed to alternating current electric fields. *Biomed. Eng. Online*, 10:9, 2011. doi: 10.1186/1475-925X-10-9.

[174] Dimova, R. Giant Vesicles and Their Use in Assays for Assessing Membrane Phase State, Curvature, Mechanics, and Electrical Properties. *Annu. Rev. Biophys.*, 48:93–119, 2019. doi: 10.1146/annurev-biophys-052118-115342.

[175] Aranda, S. et al. Morphological transitions of vesicles induced by alternating electric fields. *Biophys. J.*, 95(2):L19–L21, 2008. doi: 10.1529/biophysj.108.132548.

[176] Lu, Z. et al. Collagen type II enhances chondrogenesis in adipose tissue-derived stem cells by affecting cell shape. *Tissue Eng. - Part A*, 16(1):81–90, 2010. doi: 10.1089/ten.tea.2009.0222.

[177] Vlahovska, P.M. Electrohydrodynamics of drops and vesicles. *Annu. Rev. Fluid Mech.*, 51:305–330, 2019. doi: 10.1146/annurev-fluid-122316-050120.

[178] Yamamoto, T. et al. Stability of spherical vesicles in electric fields. *Langmuir*, 26(14):12390–12407, 2010. doi: 10.1021/la1011132.

[179] Peterlin, P. Frequency-dependent electrodeformation of giant phospholipid vesicles in AC electric field. *J. Biol. Phys.*, 36(4):339–354, 2010. doi: 10.1007/s10867-010-9187-3.

[180] Dirks, H.K. Quasi-stationary fields for microelectronic applications. *Electr. Eng.*, 79(2):145–155, 1996. doi: 10.1007/BF01232924.

[181] Haus, H.A. and Melcher, J.R. *Electromagnetic fields and energy*. Prentice Hall, Englewood Cliffs, NJ, 1989.

[182] van Rienen, U. et al. Electro-quasistatic simulations in bio-systems engineering and medical engineering. *Adv. Radio Sci.*, 3:39–49, 2005.

[183] Rylander, T., Ingelström, P. and Bondeson, A. *Computational electromagnetics*, volume 51 of *Texts in applied mathematics*. Springer, New York, 2nd edition, 2013.

[184] Somersalo, E., Cheney, M. and Isaacson, D. Existence and uniqueness for electrode models for electric current computed tomography. *SIAM J. Appl. Math.*, 52(4):1023–1040, 1992. doi: 10.1137/0152060.

[185] Svorčík, V. et al. Permittivity of polyethylene and polyethyleneterephtalate. *J. Mater. Sci. Lett.*, 19(20):1843–1845, 2000. doi: 10.1023/A:1006715028026.

[186] Yao, T. and Asayama, Y. Animal-cell culture media: History, characteristics, and current issues. *Reprod. Med. Biol.*, 16(2):99–117, 2017. doi: 10.1002/rmb2.12024.

[187] Gulich, R. et al. Dielectric spectroscopy on aqueous electrolytic solutions. *Radiat. Environ. Biophys.*, 48(1):107–114, 2009. doi: 10.1007/s00411-008-0195-7.

[188] Peyman, A., Gabriel, C. and Grant, E.H. Complex permittivity of sodium chloride solutions at microwave frequencies. *Bioelectromagnetics*, 28(4):264–274, 2007. doi: 10.1002/bem.20271.

[189] Stogryn, A. Equations for Calculating the Dielectric Constant of Saline Water. *IEEE Trans. Microw. Theory Tech.*, 19(8):733–736, 1971. doi: 10.1109/TMTT.1971.1127617.

[190] Bordi, F., Cametti, C. and Colby, R.H. Dielectric spectroscopy and conductivity of polyelectrolyte solutions. *J. Phys. Condens. Matter*, 16(49), 2004. doi: 10.1088/0953-8984/16/49/R01.

[191] Swift, C.T. An Improved Model for the Dielectric Constant of Sea Water at Microwave Frequencies. *IEEE J. Ocean. Eng.*, 2(1):104–111, 1977. doi: 10.1109/JOE.1977.1145319.

[192] Grant, F.A. Use of complex conductivity in the representation of dielectric phenomena. *J. Appl. Phys.*, 29(1):76–80, 1958. doi: 10.1063/1.1722949.

[193] Mazzoleni, A.P., Sisken, B.F. and Kahler, R.L. Conductivity values of tissue culture medium from 20°C to 40°C. *Bioelectromagnetics*, 7(1):95–99, 1986. doi: 10.1002/bem.2250070111.

[194] Foster, K.R. and Schwan, H.P. Dielectric properties of tissues and biological materials: a critical review. *Crit. Rev. Biomed. Eng.*, 17(1):25–104, 1989.

[195] Gundersen, R. and Greenebaum, B. Low-voltage ELF electric field measurements in ionic media. *Bioelectromagnetics*, 6(2):157–168, 1985. doi: 10.1002/bem.2250060207.

[196] Johnson, C.R. Computational and numerical methods for bioelectric field problems. *Crit. Rev. Biomed. Eng.*, 25(1):1–81, 1997. doi: 10.1615/CritRevBiomedEng.v25.i1.10.

[197] Motrescu, V.C. and van Rienen, U. Computation of electrostatic fields in anisotropic human tissues using the Finite Integration Technique (FIT). *Adv. Radio Sci.*, 2:309–313, 2004. doi: 10.5194/ars-2-309-2004.

[198] Logg, A., Mardal, K.A. and Wells, G. *Automated Solution of Differential Equations by the Finite Element Method*, volume 84 of *Lecture Notes in Computational Science and Engineering*. Springer, Berlin, Heidelberg, 2012. doi: 10.1007/978-3-642-23099-8.

[199] Schöberl, J. C++ 11 implementation of finite elements in NGSolve. Technical report, Vienna University of Technology, Vienna, 2014. URL `https://www.asc.tuwien.ac.at/~schoeberl/wiki/publications/ngs-cpp11.pdf`.

[200] Hackbusch, W. *Elliptic Differential Equations*, volume 18 of *Springer Series in Computational Mathematics*. Springer, Berlin, Heidelberg, 2017. doi: 10.1007/978-3-662-54961-2.

[201] Boffi, D., Brezzi, F. and Fortin, M. *Mixed Finite Element Methods and Applications*, volume 44 of *Springer Series in Computational Mathematics*. Springer, Berlin, Heidelberg, 2013. doi: 10.1007/978-3-642-36519-5.

[202] Zienkiewicz, O., Taylor, R. and Zhu, J., editors. *The Finite Element Method: its Basis and Fundamentals*. Butterworth-Heinemann, Oxford, 7th edition, 2013.

[203] Zaglmayr, S. *High Order Finite Element Methods for Electromagnetic Field Computation*. PhD thesis, Johannes Kepler Universität Linz, Austria, 2006.

[204] Ben Belgacem, F. et al. Finite Element Methods for the Temperature in Composite Media with Contact Resistance. *J. Sci. Comput.*, 63(2):478–501, 2015. doi: 10.1007/s10915-014-9907-0.

[205] Tveito, A., Mardal, K.A. and Rognes, M.E., editors. *Modeling Excitable Tissue - The EMI Framework*. Simula SpringerBriefs on Computing. Springer, Cham, 2021. doi: 10.1007/978-3-030-61157-6.

[206] Brandstetter, G. and Govindjee, S. A high-order immersed boundary discontinuous-Galerkin method for Poisson's equation with discontinuous coefficients and singular sources. *Int. J. Numer. Methods Eng.*, 101(11):847–869, 2015. doi: 10.1002/nme.4835.

[207] Clemens, M. et al. Transient electro-quasistatic adaptive simulation schemes. *IEEE Trans. Magn.*, 40(2):1294–1297, 2004. doi: 10.1109/TMAG.2004.824582.

[208] Soleimani, M., Powell, C.E. and Polydorides, N. Improving the forward solver for the complete electrode model in EIT using algebraic multigrid. *IEEE Trans. Med. Imaging*, 24(5):577–583, 2005. doi: 10.1109/TMI.2005.843741.

[209] Press, W.H. et al. *Numerical recipes : the art of scientific computing*. Cambridge Univ. Press, USA, 3rd edition, 2007.

[210] Saad, Y. *Iterative Methods for Sparse Linear Systems*. Society for Industrial and Applied Mathematics, 2nd edition, 2003. doi: 10.1137/1.9780898718003.

[211] van Rienen, U. *Numerical Methods in Computational Electrodynamics*, volume 12 of *Lecture Notes in Computational Science and Engineering*. Springer, Berlin, Heidelberg, 2001. doi: 10.1007/978-3-642-56802-2.

[212] Balay, S. et al. PETSc Web page. `https://www.mcs.anl.gov/petsc`, 2019. URL `https://www.mcs.anl.gov/petsc`.

[213] Balay, S. et al. PETSc users manual. Technical Report ANL-95/11 - Revision 3.14, Argonne National Laboratory, 2020. URL `https://www.mcs.anl.gov/petsc`.

[214] Balay, S. et al. Efficient management of parallelism in object oriented numerical software libraries. In Arge, E., Bruaset, A.M. and Langtangen, H.P., editors, *Modern Software Tools in Scientific Computing*, pages 163–202. Birkhäuser Press, 1997.

[215] Benzi, M., Golubt, G.H. and Liesen, J. Numerical solution of saddle point problems. *Acta Numer.*, 14:1–137, 2005. doi: 10.1017/S0962492904000212.

[216] Pearson, J.W. and Pestana, J. Preconditioners for Krylov subspace methods: An overview. *GAMM Mitteilungen*, 43(4):1–35, 2020. doi: 10.1002/gamm.202000015.

[217] Xu, J. and Zikatanov, L. Algebraic multigrid methods. *Acta Numer.*, 26 (2017):591–721, 2017. doi: 10.1017/S0962492917000083.

[218] Dohrmann, C.R. A preconditioner for substructuring based on constrained energy minimization. *SIAM J. Sci. Comput.*, 25(1):246–258, 2003. doi: 10.1137/S1064827502412887.

[219] Zienkiewicz, O.C. and Zhu, J.Z. A simple error estimator and adaptive procedure for practical engineerng analysis. *Int. J. Numer. Methods Eng.*, 24 (2):337–357, 1987. doi: 10.1002/nme.1620240206.

[220] Verfürth, R. *A review of a posteriori error estimation and adaptive mesh-refinement techniques*. Wiley-Teubner series in advances in numerical mathematics. Wiley-Teubner, Chichester, 1996.

[221] Oberkampf, W.L. and Roy, C.J. *Verification and Validation in Scientific Computing*. Cambridge University Press, Cambridge, 2010. doi: 10.1017/CBO9780511760396.

[222] Carstensen, C. and Merdon, C. Estimator competition for Poisson problems. *J. Comput. Math.*, 28(3):309–330, 2010. doi: 10.4208/jcm.2009.10-m1015.

[223] Zander, N. et al. The multi-level hp-method for three-dimensional problems: Dynamically changing high-order mesh refinement with arbitrary hanging nodes. *Comput. Methods Appl. Mech. Eng.*, 310:252–277, 2016. doi: 10.1016/j.cma.2016.07.007.

[224] Day, D. and Heroux, M.A. Solving complex-valued linear systems via equivalent real formulations. *SIAM J. Sci. Comput.*, 23(2):480–498, 2002. doi: 10.1137/S1064827500372262.

[225] Schöberl, J. NETGEN An advancing front 2D/3D-mesh generator based on abstract rules. *Comput. Vis. Sci.*, 1(1):41–52, 1997. doi: 10.1007/s007910050004.

[226] Hughes, T.J., Cottrell, J.A. and Bazilevs, Y. Isogeometric analysis: CAD, finite elements, NURBS, exact geometry and mesh refinement. *Comput. Methods Appl. Mech. Eng.*, 194(39-41):4135–4195, 2005. doi: 10.1016/j.cma.2004.10.008.

[227] Agudelo-Toro, A. and Neef, A. Computationally efficient simulation of electrical activity at cell membranes interacting with self-generated and externally imposed electric fields. *J. Neural Eng.*, 10(2), 2013. doi: 10.1088/1741-2560/10/2/026019.

[228] Tveito, A. et al. A Cell-Based Framework for Numerical Modeling of Electrical Conduction in Cardiac Tissue. *Front. Phys.*, 5:48, 2017. doi: 10.3389/fphy.2017.00048.

[229] Ellingsrud, A.J. et al. Finite Element Simulation of Ionic Electrodiffusion in Cellular Geometries. *Front. Neuroinform.*, 14:11, 2020. doi: 10.3389/fninf.2020.00011.

[230] Le Maître, O.P. and Knio, O.M. *Spectral Methods for Uncertainty Quantification*. Scientific Computation. Springer, Dordrecht, 2010. doi: 10.1007/978-90-481-3520-2.

[231] Gawlok, S. et al. Hiflow3 – technical report on release 2.0. *Preprint Series of the Engineering Mathematics and Computing Lab (EMCL)*, 2017. doi: 10.11588/emclpp.2017.06.42879.

[232] Lemieux, C. *Monte Carlo and Quasi-Monte Carlo Sampling*. Springer Series in Statistics. Springer, Dordrecht, 2009. doi: 10.1007/978-0-387-78165-5.

[233] Xiu, D. *Numerical Methods for Stochastic Computations: A Spectral Method Approach*. Princeton University Press, USA, 2010.

[234] Tennøe, S., Halnes, G. and Einevoll, G.T. Uncertainpy: A Python Toolbox for Uncertainty Quantification and Sensitivity Analysis in Computational Neuroscience. *Front. Neuroinform.*, 12:49, 2018. doi: 10.3389/fninf.2018.00049.

[235] Eck, V.G. et al. A guide to uncertainty quantification and sensitivity analysis for cardiovascular applications. *Int. J. Numer. Method. Biomed. Eng.*, 32(8): e02755, 2016. doi: 10.1002/cnm.2755.

[236] Zimmermann, J. and van Rienen, U. Ambiguity in the interpretation of the low-frequency dielectric properties of biological tissues. *Bioelectrochemistry*, 140:107773, 2021. doi: 10.1016/j.bioelechem.2021.107773.

[237] Gabriel, S., Lau, R.W. and Gabriel, C. The dielectric properties of biological tissues: II. Measurements in the frequency range 10 Hz to 20 GHz. *Phys. Med. Biol.*, 41:2251–2269, 1996. doi: 10.1088/0031-9155/41/11/002.

[238] Raicu, V. A simple theoretical and practical approach to measuring dielectric properties with an open-ended coaxial probe. *Meas. Sci. Technol.*, 6(4): 410–414, 1995. doi: 10.1088/0957-0233/6/4/011.

[239] Boukamp, B.A. A Linear Kronig-Kramers Transform Test for Immittance Data Validation. *J. Electrochem. Soc.*, 142(6):1885, 1995. doi: 10.1149/1.2044210.

[240] Schönleber, M., Klotz, D. and Ivers-Tiffée, E. A Method for Improving the Robustness of linear Kramers-Kronig Validity Tests. *Electrochim. Acta*, 131: 20–27, 2014. doi: 10.1016/j.electacta.2014.01.034.

[241] Urquidi-Macdonald, M., Real, S. and Macdonald, D.D. Applications of Kramers-Kronig transforms in the analysis of electrochemical impedance data-III. Stability and linearity. *Electrochim. Acta*, 35(10):1559–1566, 1990. doi: 10.1016/0013-4686(90)80010-L.

[242] Zimmermann, J. and Thiele, L. j-zimmermann/impedancefitter: v2.0.2, 2021. URL `https://doi.org/10.5281/zenodo.5116618`.

[243] Newville, M. et al. lmfit/lmfit-py 1.0.0, 2019. URL `https://doi.org/10.5281/zenodo.3588521`.

[244] Murbach, M. et al. impedance.py: A Python package for electrochemical impedance analysis. *J. Open Source Softw.*, 5(52):2349, 2020. doi: 10.21105/joss.02349.

[245] Zimmermann, J. et al. Using a Digital Twin of an Electrical Stimulation Device to Monitor and Control the Electrical Stimulation of Cells in vitro. *Front. Bioeng. Biotechnol.*, 9:765516, 2021. doi: 10.3389/fbioe.2021.765516.

[246] Mobini, S., Leppik, L. and Barker, J.H. Direct current electrical stimulation chamber for treating cells in vitro. *BioTechniques*, 60(2):95–98, 2016. doi: 10.2144/000114382.

[247] Mobini, S. et al. In vitro effect of direct current electrical stimulation on rat mesenchymal stem cells. *PeerJ*, 5:e2821, 2017. doi: 10.7717/peerj.2821.

[248] Leppik, L. et al. Construction and use of an electrical stimulation chamber for enhancing osteogenic differentiation in mesenchymal stem/stromal cells in vitro. *J. Vis. Exp.*, 2019(143), 2019. doi: 10.3791/59127.

[249] Srirussamee, K. et al. Changes in the extracellular microenvironment and osteogenic responses of mesenchymal stem/stromal cells induced by in vitro direct electrical stimulation. *J. Tissue Eng.*, 12:204173142097414, 2021. doi: 10.1177/2041731420974147.

[250] Srirussamee, K. et al. Direct electrical stimulation enhances osteogenesis by inducing Bmp2 and Spp1 expressions from macrophages and preosteoblasts. *Biotechnol. Bioeng.*, 116(12):3421–3432, 2019. doi: 10.1002/bit.27142.

[251] Schuderer, J. and Kuster, N. Effect of the Meniscus at the Solid/Liquid Interface on the SAR Distribution in Petri Dishes and Flasks. *Bioelectromagnetics*, 24(2):103–108, 2003. doi: 10.1002/bem.10066.

[252] Budde, K. et al. Requirements for Documenting Electrical Cell Stimulation Experiments for Replicability and Numerical Modeling. In *2019 41st Annu. Int. Conf. IEEE Eng. Med. Biol. Soc.*, pages 1082–1088. IEEE, 2019. doi: 10.1109/embc.2019.8856863.

[253] Feinberg, J. and Langtangen, H.P. Chaospy: An open source tool for designing methods of uncertainty quantification. *J. Comput. Sci.*, 11:46–57, 2015. doi: 10.1016/j.jocs.2015.08.008.

[254] Harris, C.R. et al. Array programming with NumPy. *Nature*, 585(7825): 357–362, 2020. doi: 10.1038/s41586-020-2649-2.

[255] Sanchez, B. et al. Basics of broadband impedance spectroscopy measurements using periodic excitations. *Meas. Sci. Technol.*, 23(10):105501, 2012. doi: 10.1088/0957-0233/23/10/105501.

[256] Hudak, E.M. et al. Electron transfer processes occurring on platinum neural stimulating electrodes: calculated charge-storage capacities are inaccessible during applied stimulation. *J. Neural Eng.*, 14(4):046012, 2017. doi: 10.1088/1741-2552/aa6945.

[257] Ragoisha, G.A. et al. Characterisation of the electrochemical redox behaviour of Pt electrodes by potentiodynamic electrochemical impedance spectroscopy. *J. Solid State Electrochem.*, 14(4):531–542, 2010. doi: 10.1007/s10008-008-0663-7.

[258] Butson, C.R. and McIntyre, C.C. Tissue and electrode capacitance reduce neural activation volumes during deep brain stimulation. *Clin. Neurophysiol.*, 116(10):2490–2500, 2005. doi: 10.1016/j.clinph.2005.06.023.

[259] Butenko, K. et al. OSS-DBS: Open-source simulation platform for deep brain stimulation with a comprehensive automated modeling. *PLoS Comput. Biol.*, 16(7):e1008023, 2020. doi: 10.1371/journal.pcbi.1008023.

[260] Butenko, K., Bahls, C. and van Rienen, U. Evaluation of Epistemic Uncertainties for Bipolar Deep Brain Stimulation in Rodent Models. In *2019 41st Annu. Int. Conf. IEEE Eng. Med. Biol. Soc.*, pages 2136–2140. IEEE, 2019. doi: 10.1109/EMBC.2019.8857910.

[261] Paap, M. et al. Deep brain stimulation by optimized stimulators in a phenotypic model of dystonia: Effects of different frequencies. *Neurobiol. Dis.*, 147, 2021. doi: 10.1016/j.nbd.2020.105163.

[262] Loppini, A. et al. Thermal effects on cardiac alternans onset and development: A spatiotemporal correlation analysis. *Phys. Rev. E*, 103(4):L040201, 2021. doi: 10.1103/PhysRevE.103.L040201.

[263] Pfau, J., Leal Ordonez, J.A. and Stieglitz, T. In Situ Measurement of Stimulus Induced pH Changes Using ThinFilm Embedded IrOx pH Electrodes. In *2018 40th Annu. Int. Conf. IEEE Eng. Med. Biol. Soc.*, pages 5049–5052. IEEE, 2018. doi: 10.1109/EMBC.2018.8513441.

[264] Yang, X. et al. Imaging the Electrochemical Impedance of Single Cells via Conductive Polymer Thin Film. *ACS Sensors*, 6(2):485–492, 2021. doi: 10.1021/acssensors.0c02051.

[265] McCreery, D. et al. Charge density and charge per phase as cofactors in neural injury induced by electrical stimulation. *IEEE Trans. Biomed. Eng.*, 37(10):996–1001, 1990. doi: 10.1109/10.102812.

[266] Bosch, R.W. et al. Electrochemical Frequency Modulation: A New Electrochemical Technique for Online Corrosion Monitoring. *Corrosion*, 57(1):60–70, 2001. doi: 10.5006/1.3290331.

[267] Poßner, L. et al. In situ impedance measurements on postmortem porcine brain. *Curr. Dir. Biomed. Eng.*, 6(3):143–146, 2020. doi: 10.1515/cdbme-2020-3037.

[268] Balint, R., Cassidy, N.J. and Cartmell, S.H. Conductive polymers: Towards a smart biomaterial for tissue engineering. *Acta Biomater.*, 10(6):2341–2353, 2014. doi: 10.1016/j.actbio.2014.02.015.

[269] Mawad, D. et al. A conducting polymer with enhanced electronic stability applied in cardiac models. *Sci. Adv.*, 2(11):e1601007, 2016. doi: 10.1126/sciadv.1601007.

[270] Gittens, R.A. et al. Electrical implications of corrosion for osseointegration of titanium implants. *J. Dent. Res.*, 90(12):1389–1397, 2011. doi: 10.1177/0022034511408428.

[271] Hanawa, T. and Ota, M. Calcium phosphate naturally formed on titanium in electrolyte solution. *Biomaterials*, 12(8):767–774, 1991. doi: 10.1016/0142-9612(91)90028-9.

[272] Narayanan, R. et al. Calcium phosphate-based coatings on titanium and its alloys. *J. Biomed. Mater. Res. Part B Appl. Biomater.*, 85B(1):279–299, 2008. doi: 10.1002/jbm.b.30932.

[273] Abasi, S. et al. Design, fabrication and testing of an electrical cell stimulation and recording apparatus (ECSARA) for cells in electroculture. *Biosens. Bioelectron.*, 147:111793, 2020. doi: 10.1016/j.bios.2019.111793.

[274] Amestoy, P.R. et al. A fully asynchronous multifrontal solver using distributed dynamic scheduling. *SIAM J. Matrix Anal. Appl.*, 23(1):15–41, 2002. doi: 10.1137/S0895479899358194.

[275] Brown, J. et al. Composable linear solvers for multiphysics. In *Proceedings - 2012 11th International Symposium on Parallel and Distributed Computing, ISPDC 2012*, pages 55–62. IEEE, 2012. doi: 10.1109/ISPDC.2012.16.

[276] Macleod, M. et al. The MDAR (Materials Design Analysis Reporting) Framework for transparent reporting in the life sciences. *Proc. Natl. Acad. Sci.*, 118(17):e2103238118, 2021. doi: 10.1073/pnas.2103238118.

[277] Portelli, L. Overcoming the Irreproducibility Barrier: Considerations to Improve the Quality of Experimental Practice When Investigating the Effects of Low-Level Electric and Magnetic Fields on In Vitro Biological Systems. In Greenebaum, B. and Barnes, F., editors, *Bioengineering and Biophysical Aspects of Electromagnetic Fields*, pages 435–462. CRC Press, Boca Raton, 4th edition, 2018. doi: 10.1201/9781315186580-12.

[278] Weltin, A. et al. New life for old wires: Electrochemical sensor method for neural implants. *J. Neural Eng.*, 17(1), 2020. doi: 10.1088/1741-2552/ab4c69.

[279] Weltin, A. et al. Standard cochlear implants as electrochemical sensors: Intracochlear oxygen measurements in vivo. *Biosens. Bioelectron.*, 199:113859, 2022. doi: 10.1016/j.bios.2021.113859.

[280] Creason, S.C., Hayes, J.W. and Smith, D.E. Fourier transform faradaic admittance measurements III. Comparison of measurement efficiency for various test signal waveforms. *J. Electroanal. Chem. Interfacial Electrochem.*, 47(1): 9–46, 1973. doi: 10.1016/S0022-0728(73)80343-2.

[281] Wilsdorf, P. et al. Simulation Experiment Schemas – Beyond Tools and Simulation Approaches. In *2019 Winter Simul. Conf.*, pages 2783–2794. IEEE, 2019. doi: 10.1109/WSC40007.2019.9004710.

[282] Ruscheinski, A. et al. An artefact-based workflow for finite element simulation studies. *Simul. Model. Pract. Theory*, 116:102464, 2022. doi: 10.1016/j.simpat.2021.102464.

[283] Zimmermann, J. et al. Numerical simulations as means for tailoring electrically conductive hydrogels towards cartilage tissue engineering by electrical stimulation. *Molecules*, 25(20):4750, 2020. doi: 10.3390/molecules25204750.

[284] Kuchta, M., Mardal, K.A. and Rognes, M.E. Solving the EMI equations using finite element methods. In Tveito, A., Mardal, K.A. and Rognes,

M.E., editors, *Modeling Excitable Tissue: The EMI Framework*, pages 56–69. Springer, Cham, 2021. doi: 10.1007/978-3-030-61157-6_5.

[285] Lamichhane, B.P. and Wohlmuth, B.I. Mortar Finite Elements for Interface Problems. *Computing*, 72:333–348, 2004. doi: 10.1007/s00607-003-0062-y.

[286] Escobar, J.F. et al. Effect of magnetic and electric fields on plasma membrane of single cells: A computational approach. *Eng. Reports*, 2:e12125, 2020. doi: 10.1002/eng2.12125.

[287] Meny, I. et al. Finite-element modeling of cell exposed to harmonic and transient electric fields. *IEEE Trans. Magn.*, 43(4):1773–1776, 2007.

[288] Zheng, Y. et al. Recent advances in microfluidic techniques for single-cell biophysical characterization. *Lab Chip*, 13(13):2464–2483, 2013. doi: 10.1039/c3lc50355k.

[289] Stacey, M.W., Sabuncu, A.C. and Beskok, A. Dielectric characterization of costal cartilage Chondrocytes. *Biochim. Biophys. Acta - Gen. Subj.*, 1840(1): 146–152, 2014. doi: 10.1016/j.bbagen.2013.08.031.

[290] Merla, C. et al. Microdosimetry for nanosecond pulsed electric field applications: A parametric study for a single cell. *IEEE Trans. Biomed. Eng.*, 58(5): 1294–1302, 2011. doi: 10.1109/TBME.2010.2104150.

[291] Vaca-González, J.J. et al. Capacitively coupled electrical stimulation of rat chondroepiphysis explants: A histomorphometric analysis. *Bioelectrochemistry*, 126:1–11, 2019. doi: 10.1016/j.bioelechem.2018.11.004.

[292] Carstensen, E.L., Miller, M.W. and Ciaravino, V. Ceramic Electrodes for ELF Bioeffects Studies. *IEEE Trans. Biomed. Eng.*, BME-31(8):557–558, 1984. doi: 10.1109/TBME.1984.325425.

[293] Ermolina, I., Polevaya, Y. and Feldman, Y. Analysis of dielectric spectra of eukaryotic cells by computer modeling. *Eur. Biophys. J.*, 29(2):141–145, 2000. doi: 10.1007/s002490050259.

[294] Braun, D. and Fromherz, P. Fluorescence interferometry of neuronal cell adhesion on microstructured silicon. *Phys. Rev. Lett.*, 81(23):5241–5244, 1998. doi: 10.1103/PhysRevLett.81.5241.

[295] Braun, D. and Fromherz, P. Imaging neuronal seal resistance on silicon chip using fluorescent voltage-sensitive dye. *Biophys. J.*, 87(2):1351–1359, 2004. doi: 10.1529/biophysj.104.039990.

[296] Kaur, G. et al. Electrically conductive polymers and composites for biomedical applications. *RSC Advances*, 5(47):37553–37567, 2015. doi: 10.1039/c5ra01851j.

[297] Mawad, D., Lauto, A. and Wallace, G.G. Conductive polymer hydrogels. In Kalia, S., editor, *Polymeric Hydrogels as Smart Biomaterials*, pages 19–44. Springer, Cham, 2016. doi: 10.1007/978-3-319-25322-0_2.

[298] Mawad, D. et al. Electroconductive Hydrogel Based on Functional Poly(Ethylenedioxy Thiophene). *Chem. Mater.*, 28(17):6080–6088, 2016. doi: 10.1021/acs.chemmater.6b01298.

[299] Daly, A.C. et al. 3D Bioprinting for Cartilage and Osteochondral Tissue Engineering. *Adv. Healthc. Mater.*, 6(22):1–20, 2017. doi: 10.1002/adhm.201700298.

[300] Li, J. et al. 3D printing of hydrogels: Rational design strategies and emerging biomedical applications. *Mater. Sci. Eng. R Rep.*, 140:100543, 2020. doi: 10.1016/j.mser.2020.100543.

[301] Van Tam, J.K. et al. Mesenchymal stem cell adhesion but not plasticity is affected by high substrate stiffness. *Sci. Technol. Adv. Mater.*, 13(6), 2012. doi: 10.1088/1468-6996/13/6/064205.

[302] Binette, J.S. et al. Tetrapolar measurement of electrical conductivity and thickness of articular cartilage. *J. Biomech. Eng.*, 126(4):475–484, 2004. doi: 10.1115/1.1785805.

[303] Chen, J. et al. Electrodeformation for single cell mechanical characterization. *J. Micromechanics Microengineering*, 21(5), 2011. doi: 10.1088/0960-1317/21/5/054012.

[304] Guido, I., Jaeger, M.S. and Duschl, C. Dielectrophoretic stretching of cells allows for characterization of their mechanical properties. *Eur. Biophys. J.*, 40(3):281–288, 2011. doi: 10.1007/s00249-010-0646-3.

[305] Cho, M.R. et al. Transmembrane calcium influx induced by ac electric fields. *FASEB J.*, 13(6):677–683, 1999.

[306] Li, S. et al. Scaffold channel size influences stem cell differentiation pathway in 3-D printed silica hybrid scaffolds for cartilage regeneration. *Biomater. Sci.*, 8(16):4458–4466, 2020. doi: 10.1039/c9bm01829h.

[307] Leguèbe, M., Poignard, C. and Weynans, L. A second-order Cartesian method for the simulation of electropermeabilization cell models. *J. Comput. Phys.*, 292:114–140, 2015. doi: 10.1016/j.jcp.2015.03.028.

[308] Guyomarc'h, G., Lee, C.O. and Jeon, K. A discontinuous Galerkin method for elliptic interface problems with application to electroporation. *Commun. Numer. Methods Eng.*, 25(10):991–1008, 2009. doi: 10.1002/cnm.1132.

[309] Perrussel, R. and Poignard, C. Asymptotic expansion of steady-state potential in a high contrast medium with a thin resistive layer. *Appl. Math. Comput.*, 221:48–65, 2013. doi: 10.1016/j.amc.2013.06.047.

[310] Fear, E.C. and Stuchly, M.A. Biological cells with gap junctions in low-frequency electric fields. *IEEE Trans. Biomed. Eng.*, 45(7):856–866, 1998. doi: 10.1109/10.686793.

[311] Ranjan, R. and Thakor, N.V. Electrical stimulation of cardiac myocytes. *Ann. Biomed. Eng.*, 23(6):812–821, 1995. doi: 10.1007/BF02584480.

[312] Lojewska, Z. et al. Analysis of the effect of medium and membrane conductance on the amplitude and kinetics of membrane potentials induced by externally applied electric fields. *Biophys. J.*, 56(1):121–128, 1989.

[313] Leguèbe, M. et al. Conducting and permeable states of cell membrane submitted to high voltage pulses: Mathematical and numerical studies validated by the experiments. *J. Theor. Biol.*, 360:83–94, 2014. doi: 10.1016/j.jtbi.2014.06.027.

[314] Asami, K. Dielectric properties of microvillous cells simulated by the three-dimensional finite-element method. *Bioelectrochemistry*, 81(1):28–33, 2011. doi: 10.1016/j.bioelechem.2011.01.002.

[315] Ciuperca, I.S., Perrussel, R. and Poignard, C. Two-scale analysis for very rough thin layers. An explicit characterization of the polarization tensor. *J. des Math. Pures Appl.*, 95(3):277–295, 2011. doi: 10.1016/j.matpur.2010.12.001.

[316] Cho, M.R. et al. Induced redistribution of cell surface receptors by alternating current electric fields. *FASEB J.*, 8(10), 1994. doi: 10.1096/fasebj.8.10.8050677.

[317] Poignard, C. et al. Ion fluxes, transmembrane potential, and osmotic stabilization: A new dynamic electrophysiological model for eukaryotic cells. *Eur. Biophys. J.*, 40(3):235–246, 2011. doi: 10.1007/s00249-010-0641-8.

[318] Casciola, M. and Tarek, M. A molecular insight into the electro-transfer of small molecules through electropores driven by electric fields. *Biochim. Biophys. Acta - Biomembr.*, 1858(10):2278–2289, 2016. doi: 10.1016/j.bbamem.2016.03.022.

[319] Shamoon, D., Lasquellec, S. and Brosseau, C. Perspective: Towards understanding the multiscale description of cells and tissues by electromechanobiology. *J. Appl. Phys.*, 123(24), 2018. doi: 10.1063/1.5018723.

[320] Ni, Y. et al. A review of the general aspects of radiofrequency ablation. *Abdom. Imaging*, 30(4):381–400, 2005. doi: 10.1007/s00261-004-0253-9.

[321] Singh, S. and Melnik, R. Thermal ablation of biological tissues in disease treatment: A review of computational models and future directions. *Electromagn. Biol. Med.*, 39(2):49–88, 2020. doi: 10.1080/15368378.2020.1741383.

[322] Nuernberger, S. et al. The influence of scaffold architecture on chondrocyte distribution and behavior in matrix-associated chondrocyte transplantation grafts. *Biomaterials*, 32(4):1032–1040, 2011. doi: 10.1016/j.biomaterials.2010.08.100.

[323] Iglesias, D. et al. The Glitter of Carbon Nanostructures in Hybrid/Composite Hydrogels for Medicinal Use. *Curr. Top. Med. Chem.*, 16(18):1976–1989, 2016. doi: 10.2174/1568026616666160215154807.

[324] Han, L. et al. A Mussel-Inspired Conductive, Self-Adhesive, and Self-Healable Tough Hydrogel as Cell Stimulators and Implantable Bioelectronics. *Small*, 13(2):1–9, 2017. doi: 10.1002/smll.201601916.

[325] Sieber, S. et al. Importance of osmolarity and oxygen tension for cartilage tissue engineering. *BioResearch Open Access*, 9(1):106–115, 2020. doi: 10.1089/biores.2020.0009.

[326] Wenger, C. et al. A Review on Tumor-Treating Fields (TTFields): Clinical Implications Inferred from Computational Modeling. *IEEE Rev. Biomed. Eng.*, 11:195–207, 2018. doi: 10.1109/RBME.2017.2765282.

[327] Sabri, E. and Brosseau, C. Proximity-induced electrodeformation and membrane capacitance coupling between cells. *Eur. Biophys. J.*, 50:713–720, 2021. doi: 10.1007/s00249-021-01504-w.

[328] Mistani, P. et al. A parallel Voronoi-based approach for mesoscale simulations of cell aggregate electropermeabilization. *J. Comput. Phys.*, 380:48–64, 2019. doi: 10.1016/j.jcp.2018.12.009.

[329] Mollenhauer, J.A. Perspectives on articular cartilage biology and osteoarthritis. *Injury*, 39S1:S5–S12, 2008. doi: 10.1016/j.injury.2008.01.044.

[330] Nagarajan, M.B. et al. Computer-aided diagnosis in phase contrast imaging x-ray computed tomography for quantitative characterization of ex vivo human

patellar cartilage. *IEEE Trans. Biomed. Eng.*, 60(10):2896–2903, 2013. doi: 10.1109/TBME.2013.2266325.

[331] Hasegawa, I. et al. Dependence of electrical conductivity on fixed charge density in articular cartilage. *Clin. Orthop. Relat. Res.*, 177:283–288, 1983. doi: 10.1097/00003086-198307000-00039.

[332] Gu, W.Y. and Justiz, M.A. Apparatus for measuring the swelling dependent electrical conductivity of charged hydrated soft tissues. *J. Biomech. Eng.*, 124(6):790–793, 2002. doi: 10.1115/1.1516571.

[333] Gabriel, S., Lau, R.W. and Gabriel, C. The dielectric properties of biological tissues: III. Parametric models for the dielectric spectrum of tissues. *Phys. Med. Biol.*, 41(11):2271–2293, 1996. doi: 10.1088/0031-9155/41/11/003.

[334] Gabriel, C. Compilation of the Dielectric Properties of Body Tissues at RF and Microwave Frequencies. Technical report, Occupational and environmental health directorate, Radiofrequency Radiation Division, Brooks Air Force Base, Texas (USA), 1997. URL `http://niremf.ifac.cnr.it/docs/DIELECTRIC/home.html`.

[335] Gabriel, C., Gabriel, S. and Corthout, E. The dielectric properties of biological tissues: I. Literature survey. *Phys. Med. Biol.*, 41(11):2231–2249, 1996. doi: 10.1088/0031-9155/41/11/001.

[336] Hasgall, P. et al. IT'IS Database for thermal and electromagnetic parameters of biological tissues. Website, 2018. URL `itis.swiss/database`. Version 4.0.

[337] Gabriel, C., Peyman, A. and Grant, E.H. Electrical conductivity of tissue at frequencies below 1 MHz. *Phys. Med. Biol.*, 54(16):4863–4878, 2009. doi: 10.1088/0031-9155/54/16/002.

[338] Logothetis, N.K., Kayser, C. and Oeltermann, A. In Vivo Measurement of Cortical Impedance Spectrum in Monkeys: Implications for Signal Propagation. *Neuron*, 55(5):809–823, 2007. doi: 10.1016/j.neuron.2007.07.027.

[339] Bédard, C. and Destexhe, A. Macroscopic models of local field potentials and the apparent 1/f noise in brain activity. *Biophys. J.*, 96(7):2589–2603, 2009. doi: 10.1016/j.bpj.2008.12.3951.

[340] Epstein, B.R. and Foster, K.R. Anisotropy in the dielectric properties of skeletal muscle. *Med. Biol. Eng. Comput.*, 21(1):51–55, 1983. doi: 10.1007/BF02446406.

[341] Gersing, E. Impedance spectroscopy on living tissue for determination of the state of organs. *Bioelectrochemistry Bioenerg.*, 45(2):145–149, 1998. doi: 10.1016/S0302-4598(98)00079-8.

[342] Gheorghiu, M., Gersing, E. and Gheorghiu, E. Quantitative analysis of impedance spectra of organs during ischemia. In *Ann. N. Y. Acad. Sci.*, volume 873, pages 65–71, 1999. doi: 10.1111/j.1749-6632.1999.tb09450.x.

[343] Casas, O. et al. In vivo and in situ ischemic tissue characterization using electrical impedance spectroscopy. In *Ann. N. Y. Acad. Sci.*, volume 873, pages 51–58, 1999. doi: 10.1111/j.1749-6632.1999.tb09448.x.

[344] Martinsen, Ø.G., Grimnes, S. and Mirtaheri, P. Non-invasive measurements of post-mortem changes in dielectric properties of haddock muscle - a pilot study. *J. Food Eng.*, 43(3):189–192, 2000. doi: 10.1016/S0260-8774(99)00151-X.

[345] Stoneman, M.R. et al. Correction of electrode polarization contributions to the dielectric properties of normal and cancerous breast tissues at audio/radiofrequencies. *Phys. Med. Biol.*, 52(22):6589–6604, 2007. doi: 10.1088/0031-9155/52/22/003.

[346] Ishai, P.B. et al. An assessment of comparative methods for approaching electrode polarization in dielectric permittivity measurements. *Rev. Sci. Instrum.*, 83(8):083118, 2012. doi: 10.1063/1.4746992.

[347] Kuang, W. and Nelson, S.O. Low-frequency dielectric properties of biological tissues: A review with some new insights. *Trans. Am. Soc. Agric. Eng.*, 41 (1):173–184, 1998. doi: 10.13031/2013.17142.

[348] Schaefer, M. et al. The complex dielectric spectrum of heart tissue during ischemia. *Bioelectrochemistry*, 58(2):171–180, 2002. doi: 10.1016/ S1567-5394(02)00152-4.

[349] Asami, K. Dielectric properties of biological tissues in which cells are connected by communicating junctions. *J. Phys. D. Appl. Phys.*, 40(12):3718–3727, 2007. doi: 10.1088/0022-3727/40/12/027.

[350] Di Biasio, A. and Cametti, C. Polarizability of spherical biological cells in the presence of localized surface charge distributions at the membrane interfaces. *Phys. Rev. E*, 82(2):021917, 2010. doi: 10.1103/PhysRevE.82.021917.

[351] Di Biasio, A., Ambrosone, L. and Cametti, C. Dielectric properties of biological cells in the dipolar approximation for the single-shell ellipsoidal model: The effect of localized surface charge distributions at the membrane interface. *Phys. Rev. E - Stat. Nonlinear, Soft Matter Phys.*, 82(4):1–9, 2010. doi: 10.1103/PhysRevE.82.041916.

[352] Asami, K. Dielectric spectroscopy reveals nanoholes in erythrocyte ghosts. *Soft Matter*, 8(11):3250–3257, 2012. doi: 10.1039/c2sm06306a.

[353] Mazzeo, B.A. and Flewitt, A.J. Two- and four-electrode, wide-bandwidth, dielectric spectrometer for conductive liquids: Theory, limitations, and experiment. *J. Appl. Phys.*, 102(10), 2007. doi: 10.1063/1.2815666.

[354] Wagner, T. et al. Impact of brain tissue filtering on neurostimulation fields: A modeling study. *Neuroimage*, 85:1048–1057, 2014. doi: 10.1016/j.neuroimage.2013.06.079.

[355] McCann, H., Pisano, G. and Beltrachini, L. Variation in Reported Human Head Tissue Electrical Conductivity Values. *Brain Topogr.*, 32(5):825–858, 2019. doi: 10.1007/s10548-019-00710-2.

[356] Raicu, V. Dielectric dispersion of biological matter: Model combining Debye-type and "universal" responses. *Phys. Rev. E*, 60(4):4677–4680, 1999. doi: 10.1103/PhysRevE.60.4677.

[357] Stoneman, M.R. et al. Non-Debye dielectric behavior and near-field interactions in biological tissues: When structure meets function. *J. Non. Cryst. Solids*, 356(11-17):772–776, 2010. doi: 10.1016/j.jnoncrysol.2009.06.056.

[358] Edd, J.F., Horowitz, L. and Rubinsky, B. Temperature dependence of tissue impedivity in electrical impedance tomography of cryosurgery. *IEEE Trans. Biomed. Eng.*, 52(4):695–701, 2005. doi: 10.1109/TBME.2005.844042.

[359] Ivorra, A. and Rubinsky, B. In vivo electrical impedance measurements during and after electroporation of rat liver. *Bioelectrochemistry*, 70(2):287–295, 2007. doi: 10.1016/j.bioelechem.2006.10.005.

[360] Haemmerich, D. et al. Electrical conductivity measurement of excised human metastatic liver tumours before and after thermal ablation. *Physiol. Meas.*, 30(5):459–466, 2009. doi: 10.1088/0967-3334/30/5/003.

[361] Raicu, V., Saibara, T. and Irimajiri, A. Dielectric properties of rat liver in vivo: A noninvasive approach using an open-ended coaxial probe at audio/radio frequencies. *Bioelectrochemistry Bioenerg.*, 47(2):325–332, 1998. doi: 10.1016/S0302-4598(98)00171-8.

[362] Onaral, B. and Schwan, H.P. Linear and nonlinear properties of platinum electrode polarisation. Part 1: frequency dependence at very low frequencies. *Med. Biol. Eng. Comput.*, 20(3):299–306, 1982. doi: 10.1007/BF02442796.

[363] Asami, K. Design of a measurement cell for low-frequency dielectric spectroscopy of biological cell suspensions. *Meas. Sci. Technol.*, 22(8), 2011. doi: 10.1088/0957-0233/22/8/085801.

[364] Tuncer, E., Serdyuk, Y.V. and Gubanski, S.M. Dielectric mixtures: Electrical properties and modeling. *IEEE Trans. Dielectr. Electr. Insul.*, 9(5):809–828, 2002. doi: 10.1109/TDEI.2002.1038664.

[365] Hanai, T., Asami, K. and Korzumi, N. Dielectric Theory of Concentrated Suspensions of Shell-Spheres in Particular Reference to the Analysis of Biological Cell Suspensions. *Bull. Inst. Chem. Res., Kyoto Univ*, 57(4):297–305, 1979.

[366] Ron, A. et al. Theoretical examination of aggregation effect on the dielectric characteristics of spherical cellular suspension. *Biophys. Chem.*, 140(1-3): 39–50, 2009. doi: 10.1016/j.bpc.2008.11.008.

[367] Bennetts, C.J., Sibole, S. and Erdemir, A. Automated generation of tissue-specific three-dimensional finite element meshes containing ellipsoidal cellular inclusions. *Comput. Methods Biomech. Biomed. Eng.*, 18(12):1293–1304, 2015. doi: 10.1080/10255842.2014.900545.

[368] Feldman, Y., Ermolina, I. and Hayashi, Y. Time domain dielectric spectroscopy study of biological systems. *IEEE Trans. Dielectr. Electr. Insul.*, 10: 728–753, 2003. doi: 10.1109/TDEI.2003.1237324.

[369] Smith, B.F., Bjørstad, P.E. and Gropp, W.D. *Domain decomposition: parallel multilevel methods for elliptic partial differential equations*. Cambridge Univ. Press, Cambridge, 1996.

[370] Bernardi, C., Maday, Y. and Rapetti, F. Basics and some applications of the mortar element method. *GAMM-Mitteilungen*, 28(2):97–123, 2005. doi: 10.1002/gamm.201490020.

[371] Stoneman, M. et al. Protein influence on the plasma membrane dielectric properties: In vivo study utilizing dielectric spectroscopy and fluorescence microscopy. *Bioelectrochemistry*, 70(2):542–550, 2007. doi: 10.1016/j.bioelechem.2006.12.008.

[372] Mazzeo, B.A. et al. Temperature-stable parallel-plate dielectric cell for broadband liquid impedance measurements. *Rev. Sci. Instrum.*, 81(12), 2010. doi: 10.1063/1.3509388.

[373] Bangerth, W. et al. Algorithms and data structures for massively parallel generic adaptive finite element codes. *ACM Trans. Math. Softw.*, 38(2), 2011. doi: 10.1145/2049673.2049678.

[374] Wieland, D.C. et al. Propagation-Based Phase Contrast Computed Tomography as a Suitable Tool for the Characterization of Spatial 3D Cell Distribution in Biomaterials. *Adv. Eng. Mater.*, 23(11):2001188, 2021. doi: 10.1002/adem.202001188.

[375] Makarov, S.N. et al. Boundary element fast multipole method for modeling electrical brain stimulation with voltage and current electrodes. *Journal of Neural Engineering*, 18(4), 2021. doi: 10.1088/1741-2552/ac17d7.

[376] Ofek, G. et al. Matrix Development in Self-Assembly of Articular Cartilage. *PLoS One*, 3(7):e2795, 2008. doi: 10.1371/journal.pone.0002795.

[377] Giaever, I. and Keese, C.R. A morphological biosensor for mammalian cells. *Nature*, 366(6455):591–592, 1993. doi: 10.1038/366591a0.

[378] Hildebrandt, C. et al. Detection of the osteogenic differentiation of mesenchymal stem cells in 2D and 3D cultures by electrochemical impedance spectroscopy. *J. Biotechnol.*, 148(1):83–90, 2010. doi: 10.1016/j.jbiotec.2010.01.007.

[379] Dodwell, T.J. et al. Multilevel Markov Chain Monte Carlo. *SIAM Rev.*, 61 (3):509–545, 2019. doi: 10.1137/19M126966X.

[380] Evers, J. and Lowery, M. The Active Electrode in the Living Brain: The Response of the Brain Parenchyma to Chronically Implanted Deep Brain Stimulation Electrodes. *Oper. Neurosurg.*, 20(2):131–140, 2020. doi: 10.1093/ons/opaa326.

[381] Boehler, C., Stieglitz, T. and Asplund, M. Nanostructured platinum grass enables superior impedance reduction for neural microelectrodes. *Biomaterials*, 67:346–353, 2015. doi: 10.1016/j.biomaterials.2015.07.036.

[382] Boehler, C. et al. NanoPt - A Nanostructured Electrode Coating for Neural Recording and Microstimulation. *ACS Appl. Mater. Interfaces*, 12(13):14855–14865, 2020. doi: 10.1021/acsami.9b22798.

[383] Presman, A.S. *Electromagnetic Fields and Life.* Springer, Boston, MA, 1970. doi: 10.1007/978-1-4757-0635-2.

[384] Glaser, R. *Heilende Magnete - strahlende Handys. Bioelektromagnetismus – Fakten und Legenden.* Wiley-VCH, Weinheim, 2012.

[385] Kell, D.B. and Oliver, S.G. Here is the evidence, now what is the hypothesis? The complementary roles of inductive and hypothesis-driven science in the post-genomic era. *BioEssays*, 26(1):99–105, 2004. doi: 10.1002/bies.10385.

[386] Collard, J.F. and Hinsenkamp, M. Cellular processes involved in human epidermal cells exposed to extremely low frequency electric fields. *Cell. Signal.*, 27(5):889–898, 2015. doi: 10.1016/j.cellsig.2015.02.007.

[387] Burny, F., Herbst, E. and Hinsenkamp, M., editors. *Electric Stimulation of Bone Growth and Repair*. Springer, Berlin, Heidelberg, 1978. doi: 10.1007/978-3-642-81193-7.

[388] Meurer, A. et al. Sympy: symbolic computing in python. *PeerJ Comput. Sci.*, 3:e103, 2017. doi: 10.7717/peerj-cs.103.

[389] Sukhorukov, V.L. et al. A single-shell model for biological cells extended to account for the dielectric anisotropy of the plasma membrane. *J. Electrostat.*, 50(3):191–204, 2001. doi: 10.1016/S0304-3886(00)00037-1.

[390] Lempka, S.F. et al. In vivo impedance spectroscopy of deep brain stimulation electrodes. *J. Neural Eng.*, 6(4), 2009. doi: 10.1088/1741-2560/6/4/046001.

[391] Weisstein, E.W. Lanczos sigma factor. From MathWorld—A Wolfram Web Resource, 2021. URL `https://mathworld.wolfram.com/LanczosSigmaFactor.html`. Last visited on 29/05/2021.

Selbstständigkeitserklärung

Hiermit erkläre ich, dass ich die vorliegende Dissertation mit dem Titel "Numerical modelling of electrical stimulation for cartilage tissue engineering" selbstständig und ohne fremde Hilfe und nur unter Verwendung der von mir angegebenen Quellen und Hilfsmittel verfasst habe.

Rostock, 29.08.2022

Julius Zimmermann